NORTHWESTERN UNIVERSITY

Transient Absorption Microscopy Study of Excited-State Dynamics and the Structural Origins in Metal Halide Perovskites

A DISSERTATION

SUBMITTED TO THE GRADUATE SCHOOL

IN PARTIAL FULFILLMENT OF THE REQUIREMENTS

for the degree

DOCTOR OF PHILOSOPHY

Field of Chemistry

By

Xinyi Jiang

EVANSTON, ILLINOIS

September 2021

Abstract

Metal halide perovskites have recently emerged as one of the most promising active layers in solar cells for their high power conversion efficiency (>25%) and ease of synthesis and deposition. Spatial heterogeneity is inevitable with current fabrication methods for both monocrystalline and polycrystalline perovskite thin films and crystals. The morphology-dependent imaging of the excited-state dynamics is crucial to the understanding of the conversion efficiency resulting from different fabrication methods. Key processes affecting the performance of the absorber layers include carrier recombination, carrier cooling, and carrier trapping, which mostly happen on the ultrafast timescale (sub-picosecond). To capture all the processes happening across a broad energy landscape, broadband detection is required. In this work, broadband pump-probe spectroscopy and confocal microscopy are combined into one setup, the transient absorption microscope (TAM), to realize hyperspectral imaging of the ultrafast dynamics in metal halide perovskites.

Studies on both perovskite thin films and crystals were performed. The first part of the thesis is focused on mapping the morphology-related carrier dynamics in polycrystalline perovskite thin films. Fundamental carrier properties like the Fermi energy level, cooling rate, and defect concentration were extracted from the transient absorption (TA) spectrum acquired at every single pixel. Hundreds of pixels were scanned in one experiment, and the correlations between the carrier properties and the morphological information, for example, grain boundary (GB), were verified using statistical models. The high-dimensional datasets containing spatial, spectral, temporal, and morphological information create the challenge of analyzing gigabytes of correlated data, which typically takes enormous computational resources. To solve this problem,

a new global analysis method based on variable projection and subsampling was invented. This method improved the spectrum-fitting speed by a factor of 1500 and was more sensitive to weak spatial and spectral features. The second part of the thesis is focused on the study of monocrystalline perovskite microcrystals or nanocrystals. As an optical microscopic tool, the spatial resolution of the TAM is limited by the light wavelength and objective lenses used. To study the impact of structural change below the diffraction limit, single-particle spectroscopy was performed on monocrystalline perovskite crystals. By varying the cations in the perovskite lattices and organic spacers between perovskite layers, different levels of lattice distortions and multiple stacking geometries were created. The lattice distortion caused by the sterically large organic spacers was found to be the determining factor in the formation of deep trap states detrimental to carrier harvesting.

Acknowledgements

Honestly, I think this is probably how far most of the potential readers of this thesis would go so I tried to put some effort into it.

Finally, this journey is going to reach an end. I do not know what to write, though I usually do. Sometimes I feel that I changed a lot during these five years, but now I realize I did not. I am still the same person that enjoys the pure fun from making discoveries. Five years is a long time, but I still remember the day I collected the first transient absorption spectrum by myself. It is like only one femtosecond has passed and the happiness still feels so real. I even remember the blue-white-red colormap used in that LabVIEW program. It was on the Christmas Eve of 2016. I don't have my families around me because it is extremely hard for an international student to step outside the States and get back on time, but I have my labmates and science around me.

Getting a PhD is not easy. Sometimes the only reason that stops you from quitting is the tiny hope at the other end of the tunnel that one day you will be addressed as a doctor, and, jokes aside, the support you get from the lovely people in your life. I would first like to thank all my friends and families, no matter we contact on a daily, monthly, or yearly basis, no matter we met in real life or online, not only for the emotional support but also for all the fun we had together.

During my PhD, I had the pleasure of learning from and working with a lot of great graduate students and postdocs. I would like to first thank Boris Spokoyny, for the laser maze game you gave me the first Christmas I joined the group (I still have it) and all the things about laser and electronics you taught me. I would like to thank Sunhong Jun for being a good friend and teaching me everything about NOPA and FROG and aligning that diabolic parabolic mirror for

me. I miss the days we spent together aligning that extremely high-power laser together after you went back to Korea. It was exciting and scary at the same time. I want to tell every colleague I had in the Harel lab, the first two years, the time we spent together, though hard, was still the happiest time I had in the grad school. Though I barely knew anything, I was learning new stuff every day, and when I ran into problems, I could always find help by walking into the lab next door. I would never have achieved what I had now without the help of all of you.

Next, I want to thank all the great advisors I met through this journey. When I first started doing research in college, I met Professor Wei Feng, who is extremely smart and nice. He is the one who led me into the world of science and showed me the beauty of it. The other advisor I had in college was Professor Fuyou Li, who really cares about students' well-being. I still remember he never let us stay too late in the lab and arranged badminton games on weekends for us. It really feels like a family there. Lastly, I want to thank my PhD advisor, Emily, for all the support and encouragement in everything. It would be impossible to list all the help you gave to me. What I realized after spending all these years in academia is that it is hard to find an advisor that cares not only about the work you do, but also about you as a real person. I am extremely lucky to meet all three of them.

List of Abbreviations

Abbreviation	Definition
2D	two-dimensional
3D	three-dimensional
AA	allylammonium
AFM	atomic force microscope/microscopy
AOM	acousto-optic modulator
BA	butylammonium
BBO	beta barium borate
BS	beam splitter
CARS	coherent anti-Stokes Raman spectroscopy
CB	conduction band
CBM	conduction band minimum
CCD	charge-coupled device
CLSM	confocal laser-scanning microscope
CMOS	complementary metal oxide semiconductor
CW	continuous-wave
DAS	decay associated spectrum/spectra
DFT	density functional theory
DJ	Dion-Jacobson
DMF	dimethylformamide
EA	ethylammonium
EDS	energy-dispersive X-ray spectroscopy

EMCCD	electron multiplying charge-coupled device
ESA	excited state absorption
FRET	Föster resonant energy transfer
FT-CARS	Fourier transform coherent anti-Stokes Raman scattering spectroscopy
GB	grain boundary
GGA	generalized gradient approximation
GI	grain interior
GSB	ground state bleaching
GT	ground truth
HB	hydrogen-bonding
IPA	iodopropylammonium
IR	infrared
iSCAT	interferometric scattering microscopy
IVM	impulsive vibrational microscope/microscopy
IVS	impulsive vibrational spectroscopy
KS	Kolmogorov–Smirnov
Laser	light amplification by stimulated emission of radiation
LDOS	local density of states
LO	longitudinal optical
MA	methylammonium
NA	numerical aperture
NOPA	noncolinear optical parametric amplifier
OPA	optical parametric amplifier
OPV	organic photovoltaic

PBE	Perdew-Burke-Ernzerhof
PIA	photo-induced absorption
PL	photoluminescence
PMMA	poly (methyl methacrylate)
PP	pixel-by-pixel
ppTB-mBJ	Tran-Blaha-Modified Becke-Johnson pseudopotential
PXRD	powder X-ray diffraction
ROI	region of interest
RP	Ruddlesden-Popper
SAS	species associated spectrum/spectra
SCXRD	single crystal X-ray diffraction
SE	stimulated emission
SEM	scanning electron microscope/microscopy
SEM-TAM	scanning electron microscope correlated transient absorption microscope
SNR	signal-to-noise ratio
SOC	spin-orbit coupling
SRS	stimulated Raman scattering
SWNT	single-walled nanotube
TA	transient absorption
TAM	transient absorption microscope/microscopy
TB-mBJ	Tran-Blaha-Modified Becke-Johnson potential
TG-FROG	transient-gating frequency resolved optical gating
TMD	transition metal dichalcogenide
TRPL	time-resolved photoluminescence

TTL	transistor–transistor logic
VB	valence band
VBM	valence band maximum
VPSS	variable projection and subsampling
WL	white light
WLC	white light continuum
XRD	X-ray diffraction
YAG	yttrium aluminum garnet

Table of Contents

List of Figures

List of Tables

CHAPTER 1 Introduction

1.1 A Brief History of Optical Microscopy

More than 300 years has passed since Robert Hooke invented the first modern optical microscope in human history. The book, *Micrographia, Or, Some Physiological Descriptions of Minute Bodies Made by Magnifying Glasses: With Observations and Inquiries Thereupon*, detailing his research, can now be easily found online and accessed for free by the public.[1] With vivid hand-drawn illustrations and scientific explanations, it is still interesting to read. As is stated in the preface of this book, observation is always the foundation of experimental sciences. The history of modern microscopy is a history of mankind developing imaging instruments to make observations at scales impossible to achieve before. Better lenses were made, and better resolutions were achieved. In 1873, 200 years after the publication of *Micrographia*, Ernst Abbe discovered Abbe's law of diffraction and laid the foundation of light microscopy. The spatial resolution of an optical microscope was found to be strictly defined by the wavelength of the light and the objective lens used. The theoretic limit of the spatial resolution that could be achieved by optical microscopes, caused by the diffraction of light, was also calculated.[2] The development of optical microscopy, however, did not stop because of the discovery of the diffraction limit. (The spatial resolution problem was later solved by the invention of electron microscopes[3] and super-resolution optical microscopes[4, 5]) The next groundbreaking discovery in the field of optical microscopy was the invention of the confocal microscope, patent filed in 1961.[6-8] By inserting a pinhole into the detection line, all out-of-focus light was rejected, and thin optical sections could be made from thick specimen and samples. Another technology widely applied nowadays in microscopy, light amplification by stimulated emission of radiation (laser),

was under development around the same time. The combination of the two cutting-edge technologies developed by that time led to the invention of the confocal laser-scanning microscope (CLSM).[9, 10] The inclusion of laser as an intense, monochromatic and coherent light source made it possible to generate clean optical sections completely free from out-of-focus stray light.

1.2 The Need of Ultrafast Temporal Resolution and the Development of Pump-Probe Spectroscopy

CLSM, though powerful, is far from being a cure-all. With the fast development of modern chemistry and biology, more demands were made on imaging tools. In a complicated chemical or biological system with many degrees of freedom, the images collected using CLSM can be highly congested and a lot of ambiguity exists in the interpretation of the images and the spectra. Temporal resolution was another problem. CLSM is a scanning-based setup, not a wide-field one. To construct a full image of the region of interest (ROI), the sample needs to be scanned pixel by pixel, either by a scanning stage or a pair of mirror galvanometers. Even with the fast mirror galvanometers, the frame rate is limited to several frames per second.[8] Any reaction that happens within one second, including protein folding, membrane diffusion, conformational fluctuation, and fluorescence decay, could not be probed.[11]

The solution to both problems was to increase the temporal resolution, as expanding the data space would not only provide better resolution but also deconvolute the images or spectra and clear the ambiguity in data interpretation. Ultrafast (sub-picosecond, 1 picosecond = 10^{-12} s)

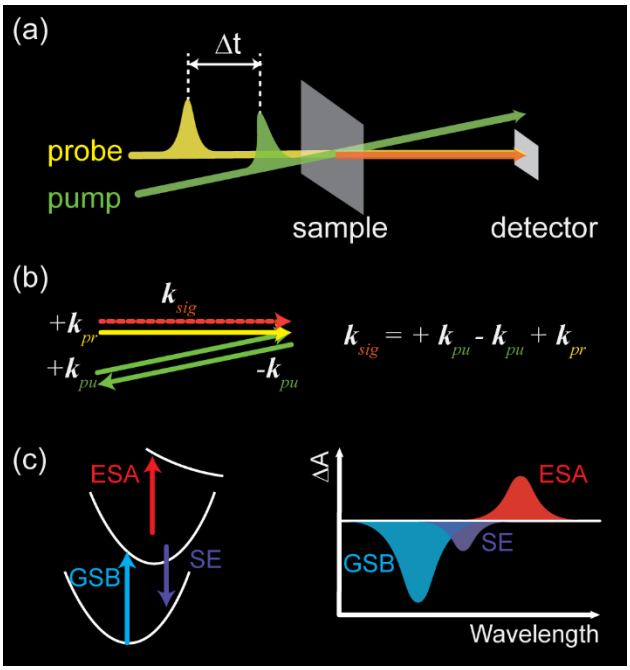

Figure 1.1 Schematic illustration of a pump-probe/TA experiment. (a) The geometry used in a pump-probe experiment. One pump and one probe beam are focused on the sample plane. The pump-probe signal is created in the same direction as the probe beam and collected by the detector. (b) The phase-matching condition of pump, probe, and signal in a pump-probe experiment. (c) Processes involved in pump-probe experiments. The absorption from the ground state to the excited state is reduced when excited-state species are created. This phenomenon is referred to as the ground state bleaching (GSB) and is negative when plotting the change in absorption. Excited state absorption (ESA) and stimulated emission (SE) are caused by the newly created excited-state species. When plotting the change in absorption, ESA is positive, and SE is negative.

spectroscopy emerged, with the development of femtosecond lasers (1 femtosecond = 10^{-15} s), as the solution to achieve femtosecond-scale temporal resolution.[12] The major difference between ultrafast spectroscopy and continuous-wave (CW) spectroscopy is that it uses ultrafast laser pulses as the excitation and probing sources. Because the energy from the light is compressed into a single pulse lasted for only tens to hundreds of femtoseconds, all the reactions are triggered within an ultrashort time window, and the following reactions are either triggered or

detected with ultrashort pulses, which interact with the sample at defined ultrashort time windows as well.

Pump-probe spectroscopy or transient absorption (TA) spectroscopy is probably one of the most widely used nonlinear spectroscopic tools, and we will focus on this spectroscopic technique only in this thesis. It is a powerful technique to probe the ultrafast dynamics with femtosecond resolution. The setup is fairly easy to construct, and the concept is straightforward to understand. Though pump-probe by nature is a third-order nonlinear technique, usually no theoretic background in nonlinear spectroscopy is required to understand or interpret the spectrum collected.

A typical geometry used in a pump-probe experiment is illustrated in Figure 1.1a. Two beams, one pump, the other probe, are focused at the sample plane. The two pulses should overlap both spatially and temporally, which is relatively easy to realize in an ensemble spectroscopic setup when the beam diameters are around several hundreds of microns. The pump pulse creates a population of excited-state species. The time-dependent changes in absorption caused by the excited states are detected through the change of the intensity of the probe, usually delayed (Δt) relatively to the pump, that transmits the sample. Basically, it is a measurement of the time-dependent absorption spectra. The signal is generated in the exact same direction as the probe (due to the phase-matching condition required for pump-probe experiments, Figure 1.1b), which can be heterodyne detected using the probe pulse. The probe pulse is also acting as the local oscillator here. It increases the signal intensity reaching the detector, which is crucial in the detection of weak high-order nonlinear signals. More details about the phase matching in

nonlinear spectroscopy can be found in the book *Principles of Nonlinear Optical Spectroscopy* by Shaul Mukamel.[13]

Three kinds of signals are generated in pump-probe spectroscopy, ground state bleaching (GSB), excited state absorption (ESA, or photo-induced absorption, PIA), and stimulated emission (SE). GSB is present when excited-state populations are created, and the absorption from the ground state to the corresponding excited state is reduced, causing a "bleach" in the absorption spectrum. When plotting the change in absorption (ΔA), GSB is always negative (Figure 1.1c). ESA or PIA is the absorption caused by the newly created excited-state species and should be positive. SE is the emission from the excited state and is negative. The interpretation of TA spectra, however, should not be limited to these three common features only. The change in the absorption spectrum can be caused by a lot of different factors, like peak broadening and shifting, the physical nature of which shall be carefully examined in order to interpret the spectrum correctly. For example, the Stark effect in semiconductors will cause a bandgap shrink, and the absorption peaks will shift accordingly and cause derivative features in the TA spectrum.[14-16] These features caused by a peak shift should not be assigned to be GSB or ESA.

To acquire a TA spectrum as is shown in Figure 1.1c, a broadband probe is required. Instead of sending in a single-color probe, a white light continuum (WLC), generated by focusing a laser beam onto a dielectric media like CaF_2, yttrium aluminum garnet (YAG), or water,[17] is used as the probe beam instead. The chirped WLC can be compressed with a pair of chirped mirrors or a pair of prisms to be used as an ultrafast probe.[15] The change in the WLC probe is detected using an array detector after different colors are spread by an optical grating.

Pump-probe spectroscopy solves the problem of probing ultrafast dynamics in a simple and elegant way; however, the space dimension is not explored. One problem with ensemble spectroscopy is that it averages over a large region. For heterogeneous samples, the difference between disparate regions is usually averaged out. For example, if feature A is present in a small grain ~10 μm^2 big, with a beam size of ~1000 μm^2, the signal intensity would be weakened by a factor of one hundred and might not even be detectable. If reaction A is only present in grain 1, while reaction B only happens in grain 2 next to grain 1, with ensemble spectroscopy, reaction A and B would be considered to be happening at the same location, which leads to incorrect interpretation of the spectrum. Ensemble spectroscopy also has limited application in the study of single particles or molecules. To solve these problems and combine the best temporal and spatial resolution into one setup, the transient absorption microscope (TAM) was invented to probe the dynamics in a selected small region, for instance, single grain or grain boundary (GB), in a heterogeneous sample. The boundary between microscopy and spectroscopy started to blur, but the application of single-color TAM was still largely limited, especially for the mapping of excited-state properties across a broad spectral range, as the absorption at one wavelength was probed a single time. To collect the dynamics across a broad energy landscape, several experiments at different wavelengths were required, posing big challenges in acquisition speed and sample stability.

1.3 Hyperspectral Imaging with Time and Spectrally Resolved Transient Absorption Microscope

1.3.1 Hyperspectral Imaging

By combining broadband pump-probe spectroscopy with confocal microscopy, hyperspectral imaging with temporal, spectral and spatial resolution can be achieved. Unlike traditional microscopy that collects the intensity of light in specific color bands, conventionally defined by the color filter used, in a hyperspectral imaging setup, the detailed spectrum of every pixel in the image is collected. The first advantage is the collection speed. By spreading the light with an optical grating and collecting the whole spectrum at the same time, only one single scan across the sample is required and there is no need to repeat the scan several times to get images in different color channels. The second advantage is the femtosecond time resolution that has never been achieved by conventional confocal microscopy. By using femtosecond pulses as the pump and probe sources, a TAM can record how the absorption at different wavelengths across the sample changes every few femtoseconds.

1.3.2 Microscope Design

The design of the TAM that can perform time and spectrally resolved hyperspectral imaging is shown in Figure 1.2. The microscope design may vary slightly for different studies in the following chapters and will be addressed in the specific chapter. The basic design is the same. The first difference between TAM and ensemble TA spectroscopy is the beam size. In ensemble TA, the beams are usually focused using a lens and the beam diameter is several hundred microns. In TAM, the beams are focused using an objective lens (usually with a high numerical

aperture value, NA), and the beam waist is several hundreds of nanometers.[2] The second main difference is that the pump and probe are colinear in a TAM, so the residual of the pump beam needs to be cleaned before reaching the detector. The microscope is built based on the CLSM geometry.

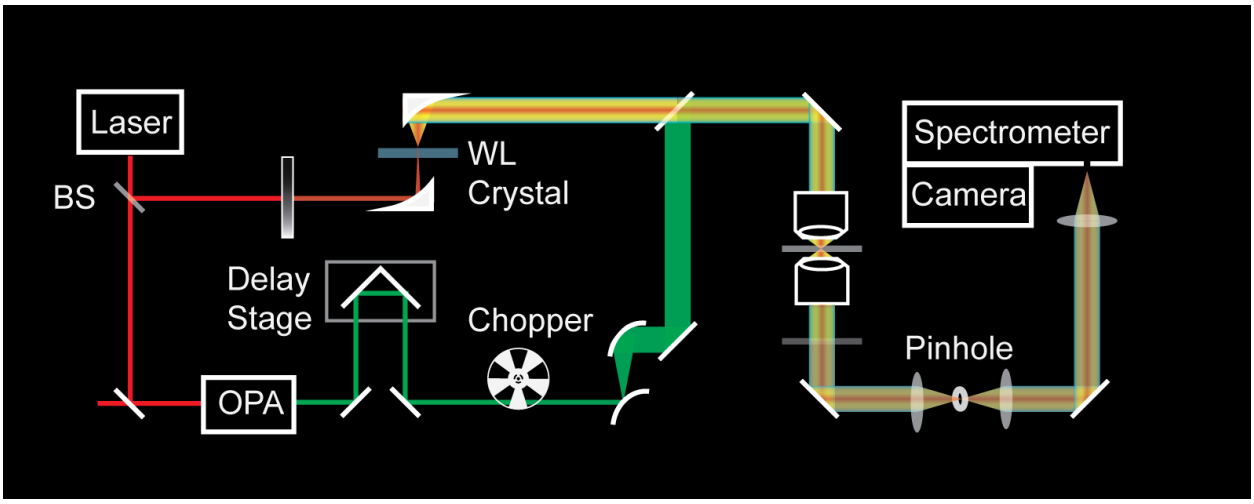

Figure 1.2 Schematic of a TAM. BS: beam splitter. OPA: optical parametric amplifier. WL Crystal: white light crystal.

The pump beam, usually set bluer than the bandgap of the material studied, first passes a delay stage. The reason why we choose to delay the pump is that the fluctuations caused by the delay stage will impact the single-color pump less than the WLC probe. There are multiple ways to generate a single-color pump. The most straightforward method would be using the tunable output from a commercial or home-built optical parametric amplifier (OPA). The pump is then modulated using a mechanical chopper. Note that the chopper and the camera are synchronized to realize referenced detection. If the chopper modulates the pump beam at the frequency *f*, the camera's acquisition frequency is always set to be *2f*, so that the first frame is taken with the

pump on (transient absorption), and the second is taken with the pump off (static absorption). By subtracting the second frame from the first, the change in absorption is acquired. Before sending the pump into the microscope body, a telescope is used to expand it to fill the back aperture of the top objective lens. Another kind of TAM design widely applied when the technique was first invented is based on lock-in detection. The pump beam is also modulated at a certain frequency using an acousto-optic modulator (AOM) instead of the mechanical chopper used in our system. The signal is collected using a lock-in amplifier synchronized to the pump modulation. The detailed scheme can be found in ref[18]. The advantage of this scheme is that it can reach a high repetition rate usually higher than 1 MHz. The disadvantage is that it is not compatible with hyperspectral imaging because only a limited number of channels are offered by lock-in amplifiers, so we did not use that design.

The probe beam is usually a WLC generated by focusing an infrared (IR) beam on a dielectric medium. In our setup, we focus a 1030-nm beam using a parabolic mirror on a YAG crystal to generate a WLC from ~500 nm to ~850 nm. The WLC is picked up and collimated using another parabolic mirror. Chirped mirrors or prisms can be used to correct the chirp if too many glass optics are used in the line. Parabolic mirrors are used instead of glass lenses. The WLC is known to be extremely sensitive to the beam pointing and alignment, and it is important to have a stable WLC to do reliable referenced detection. It is advised to separate the WLC generation part from hardware that causes strong oscillations or air disturbance (like chiller pumps and mechanical choppers). Other compressed light sources may also be used as the pump and probe. In CHAPTER 3, a home-built second-harmonic noncolinear optical parametric amplifier (2H-NOPA) was used to generate pump and probe for the impulsive vibrational

microscopy (IVM) study which requires compressed broadband pump and probe. In normal TA studies, a single-color pump and broadband probe should suffice.

The microscope body and the detection line are based on the confocal geometry. The objective lenses should be carefully chosen so that no extra chirp will be introduced to the ultrafast pulses focused by it. We used a reflective objective lens that only contains reflective optics inside. If a refractive one is used, the chirp caused by the glass inside shall be compensated before the microscope. A piezo stage was used to scan the sample. Mirror galvanometers can also be used to scan the beams, too. After the sample plane, A pinhole is used to reject the out-of-focus stray light. The probe and signal are sent into a spectrometer with an array camera attached to detect the full spectrum. The residual pump beam can be cleaned using a notch filter, or by setting the relative positions of the camera and the grating in a way that the pump wavelength is outside the acquisition range of the camera. Transient reflection signal can also be collected by adding a beam splitter above the top objective to collect the reflected probe. Nothing needs to be changed in the detection line to get the reflection signal.

A lot of other third-order spectroscopic tools can be integrated into this microscope design to realize more imaging functions, with small changes in the light source and the detection scheme, like impulsive vibrational spectroscopy (IVS, CHAPTER 3), coherent anti-Stokes Raman spectroscopy (CARS),[19, 20] stimulated Raman scattering (SRS),[21] and two-dimensional infrared spectroscopy (2D-IR).[22, 23] Another kind of TAM setup fixes the pump position and uses mirror galvanometers to scan the probe around the pump to study the diffusive behaviors of the excited-state species. Details about that setup can be found in review[24].

1.3.3 Ultrafast Microscopic Studies on Light-Harvesting Materials

TAM has been mainly used for material characterization,[15, 16, 25-36] biological imaging,[37-44] and art conservation.[45] As a non-invasive and label-free technology, fluorescent labeling is not required, which largely broadens its application range and simplifies the experimental procedures. A lot of materials that do not have emissions can still be studied using a TAM. TA spectroscopy provides information about the energy levels, population dynamics, and energy transfer between states with femtosecond temporal resolution and is widely applied in the study of light-harvesting materials. With the fast development of materials science and nanotechnology, more complicated nanostructures were synthesized, demanding a characterization tool with good temporal, spectral and spatial resolution to map the heterogeneity in morphological and photophysical properties. In this thesis, a TAM with hyperspectral imaging function was designed and prototyped to measure the ultrafast dynamics within a small homogenous region in heterogeneous light-harvesting materials. The work done on excited-state dynamics and the correlated structural origins with TAM is summarized below. The other branch of TAM studies focuses on the diffusion of excited-state species like carriers in semiconductors, including single-walled nanotube (SWNT),[46] transition metal dichalcogenide (TMD),[47, 48] perovskite,[29, 31, 33] acene,[30, 49] and porphyrin.[50] More information about that branch can be found in review[24], but will not be detailed in this thesis.

Most of the early work done on light-harvesting materials with TAM was focused on graphene,[25, 51-54] and nanotubes.[55-60] These studies represent the two major applications of TAM, with the first one focused on the spatial heterogeneity and the correlated ultrafast dynamics across a large ROI, and the second one focused on one single particle or nanotube that cannot be

probed alone in ensemble spectroscopy. The study on graphene done by Huang et. al. revealed the correlation between the electron-phonon reaction and graphene-substrate coupling. Weaker coupling between the substrate and the graphene led to weaker electron-phonon coupling and the hot-phonon effect.[51] This phenomenon was explained by the interactions between the electrons and the surface optical phonon modes of the substrate as another energy relaxation channel in follow-up studies.[25, 52] Interestingly, only minimal interaction was found between graphene oxide and the substrate.[53] The studies on single particles like single metal particles and SWNTs have been focused on the vibrational modes,[61] carrier relaxation,[60, 62] metallic state,[56] and interaction with the substrate.[57, 58] These studies laid the foundation of using TAM to probe the carrier cooling and energy relaxation processes in semiconductors.

With the development of organic photovoltaic (OPV) materials, more researches were published on organic semiconductor thin films that form complicated microstructures, like acenes.[26-28, 63, 64] And the focus shifted to structural features like crystal domains and GBs. Excited-state dynamics within individual domains of the organic semiconductors were measured and analyzed. The dynamics were found to be related to the orientations of the crystal domains and the stacking geometries of adjacent molecules.[26, 28, 63] The structures of domain interfaces and GBs were also studied. Wong et. al. reported that the domain interfaces in solution cast 6,13-bis(triisopropylsilylethynyl) pentacene (TIPS-pentacene) were made up of nanoscale crystallites interleaved by a web of interfaces, instead of abrupt GBs.[27]

1.3.4 TAM Studies on the Excited-State Dynamics of Metal Halide Perovskites

The past ten years witnessed the emergence of metal halide perovskites as one of the most promising materials as absorber layers in solar cells. Perovskite was first reported in 1983,[65] but the rediscovery of it for solar cell application took until 2012.[66-68] Within ten years of the rediscovery, the power conversion efficiency of perovskite-based solar cell has exceeded 25%.[69] Three-dimensional (3D) or bulk perovskites generally have a crystal structure of ABX_3, with A being either organic cations like $CH_3NH_3^+$ (MA) and $[HC(NH_2)_2]^+$ (FA), or inorganic cations like Cs^+ and Rb^+, B being divalent metal atoms like Pb^{2+} and Sn^{2+}, and X a halide anion. The crystal structure consists of 3D corner-sharing BX_6^{4-} octahedra with the A cations occupying the cuboctahedral site formed in the middle of eight adjacent octahedra. Recently, layered two-dimensional (2D) perovskites were discovered. Large organic spacers were inserted between perovskite layers to form the general structure of $(A')_m(A)_{n-1}B_nX_{3n+1}$, where A′ is a large monovalent (m = 2) or divalent (m = 1) organic cation, and n is an integer that represents the thickness of the inorganic perovskite layers between organic spacers. One prototypical structure of 2D perovskite is $(BA)_2(MA)_2Pb_3I_{10}$ (BA = $CH_3CH_2CH_2CH_2NH_3^+$), where perovskite quantum wells consisting of 3 layers of PbI_6^{4-} octahedra and MA cations were separated by BA layers. The discovery of the 2D perovskite family largely increased the chemical stability and offered more tunability in the optical and electronic properties.[70-75]

The extraordinary power conversion efficiency of metal halide perovskites has been mostly attributed to low recombination rates,[14, 76-81] long carrier lifetime,[78, 80-82] long diffusion lengths,[29, 31, 83-86] and defect tolerance.[87-90] Most of the spectroscopic studies on the ultrafast carrier dynamics were performed using ensemble spectroscopic tools, that average hundreds of or

thousands of μm^2 across the perovskite crystal, where different levels of spatial heterogeneity exist, determined by the fabrication methods.[91, 92] Defects like lattice interruption and inclusion of foreign atoms can happen across the sample. To fully understand the carrier dynamics and their structural origins, direct characterization of the carrier behaviors in a locally precise way is required, which is the first problem solved in this thesis. By using TAM as the main characterization tool, ultrafast carrier dynamics, like carrier cooling, carrier recombination, energy transfer between states, and transition energy of defect states within a small area ($<1\ \mu m^2$) can be studied. With the sub-micron spatial resolution, specific regions with a higher defect concentration like GBs and crystal edges can be selected out and studied separately. With other correlated microscopy, for example, scanning electron microscopy (SEM) and atomic force microscopy (AFM), a direct correlation between carrier dynamics and crystal morphology can be made.

The use of TAM, an optical microscopic tool, is limited on the imaging of structures smaller than the diffraction limit. Other than extrinsic defects, the crystal structure is another determining factor of the optical and electrical properties of perovskites. For example, in 2D perovskites, the bandgap of the crystal is largely determined by the thickness of the inorganic perovskite layers between organic spacers due to the quantum confinement effect, and the exciton binding energy is affected by the dielectric screening effect from the organic spacers.[70, 93-96] For properties that are extremely sensitive to the chemical environment, single-particle spectroscopy on phase-pure monocrystalline nanocrystal is required. This is the second problem solved in this thesis. By selecting out and focusing on single perovskite nanocrystals or microcrystals, the composition of which can be easily tuned using synthetic methods, with a TAM, the influence of angstrom level

structural difference, like lattice distortion and stacking geometry, on the photoelectric properties of perovskites were studied.

1.4 Thesis Outline

CHAPTER 2 and CHAPTER 3 are based on the spatial imaging application of TAM. Spatial heterogeneity and the correlated carrier dynamics were probed. Different data analysis methods were used or invented to extract carrier properties. CHAPTER 2 uses SEM-TAM to study the transient-sub-bandgap states at the GBs of $CH_3NH_3PbI_3$ perovskites. By correlating the TA spectrum collected at every pixel and the morphological information collected using SEM, the hot-carrier cooling processes at grain interior (GI) and GBs were studied separately. Positive correlations between sub-bandgap absorption, elevated Fermi energy level, and increased cooling speed were found at the GBs and verified with statistical tests.

In CHAPTER 3 we introduce a novel fast global analysis method based on variable projection and subsampling for TAM. The new method increases the analysis speed by more than 1500 times and is more sensitive to weak spatial and spectral features and can be used to perform background subtraction for the extraction of high-order nonlinear signals. A third-order nonlinear spectroscopic technology, IVS, was integrated into the TAM system and the new data analysis method was tested on the IVS datasets as well.

CHAPTER 4 and CHAPTER 5 are based on the single-particle imaging application of TAM. In CHAPTER 4, 2D perovskite single crystals with different A-site compositions were

synthesized. A-site cations with various sizes caused different levels of lattice distortion and led to different levels of photoluminescence (PL) quenching, which was found to be related to defect concentrations probed with single-particle TA spectroscopy.

In CHAPTER 5, the structural difference in 2D perovskites caused by the A′-site (organic spacer) is studied by including different designer molecules into the organic layer. Two molecules, allylammonium (AA) and iodopropylammonium (IPA) with different steric and dielectric properties were introduced to the same inorganic lattice and caused changes in layer stacking geometry and lattice distortion. Single-particle TA proved that the major cause of detrimental deep trap states was the distorted lattice instead of the changed stacking geometry.

CHAPTER 2 Transient Sub-Bandgap States at Grain Boundaries of $CH_3NH_3PbI_3$ Perovskite Act as Fast Temperature Relaxation Centers

2.1 Introduction

Metal halide perovskites have received intense attention as active layers in solar cells for their high power conversion efficiency (over 22%[97]) and the relatively low technical barrier in fabrication.[98] Contributing to their idiosyncratic carrier behavior, like low recombination rates,[14, 76-81] low cooling rates,[78, 80-82] and long diffusion lengths,[29, 31, 83-86] are the unique band structures that may arise from different film morphologies. The impact of the local nanostructure, such as GBs, on carrier properties has been widely studied using other microscopic methods,[99] mainly PL microscopy[100-104] and AFM,[88] along with ensemble pump-probe spectroscopy by comparing samples with different bulk morphologies.[105-107] However, the nature of the GBs and the associated defect states remain unclear. Many previous studies either performed ensemble measurements averaging over tens of microns in films, thus convolving signals from many individual grains, or studied properties like the local PL lifetime at the bandgap,[100-104] carrier diffusion,[33] and other properties[88, 108] to indirectly probe the dynamics at the defect state, along with some interesting theory works.[90, 109, 110] Until now, there has not been a direct probe of the transition energy of the defect state and population dynamics in a locally precise way so that only sections of films (e.g. interior, near edge, boundary, etc.) or single grains are probed, while simultaneously measuring hot carrier dynamics. Further, comparison of carrier properties between different morphologies has not, until now, been supported by large-data statistics. In this chapter, we present the first realization of scanning electron microscopy correlated transient absorption microscopy (SEM-TAM) on polycrystalline perovskites, which directly maps the

formation of a sub-bandgap state at GBs. The dynamics of these states are investigated together with their influence on the local carrier behaviors, suggesting the electrically-charged nature and the potential role of GBs as centers for fast carrier cooling. Furthermore, the microscope setup and the specially fabricated films gave us this capability of studying hundreds of data points in a single map, with multiple film morphologies included. A thorough statistical analysis with both parametric and non-parametric tests performed on such a big dataset enables us to draw a reliable connection between the formation of the sub-bandgap state, the doping effect at GBs and the accelerated carrier cooling process. Our findings indicate that, contrary to the conventional wisdom that the shallow defect state in perovskite GBs does not significantly change carrier dynamics ("benign"), [87-90] the cooling dynamics are strongly affected by additional energy acceptors formed by these states, which speeds up the process and leaves limited time for hot carrier extraction. The outcome of this effect, which is an accumulation of carriers at the bandedge, may play a beneficial role in conventional photovoltaics, as no evidence of a higher recombination rate is observed at GBs.

2.2 Experimental Details

2.2.1 Perovskite Film Composition and Morphology

Thin films of methylammonium lead iodide ($CH_3NH_3PbI_3$) deposited on marked glass coverslips by spin-coating perovskite precursor solution were studied. More details of the film fabrication and characterization can be found in our previous work[15] and the Appendix (section A.1.1). It is worthwhile to mention that the only difference between fabricating these particles

and continuous film made for devices is the 8% HI additive in the first step of synthesis, which is meant for grain size control only and does not change the chemical composition (proved by energy-dispersive X-ray spectroscopy, EDS, Figure_Apx A.1) or introduce any impurity as I^- is part of the $CH_3NH_3PbI_3$ lattice. The films fabricated this way form large polycrystalline particles with two distinct morphologies: small crystallites (< 0.1 μm^2) in the center and large crystallites (> 1 μm^2) in the outer ring (Figure 2.2a, more SEM images in the Appendix, Figure_Apx B.3). The GBs between crystallites are marked using dashed curves (the dense ones in inner circle not marked). While vastly different particle morphologies form depending on film coverage and fabrication conditions, these small polycrystalline particles provide a unique platform to study many morphologies and perform statistical analysis (N = 806) within a small ROI (6 μm × 5 μm). Further, the TA mapping and direct comparison between points can be performed within a single particle to eliminate possible variation in chemical composition.

2.2.2 TAM

The block diagram of the home-built TAM is shown in Figure 2.1. The fundamental 1030-nm beam was generated from an Yb:KGW amplifier system (Light Conversion, PHAROS) operating at 200 kHz with a pulse duration of 190 fs. The beam was split into pump and probe arms. The pump was focused into a beta barium borate (BBO) crystal to produce second harmonic generation light centered at 515 nm (2.41 eV) with a maximum average power of 15 μW. The pump was then delayed relative to the probe with a high resolution motorized linear stage (Aerotech). The white-light probe (1.50–1.87 eV), which covers spectral ranges both below and above the bandgap at 1.63 eV,[111] was generated by focusing the fundamental beam into a YAG crystal and then compressed with a pair of chirped mirrors (LayerTec). Both beams were

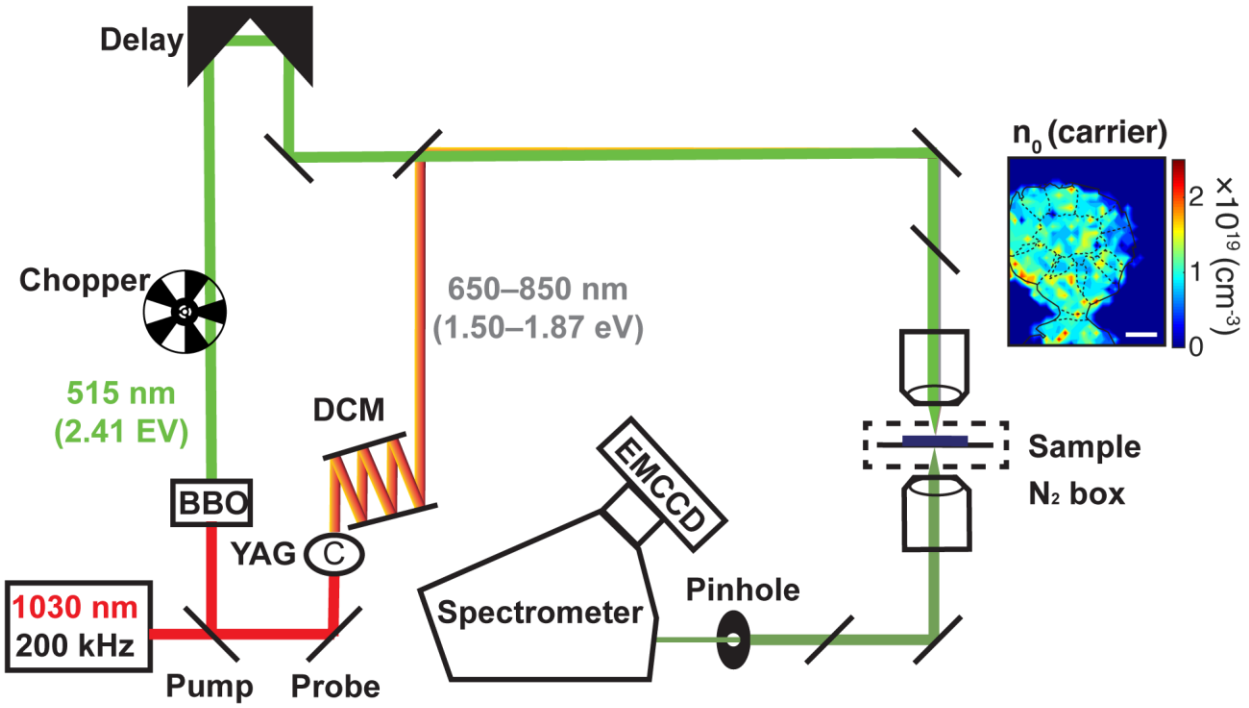

Figure 2.1 Block diagram of the TAM setup. BBO: beta barium borate crystal. DCM: double chirped mirror pair. Inset: initial carrier density map. Scale bar: 1 μm.

recombined and focused collinearly onto the sample with a 74x reflective objective (NA 0.65, Beck). The beam spot size of 540 nm was determined by measuring the power passing through a pinhole and then calculated using a Gaussian beam model. The sample was taped on a piezo-driven XYZ stage with a resolution of 0.2 μm (PiezosystemJena, Newport XPS). The sample box was purged with nitrogen gas to eliminate sample damage caused by laser heating. Control experiments are also done in the air (refer to Appendix A, section A.2.4, Figure_Apx A.13, Figure_Apx A.14). The signal was collected using a 100× refractive objective (NA 0.70, Leica), spatially filtered through a 300-μm pinhole, and then spectrally dispersed in a spectrometer (Horiba, IHR-320). The TA signal was detected using a high-speed charge-coupled device

(CCD) camera (Andor, Ixon Ultra 897). Linear absorption of probe and PL maps were measured within the same setup.

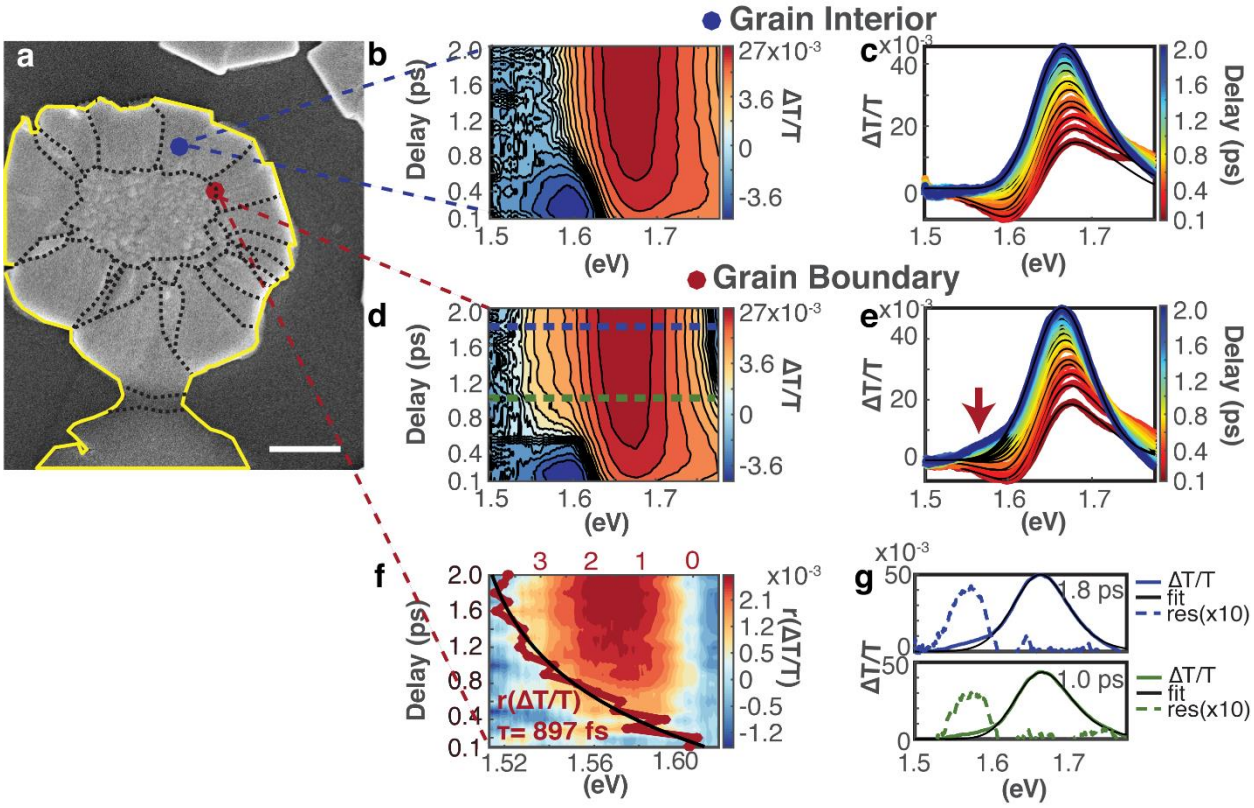

Figure 2.2 Spectrally-resolved TA spectra at GI and GB of $CH_3NH_3PbI_3$. (a) SEM image of the perovskite particle. The yellow solid curve traces the edge of the particle and the black dashed curves trace the grain boundaries between grains. The ones in the inner circle are not marked as they are too dense. Scale bar: 1 μm. (b) TA surface and (c) TA spectra with fits (black solid curves) at different pump-probe delays at one position picked in grain interiors. (d) TA surface and (e) TA spectra with fits (black solid curves) at different pump-probe delays at one position picked at grain boundaries. (f) Sub-bandgap feature extracted from fit, with spectrally integrated (1.570 ± 0.015 eV) sub-bandgap intensity (red curve) and single-exponential fit (black solid curve). The population lifetime is labeled. (g) Cuts of TA spectra at GB at 1.0 ps (green) and 1.8 ps (blue), with fits (black solid curve) and residues (dashed curve, scaled). An arcsinh-scaled color map is applied on b, d, f.

Control experiment done on films fabricated with 0% of HI can be found in the Appendix (A.2.2, Figure_Apx A.12).

2.3 Experimental Results

The TA spectra across the whole particle within the solid curve (Figure 2.2a) are measured with a single-wavelength pump at 2.41 eV and a broadband white-light probe from 1.50 to 1.87 eV, The TA spectra of two representative points picked from the GI and GB areas are displayed in Figure 2.2b−e. The conspicuous difference between the two spectra are the sub-peak below the bandgap at the GB (Figure 2.2d), which shows up as a growing feature in the time-resolved spectra (Figure 2.2e). To extract this sub-bandgap peak, a band-filling model was constructed (refer to Appendix, section A.1.3) which took into account the three prominent features and the related photophysics observed in previous ensemble measurements[14, 76, 77, 81] and the GI TA spectra here: (1.) the growing positive GSB representing the increasing amount of bandedge carriers; (2.) the high-energy tail of the GSB representing the population and cooling of hot carriers; (3.) the negative PIA below the bandgap representing the renormalized bandgap due to the presence of photo-excited carriers. All these three features are considered in the band-filling model and later subtracted from the spectra to extract the sub-bandgap state. The sub-bandgap peak centered at ~1.57 eV and the dynamics were then extracted (Figure 2.2f and g). Notably, the high-energy tail is much broader in GI (Figure 2.2c) compared to that in GB (Figure 2.2e) at 2 ps, indicating a higher quasi-temperature of the carriers in GI. Different fit algorithms were used, and all gave similar results. The center part of the particle made of small crystallites

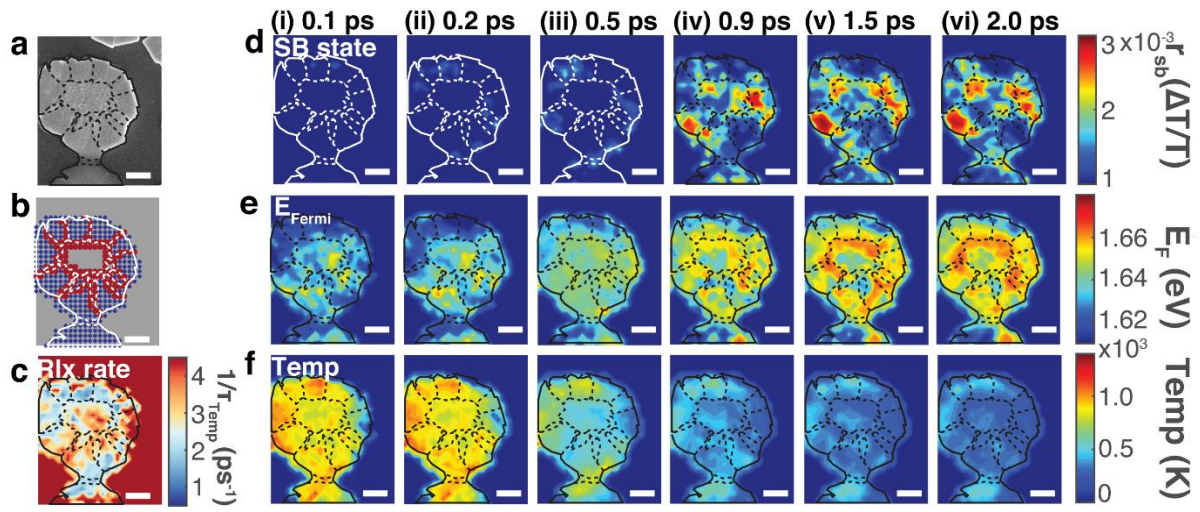

Figure 2.3 Time-resolved mapping of carrier properties extracted from SEM correlated TAM. (a) SEM image of the perovskite particle. (b) Tracing results from SEM image. Red region: inner circle which mainly contains GBs along with GBs in the outer ring. Blue region: GIs in the outer ring. (c) Map of the carrier temperature cooling rate. (d) Intensity of the sub-bandgap state map represented by integrated fit residue (1.570 ± 0.015 eV). (e) Quasi-Fermi energy map. (f) Quasi-temperature map. Scale bar: 1 μm.

(< 0.1 μm^2, sGI region), containing both grain boundaries and interiors, showed weak sub-bandgap signals and behaved differently from the GI in big grains and is considered to have formed under different mechanism. Detailed spectra and discussion can be found in Appendix,A.2.2 , Figure_Apx A.11.

The band-filling model is then applied across the whole particle to extract the sub-bandgap state and basic properties embedded in the model, describing the distribution of carriers above the bandgap. Figure 2.3 shows a correlated SEM image, maps of integrated sub-bandgap state intensity, quasi-Fermi energy and quasi-temperature at representative time points (see Figure_Apx A.4 and Figure_Apx A.5 in the Appendix for another particle). The differences

between GB and GI are prominent. In GB areas (marked by red circles in Figure 2.3b), we observe a stronger intensity of the sub-bandgap state (Figure 2.3d), accompanied by a higher quasi-Fermi energy (Figure 2.3e). The increased population at the sub-bandgap state along with the elevated quasi-Fermi energy suggests the GB is mainly doped by one kind of carrier. Otherwise, if both electrons and holes are trapped or simply recombine, the quasi-Fermi level should decrease accordingly. The relatively uniform carrier density (Appendix, Figure_Apx A.3) across the whole particle also indicates that the GBs are not acting as fast recombination centers as we do not see any notable loss of carriers, which agrees well with previous reports on the benign nature of GBs in carrier recombination in perovskites.[87-90] The quasi-temperature maps suggest that the carrier cooling is much faster in GB areas (Figure 2.3f), which is more clearly shown in the carrier cooling rate map (Figure 2.3c). We could now draw a temporary conclusion that the GBs are related to the formation of a sub-bandgap state, doping effects, and faster cooling rates. Though sub-bandgap absorption is also observed in GIs close to the edge of the particle, similar changes in the Fermi-energy level and carrier cooling dynamics are not observed. The GB states can be distinguished from the states formed at particle edges by mapping the depth of the state into bandgap. Detailed discussion may be found in the Appendix, section A.2.1.

2.4 Statistical Analysis

To better establish the correlation between the sub-bandgap state and the local carrier cooling dynamics, two-dimensional scatter plots and histograms are analyzed (Figure 2.4a−d). The

particle is divided into two separate regions (GB-red and GI-blue, Figure 2.3b, with sGI excluded due to the complicated morphology and the small sample size), and statistical analysis is performed on each, with histograms projected from each axes and median values marked by straight lines and mean values marked by stars. T-test (parametric, based on mean and standard deviation, suitable for normal distributions) and Kolmogorov–Smirnov test (KS test, non-parametric, suitable for non-normal distributions like bi-modal) are performed to test if the difference in mean and distribution between GB and GI is statistically significant, considering the various distributions these properties showed.[112-114] The ones showing a significant difference are marked with a tick near the histograms. Pearson's linear correlation coefficient are calculated to show the correlation between the properties on *x* and *y* axes and marked on the scatter plots (More details on the statistical analysis and tests can be found in the Appendix, section A.1.6 and A.1.7). The first thing to note is that the sub-bandgap state intensity is obviously higher in GBs after 0.9 ps, both shown by the histograms and the median values (Figure 2.4a−c), which aligns with the phenomenon in Figure 2.3d, that the sub-bandgap state tends to form in GBs. The temperature of GBs starts from a slightly lower value compared to the GIs but cools down more rapidly ($1/\tau_{Mdn}$ ~ 2.80 ps^{-1}, Figure 2.4b, since the distribution is bimodal, the KS-test is trusted) to a narrower distribution centered at ~300 K, with a small sub-peak at ~425 K (Figure 2.4a(iii)). The GI region, on the other hand, cools down at a slower rate ($1/\tau_{Mdn}$ ~ 2.58 ps^{-1}) and forms a flatter distribution, with stronger intensity. The cooling curves for GB and GI represented by median temperatures are shown in Figure 2.4e for directly showing the difference. A strong positive correlation between the sub-bandgap peak intensity and temperature cooling rate is observed ($p < 0.05$, Figure 2.4b). It is also important to point out again that the sub-bandgap state

is only accelerating carrier cooling, not carrier recombination, which are two different steps in photovoltaics. The high temperatures in GIs at 2.0 ps and the slow cooling rates suggest a lattice heat-up effect exerted by the hot carriers (illustrated in Figure 2.4g). For GBs, the temperature mostly relaxes rapidly to the surroundings near 300 K, denoting a negligible heating up of the lattice. Also, by applying the longitudinal optical phonon (LO-phonon) emission model to the temperature cooling curve,[14, 82] we are able to extract the time constant τ_{ave} characterizing the energy loss via phonon-emission, which represents the strength of the phonon-bottleneck effect,

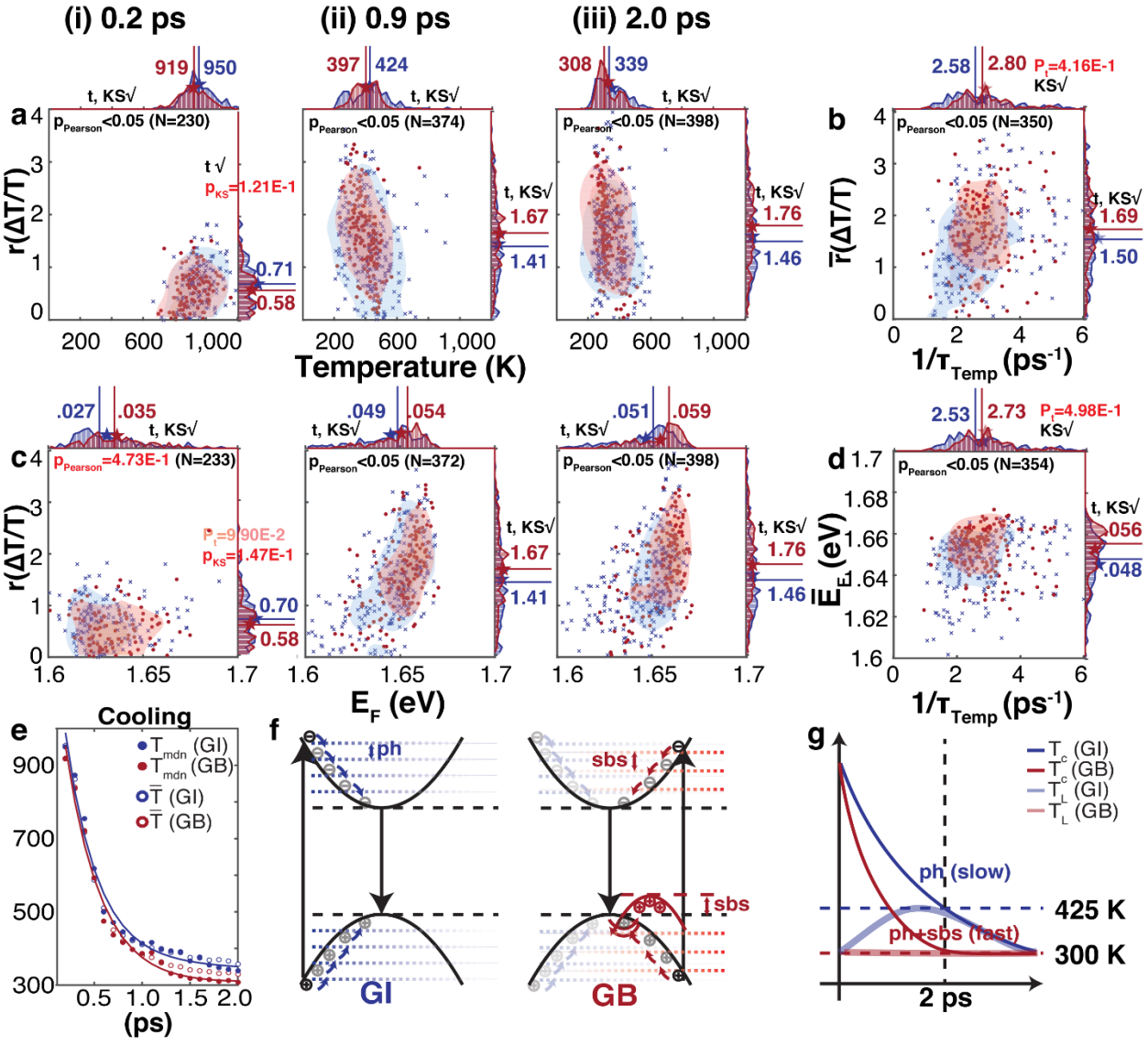

Figure 2.4 Statistical analysis on the correlation between sub-bandgap states and carrier properties. Two-dimensional scatter plots of sub-bandgap state intensity and (a) carrier temperature and (c) quasi-Fermi energy at different delay times. Two-dimensional scatter plots of carrier cooling rate and temporally averaged (b) sub-bandgap state intensity and (d) quasi-Fermi energy from 0.9 to 2.0 ps. Contour lines of 25% and 50% probability are marked. The vertical lines show the positions of median values in the histograms, with the value marked nearside. The stars show the mean values. The testing results for the t-test and KS-test are marked near each set of histograms. The results for Pearson's linear correlation test are marked on each scatter plot. (e) Cooling curves as a function of time represented using both median and mean values. (f) Illustration of the LO-phonon scattering effect as the major carrier cooling pathway at GIs and sub-bandgap state as an extra pathway at GBs. (g) Illustration of the carrier cooling curve as a function of time in different regions of the particle. T_C: carrier temperature. T_L: lattice temperature. The lattice heat-up effect is shown in the rise of T_L in GIs.

and we do not see an obvious increase in the GB region (refer to the Appendix, section A.1.4, Figure_Apx A.7). Therefore, we hypothesize that the GIs may be predominated by the widely-reported phonon-bottleneck effect in perovskites,[14, 76, 77, 115, 116] while in GBs, there must be additional cooling pathways besides LO-phonon scattering, also proved by the strong correlation between sub-bandgap state intensity and cooling rate (Figure 2.4b). This implies that other species may form at GBs to accept the extra energy from hot carriers and relieve the strain on phonons as the major energy acceptors. One of the new species is most likely to be the charged sub-bandgap state, the formation of which is reflected in the increased quasi-Fermi energy level. As is shown in the histograms in Figure 2.4c(i), the initial Fermi energy across the whole particle was uniformly distributed with no clear favor for GI or GB. A higher Fermi energy was observed in GBs only later, most clearly seen after 0.9 ps, and found to be positively correlated to the sub-

bandgap state intensity, suggesting that the doping effect of one kind of carrier is prominent in GBs where the sub-bandgap state shows up. Figure 2.4d then further links this charged sub-bandgap state to the carrier cooling process, where a positive correlation between the averaged Fermi level and the carrier cooling rate is observed. To summarize, we observe positive correlations among the formation of sub-bandgap, increased cooling rates, and elevated Fermi energy. These three linked effects are all more pronounced in GB regions proved by statistical tests. There are some overlaps in the data points or histograms from GB and GI, but this may be attributed to the sub-ensemble averaging effect within the 540-nm spot size, which means small contributions from GIs in GB points and vice versa are inevitable. That is why the difference between GI and GB might be small in value. However, the overall statistics helps us draw a more reliable conclusion compared to other studies on GBs, the dataset size of which are usually limited to single points or, at most, a single line scan over the GB. It is recommended to pay more attention to the Pearson's correlation coefficient which suggests whether the two values on x and y axes are closely correlated, for the separation and assignment of GI and GB might be blurred or inaccurate, but the correlations between the sub-bandgap state intensity, the Fermi energy, and the cooling rate definitely exist across the whole particle.

2.5 Discussion

Finally, the probable nature of the sub-bandgap state at GBs and its role in carrier cooling process are discussed. The measurements reveal that the sub-bandgap state (1.) shows up ~60 meV into the static bandgap; (2.) is a transient feature growing after initial excitation; (3.) is

relevant to the fast temperature relaxation of hot carriers (4.) likely traps only one kind of carriers. It is not an exciton, as the depth of the states falls out of the range of newly-reported binding energy,[117, 118] which would form immediately after excitation instead of growing on the order of ps (Appendix, Figure_Apx A.10). We suggest that the origin of this state is from I−I bond at GBs, which is a shallow but electrically-charged defect state (Figure 2.4e). Due to first-principles calculations done by Yin et.al., a shallow defect state (within tens of meV) above the valence band maximum (VBM) tend to form from the I−I bond in certain types of GBs in $CH_3NH_3PbI_3$.[90] The accelerated carrier cooling is due to the added cooling pathway which is the sub-bandgap state scattering, or defect scattering as is reported in other semi-conductor systems.[119, 120] The negatively charged states induce a built-in potential which quickly localizes the holes. A dynamic equilibrium then formed between the trapped holes and the hot carriers, during which the holes lose energy when they got trapped into this sub-bandgap state, and regain energy absorbed from hot carriers and come back to the valence band (VB, Figure 2.4e). At early times, the sub-bandgap states offer another pathway in GBs for carrier cooling by quickly exchanging energy with the hot carriers, while at late times, most carriers cool down to ambient temperature and the holes start piling up in this sub-bandgap state, giving rise to a stronger bleach signal. A more sophisticated kinetic model was tested to study the detailed kinetic processes (refer to the Appendix, section A.1.4), but failed to give more information than an exponential fit because of the limited time resolution (0.1 ps) and weak signal from the sub-bandgap state. Further study with finer time resolution and stronger pump intensity or increased data collecting efficiency may be done to justify the proposed mechanisms. However, the statistical analysis and tests performed in this chapter strongly supports our hypothesis that a charged sub-bandgap state is formed in GBs of perovskites and offers a faster carrier cooling

pathway. These charged states will harm the hot carrier extraction process by assisting the energy dissipation of hot carriers. The higher cooling rate will lead to an accumulation of carriers at the bandedge, as the rates of reactions generating bandedge carriers are increased, while we did not see any significant decrease in carrier density coming from carrier recombination. Along with the fact that carrier separation is easier at GBs, also proved by another study,[88] GBs might still benefit the conventional solar cells which harvest carriers at the bandedge.

2.6 Conclusion and Future Work

In conclusion, SEM-correlated transient absorption microscopy was used to identify a transient sub-bandgap state located only in the GBs of $CH_3NH_3PbI_3$ perovskite. Our findings based on statistical analysis and tests on many hundreds of spatial locations enhance the fundamental understanding of the GBs, which behave like shallow charged states accelerating carrier cooling. They also directly impact the fabrication of perovskite active layers in hot carrier devices as it provides direct evidence that sub-bandgap states in GBs offer a fast temperature relaxation pathway which harms the extraction of hot carriers. Contrary to the common belief that the shallow defect states in GBs are benign, they actually cast a strong impact on the carrier cooling dynamics and should be eliminated in hot carrier applications. The impact of GBs in conventional solar cell seems to be benign, as no enhanced carrier recombination is observed, and the sub-bandgap state probably helps with carrier separation. Further research will be focused on a detailed kinetic study on the processes affecting hot carrier extraction and carrier harvesting to gain a deeper understanding of GBs in perovskites.

CHAPTER 3 Global Analysis for Time and Spectrally Resolved Multidimensional Microscopy: Application to $CH_3NH_3PbI_3$ Perovskite Thin Films

3.1 Introduction

The great progress in material science engineering, especially in photoactive materials,[93, 121-125] in recent years opens the possibility to design and fabricate increasingly complicated microstructures to cater to different needs in energy harvesting, catalysis and biochemistry, in both academia and industry. The increased complexity of the sample systems requires new spectroscopic tools with high spatial, temporal, and spectral resolutions to investigate the complicated and naturally high-dimensional properties in a comprehensive way. A three-dimensional spatial resolution is required to make observations at the micron or nanometer scale, like probing the surface morphology or interior structure of the material; a good temporal resolution is demanded to detect ultrafast events happening within femtoseconds, like energy flows in solar cells and intermediate formation in catalysis.[126] Another essential resolution is the spectral one which enables the decomposition of the signal into different states or species. To gain a deeper insight on the sample system, like layered perovskite solar cell devices, and use the measurement results to predict and improve the properties, the combination of all three resolution is required, which motivates the development of time-resolved microscopy.

With the rapid development of femtosecond lasers,[126] tunable compressed broadband light sources,[127] fast detectors, and novel correlation tools with nanometer precision, time-resolved multidimensional microscopy has achieved great improvement in setup construction and has gained broad applications in photochemistry, photophysics, photobiology and other branches of

physical science. Different time-resolved microscopy setups detecting various forms of optical signals have been developed, such as time-resolved photoluminescence (TRPL) microscopy,[96] TA microscopy,[16, 31, 128] two-dimensional white-light microscopy,[23] Fourier transform coherent anti-Stokes Raman scattering (FT-CARS) microscopy,[129] and interferometric scattering microscopy (iSCAT).[130, 131] The field has now moved to the new era of studying real specimen with complicated and unknown properties instead of carrying on proof-of-concept experiments on conventional model systems. The current goal is no longer limited to the measurement of dynamics at a certain location and a certain energy level, but to the fast acquisition of a complete picture of all the dynamical processes of interest, like energy and charge transfer, and to understand the fundamental causes of why certain processes or properties are observed only at specific locations, in other words, the correlation between chemical properties, dynamics and morphology.

Motivated by the need to understand the relationship between local properties, dynamics and morphology in complex systems, a new kind of correlated microscopy that directly probes the correlation between the spatial and spectral properties has been developed and is gaining more attention in recent years. One example of such systems is the SEM-TAM,[16, 132] which records TA information with a femtosecond temporal resolution and a millielectronvolt (meV) spectral resolution, along with morphology information with a submicron spatial resolution. The compressed broadband probe pulse allows a fast acquisition of all dynamical processes happening across a wide spectral range with a femtosecond resolution. Take the study of light-harvesting materials as an example, the TA dataset acquired at a single pixel contains the full picture of the carrier distribution, and different carrier properties like recombination rates and

harvesting rates can be extracted. Similar data processing methods can be applied to other systems like two-dimensional heterostructure and Föster resonant energy transfer (FRET) systems to study the excited-state dynamics and energy transfer rates between different components of the system. Moreover, the high dimensionality of the datasets enables the search of correlations between different pathways and morphological features. Because of the large number of measurements acquired in one single scan, statistical analysis can be applied to verify the correlation between the spatial, spectral, and temporal properties. Pioneering studies using this approach have been carried out on perovskite solar cells, by which correlations between local carrier properties (recombination, carrier temperature, carrier cooling, transition energy, etc.) and local microstructures (GBs, edge states, defects, etc.) were directly investigated and confirmed with large-data statistics to guide the design and synthesis of better solar cell absorbing layers.[16]

However, with the increasing dimension and size of the datasets acquired by correlated time-resolved microscope, not only limited to SEM-TAM, a universal problem emerges - the fast and robust analysis of large multidimensional datasets, containing spatial, spectral, temporal, and morphological information. A single dataset can reach the size of several gigabytes which takes up a large portion of the memory in a modern PC, and the speed of data analysis decreases, unavoidably, with the size of the data. As the system complexity increases, such as when not only the active layer is studied, but rather, an entire device, the dataset size will exceed the capacity of computer memory and speed. A global analysis of the temporally and spectrally resolved spectra is usually required to decompose the highly convoluted information to access more complicated dynamics like carrier recombination, trapping, and energy transfer that may lie

beneath. A reliable way to perform global analysis on such multidimensional datasets which can precisely decompose the dynamics, while being largely immune from variance in data quality (e.g. different signal intensities resulting from variable sample thickness and morphology) is required to precisely extract the dynamics and correlate them to their structural origin. The speed of the data analysis method remains a challenge, too, as a good fit of a large dataset may require many steps of iterations and the data size further aggravates the problem. Ideally, the analysis should be finished in seconds to realize near real-time data analysis.

Herein, we propose a global analysis method that makes use of variable projection and subsampling (VPSS) to model a four-dimensional TAM dataset (two spatial, one temporal, and one spectral dimension). The method is remarkably fast (~3GB dataset can be decomposed in <1s with up to third-order exponential fitting) and exhibits superior ability in picking up spatial features with weak signal intensities that are buried in the large dataset. This is due to the fact that the correlation across the whole dataset are well-preserved. We also show the application of this VPSS method in the population fit of IVM to extract the phonon oscillations lying on the top of strong TA signal, which is oftentimes convolved with appreciable electrical noises. The method is applied to experimental TAM data on $CH_3NH_3PbI_3$ perovskite nanoparticle and films but can also be applied to all kinds of time-resolved microscopic techniques by defining customized spectral functions and temporal functions.

3.2 Methods

3.2.1 Fitting Model

The spatial-spectral-temporal microscopic dataset described here is four-dimensional (**S** (*x*, *y*, *λ*, *t*), Figure 3.1a). The experiment is carried out in a confocal-type geometry so that the sample is raster scanned across the focal spot. The third axis, *λ*, is the independent spectral variable and the fourth is the time delay, *t*, after excitation in a pump-probe experiment. The fitting procedure begins by mapping the two spatial dimensions, *x* and *y*, onto a single dimension in the data analysis called, *p*. The axial direction may also be included if the microscopic setup provides sufficient axial resolution (like a confocal fluorescence microscope or confocal transient

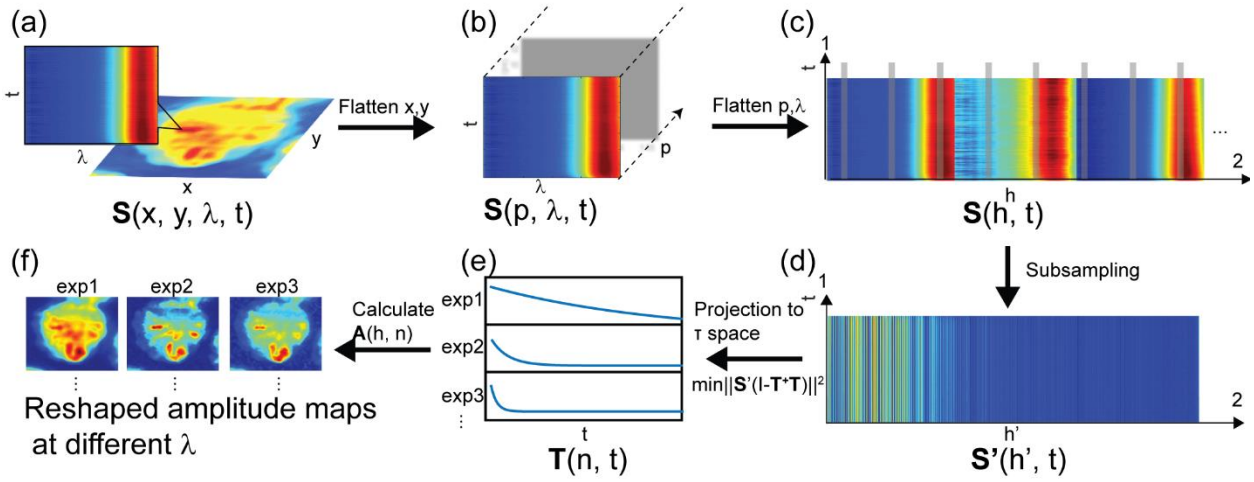

Figure 3.1 Data structure and the variable projection and subsampling method. (a) Original time-resolved microscopic dataset. (b) Dataset flattened along x and y axes. (c) Dataset flattened along p and λ axes. (d) Rearranged dataset after subsampling. (e) Temporal terms acquired after variable projection. (f) Amplitude maps corresponding to different temporal terms at different wavelengths.

reflection microscope) and the sample has sufficient heterogeneity along that directions (which is not the case for the thin films studies here within the axial spatial resolution).[133] As a result, the dataset is mapped onto a three-dimensional matrix, **S**(*p*, λ, *t*), (Figure 3.1b).

The analysis of the three-dimensional data, **S**, requires *a priori* knowledge about the mathematical form of the temporal or the spectral term. A general and simple model to represent time-dependent dynamics is a linear sum of *N* exponential decays, known as the parallel model.[134, 135] It is also a common practice to use customized functions like Gaussian, Voigt or Fermi–Dirac distribution to represent the spectral terms. The method we introduced in this chapter requires an assumption of either the temporal or the spectral terms. In this chapter, we used the *N*-exponential model to populate the initial guess of the temporal terms as an example.

For the simplicity of notation, the dimensionality of the matrix **S**(*p*, λ, *t*) was further reduced to two by flattening the spectral/spatial axes (**S**(*h*, *t*), the *h* here is a collective index that includes different spatial and spectral information). Subsampling (explained in detail in the subsampling section below) the matrix along the first dimension further reduces the work set to give $\mathbf{S}_{HK}(h,t)$, (Figure 3.1c). The multidimensional model can be represented by the following equation:

$$P_{h,k} = \sum_{n=1}^{N} A_{hn} e^{\frac{t_k}{\tau_n}} \tag{3.1}$$

or in a simpler and compact format:

$$\boldsymbol{P}_{HK} = \boldsymbol{A}_{HN}\boldsymbol{T}_{NK} \tag{3.2}$$

where **A** is a *H*-by-*N* matrix which contains the "*h*" (mixed spatial/spectral) terms in columns and **T** contains the temporal terms in rows (Figure 3.1e). On the basis of the multi-exponential model, the elements of **T** can be written as:

$$T_{n,k} = e^{\frac{t_k}{\tau_n}} \tag{3.3}$$

This procedure separates the parameters into two parts, the *H*×*N* amplitude parameters in matrix **A**, and *N* lifetime parameters in the vector $\boldsymbol{\tau}$.

3.2.2 Variable Projection

In order to find the best **P** to fit the data **S**, the parameters to minimize the error need to be solved; i.e., solve for **A** and $\boldsymbol{\tau}$ to minimize $\|\mathbf{S} - \mathbf{P}(\mathbf{A}, \boldsymbol{\tau})\|^2$. The calculation of the large **A** matrix usually takes up a lot of computational resources and is the rate-limiting step in the calculation.[135] To tackle this problem, the minimization problem was solved by using the Moore–Penrose pseudo inverse of **T** which fulfills the equation, when the rows of **T** are linearly independent:

$$\boldsymbol{A}_{HN} = \boldsymbol{S}_{HK}\boldsymbol{T}^{+}_{KN} \tag{3.4}$$

The minimization problem can be then reduced to the space of $\boldsymbol{\tau}$ only, which is $min\|\mathbf{S}(\mathbf{I}-\mathbf{T}^{+}\mathbf{T})\|^{2}$. Details about the link between the Moore–Penrose pseudo inverse and least–square solution can be found in the ref[135, 136]. After solving for the optimized **T** matrix, the **A** matrix can be directly calculated using equation (3.4). Each row of **T** carries the temporal term which is an exponential decay and each column of **A** carries the spectral term, in this case, the decay associated spectrum (DAS), at different wavelengths and different spatial locations, as *h* here is a collective index. The minimization function we used is the fminut package based on the MATLAB platform.

It is also worth noting that the current method is not limited to the parallel model only. In fact, species associated spectra (SAS) can be calculated using the same method as long as the rate constant matrix retains the same rank, a detailed discussion on the construction of the rate-constant matrix can be found in ref[134].

3.2.3 Subsampling in Multidimensional Time-Resolved Microscopy

A typical TAM dataset contains > 600 spatial locations (5×5 μm, 0.2 μm resolution), > 500 spectral points (determined by the width of the detector and the resolution of the spectrometer), and 200 time delays (20 ps, 100 fs resolution), which leads to an **S** matrix with 600 × 500 = 300,000 rows. Minimization involving such large data sets is computationally intensive. To address this problem, we implement a simple subsampling procedure that samples the **S** matrix every *l* rows, as the spectral features in TA spectra are usually broad and the change between spatial points is fairly smooth. The subsampling procedure will give us a new smaller matrix $\mathbf{S}'_{H'K}$ (Figure 3.1d). The new matrix is then used in the minimization procedure,

$min\|\mathbf{S}'(\mathbf{I}-\mathbf{T}^{+}\mathbf{T})\|^{2}$, to calculate the **T**, and then the full-sized **A** is recovered by using the full-size **S** in equation (3.4). In other words, the sub-sampled **S**' is only used for finding the optimal **T**, and the DAS is later recovered with the full-sized **S**. The recovery of the full-sized **S** is fast since it involves only simple matrix multiplication operations. The subsampling method turns out to increase the speed considerably and shows almost no information loss even when only sampling 0.1% of the full dataset in the experiment data we show below.

All the fitting procedures in this chapter were done on a PC with 64-bit Windows 7 Enterprise system, intel Core i7-5820K CPU at 3.30 GHz, and 32.0 GB of RAM.

3.3 Experimental Details

3.3.1 Transient Absorption/Impulsive Vibrational Microscopy (TAM/IVM)

A confocal microscope design, detailed in our former publication,[16] was applied to the TAM/IVM system with major modifications in the pump and probe arms, the generation of which will be discussed in separate sections below. In brief, the TAM operated in the transmission mode, with a pinhole placed at the focal point of the tube lens to spatially filter out the scatter light. The pump and probe pulses were generated from the output of one single noncolinear optical parametric amplifier (NOPA) output to realize femtosecond temporal resolution and enhanced stability. The output was modulated by a pulse shaper with a phase mask at the Fourier plane. After the pulse shaper, the pump and probe were recombined and the beam was tightly focused by a reflective objective lens (Becks, 74×, NA 0.65) onto the sample. The transmitted beam after the sample was collected by a refractive objective lens (Mitutoyo,

100×, NA 0.70) and sent to a spectrometer (Shamrock, Andor) and complementary metal oxide semiconductor (CMOS) camera (Zyla 4.2, Andor), which was synced to either an optical chopper (TAM) or a translational delay stage (rapid scan, IVM). The sample was placed onto a piezo-driven XYZ stage with a resolution of 200 nm (Piezosystem Jena, controller: Newport XPS). During the measurement, the sample was kept in a box purged with N_2 and cooled by a Peltier chip beneath the sample holder.

3.3.2 Second-Harmonic Noncolinear Optical Parametric Amplifier (2H-NOPA) and Pulse Shaping

The NOPA was built on the basis of the Yb:YAG fiber regenerative amplifier (Amplitude Satsuma, 1030 nm, pulse duration: 290 fs, average output: 20 W, repetition rate: 500 kHz). Then 6.6 W of the fundamental beam was taken and split into the pump and WLC arms. The pump was reduced to a collimated beam of 1 mm diameter and sent into a BBO crystal to produce second harmonic generation light centered at 515 nm. The WLC was generated by focusing the

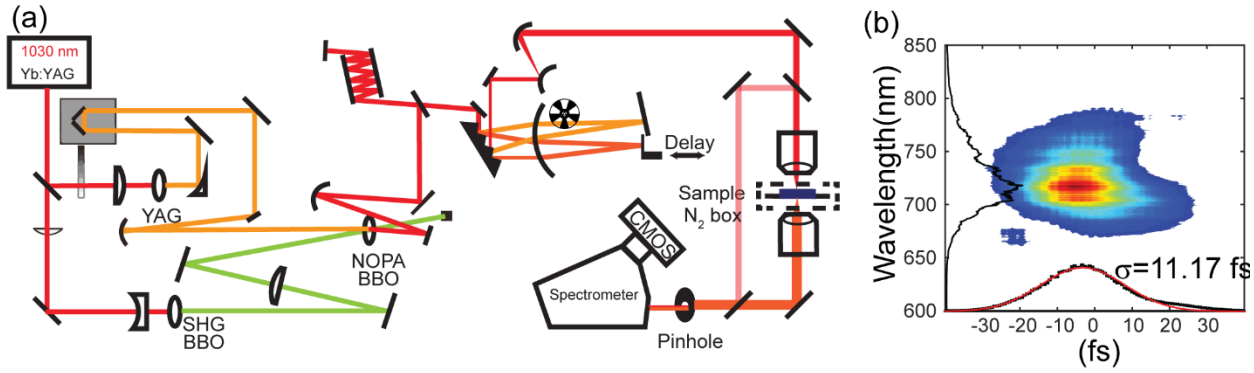

Figure 3.2 Light source and microscope setup. (a) Block diagram of the 2H-NOPA and TAM/IVM. (b) TG-FROG trace of the 2H-NOPA, with temporal and spectral profiles projected on the x and y axes. Red curve: Gaussian fit.

fundamental beam into a YAG crystal and collimated by an off-axis parabolic mirror. Both beams were recombined spatially and temporally to a BBO crystal to generate a broadband output (680 – 950 nm) and later compressed by a pair of chirped mirrors (Layertec). The pulse duration and spectral profile of the NOPA was then measured using transient-gating frequency resolved optical gating (TG-FROG, Figure 3.2b). The pulse duration was fit using a Gaussian function with σ = 11.17 fs.

The NOPA beam was spectrally dispersed and collimated by a diffraction grating (Shimadzu) and concave mirrors. At the Fourier plane, the range of 680 – 720 nm (pump) of NOPA got reflected back by a fixed planar mirror, and the range of 735 – 950 nm (probe) of NOPA got reflected back by another planar mirror, which was fixed on a motorized translational stage to generate the time delay between the pump and probe for TA measurement. The beams were spectrally recombined to a single mode and sent to the microscope.

3.3.3 Rapid Scan in IVM

A "rapid scan" scheme was applied to the IVM measurement. The design of this acquisition scheme is motivated by the fact that it is usually advantageous to finish the data acquisition process faster, not only because more data collection time is saved but also because the pulse correlation is better (in other words, the fluctuation between laser pulses is smaller).[137] It is particularly beneficial to IVM because the intensity of the IVM signal lying on the top of TA signal is usually very weak and is sensitive to a noisy environment. Instead of letting the delay stage sit at one time delay and average over a long time, as is done in conventional TA setups, which takes longer time and loses the correlation between pulses, we revolutionize the data

acquisition scheme by rapidly scanning the delay stage (Newport) and triggering the camera (Zyla 4.2, Andor) using the transistor–transistor logic (TTL) signal sent from the stage after it reaches a set point. Before the scan of the delay stage started, a "start acquisition" command was sent to the camera. The translational delay stage was configured in the way that whenever it reached the set position, it sent out a TTL signal that could be used to trigger the camera. The acquisition of a TA spectra set of 200 time delays could be finished in 2 s by using this scheme.

3.3.4 $CH_3NH_3PbI_3$ Perovskite Film Fabrication and Characterization

A 0.3 M stock solution of $CH_3NH_3PbI_3$ was prepared using $CH_3NH_3PbI_3$ powders, which was formed by precipitation from an aqueous HI solution. The powder was dissolved in anhydrous dimethylformamide (DMF, 99.8%) at 100 °C for 20 minutes to ensure complete dissolution. Only for the films with HI addition was a small amount of HI (57 wt% in water) added to the solution (8% vol/vol) in air just before use to avoid the oxidation of iodide. A perovskite layer was fabricated by spin-coating the as-prepared solution on a 170-μm-thick glass coverslip at 2,000 rpm for 30 s, followed by annealing at 100 °C for 10 min.

3.4 Experimental Results and Discussion

3.4.1 Performance Test on Dummy Datasets

Before testing the VPSS method on real data, a performance test was run on a computer created dummy dataset to test the capability of extracting different dynamics from a TAM scan. The "ground truth (GT)" used in this test was several computer-generated amplitude and peak

position maps of different DAS. TA spectra at each pixel were then created using the maps as the input. In the end, a two-dimensional matrix with one axis being the probing energy and the other being the delay lifetime was created at each pixel (like the one shown in Figure 3.3g). The surface shows the sum of the rise and fall of all the DAS. In this case three DAS were generated, shapes of which were shown in Figure 3.3h (solid lines) and the lifetimes were shown in the legend of Figure 3.3g.

The other method we chose to compare with the VPSS was pixel-by-pixel (PP) fitting, where the TA spectra at each location were fitted separately. This is the traditional way of treating a series of samples in multidimensional spectroscopy with a broadband probing source. For measurements which probe only several wavelength (like TRPL mapping), global analysis methods across the ROI were developed with a limited number of channels,[138-140] but here we are focusing on the datasets that possess a large number of elements along each dimension (usually > 100). The global analysis and target analysis on TA usually means a simultaneous analysis of all measurements done at different wavelengths and time delays.[134] When a series of samples are acquired (like with different temperature, anisotropy properties, solvent polarity or excitation wavelengths), each sample is analyzed separately. In multidimensional microscopy, like TAM, the questions become, should different spatial points be viewed as separate samples in a series, or should they be taken into account all at the same time (i.e. are they correlated to one another), and how will the two methods affect the calculation speed and analysis quality.

To better compare the speed and reliability of the two methods, all the prefitting steps were deleted, and only the same core algorithm to get the least-squares solution and the same coarse initial guess were kept. The morphology patterns were generated in the way to mimic the

different morphologies in real samples. The thin streaks in horizontal and vertical directions were used to mimic GBs or lattice mismatch sites; the wide stripes in the diagonal directions were used to mimic large grains or domains (Figure 3.3a–f). A two-dimensional Gaussian mask was applied to generate intensity gradient from the center to the edge of the sample. Outside the circle the intensity of all DAS was set to be zero to mimic the blank substrate. After the dummy

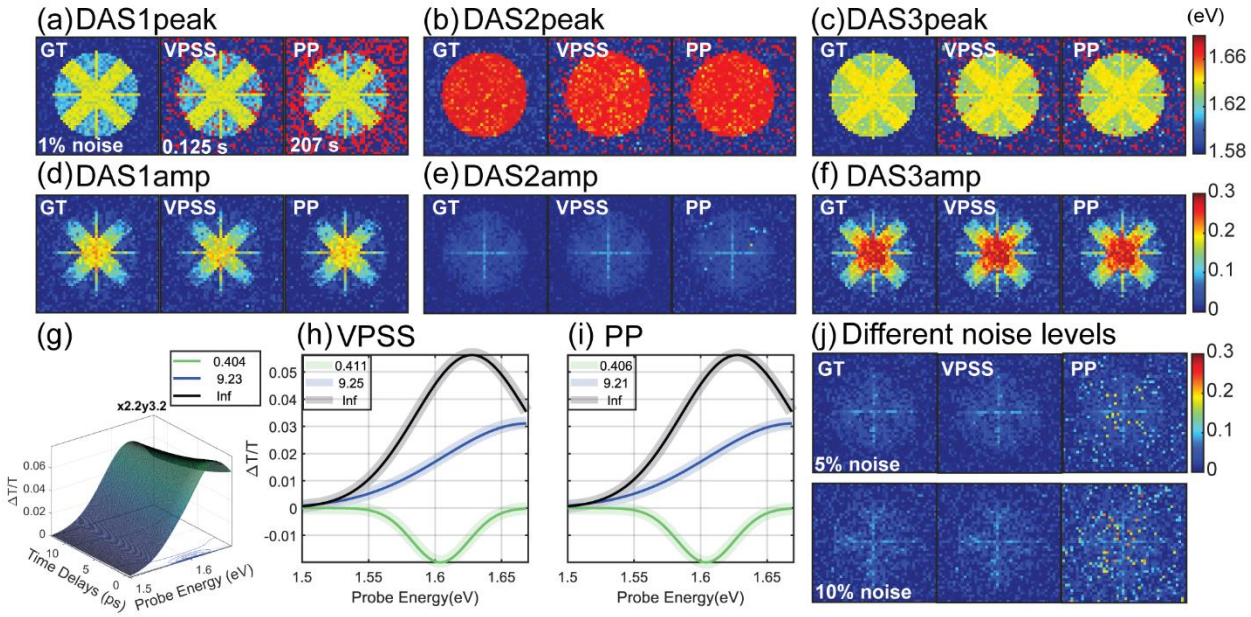

Figure 3.3 Performance test of the VPSS method compared to the ground truth (GT, 1% Gaussian noise) and PP method. (a) Peak position of DAS1; (b) Peak position of DAS2; (c) Peak position of DAS3; (d) Amplitude of DAS1; (e) Amplitude of DAS2; (f) Amplitude of DAS3. (g) Pseudocolor surface of the TA spectra (transparent surface), fitting results (black mesh) and fitting residues (projection on the xy surface) at pixel (2.2, 3.2) calculated using VPSS 1:1000. The legend shows the lifetimes of the DAS in picoseconds. Corresponding DAS at pixel (2.2, 3.2) calculated using (h) VPSS 1:1000 and (i) PP. The solid lines show the DAS from the GT. The transparent lines lying on the top shows the DAS calculated from the fitting. (j) Amplitude of DAS2 at different noise levels. Top: 5% Gaussian noise; bottom: 10% Gaussian noise.

dataset was created, different levels of Gaussian noise were applied to the maps to simulate experiment noise. Three DAS were used to simulate a semiconductor system. The first one (0.4 ps, green, Figure 3.3h) represented the fast ESA feature; the second (10 ps, blue), represented a GSB, or energy transfer process relating to the bandgap carriers; and the last (non-decaying, black) one usually represented the slow recombination process or other long-lived processes. Different peak positions and amplitudes were assigned to different regions within the sample to create diversified properties.

The peak position and amplitude maps recovered using PP and VPSS are shown in Figure 3.3a–f. In VPSS, the whole **S** matrix was first subsampled with an interval of l = 1000, and then different pixels were recovered by rearranging the **A** matrix. With a noise level as low as 1%, the VPSS was overall more stable at recovering the dynamics in GT compared to the PP method, judging by the fewer failed pixels within the sample range, especially for features that had a small amplitude (DAS2, amplitude, Figure 3.3e), and was over 1,500 times faster (0.125 s vs 207 s). The DAS recovered at a randomly picked pixel was shown in Figure 3.3h–I. Both VPSS and PP produced almost identical DAS (transparent wide lines) compared to the GT (solid thin lines). The vertical and horizontal cuts across the sample can be found in the Appendix, Figure_Apx B.2, which showed how well the fitting results matched the GT in a more detailed way. To summarize, these results validated the reliability of VPSS in extracting dynamics from complicated TAM maps.

The advantages of VPSS became more obvious while more noises were added to the dummy dataset, which was closer to actual data collection environment when running a TAM measurement, considering all the impact from shot-to-shot noise, pointing change, vibration,

temperature fluctuation etc. in an actual laser lab. Figure 3.3j shows the recovered amplitude maps of DAS2 at different noise levels. When the noise level increased to 5%, VPSS was clearly better at extracting a weak component than the PP method. It maintained a decent quality of extraction even when the noise level reached as high as 10%, while the map generated by PP was very blurred (the cross shape almost disappeared). The complete six maps at the two noise levels can be found in the Appendix, Figure_Apx B.1. For stronger features, the PP method still performed well.

3.4.2 Performance Test on Real Datasets

The performance of the new global analysis method on dummy datasets were well tested in the last section, however, it was more important to see how well the method behaved in the analysis of real experimental data, which could be much more complicated, with no well-defined pattern and more diversity in the dynamics at different locations. To test the stability of the VPSS method on real datasets, SEM-TAM measurements were run on $CH_3NH_3PbI_3$ perovskite nano islands. The SEM-TAM directly correlates the carrier properties like recombination lifetime, carrier cooling, and the existence of trap states to local microstructures like GBs and crystallite sizes, which cannot be determined using ensemble spectroscopic measurements. The TAM technique enables a temporal resolution on the scale of femtoseconds and, with the probe light acting as a natural local oscillator, is very sensitive. $CH_3NH_3PbI_3$ is an ideal film sample for TAM measurement which has strong visible absorption and long-lived carriers. With the special synthesis method developed here, a variety of spatial features like the GBs and edge states showed up in a small ROI, which provided an exemplary platform for time-resolved microscopic studies.[15] However, this kind of nanostructure carried a high density of defect and trap states,[16]

which might depress the phonon oscillation we expect to see in IVM (details of this new technique can be found in the section below), so we switched to DMF-casted $CH_3NH_3PbI_3$ perovskite continuous film in the IVM study. The fabrication methods of the two films are detailed in section 3.3.4.

In this section, we use PP as a standard method to compare with the VPSS method.[134] Physical insights gained from former studies on this system were also used to judge the quality of the fitting. The fitting results at two different locations on a heterogeneous perovskite island with different spectral features and the DAS calculated using PP and VPSS are shown in Figure

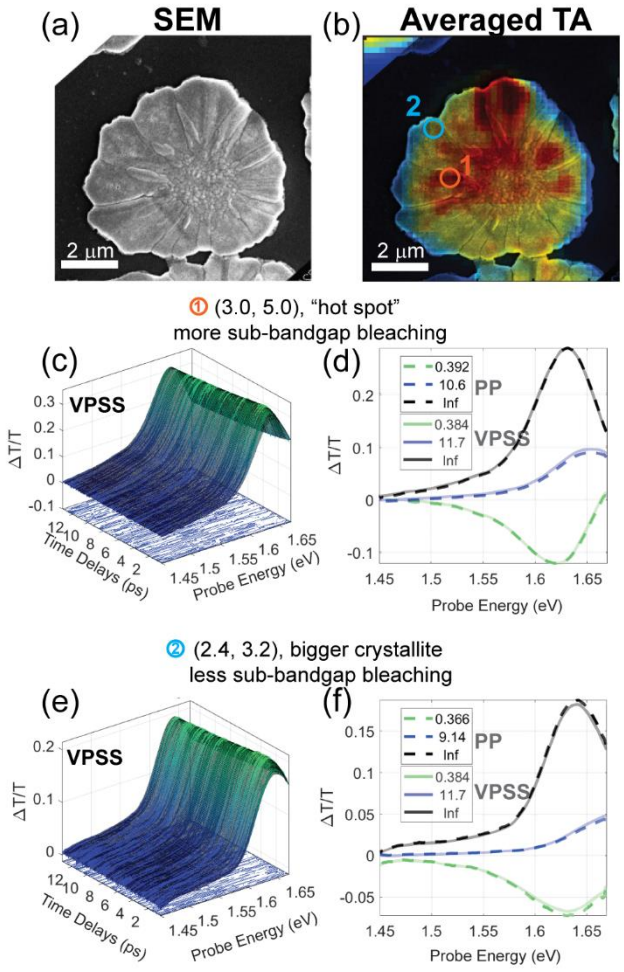

Figure 3.4 Correlated SEM-TAM maps, pseudocolor surfaces of the TA spectra (transparent surface), fitting results (black mesh), fitting residues (projection in the xy surface), and decay associated spectra (DAS) at representative pixels. (a) SEM image of the perovskite island; (b) Spectrally averaged TAM map, scale bar: 2 μm; (c) TA spectra and fitting results of pixel (3.0, 5.0) calculated using VPSS 1:1000; (d) DAS of pixel (3.0, 5.0) calculated using PP (dashed curves) and VPSS (solid curves). (e) TA spectra and fitting results of pixel (2.4, 3.2) calculated using VPSS 1:1000; (f) DAS of pixel (2.4, 3.2) calculated using PP (dashed curves) and VPSS (solid curves). The legend shows the lifetimes of the DAS in ps.

3.4c–f. Pixel 1 (3.0, 5.0), according to the correlated SEM, sat on a small perovskite crystallite, which according to our previous study,[16] formed rapidly during synthesis and was prone to the formation of trap states. Other studies also indicate that the remaining PbI_2 would lead to this kind of granular structure and a broadened TA spectrum.[141] Pixel 2 (2.4, 3.2), on the other hand, was located on a bigger, better crystallized grain. A clear difference could be found in the TA spectra at around 1.55 eV; the slope of the main bleaching peak was clearly smaller in Pixel 1, which indicated the existence of trap states below the bandgap. Three processes were present in the DAS (Figure 3.4d and 4f). The fast 300-fs component (green) accounted for the rise of the transient. It might come from hot carrier induced ESA, as is reported in many other perovskite systems,[142] but it is hard to pinpoint in this system because of the resonant excitation source, which leads to limited number of hot-carriers in the system. The weak ESA was largely overlapping with the strong and broad GSB at the bandgap, which was the reason why a negative signal below the bandgap was not observed.[143] The second component (blue) showed the recovery of the GSB slightly higher than the bandgap, which was likely caused by the cooling of carriers in those states.[143] The long-lived DAS (black) showed up right at the bandgap could be assigned to the slow carrier recombination which usually lasted nanoseconds in this perovskite system.[14] Most importantly, the DAS calculated at these two different locations using two different methods largely resembled each other and the lifetimes associated with different DAS were very close to one another (Figure 3.4d and 4f), and the physics picture gained from the VPSS fitting agreed well with former studies.[14, 16, 141, 142] Three exponential functions were used. The component number was chosen because it was the minimum needed to get a good fit of the whole spectra (also confirmed by singular value decomposition on the **S** matrix).

Datasets acquired on more homogeneous perovskite islands show much less variation between pixels and different TA spectra, which may be caused by a slower growth rate or less PbI_2 remaining in the system. More information may be found in the Appendix (Figure_Apx B.3) but is not the focus of this chapter.

To get a better understanding of how the two methods perform on microscopic data, the amplitude and peak position maps of the DAS calculated using the two methods were compared (Figure 3.5a–f). Since all three DAS showed a single peak, the peak position and the amplitude were calculated and plotted in the form of spatial maps to directly compare the difference between the results. Overall, the maps calculated using the two methods resembled each other, but clearly, the maps recovered using the VPSS methods are far less noisy and exhibit a 1,500 times improvement in speed (0.183 s vs 242 s). The l = 1000 sampling interval gave almost no

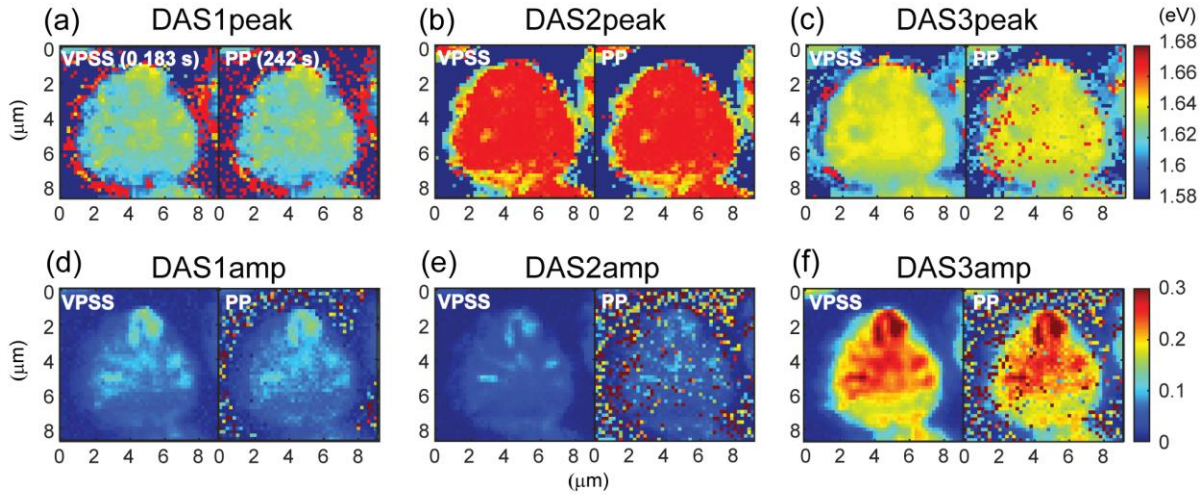

Figure 3.5 DAS peak position and amplitude maps calculated using VPSS and PP. (a) The peak position of DAS1; (b) The peak position of DAS2; (c) The peak position of DAS3; (d) The amplitude of DAS1; (e) The amplitude of DAS2; (f) The amplitude of DAS3.

loss in information compared to the results with l = 10 and 100 (Appendix, Figure_Apx B.4). Cuts along the x and y axes across the particle were also plotted to show the minimal difference in peak amplitude and position resulted from the two methods (Appendix, Figure_Apx B.5). It is worth noting that with a sub-second processing speed on real data convolved with a considerable amount of noise, this method may be easily implemented in the acquisition software itself, showing real-time DAS analysis results to users while acquiring the dataset and updating the results in real time, too. It should be noted that there are methods to generate maps using PP which are less noisy, but these involve pre-fitting to give a better initial guess and boundaries for different pixels.[16, 144, 145] However, these methods remain slow and require substantial computational resources (e.g. large memory). We want to stress again that we eliminate these steps to make the comparison simpler and more direct, and VPSS still shows faster speed and increased robustness across the whole perovskite island.

3.4.3 Weak Spectral and Spatial Features

In addition to an improvement in speed, another important advantage of the VPSS method is that it equally samples the whole dataset so that some features, which might be relatively weak compared to others, are not ignored if they manifest across the whole sample, compared to fitting each pixel individually. That is, correlations across the entire dataset are retained, which is not the case in PP. Also, at pixels that exhibit weaker signals, in other words, show poor signal-to-noise ratio (SNR), reliable DAS can still be calculated with the information gathered from the whole dataset despite the interference from the increased noise level. In simulated dummy datasets, these advantages were not very clearly shown, but both advantages are born out in the examples shown here.

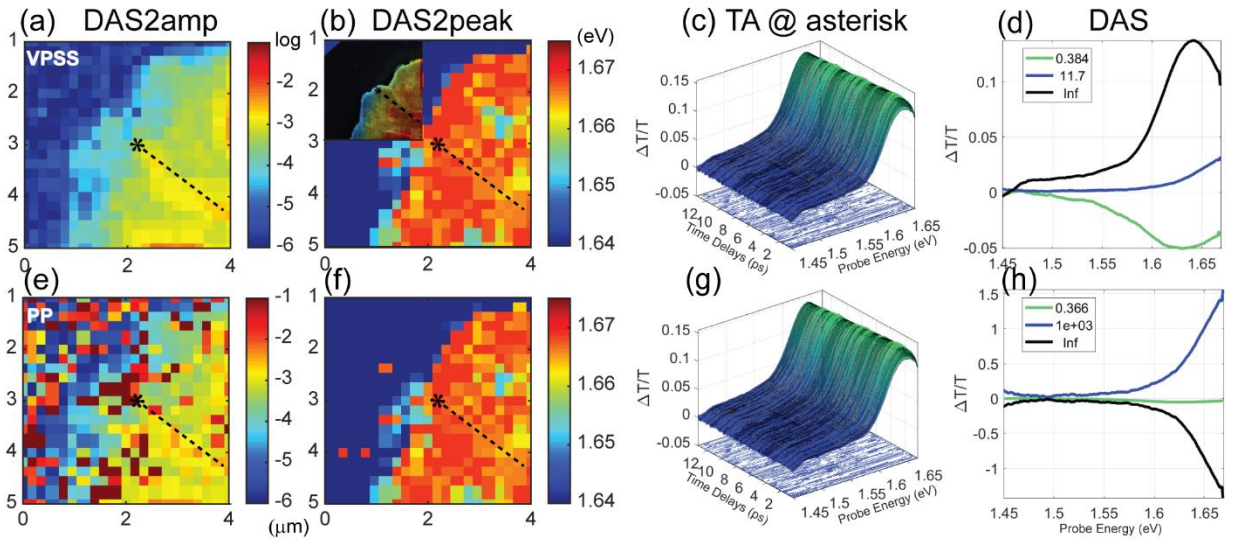

Figure 3.6. Comparison of VPSS and PP in picking up weak spectral and spatial features. Top-left part of the amplitude map (log-scaled colormap applied) of DAS2 calculated from (a)VPSS and (e) PP. Top-left part of the peak map of DAS2 calculated from (b) VPSS and (f) PP. Inset is the corresponding SEM with the spectrally averaged TA intensity map overlaid on the top of it to show the general signal intensity (red: higher, blue: weaker). Pseudocolor surfaces of the TA spectra (transparent surface), fitting results (black mesh) and fitting residues (projection on the xy surface) at the asterisk calculated using (c) VPSS and (g) PP. Corresponding DAS from (d) VPSS and (h) PP.

A great example of picking up weak spatial feature is shown in Figure 3.6a, b, e and f. The second DAS amplitude of the top-left part of the perovskite island is shown in log scale to magnify the differences between the two methods. In this region, we already reached the edge of the island (inset: SEM-TAM map. The colormap shows the averaged TA intensity. Red: higher, blue: lower) and were dealing with much weaker signal compared to the center of the particle. A large amount of noise was displayed in the PP map, but the edge structure and the GB feature (the dashed line) are well-preserved in the VPSS map.

The TA spectra at the asterisk point marked on the SEM is also shown, which is very close to the edge of the perovskite particle. Using VPSS, the weak second exponential term (roughly 17% of the third term, compared to 33% in Figure 3.4d) is captured (Figure 3.6d). With PP, however, it was ignored and replaced by the sum of two DAS with similar but reversed shapes. That is usually a sign that over-fitting occurs. In this case, it meant the PP method did not recognize the second term and was compensating for the change by subtracting two exponentials with much bigger amplitudes and oddly shaped DAS. This example showcases the capability of VPSS to pick up weak but prevalent spectral terms in the whole TAM dataset.

The strength of VPSS lies in the fast speed and the simultaneous fit of the whole dataset. One limitation of VPSS is that the subsampling process unavoidably causes a loss in information. In the examples shown here, the peaks are very broad which enables sparse sampling, but in spectra with sharper and well-separated peaks, careful planning of the sub-sampling may be necessary. Another limitation is that by projecting to τ space, we presume the DAS across the whole ROI will have a same set of lifetimes. Like in Figure 3.4, the DAS calculated using VPSS had a same set of lifetimes (0.384 ps, 11.7 ps, inf), while the lifetime of the second and third DAS calculated from PP were slightly different from the other pixel, which may happen often. A lifetime map calculated using PP is shown in the Appendix, Figure_Apx B.6. In this system, no appreciable spatial variation was observed and there is no clear pattern that can be correlated to the microstructure reflected by the SEM image, but it may affect other systems. It is true that we can increase the *N* value to make sure we capture all the principle components with similar spectral shape but different lifetimes, but the effect is limited. In summary, there is always trade-off between speed and information, but we think VPSS balances the two nicely and shows greatly

improved speed and great sensitivity in picking up weak spectral and spatial features in time-resolved microscopy.

3.4.4 Application of VPSS in the Analysis of Higher-Order Features in IVM

Another application of VPSS is to analyze the IVM signal laying on the top of TA signal. IVM is a novel tool to measure the excite-state and ground-state Raman in the time domain. With a compressed broadband excitation source, coherence between different vibrational levels can be created and directly detected in a TAM setup with no further changes in the TAM system. The coherent phonons, both ground-state and excited-state, are created by the broadband pump acting as an impulsive force on the lattice, and the change in the transmission as a function of time is detected using the delayed broadband probe. Because the Raman signal/phonon oscillation is detected directly in the time domain, it is background free and most importantly, gives us access to the low-frequency modes below 50 cm^{-1}. These features make IVM an ideal tool to study the low-frequency phonons in lead halide perovskite, likely created by the inorganic lead cage,[146] that strongly affect the carrier cooling processes through the "phonon-bottleneck effect".[14, 16] More background information about impulsive vibrational spectroscopy (with no spatial resolution) can be found in ref[143, 147, 148]. However, studies that directly probe the local phonon modes in perovskite systems with micro resolution are still lacking, which motivates the construction of the IVM. Here, we finished a proof-of-concept IVM experiment on perovskite films and used the dataset acquired from IVM as an example of using VPSS to extract coherence information from a non-traditional time-resolved microscopic dataset. In this example, we used only 10% of the dataset and got a 13-time speed improvement. The analysis results we got from PP and VPSS were almost the same, and we showed the results of VPSS in the main text only

(Figure 3.7). The results of PP and another pixel can be found in the Appendix, Figure_Apx B.8 and Figure_Apx B.9.

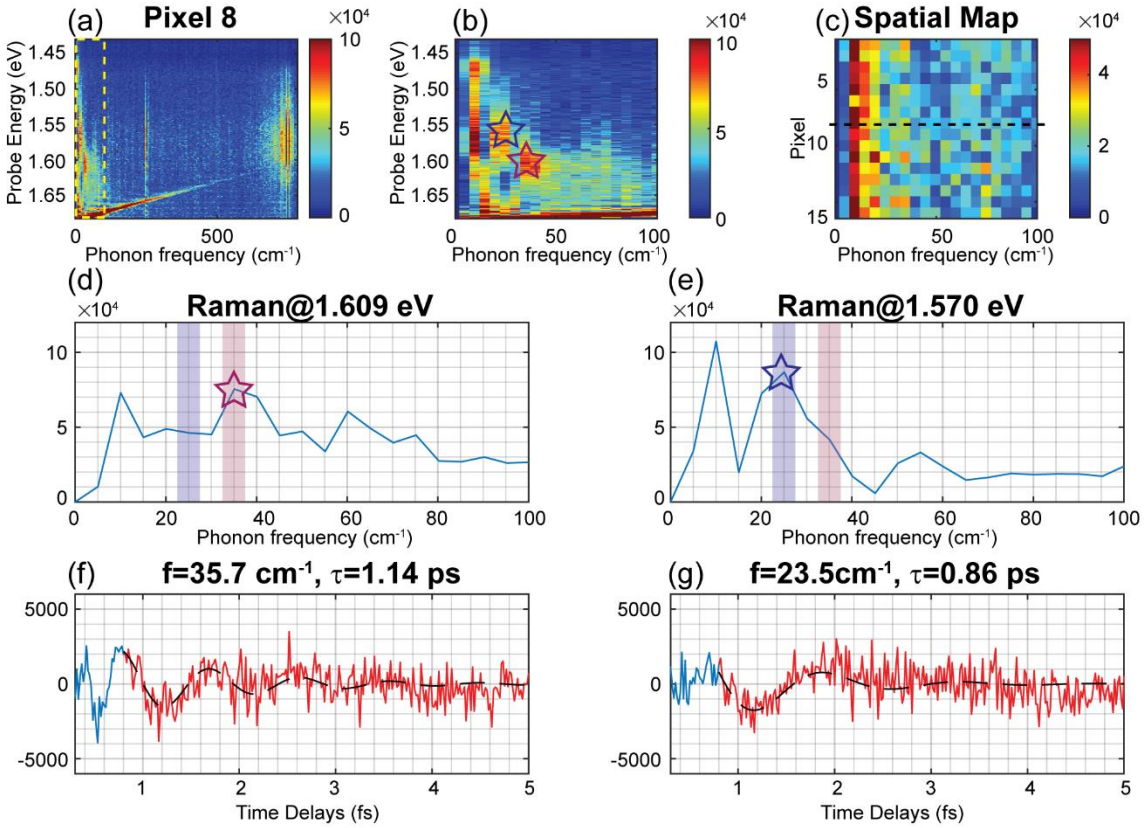

Figure 3.7. VPSS application in IVM. (a) Phonon oscillation map of the DMF-casted $CH_3NH_3PbI_3$ film. X-axis: phonon mode, y-axis: probe energy. (b) The same phonon map with the low-frequency range (yellow square) enlarged. (c) A spatial map of the spectrally averaged (along probe axis) phonon oscillation. X-axis: phonon mode, y-axis: different pixel on the film (16 pixels from a 4-by-4 raster scan, 1.25 μm resolution). The dashed line marked the pixel chosen to show, pixel 8. (d) Phonon spectra at 1.609 eV. (e) Phonon spectra at 1.570 eV. The stars show the frequency of the main oscillation from sinusoid fitting. The blue and red boxes mark the position of 20 and 35 cm^{-1} for reference. (f) Population Fitting residue at 1.609 eV. (g) Population Fitting residue at 1.570 eV. The red curve shows the region picked to perform the damping sinusoid fitting. The black dashed curve shows the damping sinusoid fitting results.

The change in TA signal, caused by phonon vibration, is much weaker and requires more sensitive detection techniques. To suppress the shot-to-shot noise caused by the light source, we applied a "rapid scan" scheme, in which, unlike the traditional chopping method, the full sequence of TA spectra is captured in a single continuous sweep of the motorized translation stage (details can be found in the Methods section). The dataset acquired this way requires a population fit first to extract the weak oscillation in the residual. One key difficulty in IVM data analysis is the overfitting at early time points. Slow phonon oscillations in perovskites, the period of which is usually in the scale of hundreds of fs,[143] at early times can be easily overfit using several exponential decays. Considering how short-lived these coherences are, such overfit will result in nearly a complete loss of the signal. One way to deal with that is to fit the oscillation using complex exponentials in the **T** matrix,[135] however, that did not give us satisfying results because of the large electrical noise from the laser (shown as sharp peaks across the whole spectrum in Figure 3.7a), which is unavoidable when entering the regime of very weak signal.

To tackle the overfitting and electrical noise issue, the population dynamics across the whole film using VPSS was first fit to reduce the chance of overfitting at individual pixels, and then Fourier transform was applied on the residues (Figure 3.7d and 7e). The residue at each probe energy was fit with a single damping sinusoid function to double check the quality of the Fourier Transform (Figure 3.7f and 7g). Because the DMF-casted perovskite film was overall uniform across a large ROI (correlated SEM in the Appendix, Figure_Apx B.7), we saw little spatial variation (Figure 3.7c, each pixel is 1.25 μm away from each other. The 16 pixels plotted here came from a 4 by 4 raster scan). Two groups of phonons were observed: one at the bandgap

(~1.6 eV, red star) with a peak at 35 cm^{-1} (1.0 terahertz, THz), which was very close to the reported 0.9–1 THz range at room temperature in the same perovskite system,[149, 150] and could be assigned to Pb−I−Pb angular distortions.[143, 146] The 20 cm^{-1} (0.6 THz, blue star) mode, 30 meV below the bandgap, was never reported, but a small phonon peak around 0.5 THz was seen in the one study carried out using 2D electronic spectra mentioned above.[143] The low frequency modes below 50 cm^{-1}, including the one around 20 cm^{-1}, were all assigned to the octahedra twist of the perovskite lattice in a theoretical study,[138] but from our results, they may have different origins as the 20 and 35 cm^{-1} modes were coupled to different transitions. The difference in the dephasing time of the two modes observed may suggest different coupling to the phonon bath. The 35 cm^{-1} mode is coupled to the transition at the bandgap, which may originate from the lattice perturbation caused by the new carriers created after excitation and holds a longer lifetime over 1 ps. What is most interesting is that the 20 cm^{-1} mode, in fact, showed up at 1.57 eV, which was exactly where we found the sub-bandgap state that accelerates carrier cooling in our previous study (CHAPTER 2).[16] This might not be a coincidence. It is possible that the cooling process is accelerated by this extra phonon mode. The dephasing lifetime is in the same order of magnitude as the cooling rate we reported in that chapter (~0.36 ps), which may suggest a correlation between these two processes. Because of the homogenous nature of the DMF-cast film sample, it was challenging to obtain a spatial map of the phonon strength, but small change in the phonon strength can still be observed in Figure 3.7c, so we hypothesize that the phonon intensity is related to the local morphology of the perovskite film. The dephasing lifetime of the phonon oscillation may be affected by the morphology too, as we observed different lifetimes compared to the results acquired on $CH_3NH_3PbI_3$ films fabricated in a different two-step method in ref[146].

The origin of the two modes and the correlation between phonon modes and morphology will require further investigation in the future.

Compared to PP, the VPSS gave us the same accuracy in extracting the phonon oscillation modes but at a faster speed. Limited by the choice of sample and weak signal intensity, the comparison in picking up spatial variation was not tested, but the key point here is that VPSS can be used as a method to reliably subtract the population dynamics and prepare the dataset for further processing like Fourier transform or fitting with customized functions.

3.5 Conclusion

We developed a global analysis procedure for time-resolved microscopy with VPSS, with the speed and robustness tested on TAM and IVM datasets acquired on $CH_3NH_3PbI_3$ perovskite films. The key advantages of this method are the fast speed (decomposing gigabytes of data within a second), and the robustness at picking up weak spatial and spectral features. VPSS is shown to be reliable in subtracting the population dynamics and preparing the datasets for higher-order feature analysis.

CHAPTER 4 Cation Engineering in Two-Dimensional Ruddlesden-Popper Lead Iodide Perovskites with Mixed Large A-Site Cations in the Cages

4.1 Introduction

Lead halide perovskites have revolutionized the fields of photovoltaics and optoelectronics as promising semiconductors.[68, 151-153] Since the first incorporation of $CsSnI_3$ and $CH_3NH_3PbI_3$ in solar cells[152, 153], high performance photovoltaic and optoelectronic devices have been achieved with this class of materials adopting a 3D perovskite structure of $APbX_3$, where A is Cs^+, $CH_3NH_3^+$ (MA), or $[HC(NH_2)_2]^+$ (FA), and X is a halide anion. The crystal structure consists of 3D corner sharing PbX_6^{4-} octahedra with the A cation occupying the cuboctahedral site formed in the middle of eight adjacent octahedra. Recently, the 2D perovskite derivatives have been demonstrated as promising more stable alternatives to their 3D counterparts for solar cells and light emitting diodes.[154] It is not only the increased chemical stability but also the more diverse and tunable optical and electronic properties that make this class of perovskites highly attractive for investigation.[70-75] The family of 2D perovskites has a general formula of $(A')_m(A)_{n-1}Pb_nX_{3n+1}$, where A′ is a large monovalent (m = 2) or divalent (m = 1) organic cation, and n is an integer that indicates the thickness of the perovskite layer. Conceptually these materials derive by slicing the 3D perovskites structure along the (100) plane and incorporating large spacer cations (A′) between the resulting layers. Most of reported 2D structures can be considered as self-assembled multiple quantum wells with charge carriers confined in the perovskite layers due to both the wider bandgap and the lower dielectric constant of the organic spacer.[70, 155-157]

With a view to further enhancing device efficiency, extensive studies have been carried out to understand the role played by the A-cations in structural, optoelectronic, and charge carrier properties. The desirable photophysical properties have been mostly attributed to the inorganic framework because, in most known compounds, the A-cation does not directly contribute to the electronic structure of band edge states, but it does so indirectly.[158] Comparative studies on the three $APbBr_3$ (A = Cs, MA or FA) perovskites showing markedly similar carrier properties and device performance further support such a picture. Nevertheless, the interplay between the A cation and the inorganic framework may influence the optoelectronic properties and carrier dynamics. For example, the bandgap of 3D $APbI_3$ decreases with increasing size of A-cation due to the decrease of octahedral tilt which is defined by the Pb-I-Pb angle.[159, 160] Moreover, there have been several proposals as how A-site cations may contribute to the remarkable carrier properties such as long-lived carriers and long carrier diffusion lengths.[161-164] These mechanistic studies suggested unusual structure-property relationships such as formation of ferroelectric domains, local symmetry breaking, large polaron formation, and dynamic Rashba effect that might be closely associated with the dynamic disorder and polarity of the A-site cations.[165-169] Despite progress in our understanding, further investigation on the structure-property relationship is hindered by the limited options of A-cations in 3D perovskites due to the geometric consideration of the so-called Goldschmidt rule.[170-172] In general, the formation of a perovskite structure depends on Goldschmidt tolerance factor (t), $t = \frac{r_A + r_X}{[\sqrt{2}(r_{Pb} + r_X)]}$, in which r_A, r_{Pb}, and r_X is the effective radii of A, Pb, and X ion. Large (such as EA) or small (such as Rb) cations can result in non-perovskite structures due to the large ionic size mismatches (i.e. $t > 1$ or $t < 0.8$).

In this chapter, we advance fundamental understanding on the structure-property relationship in lead iodide perovskites by studying new 2D crystal structures with unusual A-cations which do not follow the Goldschmidt rule and use these materials to perform ultrafast spectroscopic studies. Large organic cations such as guanidinium, dimethylammonium, and ethylammonium cannot by themselves crystallize in a 3D perovskite structure but can be alloyed into the 3D lattice of $MAPbI_3$ or $CsPbI_3$ to form mixed-cation compositions which is referred to as tuning of the effective Goldschmidt tolerance factor.[173-175] Some other large cations such as ethylenediammonium can be incorporated into a 3D perovskite structure with expelling metal and halide atoms from the structure, forming a discontinuous perovskite lattice.[176-178] While chemical engineering of 2D perovskites has focused in the past on changing the organic cation occupying the A′-site[73, 179], recent studies pointed out that the Goldschmidt rule could be relaxed in the 2D perovskites,[180] allowing large organic cations to occupy the perovskite cages (A-site). This was unambiguously demonstrated by a few crystallographically well characterized 2D perovskites including (*n*-$C_6H_{13}NH_3)_2[C(NH_2)_3]Pb_2I_{7,}$[180] (*n*-$C_5H_{11}NH_3)_2[C(NH_2)_3]Pb_2I_{7,}$[181] (*i*-PA)$_2$(*i*-PA)$Sn_2I_7$ [*i*-PA = $(CH_3)_2CHNH_3^+$],[158] and $(EA)_2(EA)_2Pb_3X_{10}$ (X = Cl, Br).[182-184] The relaxed Goldschmidt rule significantly expands the library of 2D perovskites, providing a new platform for investigating the role of the A-cation on the structural and photophysical properties.

Here we report a 2D tri-layered perovskite $(BA)_2(EA)_2Pb_3I_{10}$ (BA is *n*-butylammonium) which incorporates large EA cation in the lead iodide perovskite cage. The structure features a significantly stretched perovskite cage with elongated Pb-I bond lengths and a higher level of octahedral distortion compared to the prototypical $(BA)_2(MA)_2Pb_3I_{10}$. To provide a clearer picture of the interplay between the A-cation and the inorganic structure in determining the properties, we

synthesized a series of A-cation alloyed 2D perovskites $(BA)_2(EA_xMA_{1-x})_2Pb_3I_{10}$ and investigated their crystal structures, optical and electronic properties, and excited state dynamics using a range of structural and spectroscopic techniques in combination with theoretical calculations.

The single-crystal X-ray diffraction (SCXRD) measurements show that the average Pb-I bond length and the level of octahedral distortion increases with increasing the amount of EA cation (equivalent to increasing the size of A-cation), while the octahedral tilt is retained. Contrary to the bandgap redshift due to less octahedral tilting in 3D $APbI_3$ with increasing cation size (such as bandgap shift from orthorhombic $CsPbI_3$ to tetragonal $MAPbI_3$ and to cubic $FAPbI_3$ at room temperature,[185] or bandgap redshift in the alloys with an increasing average cation size[186]), the alloyed 2D perovskites exhibit blue-shifted bandgap with increasing EA content. The bandgap blueshift is consistent with band structure calculations, which point to the crucial role of Pb-I bond length as opposed to octahedral tilting in determining the bandgap of these EA-based halide perovskites. Moreover, the structural evolution with increasing the EA content further leads to gradual PL quenching and more asymmetric PL peaks. Transient absorption spectroscopy measurements on these alloys reveal the existence of a broad distribution of trap states below the optical bandgap. The energetic distribution of these trap states is broader with increasing EA content, which likely are responsible for PL peak asymmetry and quenching. These results provide guidelines for rational design of new and more efficient 2D perovskite materials for optoelectronic applications.

4.2 Experimental Results and Discussion

4.2.1 Crystal Structure of $(BA)_2(EA)_2Pb_3I_{10}$

Single crystals of $(BA)_2(EA)_2Pb_3I_{10}$ were grown from concentrated hydroiodic acid using an off-stoichiometry protocol (see Methods section in the Appendix C.1 for more details). Crystallographic data and structural refinement information of $(BA)_2(EA)_2Pb_3I_{10}$ are provided in Table_Apx C.2. The crystal structure consists of three layers of corner-connected PbI_6^{4-}octahedra with a bilayer of BA cations as spacers separating the perovskite slabs (Figure 4.1a), and the EA cations filling in the perovskite cavities (Figure 4.1b). The perovskite cages exhibit a combination of short and long Pb-I bonds along the out-of-plane direction

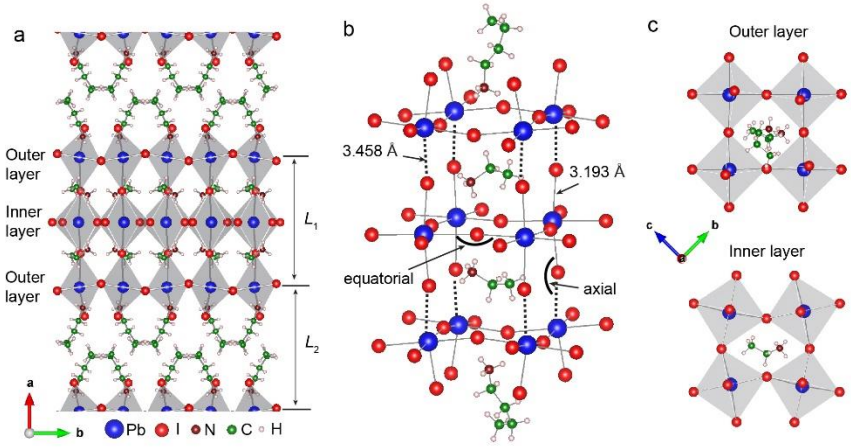

Figure 4.1 The crystal structure of $(BA)_2(EA)_2Pb_3I_{10}$. (a) Side-view of the crystal structure along c direction. Also illustrated are the definition of the thickness of perovskite slab (L1) and the interlayer distance (L2). (b) Crystal structure of the perovskite cages showing the occupation of the EA cations in the cuboctahedral sites. The dash lines highlight the longest Pb-I bonds. Also illustrated are the definition of equatorial and axial Pb-I-Pb angles. (c) Top-view of the outer layer and inner layer, which clearly shows different in-plane tilt.

(perpendicular to the layers), while almost the same Pb-I bond lengths along the in-plane directions. A view along *c* direction clearly shows that the structural distortion of the inner layer is different from that of the two outer layers. The inner layer exhibits less out-of-plane octahedral distortion but more in-plane octahedral tilting, while the outer layer displays more out-of-plane octahedral distortion but less in-plane octahedral tilting (Figure 4.1c). The inner layer can be viewed as templated by two cage EA cations, while the outer layer is templated by one interlayer BA cation and one cage EA cation. As a result, the inorganic framework distorts in a different way to accommodate the one of the possible conformations of these organic cations. The structural characteristics are similar to the previously reported single-cation templated 2D perovskites $(EA)_2(EA)_2Pb_3X_{10}$ ($X = Cl^-, Br^-$).[182] However, the iodide-based compounds have not been reported probably because the EA cation is too small to serve as interlayer spacer for the iodide perovskites.

Owing to the much larger size of EA (effective radius r = 274 pm) relative to MA (r = 217 pm), the incorporation of EA cation in the cage significantly modulates the structural and bonding properties compared to previously reported 2D structures with MA cation in the cage. To illustrate the unique structural characteristics, we compare the structural parameters and bonding properties of $(BA)_2(EA)_2Pb_3I_{10}$ with the prototypical $(BA)_2(MA)_2Pb_3I_{10}$. The results are summarized in Table 4.1. $(BA)_2(EA)_2Pb_3I_{10}$ crystallizes in the orthorhombic space group $Cmc2_1$ with cell parameters a = 52.0158(16) Å, b = 8.9727(3) Å, and c = 8.9745(3) Å, while $(BA)_2(MA)_2Pb_3I_{10}$ crystallizes in the orthorhombic space group $C2cb$ with cell parameters a = 8.9275(6) Å, b = 51.959(4) Å, and c = 8.8777(6) Å.[187] One obvious difference between the two compounds is that the presence of EA cation in the cage significantly stretches the Pb-I bond

distances, expanding the unit cell of $(BA)_2(EA)_2Pb_3I_{10}$ in the three directions. The $(BA)_2(EA)_2Pb_3I_{10}$ exhibits much longer Pb-I bonds compared to any reported 2D lead iodide perovskites with n = 3 (Table_Apx C.3). For example, the average Pb-I bond length of $(BA)_2(EA)_2Pb_3I_{10}$ is 3.213 Å, while that of $(BA)_2(MA)_2Pb_3I_{10}$ is 3.163 Å. The longest Pb-I bond length in $(BA)_2(EA)_2Pb_3I_{10}$ is 3.458 Å (highlighted as dash bonds in Figure 4.1b), which is one of the longest bonds in all reported lead iodide perovskites. As a result, the volume of the unit cell increases by 70.6 $Å^3$, corresponding to ~1.7 % volume expansion, for $(BA)_2(EA)_2Pb_3I_{10}$ compared to $(BA)_2(MA)_2Pb_3I_{10}$. If only the inorganic framework is considered, the volume expansion is even more significant, as indicated by the ~4.6 % expansion of the perovskite cage volume defined by the volume of the cuboid made up by eight adjacent Pb atoms at the cuboid corners.

Table 4.1 Comparison of the structural and bonding parameters between $(BA)_2(MA)_2Pb_3I_{10}$ and $(BA)_2(EA)_2Pb_3I_{10}$.

Structure/comparison	$(BA)_2(EA)_2Pb_3I_{10}$	$(BA)_2(MA)_2Pb_3I_{10}$	Difference (EA-MA)
Formula weight	2131.05	2103.00	28.05
Crystal system	orthorhombic	orthorhombic	/
Space group	*Cmc*2_1	*C*2*cb*	/
Unit cell dimensions	*a* = 52.0158(16) Å *b* = 8.9727(3) Å	*a* = 8.9275(6) Å *b* = 51.959(4) Å	/

	c = 8.9745(3) Å	c = 8.8777(6) Å	
	α, β, γ = 90 °	α, β, γ = 90 °	
Volume of unit cell (Å^3)	4188.6(2)	4118.0(5)	70.6 (~1.7%)
Volume of perovskite cage (Å^3)	267.2	255.1	12.1 (~4.7%)
L_1 (cage) (Å)	13.274	12.876	0.398 (~3.1%)
L_2 (spacer) (Å)	12.734	13.834	-1.100 (~8.0%)
Average Pb-I bong length (Å)	3.213	3.163	0.050 (~1.6%)
Average quadratic elongation ($\langle\lambda\rangle$)	1.00117	1.00058	5.9×10^{-4}
Average bond angle variance (deg^2)	19.3	4.4	14.9
Average Pb-I-Pb bond angle (deg)	166	170	-4

In addition to the lattice expansion, the incorporation of EA cation in the cage induces a higher level of structural distortion. In general, structural distortions of the inorganic framework can be categorized into two types. One is the geometrical distortion of the PbI_6^{4-} octahedra themselves, which can be quantified by octahedral distortion parameters of bond length quadratic elongation ($\langle\lambda\rangle$) and bond angle variance (σ^2)[188]

$$\langle \Lambda \rangle = \frac{1}{6} \sum_{\{i=1\}}^{6} \left(\frac{d_i}{d_o} \right)^2 \quad (4.1)$$

$$\sigma^2 = \frac{1}{11} \sum_{\{i=1\}}^{12} (\alpha_i - 90)^2 \quad (4.2)$$

where d_i is the Pb-I bond length, d_o is the mean Pb-I bond distance, α_i is the I-Pb-I bond angles of the octahedra. In an ideal PbI_6 octahedron, both $\langle \lambda \rangle$ and σ^2 are equal to 1. Larger $\langle \lambda \rangle$ indicates a more stretched octahedron, while larger σ^2 indicates higher deviation of Pb position from the center. The average $\langle \lambda \rangle$ and σ^2 of overall structure $(BA)_2(EA)_2Pb_3I_{10}$ is calculated to be 1.00117 and 19.3 deg^2, which is higher than that of $(BA)_2(MA)_2Pb_3I_{10}$ (1.00058 and 4.4 deg^2), respectively. The other type of structural distortion is the larger global distortion between adjacent octahedra (i.e. octahedral tilting), which can be determined from the Pb−I−Pb bond angle. In an ideal cubic perovskite with no octahedral tilting, the Pb−I−Pb bond angle is equal to 180°. The average Pb-I-Pb angle is 166 deg and 170 deg for $(BA)_2(EA)_2Pb_3I_{10}$ and $(BA)_2(MA)_2Pb_3I_{10}$, respectively, indicating a slightly higher octahedral tilting in the former.

It is also interesting to point out that when switching the A-cation from MA to EA the thickness of the perovskite slab (defined as L_1 in Figure 4.1a) is increased slightly from 12.876 Å to 13.276 Å, while the interlayer distance (defined as L_2 in Figure 4.1a) is reduced from 13.834 Å to 12.734 Å. This has been considered as an indicator of inherent strain relaxation in 2D structures.[180, 189] Although the incorporation of EA cation in the perovskite cage creates large strain on the inorganic framework, this strain can be readily dissipated into the interlayer space

via octahedral distortion of the outer layers. As a result, the BA cations change the molecular conformation to accommodate the distortion. In addition, from the viewpoint of the recent proposed 'lattice mismatch model',[189] one may expect that substitution of the MA by EA will enhance the initial in-plane strain between the $(BA)_2PbI_4$ and 3D-like layers when they are associated to form in-plane coherent interface in a multilayered composite. Although the 3D $EAPbI_3$ structure does not exist, simple considerations based on the Goldschmidt rule predict a larger volume for the hypothetic unit cell of $EAPbI_3$ than for the unit cell of $MAPbI_3$ and thus a larger in-plane mismatch with $(BA)_2PbI_4$.

4.2.2 Structural Evolution of $(BA)_2(EA_xMA_{1-x})_2Pb_3I_{10}$ Alloys

To better illustrate the influence of A-cation on the structural properties, we further synthesized a series of single-crystal A-cation alloyed 2D perovskites of $(BA)_2(EA_xMA_{1-x})_2Pb_3I_{10}$ using precursor solutions containing mixed MA and EA cations. The MA to EA ratios determined by ^1H NMR measurements on three representative alloys are 0.73/0.27, 0.55/0.45 and 0.35/0.65, respectively. The determined MA to EA ratio is slightly higher than the ratio in the precursor solution (Figure_Apx C.2), indicating the inorganic lattice enthalpically prefer MA cation. However, entropic gain will drive the mixing of the two cations. The compounds are described as $MA_{0.73}EA_{0.27}$, $MA_{0.55}EA_{0.45}$ and $MA_{0.35}EA_{0.65}$ for the following discussion. Figure_Apx C.3 show the calculated tolerance factor as a function of EA content. Using the tolerance factor of $FAPbI_3$ as a reference point, the ability to incorporate large EA cation with content exceeding 0.62 stems from the relaxed tolerance factor requirement in 2D perovskites. Crystal structures of these alloys were solved using single-crystal X-ray diffraction for structural comparison. Because the MA and EA cations are highly disordered in our single-crystal X-ray

diffraction data, we cannot distinguish and model them accurately. Therefore, the structures were refined as either MA or EA as the A-cation, depending on which one gives better refinement, but this will not influence the structures of the inorganic framework. The crystallographic data and structural refinement information are provided in Table_Apx C.4. These alloys crystallize in the monoclinic space group *Cc*, which has a lower symmetry than the pure A-cation structures.

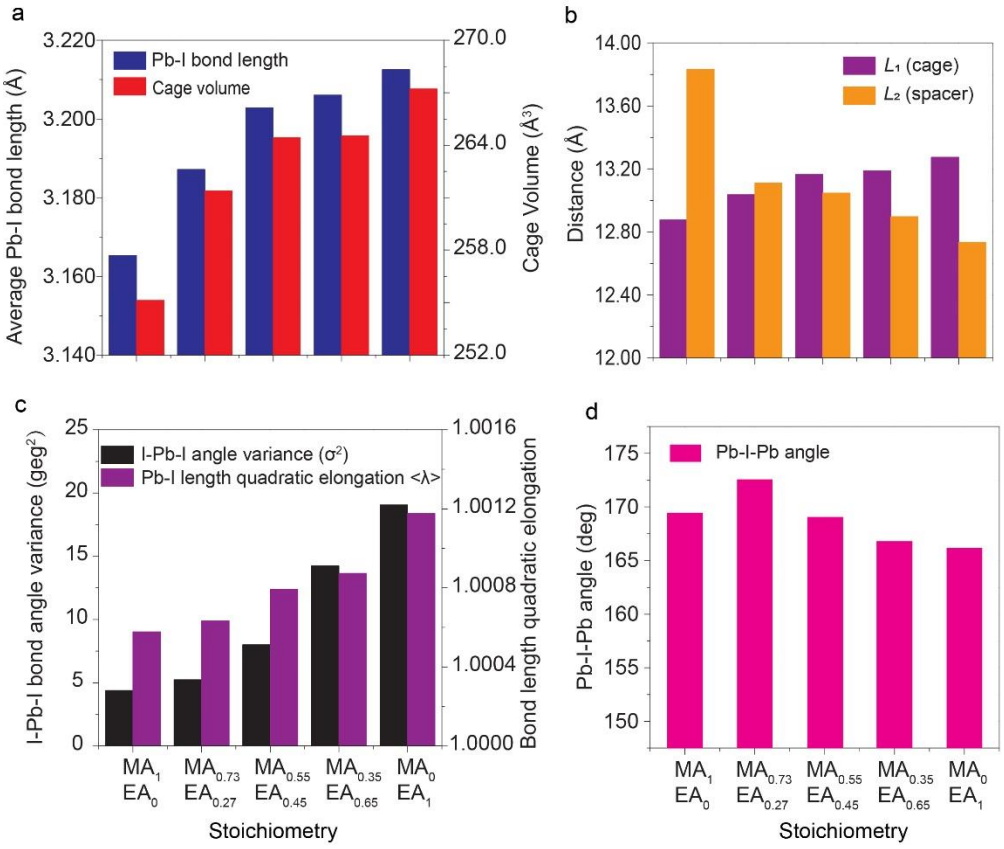

Figure 4.2 Structural properties of $(BA)_2(EA_xMA_{1-x})_2Pb_3I_{10}$ alloys. The trends of (a) average Pb-I bond length and cage volume, (b) thickness of the perovskite slab (L_1) and interlayer spacer distance (L_2), (c) average I-Pb-I angle variance and Pb-I length quadratic elongation, (d) average Pb-I-Pb angle as a function of alloying degree.

Cation alloying can be viewed as an effective approach to tune the average size of A-cation. Figure 4.2 shows the trends of several structural parameters as the EA/MA ratio (or the average size of A-cation) increases. For example, the average Pb-I bond length and cage volume increase with increasing the EA/MA ratio (Figure 4.2a). The thickness of the perovskite slab (L_1) also increases with increasing the EA/MA ratio, while the interlayer distance decreases (Figure 4.2b). The interlayer distance is indeed changing as a result of a strain along the stacking axis opposite to the in-plane initial strain.[189] We consider this as an indicator of increasing strain in the alloys with more EA cations in the cages. Furthermore, incorporation of more EA cations induces a larger deviation from the ideal PbI_6^{4-} octahedron, as demonstrated by the increasing $\langle\lambda\rangle$ and σ^2 (Figure 4.2c). Interestingly, the average octahedral tilting angle remains quite similar (Figure 4.2d), which appears to slightly increase and then decrease. In fact, the even slightly smaller tilting angle in the EA structure than MA structure is counterintuitive, because one may expect that EA cation will stretch Pb-I-Pb bond angle (make it closer to 180°) due to the much larger effective radius, similarly to the structural evolution from orthorhombic $CsPbI_3$ to tetragonal $MAPbI_3$ then to cubic $FAPbI_3$ (Table_Apx C.5). However, octahedral tilting is an efficient way to relax internal stress[189] related to the formation of the multilayered composite. These two effects play in opposite directions.

The above comparisons are focused on the average of overall structure (i.e. two outer layers + one inner layer). However, it is important to point out that the inner and outer layers exhibit distinctive structural properties. Figure 4.3 provides the trends of the octahedral distortion and octahedral tilt of the inner and outer layers as a function of alloying degree. The outer layer exhibits higher octahedral distortion than the inner layer, as demonstrated by larger $\langle\lambda\rangle$ and σ^2 in

all compounds. Both the inner and outer layers show an increasing trend of the σ^2 with increasing the EA content (Figure 4.3a). The $\langle\lambda\rangle$ of the inner layer is slightly reduced in the EA alloys compared to the MA structure (Figure 4.3b). Therefore, the increasing trend of the $\langle\lambda\rangle$ in the overall structure is mainly determined by the outer layer, which exhibits larger $\langle\lambda\rangle$ with an increasing EA content (Figure 4.3b). This is because the incorporation of EA cations in the cage induces a greater impact on elongating the longest Pb-I bonds (highlighted as dash lines in Figure 4.1b) than the other bonds.

Due to the anisotropic 2D structure, we categorized the Pb–I–Pb angles into two groups: equatorial angle and axial angle (see Figure 4.1b for definition) for the comparison of octahedral tilt. As shown in Figure 4.3c, the average axial angle increases from 170 deg (MA) to 178 deg ($MA_{0.73}EA_{0.27}$) and then slightly decreases to 174 deg (EA). The average equatorial angle of the

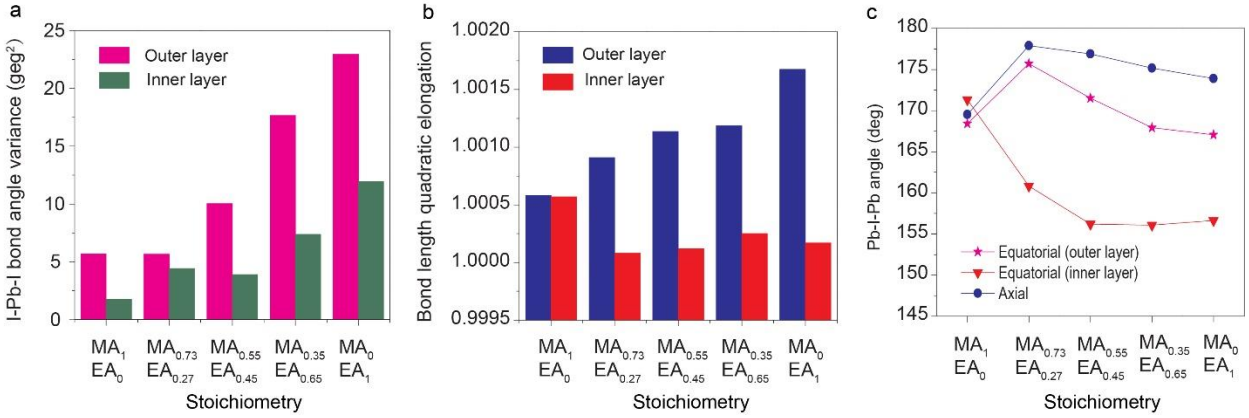

Figure 4.3 Structural properties of the inner and outer layers in the set of $(BA)_2(EA_xMA_{1-x})_2Pb_3I_{10}$. The trends of (a) average I-Pb-I angle variance, (b) Pb-I length quadratic elongation, (c) average equatorial Pb-I-Pb angle of the inner and outer layers as a function of alloying degree. Panel c also shows the trend of axial Pb-I-Pb angle.

outer layer also increases from 168 deg (MA) to 176 deg ($MA_{0.73}EA_{0.27}$) and then decreases to 167 deg (EA). However, the average equatorial angle of the inner layer exhibits an opposite trend, which dramatically decreases from 170 deg (MA) to 156 deg ($MA_{0.55}EA_{0.45}$) and then remains almost unchanged. The results show that the incorporation of the EA cations in the cage induces a larger in-plane tilt in the inner layer. However, when the overall structures are considered, this effect is partially cancelled due to the smaller in-plane tilt of the out layer and the smaller tilt along the stacking direction. Because the inner layer is templated by the two cage EA cations, the larger in-plane tilt of the inner layer is probably due to steric and Coulombic interactions between the EA cations and inorganic framework. For example, because the EA cation exhibits a more anisotropic shape than the MA cation, the octahedra of the inner layer have to tilt in a certain way to accommodate the EA configuration (as highlighted in Figure 4.1c).

4.2.3 Optical Properties of $(BA)_2(EA_xMA_{1-x})_2Pb_3I_{10}$ (x = 0-1)

Absorption spectra collected on exfoliated single crystals show a continuous blue shift of the excitonic absorption peak as the EA content increases (Figure 4.4a). Absorption spectra of 15 randomly selected exfoliated crystals of $MA_{0.55}EA_{0.45}$ show close excitonic absorption peaks, confirming no phase segregation into the MA and EA structures (Figure_Apx C.4). PL spectra of the corresponding bulk single crystals also exhibit blue shift (Figure 4.4b). The tuning of the bandgap can also be seen in the crystal color, which gradually changes from red to black with decreasing the EA content (Figure_Apx C.5). The $(BA)_2(EA)_2Pb_3I_{10}$ has a PL emission peak located at 585 nm (corresponding to an optical bandgap of 2.12 eV), which is significantly blue shifted from that of $(BA)_2(MA)_2Pb_3I_{10}$ at 620 nm (2.00 eV). In fact, $(BA)_2(EA)_2Pb_3I_{10}$ exhibits

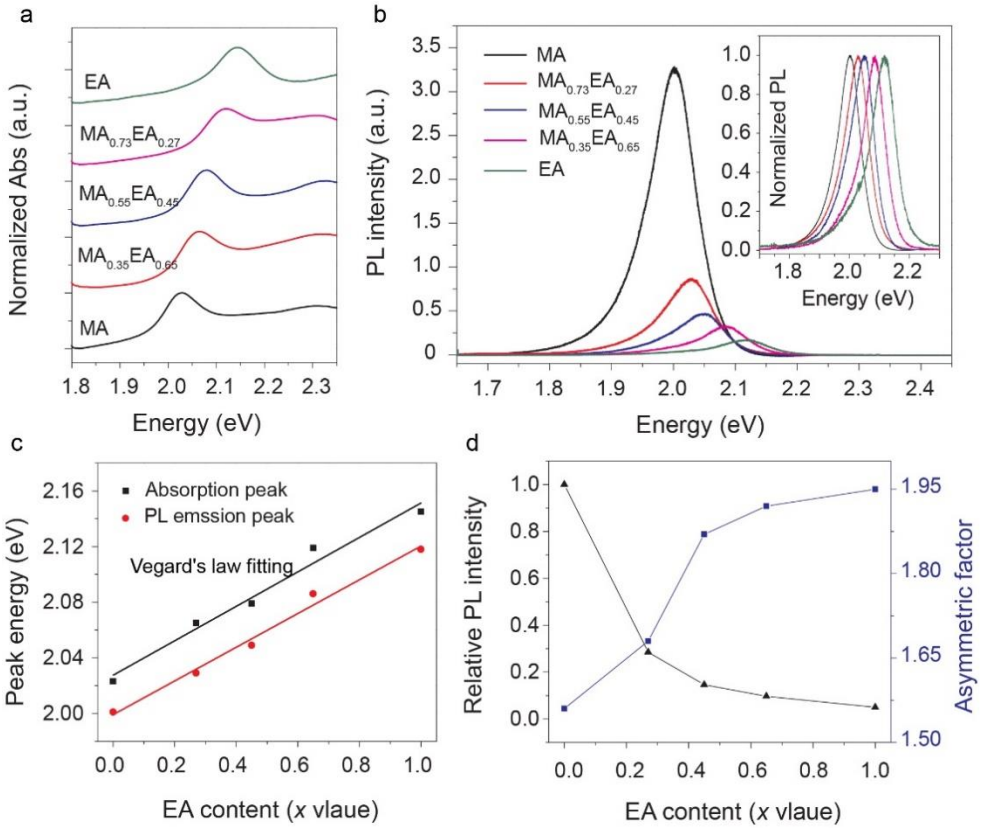

Figure 4.4 Optical properties of the $(BA)_2(EA_xMA_{1-x})_2Pb_3I_{10}$ alloys. (a) Absorption spectra of the alloys. (b) PL spectra of the alloys. Normalized spectra are shown in the inset. (c) The plot of excitonic absorption peak and emission peak as a function of the EA content. The straight lines are the fits using the Vegard's law (d) Plot of relative PL intensity and PL asymmetric factor as a function of the EA content.

the highest bandgap among all previously reported n = 3 lead iodide 2D perovskites (Table_Apx C.3). We note that the PL spectra collected in the interior and edge of the $(BA)_2(EA)_2Pb_3I_{10}$ are almost unchanged (Figure_Apx C.6). Figure 4.4c shows the plot of excitonic absorption/emission peaks as a function of x value, conforming to the Vegard's law approximation (fitting lines).

Besides the tuning of the bandgap, the PL intensity is quenched in the structure with an increasing EA fraction (i.e. *x* value) (Figure 4.4b and 4d). As an example, the PL intensity of $(BA)_2(EA)_2Pb_3I_{10}$ is about 20 times weaker than that of $(BA)_2(MA)_2Pb_3I_{10}$. Note that the PL spectra were collected on bulk single crystals with freshly cleaved surfaces under the same laser excitation power density. Such strong PL quenching seems to be associated with the higher octahedral distortion and elongated Pb-I bond length, as will be discussed below. Another interesting characteristic is that, each PL spectrum displays an asymmetric line-shape, tailing to lower energy. We introduce an asymmetric factor to quantify the PL tailing effect:

$$A_S = \frac{H_r}{H_b} \tag{4.3}$$

where H_b and H_r are the peak half-widths at 10% of the peak height. H_b corresponds to the blue (higher energy) side, while H_r characterizes the red (lower energy) side relative to the peak position. As shown in Figure 4.4d, the asymmetric factor increases as the EA content increases and is anti-correlated with the relative PL intensity. The low-energy tail in the static PL spectra can be attributed to the radiative recombination of trap states below the bandgaps, as has been previously suggested.[190] Further investigation of the trap states is discussed in a separate section below using ultrafast spectroscopic techniques.

Having characterized the structural and optical properties, we turn to understand and derive the structure-property relationship. Table 4.2 summarizes the optical and structural properties of the set of $(BA)_2(EA_xMA_{1-x})_2Pb_3I_{10}$. Optical transitions in perovskite materials occur between filled Pb(6s)−I(5p) hybrid orbitals and empty Pb(6p) orbitals of the inorganic layer (vide infra).

As a result, the optical bandgap can be correlated with the degree of anti-bonding overlap between the Pb(6s) and I(5p) orbitals, which is strongly modulated by the bonding parameters such as Pb-I-Pb bond angle and Pb-I bond length.[159] While the A-cations do not directly contribute to the electronic band structure close to the band edges, they have a strong influence on the tilting of PbI_6^{4-} octahedra and in turn affect the degree of orbital overlap between Pb and I orbitals. For example, there is a systematic decreasing trend in the bandgap with increasing the size of A-cation in the perovskite phases of 3D $APbI_3$ (A = Cs, MA, FA) at room temperature (Table_Apx C.5). This is because the octahedral tilting decreases (or Pb-I-Pb bond angle increases) while the Pb-I bond length almost remains unchanged as the cation size increases, leading to an increased overlap of the Pb(6s) and I(5p) orbitals and in turn a more destabilized VB.[158, 185]

Table 4.2 Comparison of optical properties and structural parameters for $(BA)_2(EA_xMA_{1-x})_2Pb_3I_{10}$

	EA	**$EA_{0.65}MA_{0.35}$**	**$EA_{0.45}MA_{0.55}$**	**$EA_{0.27}MA_{0.73}$**	**MA**
Absorption peak (eV)	2.145	2.119	2.079	2.065	2.023
PL emission (eV)	2.118	2.086	2.049	2.029	2.001
Relative PL intensity	0.050	0.097	0.146	0.285	1
PL asymmetric factor	1.95	1.92	1.87	1.68	1.56

Ave. Pb-I bond length (Å)	3.213	3.206	3.203	3.178	3.165
Ave. cage volume ($Å^3$)	267.2	264.5	264.4	259.5	255.1
Ave. Pb-I-Pb bond angle (°)	166	167	169	172	169
Quadratic elongation ($\langle\lambda\rangle$)	1.00117	1.00087	1.00079	1.00063	1.00058
Bond angle variance (σ^2, deg^2)	19.3	14.2	8.0	5.8	4.4

Interestingly, the average octahedral tilting of the overall structure in the set of $(BA)_2(EA_xMA_{1-x})_2Pb_3I_{10}$ alloys remains similar. The wider optical bandgap can thus be attributed to the gradually increasing Pb-I bond elongation which leads to less overlap between the electron wave functions of the Pb(6s) and I(5p) orbitals and narrower band widths. In fact, the trend is consistent with high-pressure studies on 2D perovskites, which show bandgap redshift with decreasing Pb-I bond length under pressure.[191] The alloying of EA cation into the cage acts like "negative chemical pressure" to expand the crystal structure, which can be a generic approach to tune the optoelectronic properties of 2D perovskites.[191] Similar bandgap blueshift in the 3D "hollow" perovskites with increasing Pb-I bond lengths has also been observed.[177, 178]

Another interesting structure-property relationship is that the PL quenching seems to correlate with Pb-I bond length and/or individual PbI_6^{4-} octahedral distortion. PL efficiency is

determined by the relative ratio of radiative recombination rate to non-radiative recombination rate.[192] The radiative recombination rates of these alloys are expected to be similar, as they likely have similar exciton binding energies. Therefore, the pronounced PL quenching which usually indicates poor photophysical properties in a direct band gap semiconductor might originate from more non-radiative recombination losses in the structures with higher EA content. Comparable photophysical properties have been reported in the perovskite phases of orthorhombic $CsPbI_3$, tetragonal $MAPbI_3$, and cubic $FAPbI_3$, which exhibit almost ideal PbI_6^{4-} octahedra and constant Pb-I bond length but different octahedral tilting (Table_Apx C.5). In conjunction with the observations here, the photophysical properties of these 2D perovskite materials appear to be mostly governed by the Pb-I bond length and/or octahedral distortion, with no noticeable effect of octahedral tilting.

4.2.4 Electronic Structure and Dielectric Properties

We next consider how the A-site cations affect the electronic structure and dielectric properties from a theoretical perspective. In this respect, we first performed Density Functional Theory (DFT) based calculations using the Perdew-Burke-Ernzerhof (PBE) functional and including spin-orbit coupling (SOC), which will be the default level of theory if not otherwise stated. Figure 4.5a and 5b compare the computed band structures of $(BA)_2(EA)_2Pb_3I_{10}$ and $(BA)_2(MA)_2Pb_3I_{10}$. Both band structures present an almost direct bandgap at Γ, and the calculated bandgaps are 0.86 eV and 0.50 eV for the EA and MA structure, respectively. In $(BA)_2(EA)_2Pb_3I_{10}$, a slightly indirect band gap appears owing to the breaking of symmetry along Γ-X direction (not shown). The slight shift of VBM from Γ points to possible Rashba effect due to the giant SOC of Pb atom.[193] Moreover, the band structures of both compounds show that dispersive bands are only

present in the 2D plane while flat bands occur along Γ-Y. This suggests little or no electronic coupling along the direction that corresponds to the layer stacking axis.

The DFT predicted bandgaps are underestimated compared to the experimental results as expected when using the PBE functional and taking SOC into account. We further used the recently

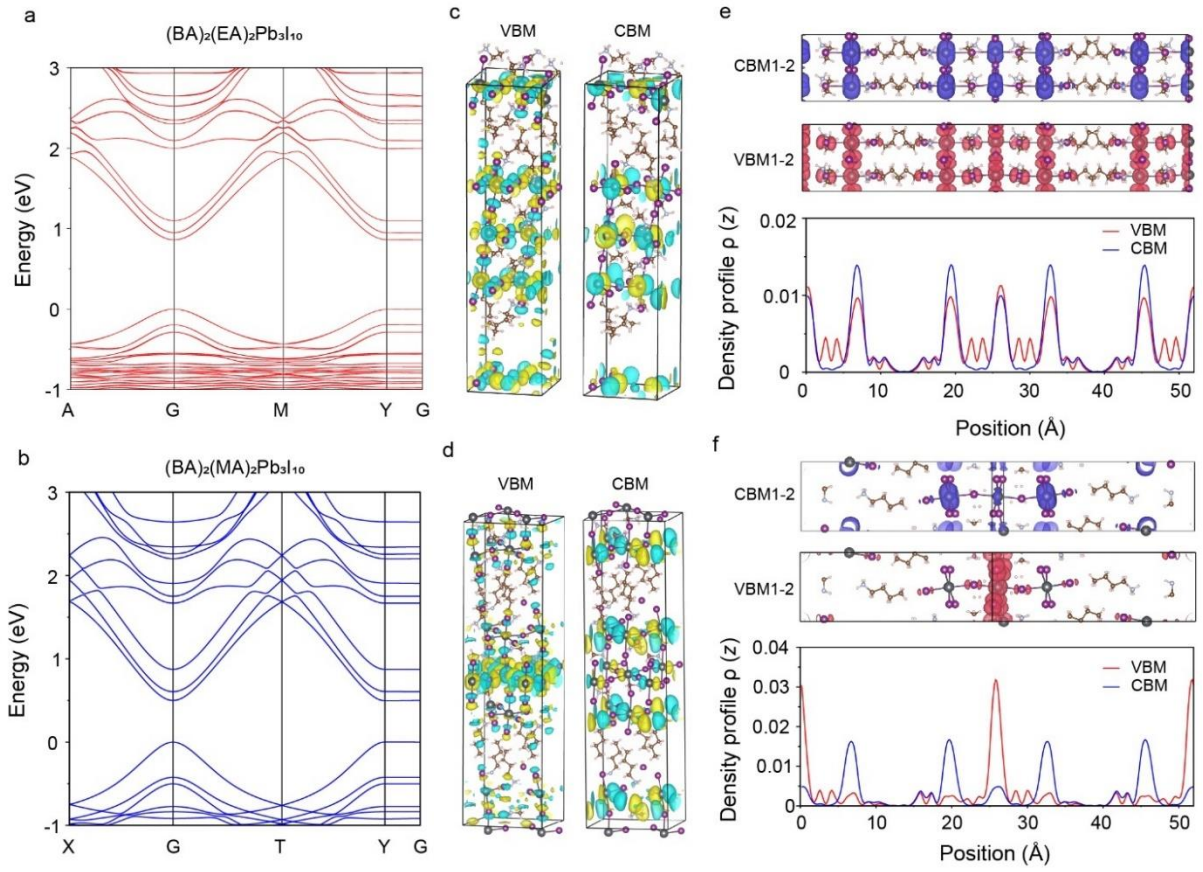

Figure 4.5 Comparison of electronic band structures of $(BA)_2(EA)_2Pb_3I_{10}$ and $(BA)_2(MA)_2Pb_3I_{10}$. Calculated electronic band structures including SOC of (a) $(BA)_2(EA)_2Pb_3I_{10}$ and (b) $(BA)_2(MA)_2Pb_3I_{10}$. Wave-functions computed without SOC at Γ for (c) $(BA)_2(EA)_2Pb_3I_{10}$ and (d) $(BA)_2(MA)_2Pb_3I_{10}$, show the orbital hybridizations at VBM and CBM. Local density of states computed with SOC at VBM and CBM for (e) $(BA)_2(EA)_2Pb_3I_{10}$ and (f) $(BA)_2(MA)_2Pb_3I_{10}$. The density profiles of the two structures along the stacking direction are also shown. All results have been obtained using the PBE functional.

reported Tran-Blaha-Modified Becke-Johnson potential optimized for 2D perovskites to improve the accuracy of bandgap prediction (ppTB-mBJ).[194] Using ppTB-mBJ with the organic cations substituted by Cs (see ref[194] for more details), the calculated bandgaps become 2.62 eV and 2.53 eV for $(BA)_2(EA)_2Pb_3I_{10}$ and $(BA)_2(MA)_2Pb_3I_{10}$, respectively, which are in better agreement with the experiment given that excitonic effects are not considered. Overall, regardless of the level of theory, $(BA)_2(EA)_2Pb_3I_{10}$ exhibits a larger bandgap compared to $(BA)_2(MA)_2Pb_3I_{10}$.

We next plot the wave functions to highlight the nature of electronic states at the band edges. Wave functions at the Γ point show an antibonding hybridization between Pb(6s) and I(5p) orbitals at the VBM while the conduction band minima (CBM) is mainly made of bonding type between Pb(6p) states (see Figure 4.5c and 5d for the EA and MA structure, respectively). Comparing the two structures, we find that the CBM is less stabilized in $(BA)_2(EA)_2Pb_3I_{10}$ because the longer Pb-Pb distances result in weaker bonding interactions and reduced bandwidth. Similarly, VBM is also less destabilized in $(BA)_2(EA)_2Pb_3I_{10}$ due to weaker anti-bonding interactions associated with longer Pb-I bonds. The combined effect of less stabilized CBM and VBM in $(BA)_2(EA)_2Pb_3I_{10}$ therefore results in the wider bandgap. As discussed above, the longer Pb-I bonds result in reduced orbital overlap in the EA structure. In general, the extent of orbital overlap defines the electronic band width. As shown in Figure 4.5a and 5b, the calculated band widths of the VB as well as the CB for the EA structure are much narrower, thus contribute to the wider bandgap.

As mentioned above, in $(BA)_2(EA)_2Pb_3I_{10}$, the bands are less dispersive than in $(BA)_2(MA)_2Pb_3I_{10}$ as can be inferred from their band widths in Figure 4.5a and 5b. That is, the extent of orbital overlap as discussed above generally defines the electronic bandwidth. As it is clearly shown in Figure 4.5a and 5b, the band widths of the VB as well as the CB for the EA

compound are much narrower. Accordingly, the calculated reduced effective masses (using ppTB-mBJ) are larger for $(BA)_2(EA)_2Pb_3I_{10}$ (~0.34m_0 to 0.69m_0) as compared to $(BA)_2(MA)_2Pb_3I_{10}$ (~0.20m_0) (Table_Apx C.6). We note that the predicted reduced mass of $(BA)_2(MA)_2Pb_3I_{10}$ is in good agreement with the experimentally reported 0.201m_0 using magneto-absorption experiments[195] whereas that of $(BA)_2(EA)_2Pb_3I_{10}$, for which no experimental data is currently available, appears to be much higher (note, ppTB-mBJ generally overestimates the effective masses, see ref[194]). These results suggest that photogenerated carriers are probably less mobile in $(BA)_2(EA)_2Pb_3I_{10}$ than in $(BA)_2(MA)_2Pb_3I_{10}$.

The localization of the carriers can influence the recombination process of the generated electron-hole pairs. In Figure 4.5e and 5f, we plot the local density of states (LDOS) and their profiles for both compounds at VBM and CBM to show the spatial localization of holes and electrons, considering the static averaged crystallographic structured. In $(BA)_2(MA)_2Pb_3I_{10}$, holes (at VBM) are localized on the inner layer whereas the electrons (at CBM) appear at the outer layers.[195] In contrast, both holes and electrons are delocalized on the three layers for $(BA)_2(EA)_2Pb_3I_{10}$. This suggests that generated hole-electron pairs are probably spatially more evenly distributed in $(BA)_2(EA)_2Pb_3I_{10}$ as compared to $(BA)_2(MA)_2Pb_3I_{10}$. The origin of these different spatial localizations is discussed in the supporting information.

By applying the composite approach, detailed in ref[155, 196], we obtained the band energy alignment between the inorganic well and the organic spacer barrier. The ppTB-mBJ bandgaps were used for constructing the CB alignment (Figure_Apx C.7). The confinement potentials (V_h for holes, V_e for electrons) are more balanced in $(BA)_2(EA)_2Pb_3I_{10}$ (2.6 eV versus 2.1 eV) than in $(BA)_2(MA)_2Pb_3I_{10}$ (3.3 eV versus 1.5 eV). Figure_Apx C.8 shows high-frequency dielectric

constant profiles [$\varepsilon_\infty(z)$] along the stacking axis for the two compounds. ε_∞ varies from 2.4 [2.2] for $(BA)_2(EA)_2Pb_3I_{10}$ [$(BA)_2(MA)_2Pb_3I_{10}$] in the organic spacer layer to 5.3 [5.1] in the inorganic layer. The two compounds present similar dielectric contrasts between the inorganic and the organic layers, which may suggest similar exciton binding energies in the two structures. The slightly different ε_∞ in $(BA)_2(EA)_2Pb_3I_{10}$ can be understood by the volumetric expansion of inorganic layers and the compression of organic spacer layers as compared to $(BA)_2(MA)_2Pb_3I_{10}$. Nevertheless, the dielectric environment is similar in the two compounds.

4.2.5 Excited-State Dynamics

We further studied the excited-state dynamics using ultrafast TA spectroscopy. Except for a few reports,[190] we note that the excited-state dynamics of 2D perovskites with n > 1 remain largely unexplored. Figure 4.6 shows the normalized TA spectra of $(BA)_2(EA_xMA_{1-x})_2Pb_3I_{10}$ (x = 0, 0.27, 0.45, 0.67, 1) obtained with 2.41 eV pump and broadband probe (1.74–2.28 eV) on exfoliated single crystals. For all five compositions, the TA spectra largely resemble each other. There are four features to pay attention to: (1) a strong GSB at the bandgap, (2) a short-lived ESA below the bandgap, which is most prominent in the 0.40-ps cut and disappeared before 0.80 ps, (3) a long-lived ESA above the bandgap, the intensity of which remains largely unchanged within the first 8 ps, and (4) a weak bleaching below the bandgap, which becomes visible after the overlapping ESA disappears near 0.8 ps. The relative locations and shapes of the four features do not change much across the entire series of samples we made, indicating similar electronic structures and almost identical mechanisms behind the excited-state dynamics, which agrees with the band structure calculations conducted in the section above. The fact that no overlap occurred between all five spectra, along with the structural characterization we presented above, confirm the pure

nature of the *n* = 3 structure (i.e. absence of other *n*-value structures) and the uniform cation alloying.

The normalized dynamics of the four features in the pure MA and EA structures extracted at representative energy are plotted in Figure 4.7a and 7b. Convolution between different features

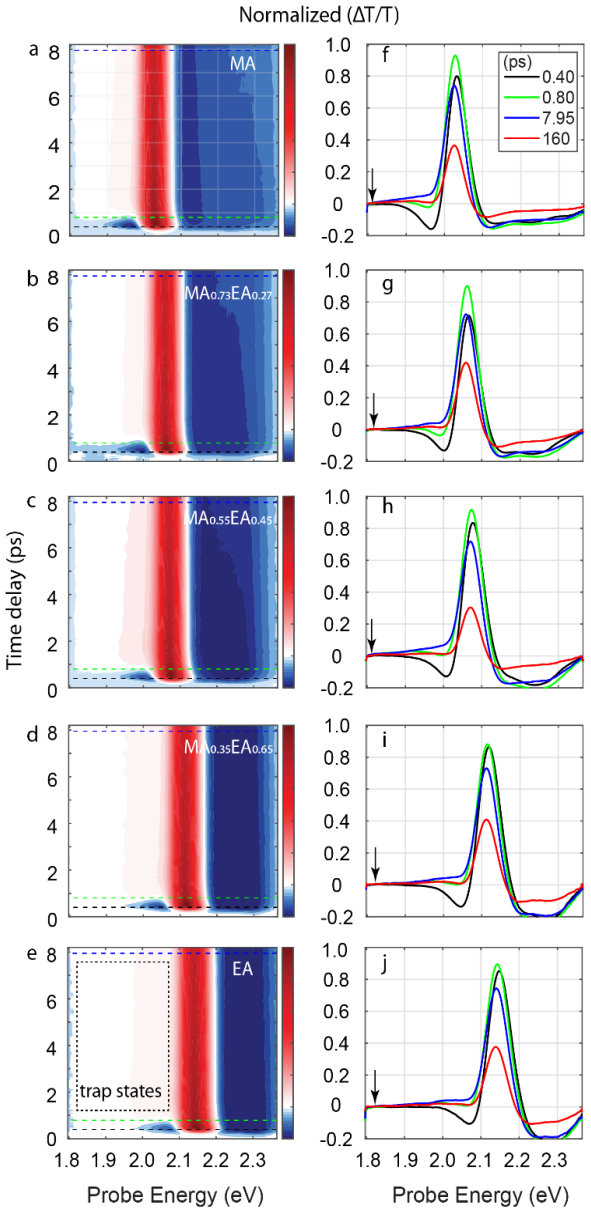

Figure 4.6 Pseudocolor plots of the normalized transient absorption (TA) spectra of the (a) MA, (b) $MA_{0.73}EA_{0.27}$, (c) $MA_{0.55}EA_{0.45}$, (d) $MA_{0.35}EA_{0.65}$, and (e) EA structures obtained with 2.41 eV pump for the first 8 ps. Dash lines indicate the cuts at delay time of 0.40 ps (black), 0.80 ps (green), and 7.95 ps (black). TA spectra cuts of the (f) MA, (g) $MA_{0.73}EA_{0.27}$, (h) $MA_{0.55}EA_{0.45}$, (i) $MA_{0.35}EA_{0.65}$, and (j) EA structures at four representative delay time points (t = 0.40, 0.80, 7.95, 160 ps). The arrows in f-g indicate the zero cross points of the curves at 7.95 ps.

exists because of unavoidable spectral overlap. To better decompose the highly convoluted TA spectra, spectra at late time delays (> 160 ps) were acquired and a global analysis was performed

on each TA spectra. Similar decay associated spectra (DAS) were generated from all five compositions (Figure_Apx C.9). Only the ones from pure $(BA)_2(MA)_2Pb_3I_{10}$ and $(BA)_2(EA)_2Pb_3I_{10}$ are plotted here (Figure 4.7c and 7d). Three processes were gleaned from the global analysis. The pale green one shows a derivative shape and has a lifetime < 1 ps. The second component (blue, Figure 4.7c and 7d) with picoseconds lifetime has a broad bleaching peak below the bandgap. The last component (black, Figure 4.7c and 7d) comes with a relatively long lifetime and a bleaching at the bandgap. With the spectra and dynamics decomposed, we next discuss the assignment of the four features and analyze the dynamic processes.

The bandgap bleaching peak (blue, Figure 4.7a and 7b) with two main processes can be assigned to the band-edge population. The growing process likely comes from the fast bandgap bleaching and hot carrier relaxation, as its formation time aligns well with the lifetime of the first DAS, which will be discussed below. The decaying one has a relatively long lifetime and the spectra features overlap the last DAS, which presumably is associated with the recombination process usually lasting nanoseconds in perovskite materials.[14] The short-lived ESA feature

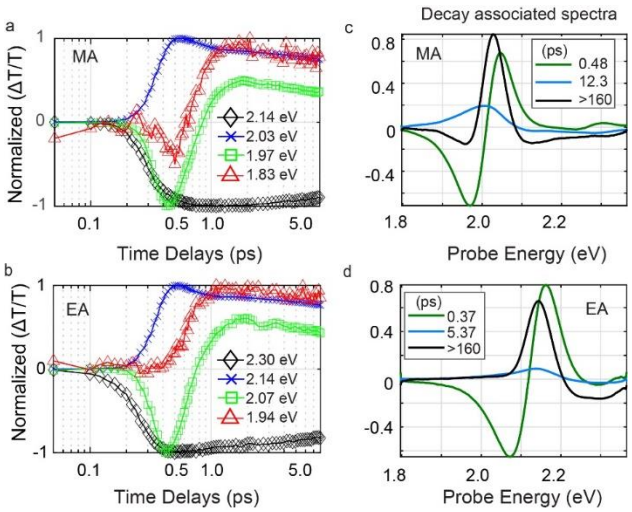

Figure 4.7 Normalized dynamics of bleaching below the bandgap (triangle), absorption below the bandgap (square), bleaching at the bandgap (cross), and absorption above the bandgap (diamond) of (a) $(BA)_2(MA)_2Pb_3I_{10}$ and (b) $(BA)_2(EA)_2Pb_3I_{10}$. Decay associated spectra of (c) $(BA)_2(MA)_2Pb_3I_{10}$ and (b) $(BA)_2(EA)_2Pb_3I_{10}$ obtained with global analysis.

(green, squares), is most-likely to be associated with the shot-lived hot carriers.[14, 190, 197, 198] The fact that the absolute intensity of the peak decreased with an increasing bandgap value (as well as the *x* value) is probably due to less excess energy of initial generated hot carriers.[199] The first DAS, largely associated with this feature, may indicate the flow from higher energy levels to the bandgap. The long-lived ESA above the bandgap (black, diamonds) show no obvious decay before 8 ps, and has similar dynamics to the main bleaching peak, as they both show up in the last DAS. We assign it to the ESA caused by band edge carrier, as higher band can be easily accessed according to the DFT calculation (Figure 4.5a and 5b). Another explanation could be that this peak is generated by the blue shift of the bandgap after excitation, however, we believe this likely to be less feasible as the amount of the blue shift did not change as a function of photo-excited carrier density or delay time (see details about the fluence-dependent study in Figure_Apx C.10 and Figure_Apx C.11).

Though largely overlapping with the ESA, the bleaching below the bandgap (red, triangles) shows completely different growing dynamics compared to the main bleaching peak (blue, crosses). The energy of this sub-bandgap peak happens to overlap with the only peak in the second DAS. This indicates that this bleaching feature may be a separate process happening in the system other than hot-carrier cooling and bandgap renormalization summarized by the first and the last DAS. Judging by the peak location, it is most likely attributed to the trap states below the bandgap, as also suggested by other report.[190] The lifetime of the second DAS is slightly longer than expected but still within the same scale of magnitude. This is probably because this peak convolves a lot with the main bleaching peak, and there is energy transfer back and forth between the two states.

As discussed above, the main electronic transitions of excited states are qualitatively similar in these structures. This can be understood by the fact that electronic band structures are mainly determined by the inorganic frameworks which are all made of 2D corner sharing PbX_6^{4-} octahedra. However, the change of octahedral parameters such as distortion level and Pb-I bond length can modify the energy landscape, especially for the sub-bandgap states. As is shown in the TA surfaces in Figure 4.6a–e, the bleaching peak below the bandgap is getting broader (the pale red area below the bandgap) with an increasing amount of EA, indicating wider energetic distribution of these states. Such wider energetic distribution is well correlated with larger octahedral distortion and variation of Pb-I bond length in the structures with an increasing EA content.

Lastly, we discuss several possible explanations for the PL quenching. Worse crystals with more defects can lead to PL quenching. However, the clear trend of PL quenching cannot be simply attributed to the crystal quality, because all the crystals were synthesized in a similar condition. The SCXRD data show that the EA structure has the best refinement (Table_Apx C.2 and Table_Apx C.3), indicating the crystal quality is at least comparable (if not better) to other structures. In contrast, the EA structure has the least PL emission. Therefore, the PL quenching might stem from the inherent structures with varied bonding characters.

Phonons that interact with charge carriers significantly impact non-radiative recombination rates. For example, a recent work established a correlation between the nonradiative recombination rate and molecular rigidity of spacer cations in 2D perovskites through exciton-phonon interaction.[192] Charge carriers in perovskite materials are mainly coupled to the low-frequency vibrational modes of the Pb-I framework. One may expect that the elongated Pb-I bond length

leads to softened phonon modes, which is especially assisted by the stereochemical activity of the Pb^{2+} $6s^2$ lone pair of electrons. This process can induce more phonon mediated non-radiative recombination paths via exciton-phonon interaction. Indeed, the emission peak width is larger in the $(BA)_2(EA)_2Pb_3I_{10}$ relative to $(BA)_2(MA)_2Pb_3I_{10}$, indicating a stronger exciton phonon interaction in the former.

A second explanation is that, the Pb-I bond strength may influence the thermodynamics of interstitial iodine defects which could introduce deep energy levels within the bandgap. A recent proposal suggested the key to explaining the so-called defect tolerance in perovskites lays in the photochemical properties of such defects.[200] Such defects acting as recombination centers can accelerate non-radiative recombination of charge carriers and thus reduce the PL. Our TA measurements reveal the existence of the trap states by applying global analysis and separate the energy transferring processes related to this state. The broader energetic distribution of the trap states correlates well to the PL quenching, while the radiative emission from these trap states may lead to the asymmetric PL peak in the higher EA content structures.

4.3 Conclusion

The Goldschmidt rule of perovskite cage stability is significantly relaxed with EA as the cage cation. This cation is larger than the rule allows yet it incorporates in the perovskite cage by stretching it, giving rise to a stretched version of the $n = 3$ 2D perovskite structure featuring the longest Pb-I bond lengths and extremely large octahedral distortion. In contrast to the bandgap redshift in 3D $APbI_3$ with increasing the cation size, the alloyed 2D perovskites exhibit blue-shifted

bandgap with increasing EA content (equivalent to increasing the size of A-cation). The bandgap blueshift is consistent with the band structure calculations and can be explained by the significant volumetric expansion of the perovskite cage with increased Pb-I bond length. Moreover, it is found that the structure with larger octahedral distortion and longer Pb-I bond length has stronger PL quenching and more asymmetric PL peak. Transient absorption spectroscopy measurements reveal similar excited-state dynamics and the existence of a broad distribution of trap states below the bandgap. The energetic distribution of trap states is broader with lager octahedral distortion and/or longer Pb-I bond length, which might be responsible for the asymmetricity and quenching of the PL emission. Our results provide guidelines for rational design of new and more efficient perovskite materials for optoelectronic applications.

CHAPTER 5 Synthetic and Structure-Property Tailoring of Multilayer (100) Lead Iodide Perovskites with Trap-State Emission

5.1 Introduction

Metal halide perovskites are a highly attractive class of low-cost semiconductors that have proven to be suitable for a wide range of applications including solar cells [153, 201-208], light emission [209-211], radiation detection,[212-216] and lasing [217, 218]. 2D hybrid perovskites provide a viable architecture to perform small molecule reactions in the solid state by utilizing the chemical reactivity of functional organic layers to orchestrate covalent and noncovalent interactions, and to deliver a final material with distinct structural and/or electronic properties.[95, 219-223] The inclusion of designer molecules with targeted functionalities unlocks the potential to achieve a better chemical, structural and photophysical understanding of 2D perovskites.

The soft lattice of metal halide perovskites bestows an intriguing defect-tolerant nature and photophysics that are still not well understood.[224] Asymmetric and multi-modal PL emissions have been observed in multiple metal halide perovskites, including intrinsic charge traps related to iodine redox chemistry [200, 225-227] , photoinduced formation of emissive sub-bandgap defect states[228], in-gap states[229, 230], GBs[231] and edge states[232]. Different strategies have been examined to regulate the luminescent properties through defect engineering and environment control.[226-228, 233-236] Within the family of multilayer (100) Ruddlesden-Popper (RP) perovskites, the direct correlation between structural properties and trap emission has not been analyzed, to our knowledge.

In this chapter, we explored the synthesis and characterization of multilayer (100) lead iodide perovskites, incorporating the bifunctional organic molecules of AA and IPA to produce three new homologous series: $(AA)_2MA_{n-1}Pb_nI_{3n+1}$, $[(AA)_x(IPA)_{1-x}]_2MA_{n-1}Pb_nI_{3n+1}$ and $(IPA)_2MA_{n-1}Pb_nI_{3n+}1$ (n=3-4). The meta-synthetic transformation of the AA organic layers within the 2D hybrid perovskite structure attests as a unique strategy for performing chemical transformations in the solid state, which takes place before the formation of the final product and leads to compounds with novel composition, inaccessible through traditional synthetic routes. The incorporation of the AA cation with the terminal unsaturated bond leads to smaller steric interactions and tighter packing between the organic-inorganic layers and impacts the dielectric profile of the 2D perovskite. On the other hand, the incorporation of the polarizable iodine atom on the IPA cation induces greater steric interactions between the organic layers and organic-inorganic layers. The distinct chemical identities of the functional groups inhered to the organic spacers yield different structures, optoelectronic properties, and carrier dynamics. SCXRD reveals that $(AA)_2MA_2Pb_3I_{10}$ (AA_n3) is a unique structure type with an offset (0, < ½), while $(IPA)_2MA_2Pb_3I_{10}$ (IPA_n3) and the alloyed $[(AA)_x(IPA)_{1-x}]_2MA_2Pb_3I_{10}$ crystallize in the RP structure. The adjacent I···I distance in AA_n3 is ~ 5.6 Å assembling the consecutive $[PbI_6]$ layers closer together among all reported n=3 RP lead iodide perovskites while IPA_n3 presents significantly larger adjacent I···I distance of ~ 8.4 Å. Similarly, IPA_n3 exhibits higher distortions of the equatorial Pb-I-Pb angles in comparison to AA_n3, which leads to a blueshift of its absorption and PL emission compared to AA_n3.

The excited-state dynamics were studied for AA_n3, IPA_n3, $[(AA)_{0.5}(IPA)_{0.5}]_2MA_2Pb_3I_{10}$ ((AA)(IPA)_n3), and $(BA)_2MA_2Pb_3I_{10}$ (BA_n3) by TA spectroscopy, where the formation of

long-lived trap states with broad white-light emission were observed. The trap-state emission can be correlated to the lattice distortion induced by the inclusion of the bifunctional organic molecules with characteristic functional groups. The incorporation of the IPA cation induces the largest lattice distortions that give rise to a new ensemble of states deep into the bandgap. Notably, these deep trap states reduce the recombination lifetime of the bandedge carriers and show an elongated ~100-ps recombination lifetime, which is even longer than the bandedge recombination lifetime. Such behaviors indicate the formation of a new radiative recombination pathway rooted from the designer molecules included in the meta-synthesis procedure.

5.2 Experimental Results and Discussion

5.2.1 Synthesis and Structural Characterization

The spacer cations employed here, AA and IPA, consist of a core alkylammonium skeleton of three carbons, where AA inheres a terminal alkene group and IPA contains an iodine heteroatom on the alkylammonium chain. The targeted synthesis of the studied multilayer perovskites was developed on the solution method based on aqueous hydroiodic acid. The detailed methods can be found in the Appendix, section D.1. The powder X-ray diffraction (PXRD) patterns of crystals

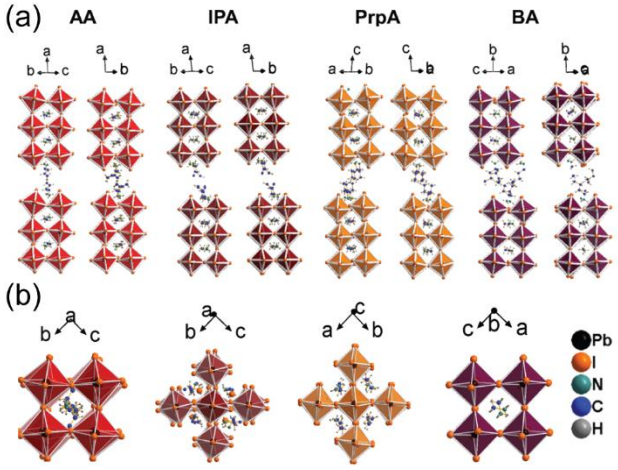

Figure 5.1 (**a**) Comparative view of the offset geometry in the consecutive [PbI_6] layers (**b**) Comparative view along the stacking axis between the (*n*=3) compounds $(AA)_2(MA)_2Pb_3I_{10}$, $(IPA)_2(MA)_2Pb_3I_{10}$, $(PrpA)_2(MA)_2Pb_3I_{10}$ and $(BA)_2(MA)_2Pb_3I_{10}$.

$(AA)_2MA_{n-1}Pb_nI_{3n+1}$, $(IPA)_2MA_{n-1}Pb_nI_{3n+}1$ and $[(AA)_x(IPA)_{1-x}]_2MA_{n-1}Pb_nI_{3n+1}$ (n = 3 and 4) are shown in the Appendix, Figure_Apx D.1, with negligible reflections from secondary phases to confirm the phase-pure synthesis of the compounds.

The crystal structures of the n=3 series: AA_n3, IPA_n3, and (AA)(IPA)_n3 were solved from SCXRD data collected at room temperature (Figure 5.1). The crystal structure of AA_n3 consists of $[Pb_3I_{10}]^{4-}$ inorganic layers that are alternated with AA organic layers. The electrostatic interactions between the organic-inorganic layers yield a three-layer perovskite structure in which the inorganic layers stack on top of each other along the stacking axis *a* (Figure 5.1a). Hence, there is no offset of the consecutive inorganic layers, along the *a* stacking axis with respect to the *bc* plane. Along the *b* stacking axis with respect to the *ac* plane, there is an offset < ½. Therefore, AA_n3 is a new, unique structure type, between the RP type and the Dion-Jacobson (DJ) type. This is the first report of a monoammonium cation affording a non-RP structure type, which is evidently due to the additional hydrogen-bonding (HB) interactions induced from the terminal C=C, alkene group in the allylammonium cation. A comparison of the crystal structures of AA_n3 and $(PrpA)_2MA_2Pb_3I_{10}$ (n=3), which consists of organic layers with the saturated cation propylammonium, proves the definite effect of the terminal alkene group on the resultant 2D perovskite structure. $(PrpA)_2MA_2Pb_3I_{10}$ (n=3) adopts the RP structure with the staggered arrangement of the successive $[Pb_3I_{10}]^{4-}$ inorganic layers (Figure 5.1a).

The crystal structure of IPA_n3 consists of $[Pb_3I_{10}]^{4-}$ inorganic layers that are alternated with IPA organic layers, where there is an iodine atom on the second carbon of the propylammonium skeleton (Figure 5.1). The presence and position of the iodine atom on the alkylammonium

cation induces greater steric interactions and bulkiness within the organic layers. Consequently, the RP structure is templated with two offset layers per unit cell. The inclusion of IPA also causes different levels of lattice distortions, reflected by the Pb-I-Pb angle (Figure 5.2). The iodine atom of the IPA instigates greater distortion of the equatorial Pb-I-Pb angle versus the axial angle. Therefore, the two compounds consisting of IPA showed the biggest distortion in the equatorial angles, but the smallest in the axial angles.

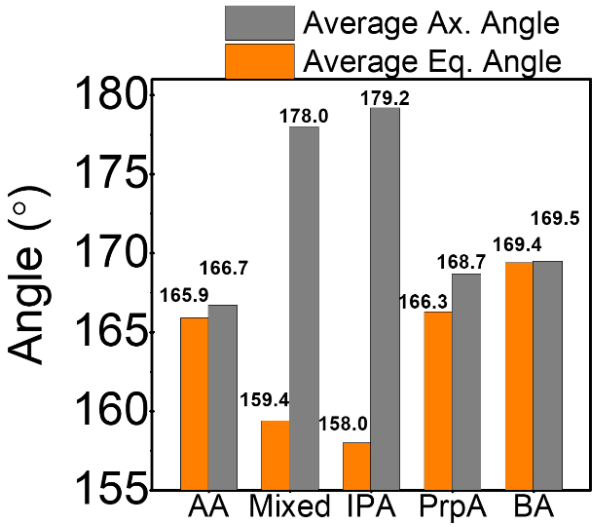

Figure 5.2 Average axial and equatorial Pb−I−Pb angles of (n=3) compounds $(AA)_2(MA)_2Pb_3I_{10}$, $[(AA)_x(IPA)_{1-x}]_2(MA)_2Pb_3I_{10}$, $(IPA)_2(MA)_2Pb_3I_{10}$, $(PrpA)_2(MA)_2Pb_3I_{10}$ and $(BA)_2(MA)_2Pb_3I_{10}$.

5.2.2 Excited-State Dynamics

We measured the TA spectra of the AA/IPA series to study how their lattice structures – in particular the inclusion of iodine atoms and double bonds in the organic spacer layers – and distortions in these structures affect their excited-state dynamics. We acquired TA spectra on exfoliated single crystals with a broadband probe from 1.5 to 2.4 eV after pumping the sample at 2.41 eV (0.36 eV above the bandgap). These spectra (Figure 5.3) contain both positive ESA (blue) and negative GSB (red). The ESA features are similar among all four compounds studied and have been attributed previously to intraband absorptions of carriers at and above the band-edge.[14, 199, 237, 238] Here we focus on the energies and dynamics of the negative bleaching signals,

which reflect the changing populations of states with energies at and below the bandgap. These signals originate from bleaching of the bandgap exciton at 2.05 eV and two sets of sub-bandgap

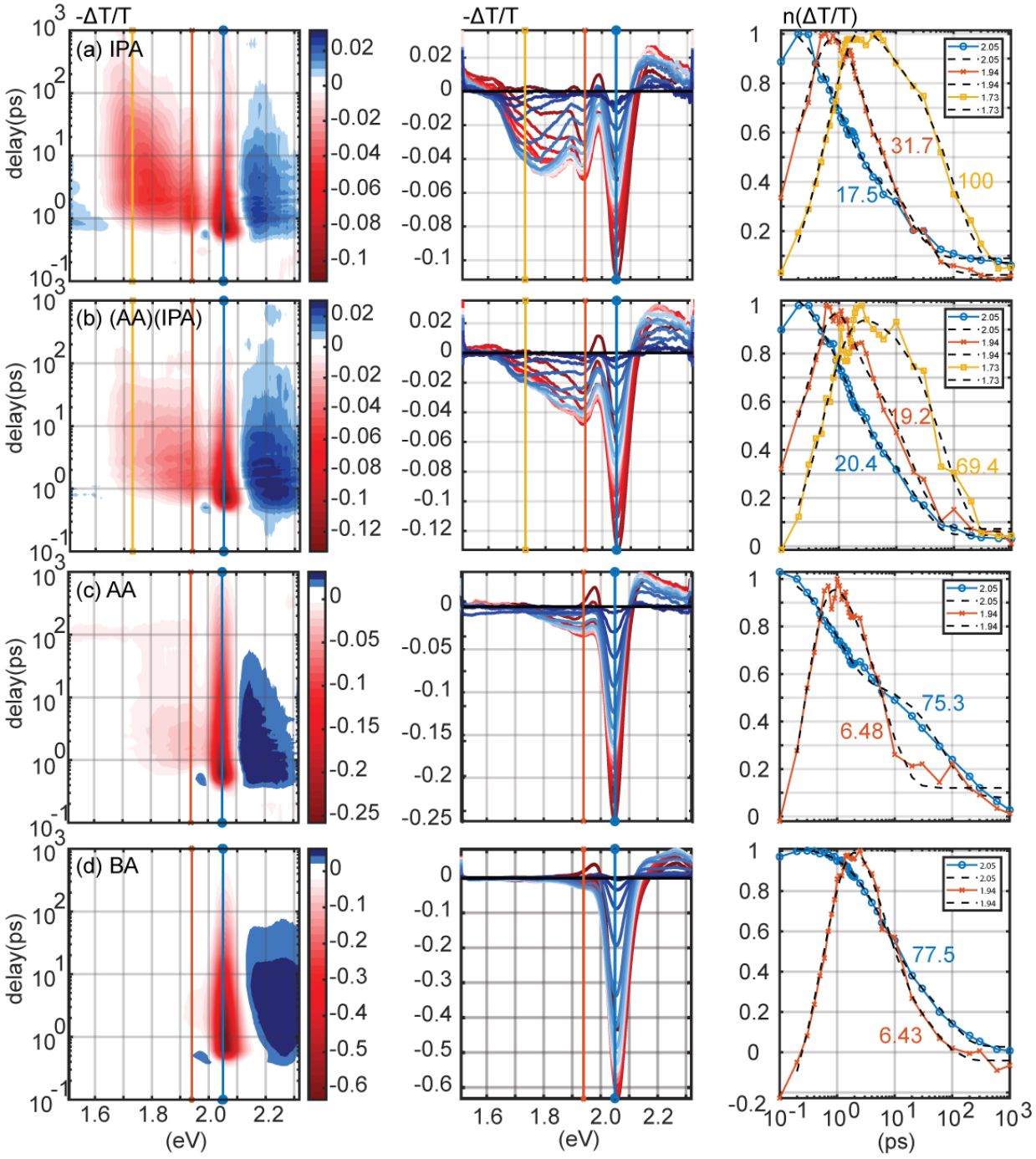

Figure 5.3 Excited-state dynamics of the n=3 allylamine 2D perovskite series with varying IPA concentration. (Left) Transient absorption surface of IPA_n3, (AA)(IPA)_n3, AA_n3 and BA_n3 crystals. Different levels of signal intensity are plotted as a function of probing energy (x-axis) and delay time after excitation at 2.41 eV (y-axis). Red represents the negative bleaching signal and blue represents the positive absorption signal. (Middle) Transient absorption spectra at different time delays from 0 (red) to 1 ns (blue). (Right) Normalized TA signal intensity at representative energy (each probing energy is marked using a colored line in the left and middle column with the corresponding color). The longest decay lifetimes in picosecond (assigned to be the carrier recombination lifetimes) were extracted using multi-exponential fits and marked near the cuts.

states, "ladder states" at ~1.94 eV, and "sink states" at ~1.73 eV. PL originates from all three sets of states (Appendix, Figure_Apx D.3).

Figure 5.3 (left two columns) shows that the bandgap bleaches peak at 2.05 eV for all four samples, consistent with the previously reported value for *n*=3 perovskites[96] and with the ground state absorption spectra in the Appendix, Figure_Apx D.2**.** The most distinct difference between these structures lies in the peaks below the bandgap. The intensities of the ladder state features (1.94 eV, red lines) are 45%/37%/16%/5% of the intensities of the bandgap features (2.05 eV, blue lines) for IPA_n3/(AA)(IPA)_n3/AA_n3/BA_n3. The intensities of the sink state features (1.73 eV, yellow lines) are 36%/15%/0/0 of the intensities of the bandgap peaks, *i.e.*, only IPA structures form the sink states. Both intermediate-energy state and the deep sink state are introduced more into the crystal structure by the inclusion of IPA than AA or BA alone.

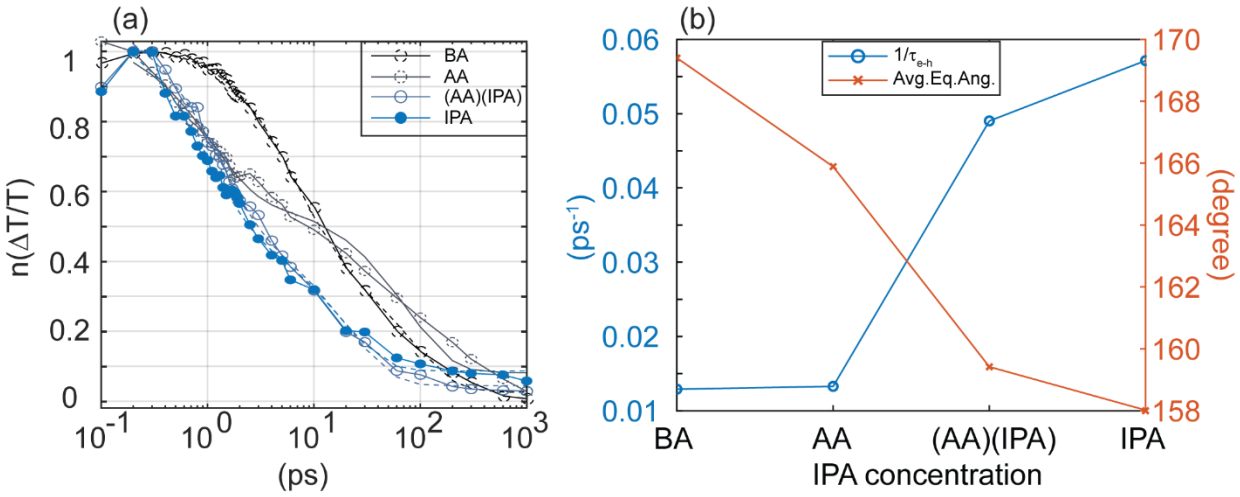

Figure 5.4 (a) The normalized TA signal intensity extracted at the bandgaps showing the recombination dynamics at the bandgaps of crystals containing different cations. (b) The correlation between the lattice distortion and recombination lifetimes. The left axis shows the speed of the recombination and the right axis shows the average equatorial Pb-I-Pb bond angle solved by x-ray crystallography indicating the level of distortion inside the inorganic structures. A clear negative correlation can be observed between the level of distortion and the speed of recombination, suggesting the direct effect of lattice distortion on excited-state dynamics.

Figure 5.3 (right column) shows the normalized intensity of the bleaching signals as a function of the delay time at the three peak energies (bandgap, ladder, and sink), and Figure 5.4a compiles the dynamics of the bandgap states of all four samples. Multi-exponential fits were applied to the kinetic trace for each state, and the components corresponding to decays were averaged (weighted by their amplitudes) to determine the average recombination lifetime for each type of state within each type of sample; these lifetimes are written adjacent to the corresponding kinetic trace. The two crystals containing IPA both show energy flow from bandgap states to ladder states to sink states with similar dynamics. The average lifetime of the

bandgap states in IPA-containing crystals (blue) is τ~20 ps, and the sink states have a ~100-ps lifetime, which is even longer than the bandgap recombination lifetime of BA crystals with many fewer below-bandgap traps. The bandgap states of the BA sample (black) depopulate more slowly (τ~70 ps) and plateau at 1 ps, probably because of the absence of a sink state and the low concentration of the shallow traps (ladder). The bandgap states of AA crystals show two distinct regimes of population decay, dynamics that resemble those of IPA before 2 ps and dynamics that resemble those of BA after 20 ps. We suspect that bandgap excitons are first drained by the ladder state, but without the sink state, the shallow ladder states quickly get saturated.

We can relate the presence of the sink states to the lattice distortion caused by IPA, Figure 5.4b. This figure is a plot of both the average recombination rate of the bandedge exciton and the average bond angle of equatorial Pb-I-Pb bonds, *vs*. IPA concentration. The smaller the Pb-I-Pb bond angle, the greater the lattice is distorted from the strain-free inorganic cage in BA. The lifetime of the band-edge state decreases with increasing lattice distortion, and the biggest change in both the lifetime and the bond angle occurs when the IPA is added to the lattice. The inclusion of AA causes the greatest change in the stacking geometry but does not appear to influence the exciton dynamics.

One explanation for the relatively long lifetime of excitons in the sink states is that these states have spatially separated electrons and holes, such that charge recombination (including radiative recombination) is suppressed;[239] this explanation, where electrons are attracted to neutral Pb vacancies, has been proposed previously, but not proven, for BA perovskites. In the IPA samples, the iodine might serve as a site for the localization of the holes.

5.3 Conclusion

We present the successful synthesis and characterization of three new homologous series of (100) lead iodide perovskites: $(AA)_2MA_{n-1}Pb_nI_{3n+1}$, $[(AA)_x(IPA)_{1-x}]_2MA_{n-1}Pb_nI_{3n+1}$ and $(IPA)_2MA_{n-1}Pb_nI_{3n+}1$ (n=3-4), which incorporate the bifunctional organic molecules of AA and IPA. $(AA)_2MA_2Pb_3I_{10}$ has a unique structure type with an offset (0, < ½) and is the first example of halide perovskite with a monoammonium spacer cation that deviates from the classic RP structure type. $(IPA)_2MA_2Pb_3I_{10}$ and the alloyed $[(AA)_x(IPA)_{1-x}]_2MA_2Pb_3I_{10}$ crystallize in the RP structure with big distortions in the equatorial Pb-I-Pb angles. The excited-state dynamics were investigated by TA spectroscopy, where the formation of a long-lived (~100 ps) trap state ensemble with broad white-light emission was distinguished to be related to the lattice distortions induced by the incorporation of the IPA cations. The exploration on synthesis, optoelectronic properties, and carrier dynamics of the novel compounds reported here provides novel insights on the predictive synthesis of multilayer halide perovskites with fascinating photophysical behavior.

References

1. Hooke, R., *Micrographia: Or some physiological descriptions of minute bodies made by magnifying glasses, with observations and inquiries thereupon*. J. Martyn and J. Allestry: London, **1665**.

2. Abbe, E., Beiträge zur theorie des mikroskops und der mikroskopischen wahrnehmung. *Archiv für mikroskopische Anatomie* **1873,** *9*, 413-468.

3. Ruska, E., The development of the electron microscope and of electron microscopy. *Bioscience Reports* **1987,** *7*, 607-629.

4. Moerner, W. E., Single-molecule spectroscopy, imaging, and photocontrol: Foundations for super-resolution microscopy (nobel lecture). *Angewandte Chemie International Edition* **2015,** *54*, 8067-8093.

5. Betzig, E., Single molecules, cells, and super-resolution optics (nobel lecture). *Angewandte Chemie International Edition* **2015,** *54*, 8034-8053.

6. Marvin, M. Microscopy apparatus. US3013467A, **1961**.

7. Minsky, M., Memoir on inventing the confocal scanning microscope. *Scanning* **1988,** *10*, 128-138.

8. Pawley, J., *Handbook of biological confocal microscopy*. Springer Science & Business Media: New York, **1995**.

9. Carlsson, K.; Danielsson, P.-E.; Lenz, R.; Liljeborg, A.; Majlöf, L.; Åslund, N., Three-dimensional microscopy using a confocal laser scanning microscope. *Optics Letters* **1985,** *10*, 53-55.

10. Carlsson, K.; Åslund, N., Confocal imaging for 3-d digital microscopy. *Applied Optics* **1987,** *26*, 3232-3238.

11. Shen, H.; Tauzin, L. J.; Baiyasi, R.; Wang, W. X.; Moringo, N.; Shuang, B.; Landes, C. F., Single particle tracking: From theory to biophysical applications. *Chemical Reviews* **2017,** *117*, 7331-7376.

12. Mourou, G., Nobel lecture: Extreme light physics and application. *Reviews of Modern Physics* **2019,** *91*.

13. Mukamel, S., *Principles of nonlinear optical spectroscopy*. Oxford University Press: New York, **1995**.

14. Yang, Y.; Ostrowski, D. P.; France, R. M.; Zhu, K.; van de Lagemaat, J.; Luther, J. M.; Beard, M. C., Observation of a hot-phonon bottleneck in lead-iodide perovskites. *Nature Photonics* **2015,** *10*, 53-59.

15. Nah, S.; Spokoyny, B.; Stoumpos, C.; Soe, C. M. M.; Kanatzidis, M.; Harel, E., Spatially segregated free-carrier and exciton populations in individual lead halide perovskite grains. *Nature Photonics* **2017,** *11*, 285-288.

16. Jiang, X.; Hoffman, J.; Stoumpos, C. C.; Kanatzidis, M. G.; Harel, E., Transient sub-band-gap states at grain boundaries of ch3nh3pbi3 perovskite act as fast temperature relaxation centers. *ACS Energy Letters* **2019,** *4*, 1741-1747.

17. Dubietis, A.; Tamošauskas, G.; Šuminas, R.; Jukna, V.; Couairon, A., Ultrafast supercontinuum generation in bulk condensed media. *Lithuanian Journal of Physics* **2017,** *57*.

18. Fischer, M. C.; Wilson, J. W.; Robles, F. E.; Warren, W. S., Invited review article: Pump-probe microscopy. *Review of Scientific Instruments* **2016,** *87*, 031101.

19. Levitt, J. M.; Katz, O.; Silberberg, Y., Frequency-encoded multiplexed cars microscopy by rapid pulse shaping. *Journal of Modern Optics* **2014,** *61*, 872-876.

20. Liao, C. S.; Wang, P.; Wang, P.; Li, J.; Lee, H. J.; Eakins, G.; Cheng, J. X., Spectrometer-free vibrational imaging by retrieving stimulated raman signal from highly scattered photons. *Science Advances* **2015,** *1*, e1500738.

21. Crisafi, F.; Kumar, V.; Scopigno, T.; Marangoni, M.; Cerullo, G.; Polli, D., In-line balanced detection stimulated raman scattering microscopy. *Scientific Reports* **2017,** *7*, 10745.

22. Shim, S. H.; Zanni, M. T., How to turn your pump-probe instrument into a multidimensional spectrometer: 2d ir and vis spectroscopies via pulse shaping. *Physical Chemistry Chemical Physics* **2009,** *11*, 748-761.

23. Jones, A. C.; Kearns, N. M.; Ho, J. J.; Flach, J. T.; Zanni, M. T., Impact of non-equilibrium molecular packings on singlet fission in microcrystals observed using 2d white-light microscopy. *Nature Chemistry* **2019**.

24. Deng, S. B.; Blach, D. D.; Jin, L. R.; Huang, L. B., Imaging carrier dynamics and transport in hybrid perovskites with transient absorption microscopy. *Advanced Energy Materials* **2020,** *10*, 1903781.

25. Gao, B.; Hartland, G.; Fang, T.; Kelly, M.; Jena, D.; Xing, H. G.; Huang, L., Studies of intrinsic hot phonon dynamics in suspended graphene by transient absorption microscopy. *Nano Letters* **2011,** *11*, 3184-3189.

26. Wong, C. Y.; Penwell, S. B.; Cotts, B. L.; Noriega, R.; Wu, H.; Ginsberg, N. S., Revealing exciton dynamics in a small-molecule organic semiconducting film with subdomain transient absorption microscopy. *The Journal of Physical Chemistry C* **2013,** *117*, 22111-22122.

27. Wong, C. Y.; Cotts, B. L.; Wu, H.; Ginsberg, N. S., Exciton dynamics reveal aggregates with intermolecular order at hidden interfaces in solution-cast organic semiconducting films. *Nature Communications* **2015,** *6*, 5946.

28. Wong, C. Y.; Folie, B. D.; Cotts, B. L.; Ginsberg, N. S., Discerning variable extents of interdomain orientational and structural heterogeneity in solution-cast polycrystalline organic semiconducting thin films. *The Journal of Physical Chemistry Letters* **2015,** *6*, 3155-3162.

29. Guo, Z.; Manser, J. S.; Wan, Y.; Kamat, P. V.; Huang, L., Spatial and temporal imaging of long-range charge transport in perovskite thin films by ultrafast microscopy. *Nature Communications* **2015,** *6*, 7471.

30. Wan, Y.; Guo, Z.; Zhu, T.; Yan, S. X.; Johnson, J.; Huang, L. B., Cooperative singlet and triplet exciton transport in tetracene crystals visualized by ultrafast microscopy. *Nature Chemistry* **2015,** *7*, 785-792.

31. Guo, Z.; Wan, Y.; Yang, M.; Snaider, J.; Zhu, K.; Huang, L., Long-range hot-carrier transport in hybrid perovskites visualized by ultrafast microscopy. *Science* **2017,** *356*, 59-62.

32. Nah, S.; Spokoyny, B. M.; Soe, C. M. M.; Stoumpos, C. C.; Kanatzidis, M. G.; Harel, E., Ultrafast imaging of carrier cooling in metal halide perovskite thin films. *Nano Letters* **2018,** *18*, 1044-1048.

33. Snaider, J. M.; Guo, Z.; Wang, T.; Yang, M. J.; Yuan, L.; Zhu, K.; Huan, L. B., Ultrafast imaging of carrier transport across grain boundaries in hybrid perovskite thin films. *ACS Energy Letters* **2018,** *3*, 1402-1408.

34. Deeb, C.; Guo, Z.; Yang, A.; Huang, L.; Odom, T. W., Correlating nanoscopic energy transfer and far-field emission to unravel lasing dynamics in plasmonic nanocavity arrays. *Nano Letters* **2018,** *18*, 1454-1459.

35. Shi, E.; Deng, S.; Yuan, B.; Gao, Y.; Akriti; Yuan, L.; Davis, C. S.; Zemlyanov, D.; Yu, Y.; Huang, L.; Dou, L., Extrinsic and dynamic edge states of two-dimensional lead halide perovskites. *ACS Nano* **2019,** *13*, 1635-1644.

36. Jiang, X.; Jun, S.; Hoffman, J.; Kanatzidis, M. G.; Harel, E., Global analysis for time and spectrally resolved multidimensional microscopy: Application to ch3nh3pbi3 perovskite thin films. *The Journal of Physical Chemistry A* **2020,** *124*, 4837-4847.

37. Tong, L.; Liu, Y.; Dolash, B. D.; Jung, Y.; Slipchenko, M. N.; Bergstrom, D. E.; Cheng, J. X., Label-free imaging of semiconducting and metallic carbon nanotubes in cells and mice using transient absorption microscopy. *Nature Nanotechnology* **2011,** *7*, 56-61.

38. Chen, T.; Chen, S. H.; Zhou, J. H.; Liang, D. H.; Chen, X. Y.; Huang, Y. Y., Transient absorption microscopy of gold nanorods as spectrally orthogonal labels in live cells. *Nanoscale* **2014,** *6*, 10536-10539.

39. Chen, T.; Huang, Y., Label-free transient absorption microscopy for red blood cell flow velocity measurement in vivo. *Analytical Chemistry* **2017,** *89*, 10120-10123.

40. Zhang, L.; Zou, X.; Zhang, B.; Cui, L.; Zhang, J.; Mao, Y.; Chen, L.; Ji, M., Label-free imaging of hemoglobin degradation and hemosiderin formation in brain tissues with femtosecond pump-probe microscopy. *Theranostics* **2018,** *8*, 4129-4140.

41. Chen, A. J.; Yuan, X.; Li, J.; Dong, P.; Hamza, I.; Cheng, J. X., Label-free imaging of heme dynamics in living organisms by transient absorption microscopy. *Analytical Chemistry* **2018,** *90*, 3395-3401.

42. Francis, A. T.; Berry, K.; Thomas, E. C.; Hill, A. H.; Fu, D., In vitro quantification of single red blood cell oxygen saturation by femtosecond transient absorption microscopy. *The Journal of Physical Chemistry Letters* **2019,** *10*, 3312-3317.

43. Dong, P. T.; Lin, H.; Huang, K. C.; Cheng, J. X., Label-free quantitation of glycated hemoglobin in single red blood cells by transient absorption microscopy and phasor analysis. *Science Advances* **2019,** *5*, eaav0561.

44. Francis, A. T.; Shears, M. J.; Murphy, S. C.; Fu, D., Direct quantification of single red blood cell hemoglobin concentration with multiphoton microscopy. *Analytical Chemistry* **2020,** *92*, 12235-12241.

45. Villafana, T. E.; Brown, W. P.; Delaney, J. K.; Palmer, M.; Warren, W. S.; Fischer, M. C., Femtosecond pump-probe microscopy generates virtual cross-sections in historic artwork. *Proceedings of the National Academy of Sciences of the United States of America* **2014,** *111*, 1708-1713.

46. Ruzicka, B. A.; Wang, R.; Lohrman, J.; Ren, S. Q.; Zhao, H., Exciton diffusion in semiconducting single-walled carbon nanotubes studied by transient absorption microscopy. *Physical Review B* **2012,** *86*, 205417.

47. Kumar, N.; He, J. Q.; He, D. W.; Wang, Y. S.; Zhao, H., Charge carrier dynamics in bulk mos2 crystal studied by transient absorption microscopy. *Journal of Applied Physics* **2013,** *113*, 133702.

48. Cui, Q.; He, J.; Bellus, M. Z.; Mirzokarimov, M.; Hofmann, T.; Chiu, H. Y.; Antonik, M.; He, D.; Wang, Y.; Zhao, H., Transient absorption measurements on anisotropic monolayer res2. *Small* **2015,** *11*, 5565-5571.

49. Zhu, T.; Wan, Y.; Guo, Z.; Johnson, J.; Huang, L., Two birds with one stone: Tailoring singlet fission for both triplet yield and exciton diffusion length. *Advanced Materials* **2016,** *28*, 7539-7547.

50. Wan, Y.; Stradomska, A.; Knoester, J.; Huang, L., Direct imaging of exciton transport in tubular porphyrin aggregates by ultrafast microscopy. *Journal of the American Chemical Society* **2017,** *139*, 7287-7293.

51. Huang, L.; Hartland, G. V.; Chu, L. Q.; Luxmi; Feenstra, R. M.; Lian, C.; Tahy, K.; Xing, H., Ultrafast transient absorption microscopy studies of carrier dynamics in epitaxial graphene. *Nano Letters* **2010,** *10*, 1308-1313.

52. Graham, M. W.; Shi, S. F.; Wang, Z. H.; Ralph, D. C.; Park, J.; McEuen, P. L., Transient absorption and photocurrent microscopy show that hot electron supercollisions describe the rate-limiting relaxation step in graphene. *Nano Letters* **2013,** *13*, 5497-5502.

53. Murphy, S.; Huang, L., Transient absorption microscopy studies of energy relaxation in graphene oxide thin film. *Journal of Physics: Condensed Matter* **2013,** *25*, 144203.

54. Huang, K. C.; McCall, J.; Wang, P.; Liao, C. S.; Eakins, G.; Cheng, J. X.; Yang, C., High-speed spectroscopic transient absorption imaging of defects in graphene. *Nano Letters* **2018,** *18*, 1489-1497.

55. Hartland, G. V., Ultrafast studies of single semiconductor and metal nanostructures through transient absorption microscopy. *Chemical Science* **2010,** *1*, 303-309.

56. Jung, Y.; Slipchenko, M. N.; Liu, C. H.; Ribbe, A. E.; Zhong, Z. H.; Yang, C.; Cheng, J. X., Fast detection of the metallic state of individual single-walled carbon nanotubes using a transient-absorption optical microscope. *Physical Review Letters* **2010,** *105*, 217401.

57. Gao, B.; Hartland, G. V.; Huang, L., Transient absorption spectroscopy and imaging of individual chirality-assigned single-walled carbon nanotubes. *ACS Nano* **2012,** *6*, 5083-5090.

58. Gao, B.; Hartland, G. V.; Huang, L. B., Transient absorption spectroscopy of excitons in an individual suspended metallic carbon nanotube. *Journal of Physical Chemistry Letters* **2013,** *4*, 3050-3055.

59. Lo, S. S.; Devadas, M. S.; Major, T. A.; Hartland, G. V., Optical detection of single nano-objects by transient absorption microscopy. *Analyst* **2013,** *138*, 25-31.

60. Yabuta, M.; Takeda, A.; Sugimoto, T.; Watanabe, K.; Kudo, A.; Matsumoto, Y., Particle size dependence of carrier dynamics and reactivity of photocatalyst bivo4 probed with single-particle transient absorption microscopy. *The Journal of Physical Chemistry C* **2017,** *121*, 22060-22066.

61. van Dijk, M. A.; Lippitz, M.; Orrit, M., Detection of acoustic oscillations of single gold nanospheres by time-resolved interferometry. *Physical Review Letters* **2005,** *95*, 267406.

62. Del Fatti, N.; Christofilos, D.; Vallée, F.; Christofilos, D., Optical response of a single gold nanoparticle. *Gold Bulletin* **2008,** *41*, 147-158.

63. Sharifzadeh, S.; Wong, C. Y.; Wu, H.; Cotts, B. L.; Kronik, L.; Ginsberg, N. S.; Neaton, J. B., Relating the physical structure and optoelectronic function of crystalline tips-pentacene. *Advanced Functional Materials* **2015,** *25*, 2038-2046.

64. Pandya, R.; Chen, R. Y. S.; Gu, Q. F.; Gorman, J.; Auras, F.; Sung, J.; Friend, R.; Kukura, P.; Schnedermann, C.; Rao, A., Femtosecond transient absorption microscopy of singlet exciton motion in side-chain engineered perylene-diimide thin films. *The Journal of Physical Chemistry A* **2020,** *124*, 2721-2730.

65. Wells, H. L., Über die cäsium-und kalium-bleihalogenide. *Zeitschrift für anorganische Chemie* **1893,** *3*, 195-210.

66. Chung, I.; Lee, B.; He, J.; Chang, R. P.; Kanatzidis, M. G., All-solid-state dye-sensitized solar cells with high efficiency. *Nature* **2012,** *485*, 486-489.

67. Kim, H.-S.; Lee, C.-R.; Im, J.-H.; Lee, K.-B.; Moehl, T.; Marchioro, A.; Moon, S.-J.; Humphry-Baker, R.; Yum, J.-H.; Moser, J. E., Lead iodide perovskite sensitized all-solid-state submicron thin film mesoscopic solar cell with efficiency exceeding 9%. *Scientific Reports* **2012,** *2*, 1-7.

68. Lee, M. M.; Teuscher, J.; Miyasaka, T.; Murakami, T. N.; Snaith, H. J., Efficient hybrid solar cells based on meso-superstructured organometal halide perovskites. *Science* **2012,** *338*, 643-647.

69. Yoo, J. J.; Seo, G.; Chua, M. R.; Park, T. G.; Lu, Y.; Rotermund, F.; Kim, Y. K.; Moon, C. S.; Jeon, N. J.; Correa-Baena, J. P.; Bulovic, V.; Shin, S. S.; Bawendi, M. G.; Seo, J., Efficient perovskite solar cells via improved carrier management. *Nature* **2021,** *590*, 587-593.

70. Katan, C.; Mercier, N.; Even, J., Quantum and dielectric confinement effects in lower-dimensional hybrid perovskite semiconductors. *Chemical Reviews* **2019,** *119*, 3140-3192.

71. Leveillee, J.; Katan, C.; Even, J.; Ghosh, D.; Nie, W.; Mohite, A. D.; Tretiak, S.; Schleife, A.; Neukirch, A. J., Tuning electronic structure in layered hybrid perovskites with organic spacer substitution. *Nano Letters* **2019,** *19*, 8732-8740.

72. Saparov, B.; Mitzi, D. B., Organic–inorganic perovskites: Structural versatility for functional materials design. *Chemical Reviews* **2016,** *116*, 4558-4596.

73. Gao, Y.; Shi, E.; Deng, S.; Shiring, S. B.; Snaider, J. M.; Liang, C.; Yuan, B.; Song, R.; Janke, S. M.; Liebman-Peláez, A.; Yoo, P.; Zeller, M.; Boudouris, B. W.; Liao, P.; Zhu,

C.; Blum, V.; Yu, Y.; Savoie, B. M.; Huang, L.; Dou, L., Molecular engineering of organic–inorganic hybrid perovskites quantum wells. *Nature Chemistry* **2019,** *11*, 1151-1157.

74. Gao, Y.; Wei, Z.; Yoo, P.; Shi, E.; Zeller, M.; Zhu, C.; Liao, P.; Dou, L., Highly stable lead-free perovskite field-effect transistors incorporating linear π-conjugated organic ligands. *Journal of the American Chemical Society* **2019,** *141*, 15577-15585.

75. Fu, Y.; Zheng, W.; Wang, X.; Hautzinger, M. P.; Pan, D.; Dang, L.; Wright, J. C.; Pan, A.; Jin, S., Multicolor heterostructures of two-dimensional layered halide perovskites that show interlayer energy transfer. *Journal of the American Chemical Society* **2018,** *140*, 15675-15683.

76. Price, M. B.; Butkus, J.; Jellicoe, T. C.; Sadhanala, A.; Briane, A.; Halpert, J. E.; Broch, K.; Hodgkiss, J. M.; Friend, R. H.; Deschler, F., Hot-carrier cooling and photoinduced refractive index changes in organic-inorganic lead halide perovskites. *Nature Communications* **2015,** *6*, 8420.

77. Yang, J.; Wen, X.; Xia, H.; Sheng, R.; Ma, Q.; Kim, J.; Tapping, P.; Harada, T.; Kee, T. W.; Huang, F.; Cheng, Y. B.; Green, M.; Ho-Baillie, A.; Huang, S.; Shrestha, S.; Patterson, R.; Conibeer, G., Acoustic-optical phonon up-conversion and hot-phonon bottleneck in lead-halide perovskites. *Nature Communications* **2017,** *8*, 14120.

78. Niesner, D.; Zhu, H.; Miyata, K.; Joshi, P. P.; Evans, T. J.; Kudisch, B. J.; Trinh, M. T.; Marks, M.; Zhu, X. Y., Persistent energetic electrons in methylammonium lead iodide perovskite thin films. *Journal of the American Chemical Society* **2016,** *138*, 15717-15726.

79. Frost, J. M.; Whalley, L. D.; Walsh, A., Slow cooling of hot polarons in halide perovskite solar cells. *ACS Energy Letters* **2017,** *2*, 2647-2652.

80. Zhu, H.; Miyata, K.; Fu, Y.; Wang, J.; Joshi, P. P.; Niesner, D.; Williams, K. W.; Jin, S.; Zhu, X. Y., Screening in crystalline liquids protects energetic carriers in hybrid perovskites. *Science* **2016,** *353*, 1409-1413.

81. Li, M.; Bhaumik, S.; Goh, T. W.; Kumar, M. S.; Yantara, N.; Gratzel, M.; Mhaisalkar, S.; Mathews, N.; Sum, T. C., Slow cooling and highly efficient extraction of hot carriers in colloidal perovskite nanocrystals. *Nature Communications* **2017,** *8*, 14350.

82. Fu, J.; Xu, Q.; Han, G.; Wu, B.; Huan, C. H. A.; Leek, M. L.; Sum, T. C., Hot carrier cooling mechanisms in halide perovskites. *Nature Communications* **2017,** *8*, 1300.

83. Stranks, S. D.; Eperon, G. E.; Grancini, G.; Menelaou, C.; Alcocer, M. J.; Leijtens, T.; Herz, L. M.; Petrozza, A.; Snaith, H. J., Electron-hole diffusion lengths exceeding 1 micrometer in an organometal trihalide perovskite absorber. *Science* **2013,** *342*, 341-344.

84. Xing, G.; Mathews, N.; Sun, S.; Lim, S. S.; Lam, Y. M.; Gratzel, M.; Mhaisalkar, S.; Sum, T. C., Long-range balanced electron- and hole-transport lengths in organic-inorganic ch3nh3pbi3. *Science* **2013,** *342*, 344-347.

85. Levine, I.; Gupta, S.; Brenner, T. M.; Azulay, D.; Millo, O.; Hodes, G.; Cahen, D.; Balberg, I., Mobility-lifetime products in mapbi3 films. *The Journal of Physical Chemistry Letters* **2016,** *7*, 5219-5226.

86. Motta, C.; El-Mellouhi, F.; Sanvito, S., Charge carrier mobility in hybrid halide perovskites. *Scientific Reports* **2015,** *5*, 12746.

87. Yin, W. J.; Shi, T.; Yan, Y., Unique properties of halide perovskites as possible origins of the superior solar cell performance. *Advanced Materials* **2014,** *26*, 4653-4658.

88. Yun, J. S.; Ho-Baillie, A.; Huang, S. J.; Woo, S. H.; Heo, Y.; Seidel, J.; Huang, F. Z.; Cheng, Y. B.; Green, M. A., Benefit of grain boundaries in organic-inorganic halide planar perovskite solar cells. *The Journal of Physical Chemistry Letters* **2015,** *6*, 875-880.

89. Yin, W.-J.; Shi, T.; Yan, Y., Unusual defect physics in ch3nh3pbi3 perovskite solar cell absorber. *Applied Physics Letters* **2014,** *104*, 063903.

90. Yin, W.-J.; Chen, H.; Shi, T.; Wei, S.-H.; Yan, Y., Origin of high electronic quality in structurally disordered ch3nh3pbi3and the passivation effect of cl and o at grain boundaries. *Advanced Electronic Materials* **2015,** *1*, 1500044.

91. Ball, J. M.; Petrozza, A., Defects in perovskite-halides and their effects in solar cells. *Nature Energy* **2016,** *1*.

92. Shamsi, J.; Urban, A. S.; Imran, M.; De Trizio, L.; Manna, L., Metal halide perovskite nanocrystals: Synthesis, post-synthesis modifications, and their optical properties. *Chemical Reviews* **2019,** *119*, 3296-3348.

93. Saparov, B.; Mitzi, D. B., Organic-inorganic perovskites: Structural versatility for functional materials design. *Chemical Reviews* **2016,** *116*, 4558-4596.

94. Straus, D. B.; Kagan, C. R., Electrons, excitons, and phonons in two-dimensional hybrid perovskites: Connecting structural, optical, and electronic properties. *The Journal of Physical Chemistry Letters* **2018,** *9*, 1434-1447.

95. Smith, M. D.; Pedesseau, L.; Kepenekian, M.; Smith, I. C.; Katan, C.; Even, J.; Karunadasa, H. I., Decreasing the electronic confinement in layered perovskites through intercalation. *Chemical Science* **2017,** *8*, 1960-1968.

96. Blancon, J. C.; Tsai, H.; Nie, W.; Stoumpos, C. C.; Pedesseau, L.; Katan, C.; Kepenekian, M.; Soe, C. M. M.; Appavoo, K.; Sfeir, M. Y.; Tretiak, S.; Ajayan, P. M.; Kanatzidis, M. G.; Even, J.; Crochet, J. J.; Mohite, A. D., Perovskite physics extremely efficient

internal exciton dissociation through edge states in layered 2d perovskites. *Science* **2017,** *355*, 1288-1291.

97. Green, M. A.; Hishikawa, Y.; Dunlop, E. D.; Levi, D. H.; Hohl-Ebinger, J.; Ho-Baillie, A. W. Y., Solar cell efficiency tables (version 51). *Progress in Photovoltaics* **2018,** *26*, 3-12.

98. Gao, P.; Gratzel, M.; Nazeeruddin, M. K., Organohalide lead perovskites for photovoltaic applications. *Energy & Environmental Science* **2014,** *7*, 2448-2463.

99. Lee, J.-W.; Bae, S.-H.; De Marco, N.; Hsieh, Y.-T.; Dai, Z.; Yang, Y., The role of grain boundaries in perovskite solar cells. *Materials Today Energy* **2018,** *7*, 149-160.

100. deQuilettes, D. W.; Vorpahl, S. M.; Stranks, S. D.; Nagaoka, H.; Eperon, G. E.; Ziffer, M. E.; Snaith, H. J.; Ginger, D. S., Solar cells. Impact of microstructure on local carrier lifetime in perovskite solar cells. *Science* **2015,** *348*, 683-686.

101. Yang, M.; Zeng, Y.; Li, Z.; Kim, D. H.; Jiang, C. S.; van de Lagemaat, J.; Zhu, K., Do grain boundaries dominate non-radiative recombination in ch3nh3pbi3 perovskite thin films? *Physical Chemistry Chemical Physics* **2017,** *19*, 5043-5050.

102. Mamun, A. A.; Ava, T. T.; Jeong, H. J.; Jeong, M. S.; Namkoong, G., A deconvoluted pl approach to probe the charge carrier dynamics of the grain interior and grain boundary of a perovskite film for perovskite solar cell applications. *Physical Chemistry Chemical Physics* **2017,** *19*, 9143-9148.

103. Li, C.; Zhong, Y.; Luna, C. A. M.; Unger, T.; Deichsel, K.; Graser, A.; Kohler, J.; Kohler, A.; Hildner, R.; Huettner, S., Emission enhancement and intermittency in polycrystalline organolead halide perovskite films. *Molecules* **2016,** *21*, 1081.

104. Li, W.; Yadavalli, S. K.; Lizarazo-Ferro, D.; Chen, M.; Zhou, Y.; Padture, N. P.; Zia, R., Subgrain special boundaries in halide perovskite thin films restrict carrier diffusion. *ACS Energy Letters* **2018,** *3*, 2669-2670.

105. Grancini, G.; Viola, D.; Gandini, M.; Altamura, D.; Pogna, E. A. A.; D'Innocenzo, V.; Bargigia, I.; Giannini, C.; Cerullo, G.; Petrozza, A., Lattice distortions drive electron-hole correlation within micrometer-size lead-iodide perovskite crystals. *ACS Energy Letter* **2017,** *2*, 265-269.

106. Bakulin, A. A.; Selig, O.; Bakker, H. J.; Rezus, Y. L.; Muller, C.; Glaser, T.; Lovrincic, R.; Sun, Z.; Chen, Z.; Walsh, A.; Frost, J. M.; Jansen, T. L., Real-time observation of organic cation reorientation in methylammonium lead iodide perovskites. *The Journal of Physical Chemistry Letters* **2015,** *6*, 3663-3669.

107. Grancini, G.; Srimath Kandada, A. R.; Frost, J. M.; Barker, A. J.; De Bastiani, M.; Gandini, M.; Marras, S.; Lanzani, G.; Walsh, A.; Petrozza, A., Role of microstructure in the electron-hole interaction of hybrid lead-halide perovskites. *Nature Photonics* **2015,** *9*, 695-701.

108. Shao, Y.; Fang, Y.; Li, T.; Wang, Q.; Dong, Q.; Deng, Y.; Yuan, Y.; Wei, H.; Wang, M.; Gruverman, A.; Shield, J.; Huang, J., Grain boundary dominated ion migration in polycrystalline organic–inorganic halide perovskite films. *Energy & Environmental Science* **2016,** *9*, 1752-1759.

109. Sherkar, T. S.; Momblona, C.; Gil-Escrig, L.; Avila, J.; Sessolo, M.; Bolink, H. J.; Koster, L. J. A., Recombination in perovskite solar cells: Significance of grain boundaries, interface traps, and defect ions. *ACS Energy Letters* **2017,** *2*, 1214-1222.

110. Olyaeefar, B.; Ahmadi-Kandjani, S.; Asgari, A., Classical modelling of grain size and boundary effects in polycrystalline perovskite solar cells. *Solar Energy Materials and Solar Cells* **2018,** *180*, 76-82.

111. Nah, S.; Spokoyny, B.; Jiang, X.; Stoumpos, C.; Soe, C. M. M.; Kanatzidis, M. G.; Harel, E., Transient sub-bandgap states in halide perovskite thin films. *Nano Lett* **2018,** *18*, 827-831.

112. Harris, D. C., *Quantitative chemical analysis*. Macmillan: New York, **2010**.

113. Kvam, P. H.; Vidakovic, B., *Nonparametric statistics with applications to science and engineering*. John Wiley & Sons: New Jersey, **2007**.

114. Marsaglia, G.; Tsang, W. W.; Wang, J., Evaluating kolmogorov's distribution. *Journal of Statistical Software* **2003,** *8*.

115. Li, M.; Fu, J.; Xu, Q.; Sum, T. C., Slow hot-carrier cooling in halide perovskites: Prospects for hot-carrier solar cells. *Advanced Materials* **2019**, e1802486.

116. Joshi, P. P.; Maehrlein, S. F.; Zhu, X., Dynamic screening and slow cooling of hot carriers in lead halide perovskites. *Advanced Materials* **2019**, e1803054.

117. Miyata, A.; Mitioglu, A.; Plochocka, P.; Portugall, O.; Wang, J. T. W.; Stranks, S. D.; Snaith, H. J.; Nicholas, R. J., Direct measurement of the exciton binding energy and effective masses for charge carriers in organic-inorganic tri-halide perovskites. *Nature Physics* **2015,** *11*, 582-587.

118. Umari, P.; Mosconi, E.; De Angelis, F., Infrared dielectric screening determines the low exciton binding energy of metal-halide perovskites. *The Journal of Physical Chemistry Letters* **2018,** *9*, 620-627.

119. Allan, G.; Delerue, C., Fast relaxation of hot carriers by impact ionization in semiconductor nanocrystals: Role of defects. *Physical Review B* **2009,** *79*, 195324.

120. Haag, H.; Hönerlage, B.; Briot, O.; Aulombard, R. L., Influence of defect states on the nonlinear optical properties of gan. *Physical Review B* **1999,** *60*, 11624-11630.

121. Han, G. H.; Duong, D. L.; Keum, D. H.; Yun, S. J.; Lee, Y. H., Van der waals metallic transition metal dichalcogenides. *Chemical Reviews* **2018,** *118*, 6297-6336.

122. Carey, G. H.; Abdelhady, A. L.; Ning, Z.; Thon, S. M.; Bakr, O. M.; Sargent, E. H., Colloidal quantum dot solar cells. *Chemical Reviews* **2015,** *115*, 12732-12763.

123. Hildebrandt, N.; Spillmann, C. M.; Algar, W. R.; Pons, T.; Stewart, M. H.; Oh, E.; Susumu, K.; Diaz, S. A.; Delehanty, J. B.; Medintz, I. L., Energy transfer with semiconductor quantum dot bioconjugates: A versatile platform for biosensing, energy harvesting, and other developing applications. *Chemical Reviews* **2017,** *117*, 536-711.

124. Cheng, Y. J.; Yang, S. H.; Hsu, C. S., Synthesis of conjugated polymers for organic solar cell applications. *Chemical Reviews* **2009,** *109*, 5868-5923.

125. Ueno, K.; Oshikiri, T.; Sun, Q.; Shi, X.; Misawa, H., Solid-state plasmonic solar cells. *Chemical Reviews* **2018,** *118*, 2955-2993.

126. Strickland, D.; Mourou, G., Compression of amplified chirped optical pulses. *Optics Communications* **1985,** *55*, 447-449.

127. Manzoni, C.; Cerullo, G., Design criteria for ultrafast optical parametric amplifiers. *Journal of Optics* **2016,** *18*.

128. Penwell, S. B.; Ginsberg, L. D. S.; Noriega, R.; Ginsberg, N. S., Resolving ultrafast exciton migration in organic solids at the nanoscale. *Nature Materials* **2017,** *16*, 1136-1141.

129. Duarte, A. S.; Schnedermann, C.; Kukura, P., Wide-field detected fourier transform cars microscopy. *Scientific Reports* **2016,** *6*, 37516.

130. Ortega Arroyo, J.; Cole, D.; Kukura, P., Interferometric scattering microscopy and its combination with single-molecule fluorescence imaging. *Nature Protocols* **2016,** *11*, 617-633.

131. Delor, M.; Weaver, H. L.; Yu, Q.; Ginsberg, N. S., Imaging material functionality through three-dimensional nanoscale tracking of energy flow. *Nature Materials* **2019**.

132. Grancini, G.; Viola, D.; Gandini, M.; Altamura, D.; Pogna, E. A. A.; D'Innocenzo, V.; Bargigia, I.; Giannini, C.; Cerullo, G.; Petrozza, A., Lattice distortions drive electron-hole correlation within micrometer-size lead-iodide perovskite crystals. *ACS Energy Letters* **2017,** *2*, 265-269.

133. Gustafsson, M. G. L., Extended resolution fluorescence microscopy. *Current Opinion in Structural Biology* **1999,** *9*, 627-628.

134. van Stokkum, I. H.; Larsen, D. S.; van Grondelle, R., Global and target analysis of time-resolved spectra. *Biochimica et Biophysica Acta* **2004,** *1657*, 82-104.

135. Volpato, A.; Bolzonello, L.; Meneghin, E.; Collini, E., Global analysis of coherence and population dynamics in 2d electronic spectroscopy. *Optics Express* **2016,** *24*, 24773-24785.

136. Penrose, R., A generalized inverse for matrices. *Mathematical Proceedings of the Cambridge Philosophical Society* **2008,** *51*, 406-413.

137. Kearns, N. M.; Mehlenbacher, R. D.; Jones, A. C.; Zanni, M. T., Broadband 2d electronic spectrometer using white light and pulse shaping: Noise and signal evaluation at 1 and 100 khz. *Optics Express* **2017,** *25*, 7869-7883.

138. Snellenburg, J. J.; Laptenok, S. P.; Seger, R.; Mullen, K. M.; van Stokkum, I. H. M., Glotaran: A java-based graphical user interface for the r package timp. *Journal of Statistical Software* **2012,** *49*, 1-22.

139. Warren, S. C.; Margineanu, A.; Alibhai, D.; Kelly, D. J.; Talbot, C.; Alexandrov, Y.; Munro, I.; Katan, M.; Dunsby, C.; French, P. M., Rapid global fitting of large fluorescence lifetime imaging microscopy datasets. *PLOS One* **2013,** *8*, e70687.

140. Bucherl, C. A.; Bader, A.; Westphal, A. H.; Laptenok, S. P.; Borst, J. W., Fret-flim applications in plant systems. *Protoplasma* **2014,** *251*, 383-394.

141. Jacobsson, T. J.; Correa-Baena, J. P.; Halvani Anaraki, E.; Philippe, B.; Stranks, S. D.; Bouduban, M. E.; Tress, W.; Schenk, K.; Teuscher, J.; Moser, J. E.; Rensmo, H.; Hagfeldt, A., Unreacted pbi2 as a double-edged sword for enhancing the performance of perovskite solar cells. *Journal of the American Chemical Society* **2016,** *138*, 10331-10343.

142. Mondal, N.; Samanta, A., Complete ultrafast charge carrier dynamics in photo-excited all-inorganic perovskite nanocrystals (cspbx3). *Nanoscale* **2017,** *9*, 1878-1885.

143. Monahan, D. M.; Guo, L.; Lin, J.; Dou, L.; Yang, P.; Fleming, G. R., Room-temperature coherent optical phonon in 2d electronic spectra of ch3nh3pbi3 perovskite as a possible cooling bottleneck. *The Journal of Physical Chemistry Letters* **2017,** *8*, 3211-3215.

144. Nah, S.; Spokoyny, B.; Jiang, X.; Stoumpos, C.; Soe, C. M. M.; Kanatzidis, M. G.; Harel, E., Transient sub-bandgap states in halide perovskite thin films. *Nano Letters* **2018,** *18*, 827-831.

145. Ruckebusch, C.; Sliwa, M.; Pernot, P.; de Juan, A.; Tauler, R., Comprehensive data analysis of femtosecond transient absorption spectra: A review. *Journal of Photochemistry and Photobiology C: Photochemistry Reviews* **2012,** *13*, 1-27.

146. Leguy, A. M.; Goni, A. R.; Frost, J. M.; Skelton, J.; Brivio, F.; Rodriguez-Martinez, X.; Weber, O. J.; Pallipurath, A.; Alonso, M. I.; Campoy-Quiles, M.; Weller, M. T.; Nelson, J.; Walsh, A.; Barnes, P. R., Dynamic disorder, phonon lifetimes, and the assignment of modes to the vibrational spectra of methylammonium lead halide perovskites. *Physical Chemistry Chemical Physics* **2016,** *18*, 27051-27066.

147. Liebel, M.; Schnedermann, C.; Wende, T.; Kukura, P., Principles and applications of broadband impulsive vibrational spectroscopy. *The Journal of Physical Chemistry A* **2015,** *119*, 9506-9517.

148. Batignani, G.; Fumero, G.; Kandada, A. R. S.; Cerullo, G.; Gandini, M.; Ferrante, C.; Petrozza, A.; Scopigno, T., Probing femtosecond lattice displacement upon photo-carrier generation in lead halide perovskite. *Nature Communications* **2018,** *9*.

149. Wang, H.; Valkunas, L.; Cao, T.; Whittaker-Brooks, L.; Fleming, G. R., Coulomb screening and coherent phonon in methylammonium lead iodide perovskites. *The Journal of Physical Chemistry Letters* **2016,** *7*, 3284-3289.

150. Kim, H.; Hunger, J.; Canovas, E.; Karakus, M.; Mics, Z.; Grechko, M.; Turchinovich, D.; Parekh, S. H.; Bonn, M., Direct observation of mode-specific phonon-band gap coupling in methylammonium lead halide perovskites. *Nature Communications* **2017,** *8*, 687.

151. Fu, Y.; Zhu, H.; Chen, J.; Hautzinger, M. P.; Zhu, X. Y.; Jin, S., Metal halide perovskite nanostructures for optoelectronic applications and the study of physical properties. *Nature Reviews Materials* **2019,** *4*, 169-188.

152. Chung, I.; Lee, B.; He, J.; Chang, R. P. H.; Kanatzidis, M. G., All-solid-state dye-sensitized solar cells with high efficiency. *Nature* **2012,** *485*, 486.

153. Kojima, A.; Teshima, K.; Shirai, Y.; Miyasaka, T., Organometal halide perovskites as visible-light sensitizers for photovoltaic cells. *Journal of the American Chemical Society* **2009,** *131*, 6050-6051.

154. Mao, L.; Stoumpos, C. C.; Kanatzidis, M. G., Two-dimensional hybrid halide perovskites: Principles and promises. *Journal of the American Chemical Society* **2019,** *141*, 1171-1190.

155. Traore, B.; Pedesseau, L.; Assam, L.; Che, X.; Blancon, J.-C.; Tsai, H.; Nie, W.; Stoumpos, C. C.; Kanatzidis, M. G.; Tretiak, S.; Mohite, A. D.; Even, J.; Kepenekian, M.; Katan, C., Composite nature of layered hybrid perovskites: Assessment on quantum and dielectric confinements and band alignment. *ACS Nano* **2018,** *12*, 3321-3332.

156. Ishihara, T.; Takahashi, J.; Goto, T., Exciton state in two-dimensional perovskite semiconductor $(c_{10}h_{21}nh_3)_2pbi_4$. *Solid State Communications* **1989,** *69*, 933-936.

157. Xu, C.-q.; Kondo, T.; Sakakura, H.; Kumata, K.; Takahashi, Y.; Ito, R., Optical third-harmonic generation in layered perovskite-type material $(c_{10}h_{21}nh_3)_2pbi_4$. *Solid State Communications* **1991,** *79*, 245-248.

158. Stoumpos, C. C.; Mao, L.; Malliakas, C. D.; Kanatzidis, M. G., Structure–band gap relationships in hexagonal polytypes and low-dimensional structures of hybrid tin iodide perovskites. *Inorganic Chemistry* **2017,** *56*, 56-73.

159. Knutson, J. L.; Martin, J. D.; Mitzi, D. B., Tuning the band gap in hybrid tin iodide perovskite semiconductors using structural templating. *Inorganic Chemistry* **2005,** *44*, 4699-4705.

160. Stoumpos, C. C.; Kanatzidis, M. G., The renaissance of halide perovskites and their evolution as emerging semiconductors. *Accounts of Chemical Research* **2015,** *48*, 2791-2802.

161. Miyata, K.; Atallah, T. L.; Zhu, X.-Y., Lead halide perovskites: Crystal-liquid duality, phonon glass electron crystals, and large polaron formation. *Science Advances* **2017,** *3*.

162. Zhu, H.; Miyata, K.; Fu, Y.; Wang, J.; Joshi, P. P.; Niesner, D.; Williams, K. W.; Jin, S.; Zhu, X.-Y., Screening in crystalline liquids protects energetic carriers in hybrid perovskites. *Science* **2016,** *353*, 1409-1413.

163. Hutter, E. M.; Gélvez-Rueda, M. C.; Osherov, A.; Bulović, V.; Grozema, F. C.; Stranks, S. D.; Savenije, T. J., Direct–indirect character of the bandgap in methylammonium lead iodide perovskite. *Nature Materials* **2016,** *16*, 115.

164. Zhu, H.; Trinh, M. T.; Wang, J.; Fu, Y.; Joshi, P. P.; Miyata, K.; Jin, S.; Zhu, X. Y., Organic cations might not be essential to the remarkable properties of band edge carriers in lead halide perovskites. *Advanced Materials* **2017**, 1603072.

165. Guo, Y.; Yaffe, O.; Paley, D. W.; Beecher, A. N.; Hull, T. D.; Szpak, G.; Owen, J. S.; Brus, L. E.; Pimenta, M. A., Interplay between organic cations and inorganic framework and incommensurability in hybrid lead-halide perovskite $ch_3nh_3pbbr_3$. *Physical Review Materials* **2017,** *1*, 042401.

166. Egger, D. A.; Bera, A.; Cahen, D.; Hodes, G.; Kirchartz, T.; Kronik, L.; Lovrincic, R.; Rappe, A. M.; Reichman, D. R.; Yaffe, O., What remains unexplained about the properties of halide perovskites? *Advanced Materials* **2018,** *30*, 1800691.

167. Katan, C.; Mohite, A. D.; Even, J., Entropy in halide perovskites. *Nature Materials* **2018,** *17*, 377-379.

168. Miyata, K.; Zhu, X. Y., Ferroelectric large polarons. *Nature Materials* **2018,** *17*, 379-381.

169. Stranks, S. D.; Plochocka, P., The influence of the rashba effect. *Nature Materials* **2018,** *17*, 381-382.

170. Kieslich, G.; Sun, S.; Cheetham, A. K., Solid-state principles applied to organic-inorganic perovskites: New tricks for an old dog. *Chemical Science* **2014,** *5*, 4712-4715.

171. Travis, W.; Glover, E. N. K.; Bronstein, H.; Scanlon, D. O.; Palgrave, R. G., On the application of the tolerance factor to inorganic and hybrid halide perovskites: A revised system. *Chemical Science* **2016,** *7*, 4548-4556.

172. Fu, Y.; Wu, T.; Wang, J.; Zhai, J.; Shearer, M. J.; Zhao, Y.; Hamers, R. J.; Kan, E.; Deng, K.; Zhu, X. Y.; Jin, S., Stabilization of the metastable lead iodide perovskite phase via surface functionalization. *Nano Letters* **2017,** *17*, 4405-4414.

173. Ke, W.; Spanopoulos, I.; Stoumpos, C. C.; Kanatzidis, M. G., Myths and reality of $hpbi_3$ in halide perovskite solar cells. *Nature Communications* **2018,** *9*, 4785.

174. Jodlowski, A. D.; Roldán-Carmona, C.; Grancini, G.; Salado, M.; Ralaiarisoa, M.; Ahmad, S.; Koch, N.; Camacho, L.; de Miguel, G.; Nazeeruddin, M. K., Large guanidinium cation mixed with methylammonium in lead iodide perovskites for 19% efficient solar cells. *Nature Energy* **2017,** *2*, 972-979.

175. Peng, W.; Miao, X.; Adinolfi, V.; Alarousu, E.; El Tall, O.; Emwas, A.-H.; Zhao, C.; Walters, G.; Liu, J.; Ouellette, O.; Pan, J.; Murali, B.; Sargent, E. H.; Mohammed, O. F.; Bakr, O. M., Engineering of $ch_3nh_3pbi_3$ perovskite crystals by alloying large organic cations for enhanced thermal stability and transport properties. *Angewandte Chemie International Edition* **2016,** *55*, 10686-10690.

176. Ke, W.; Stoumpos, C. C.; Zhu, M.; Mao, L.; Spanopoulos, I.; Liu, J.; Kontsevoi, O. Y.; Chen, M.; Sarma, D.; Zhang, Y.; Wasielewski, M. R.; Kanatzidis, M. G., Enhanced photovoltaic performance and stability with a new type of hollow 3d perovskite {en}$fasni_3$. *Science Advances* **2017,** *3*, e1701293.

177. Spanopoulos, I.; Ke, W.; Stoumpos, C. C.; Schueller, E. C.; Kontsevoi, O. Y.; Seshadri, R.; Kanatzidis, M. G., Unraveling the chemical nature of the 3d "hollow" hybrid halide perovskites. *Journal of the American Chemical Society* **2018,** *140*, 5728-5742.

178. Leblanc, A.; Mercier, N.; Allain, M.; Dittmer, J.; Pauporté, T.; Fernandez, V.; Boucher, F.; Kepenekian, M.; Katan, C., Enhanced stability and band gap tuning of α-$[hc(nh_2)_2]pbi_3$ hybrid perovskite by large cation integration. *ACS Applied Materials & Interfaces* **2019,** *11*, 20743-20751.

179. Passarelli, J. V.; Fairfield, D. J.; Sather, N. A.; Hendricks, M. P.; Sai, H.; Stern, C. L.; Stupp, S. I., Enhanced out-of-plane conductivity and photovoltaic performance in n = 1 layered perovskites through organic cation design. *Journal of the American Chemical Society* **2018,** *140*, 7313-7323.

180. Fu, Y.; Hautzinger, M. P.; Luo, Z.; Wang, F.; Pan, D.; Aristov, M. M.; Guzei, I. A.; Pan, A.; Zhu, X.; Jin, S., Incorporating large a cations into lead iodide perovskite cages: Relaxed goldschmidt tolerance factor and impact on exciton–phonon interaction. *ACS Central Science* **2019,** *5*, 1377-1386.

181. Xu, Z.; Li, Y.; Liu, X.; Ji, C.; Chen, H.; Li, L.; Han, S.; Hong, M.; Luo, J.; Sun, Z., Highly sensitive and ultrafast responding array photodetector based on a newly tailored 2d lead iodide perovskite crystal. *Advanced Optical Materials* **2019,** *7*, 1900308.

182. Mao, L.; Wu, Y.; Stoumpos, C. C.; Traore, B.; Katan, C.; Even, J.; Wasielewski, M. R.; Kanatzidis, M. G., Tunable white-light emission in single-cation-templated three-layered 2d perovskites $(ch_3ch_2nh_3)_4pb_3br_{10-x}cl_x$. *Journal of the American Chemical Society* **2017,** *139*, 11956-11963.

183. Geselle, M.; Fuess, H., Crystal structure of tetrakis(ethylammonium) decachlorotriplumbate(ii), $(c_2h_5nh_3)_4pb_3cl_{10}$. *Zeitschrift für Kristallographie - New Crystal Structures* **1997,** *212*, 241.

184. Wang, S.; Liu, X.; Li, L.; Ji, C.; Sun, Z.; Wu, Z.; Hong, M.; Luo, J., An unprecedented biaxial trilayered hybrid perovskite ferroelectric with directionally tunable photovoltaic effects. *Journal of the American Chemical Society* **2019,** *141*, 7693-7697.

185. Stoumpos, C. C.; Malliakas, C. D.; Kanatzidis, M. G., Semiconducting tin and lead iodide perovskites with organic cations: Phase transitions, high mobilities, and near-infrared photoluminescent properties. *Inorganic chemistry* **2013,** *52*, 9019-9038.

186. Dai, J.; Fu, Y.; Manger, L. H.; Rea, M. T.; Hwang, L.; Goldsmith, R. H.; Jin, S., Carrier decay properties of mixed cation formamidinium–methylammonium lead iodide perovskite $[hc(nh_2)_2]_{1-x}[ch_3nh_3]_xpbi_3$ nanorods. *The Journal of Physical Chemistry Letters* **2016,** *7*, 5036-5043.

187. Stoumpos, C. C.; Cao, D. H.; Clark, D. J.; Young, J.; Rondinelli, J. M.; Jang, J. I.; Hupp, J. T.; Kanatzidis, M. G., Ruddlesden–popper hybrid lead iodide perovskite 2d homologous semiconductors. *Chemistry of Materials* **2016,** *28*, 2852-2867.

188. Du, K.-z.; Tu, Q.; Zhang, X.; Han, Q.; Liu, J.; Zauscher, S.; Mitzi, D. B., Two-dimensional lead(ii) halide-based hybrid perovskites templated by acene alkylamines: Crystal structures, optical properties, and piezoelectricity. *Inorganic Chemistry* **2017,** *56*, 9291-9302.

189. Kepenekian, M.; Traore, B.; Blancon, J.-C.; Pedesseau, L.; Tsai, H.; Nie, W.; Stoumpos, C. C.; Kanatzidis, M. G.; Even, J.; Mohite, A. D.; Tretiak, S.; Katan, C., Concept of lattice mismatch and emergence of surface states in two-dimensional hybrid perovskite quantum wells. *Nano Letters* **2018,** *18*, 5603-5609.

190. Wu, X.; Trinh, M. T.; Zhu, X. Y., Excitonic many-body interactions in two-dimensional lead iodide perovskite quantum wells. *The Journal of Physical Chemistry C* **2015,** *119*, 14714-14721.

191. Liu, G.; Gong, J.; Kong, L.; Schaller, R. D.; Hu, Q.; Liu, Z.; Yan, S.; Yang, W.; Stoumpos, C. C.; Kanatzidis, M. G.; Mao, H.-k.; Xu, T., Isothermal pressure-derived metastable states in 2d hybrid perovskites showing enduring bandgap narrowing. *Proceedings of the National Academy of Sciences of the United States of America* **2018,** *115*, 8076-8081.

192. Gong, X.; Voznyy, O.; Jain, A.; Liu, W.; Sabatini, R.; Piontkowski, Z.; Walters, G.; Bappi, G.; Nokhrin, S.; Bushuyev, O.; Yuan, M.; Comin, R.; McCamant, D.; Kelley, S. O.;

Sargent, E. H., Electron–phonon interaction in efficient perovskite blue emitters. *Nature Materials* **2018,** *17*, 550-556.

193. Pedesseau, L.; Sapori, D.; Traore, B.; Robles, R.; Fang, H.-H.; Loi, M. A.; Tsai, H.; Nie, W.; Blancon, J.-C.; Neukirch, A.; Tretiak, S.; Mohite, A. D.; Katan, C.; Even, J.; Kepenekian, M., Advances and promises of layered halide hybrid perovskite semiconductors. *ACS Nano* **2016,** *10*, 9776-9786.

194. Traoré, B.; Bouder, G.; Lafargue-Dit-Hauret, W.; Rocquefelte, X.; Katan, C.; Tran, F.; Kepenekian, M., Efficient and accurate calculation of band gaps of halide perovskites with the tran-blaha modified becke-johnson potential. *Physical Review B* **2019,** *99*, 035139.

195. Blancon, J. C.; Stier, A. V.; Tsai, H.; Nie, W.; Stoumpos, C. C.; Traoré, B.; Pedesseau, L.; Kepenekian, M.; Katsutani, F.; Noe, G. T.; Kono, J.; Tretiak, S.; Crooker, S. A.; Katan, C.; Kanatzidis, M. G.; Crochet, J. J.; Even, J.; Mohite, A. D., Scaling law for excitons in 2d perovskite quantum wells. *Nature Communications* **2018,** *9*, 2254.

196. Even, J.; Pedesseau, L.; Katan, C., Understanding quantum confinement of charge carriers in layered 2d hybrid perovskites. *ChemPhysChem* **2014,** *15*, 3733-3741.

197. Mondal, A.; Aneesh, J.; Kumar Ravi, V.; Sharma, R.; Mir, W. J.; Beard, M. C.; Nag, A.; Adarsh, K. V., Ultrafast exciton many-body interactions and hot-phonon bottleneck in colloidal cesium lead halide perovskite nanocrystals. *Physical Review B* **2018,** *98*, 115418.

198. Nah, S.; Spokoyny, B.; Stoumpos, C.; Soe, C. M. M.; Kanatzidis, M.; Harel, E., Spatially segregated free-carrier and exciton populations in individual lead halide perovskite grains. *Nature Photonics* **2017,** *11*, 285.

199. Mondal, A.; Aneesh, J.; Ravi, V. K.; Sharma, R.; Mir, W. J.; Beard, M. C.; Nag, A.; Adarsh, K. V., Ultrafast exciton many-body interactions and hot-phonon bottleneck in colloidal cesium lead halide perovskite nanocrystals. *Physical Review B* **2018,** *98*.

200. De Angelis, F.; Petrozza, A., Clues from defect photochemistry. *Nature Materials* **2018,** *17*, 383-384.

201. Chung, I.; Lee, B.; He, J.; Chang, R. P. H.; Kanatzidis, M. G., All-solid-state dye-sensitized solar cells with high efficiency. *Nature* **2012,** *485*, 486-489.

202. Kim, H.-S.; Lee, C.-R.; Im, J.-H.; Lee, K.-B.; Moehl, T.; Marchioro, A.; Moon, S.-J.; Humphry-Baker, R.; Yum, J.-H.; Moser, J. E.; Grätzel, M.; Park, N.-G., Lead iodide perovskite sensitized all-solid-state submicron thin film mesoscopic solar cell with efficiency exceeding 9%. *Scientific Reports* **2012,** *2*, 591.

203. Lee, M. M.; Teuscher, J.; Miyasaka, T.; Murakami, T. N.; Snaith, H. J., Efficient hybrid solar cells based on meso-superstructured organometal halide perovskites. *Science* **2012,** *338*, 643.

204. Stoumpos, C. C.; Kanatzidis, M. G., Halide perovskites: Poor man's high-performance semiconductors. *Advanced Materials* **2016,** *28*, 5778-5793.

205. Tsai, H.; Nie, W.; Blancon, J.-C.; Stoumpos, C. C.; Asadpour, R.; Harutyunyan, B.; Neukirch, A. J.; Verduzco, R.; Crochet, J. J.; Tretiak, S.; Pedesseau, L.; Even, J.; Alam, M. A.; Gupta, G.; Lou, J.; Ajayan, P. M.; Bedzyk, M. J.; Kanatzidis, M. G.; Mohite, A. D., High-efficiency two-dimensional ruddlesden–popper perovskite solar cells. *Nature* **2016,** *536*, 312.

206. Arora, N.; Dar, M. I.; Hinderhofer, A.; Pellet, N.; Schreiber, F.; Zakeeruddin, S. M.; Grätzel, M., Perovskite solar cells with cuscn hole extraction layers yield stabilized efficiencies greater than 20%. *Science* **2017,** *358*, 768-771.

207. Yang, W. S.; Park, B.-W.; Jung, E. H.; Jeon, N. J.; Kim, Y. C.; Lee, D. U.; Shin, S. S.; Seo, J.; Kim, E. K.; Noh, J. H.; Seok, S. I., Iodide management in formamidinium-lead-halide–based perovskite layers for efficient solar cells. *Science* **2017,** *356*, 1376-1379.

208. Tsai, H.; Asadpour, R.; Blancon, J.-C.; Stoumpos, C. C.; Durand, O.; Strzalka, J. W.; Chen, B.; Verduzco, R.; Ajayan, P. M.; Tretiak, S.; Even, J.; Alam, M. A.; Kanatzidis, M. G.; Nie, W.; Mohite, A. D., Light-induced lattice expansion leads to high-efficiency perovskite solar cells. *Science* **2018,** *360*, 67-70.

209. Cao, Y.; Wang, N.; Tian, H.; Guo, J.; Wei, Y.; Chen, H.; Miao, Y.; Zou, W.; Pan, K.; He, Y.; Cao, H.; Ke, Y.; Xu, M.; Wang, Y.; Yang, M.; Du, K.; Fu, Z.; Kong, D.; Dai, D.; Jin, Y.; Li, G.; Li, H.; Peng, Q.; Wang, J.; Huang, W., Perovskite light-emitting diodes based on spontaneously formed submicrometre-scale structures. *Nature* **2018,** *562*, 249-253.

210. Lin, K.; Xing, J.; Quan, L. N.; de Arquer, F. P. G.; Gong, X.; Lu, J.; Xie, L.; Zhao, W.; Zhang, D.; Yan, C.; Li, W.; Liu, X.; Lu, Y.; Kirman, J.; Sargent, E. H.; Xiong, Q.; Wei, Z., Perovskite light-emitting diodes with external quantum efficiency exceeding 20 per cent. *Nature* **2018,** *562*, 245-248.

211. Sutherland, B. R.; Sargent, E. H., Perovskite photonic sources. *Nature Photonics* **2016,** *10*, 295.

212. Fang, Y.; Dong, Q.; Shao, Y.; Yuan, Y.; Huang, J., Highly narrowband perovskite single-crystal photodetectors enabled by surface-charge recombination. *Nature Photonics* **2015,** *9*, 679-686.

213. Wei, H.; Fang, Y.; Mulligan, P.; Chuirazzi, W.; Fang, H.-H.; Wang, C.; Ecker, B. R.; Gao, Y.; Loi, M. A.; Cao, L.; Huang, J., Sensitive x-ray detectors made of methylammonium lead tribromide perovskite single crystals. *Nature Photonics* **2016,** *10*, 333-339.

214. Wei, H.; DeSantis, D.; Wei, W.; Deng, Y.; Guo, D.; Savenije, T. J.; Cao, L.; Huang, J., Dopant compensation in alloyed ch3nh3pbbr3−xclx perovskite single crystals for gamma-ray spectroscopy. *Nature Materials* **2017,** *16*, 826-833.

215. He, Y.; Ke, W.; Alexander, G. C. B.; McCall, K. M.; Chica, D. G.; Liu, Z.; Hadar, I.; Stoumpos, C. C.; Wessels, B. W.; Kanatzidis, M. G., Resolving the energy of γ-ray photons with mapbi3 single crystals. *ACS Photonics* **2018,** *5*, 4132-4138.

216. He, Y.; Matei, L.; Jung, H. J.; McCall, K. M.; Chen, M.; Stoumpos, C. C.; Liu, Z.; Peters, J. A.; Chung, D. Y.; Wessels, B. W.; Wasielewski, M. R.; Dravid, V. P.; Burger, A.; Kanatzidis, M. G., High spectral resolution of gamma-rays at room temperature by perovskite cspbbr3 single crystals. *Nature Communications* **2018,** *9*, 1609.

217. Zhu, H.; Fu, Y.; Meng, F.; Wu, X.; Gong, Z.; Ding, Q.; Gustafsson, M. V.; Trinh, M. T.; Jin, S.; Zhu, X. Y., Lead halide perovskite nanowire lasers with low lasing thresholds and high quality factors. *Nature Materials* **2015,** *14*, 636-642.

218. Zhang, H.; Liao, Q.; Wu, Y.; Zhang, Z.; Gao, Q.; Liu, P.; Li, M.; Yao, J.; Fu, H., 2d ruddlesden–popper perovskites microring laser array. *Advanced Materials* **2018,** *30*, 1706186.

219. Dolzhenko, Y. I.; Inabe, T.; Maruyama, Y., In situ x-ray observation on the intercalation of weak interaction molecules into perovskite-type layered crystals (c9h19nh3)2pbi4 and (c10h21nh3)2cdcl4. *Bulletin of the Chemical Society of Japan* **1986,** *59*, 563-567.

220. Papavassiliou, G. C.; Koutselas, I. B.; Terzis, A.; Whangbo, M. H., Structural and electronic properties of the natural quantum-well system (c6h5ch2ch2nh3)2sni4. *Solid State Communications* **1994,** *91*, 695-698.

221. Mitzi, D. B.; Dimitrakopoulos, C. D.; Kosbar, L. L., Structurally tailored organic−inorganic perovskites: Optical properties and solution-processed channel materials for thin-film transistors. *Chemistry of Materials* **2001,** *13*, 3728-3740.

222. Mitzi, D. B.; Medeiros, D. R.; Malenfant, P. R. L., Intercalated organic−inorganic perovskites stabilized by fluoroaryl−aryl interactions. *Inorganic Chemistry* **2002,** *41*, 2134-2145.

223. Billing, D. G.; Lemmerer, A., Synthesis, characterization and phase transitions of the inorganic–organic layered perovskite-type hybrids [(cnh2n+1nh3)2pbi4] (n = 12, 14, 16 and 18). *New Journal of Chemistry* **2008,** *32*, 1736-1746.

224. Kumar, S.; Hodes, G.; Cahen, D., Defects in halide perovskites: The lattice as a boojum? *MRS Bulletin* **2020,** *45*, 478-484.

225. Meggiolaro, D.; Motti, S. G.; Mosconi, E.; Barker, A. J.; Ball, J.; Andrea Riccardo Perini, C.; Deschler, F.; Petrozza, A.; De Angelis, F., Iodine chemistry determines the defect tolerance of lead-halide perovskites. *Energy & Environmental Science* **2018,** *11*, 702-713.

226. Yin, J.; Naphade, R.; Gutiérrez Arzaluz, L.; Brédas, J.-L.; Bakr, O. M.; Mohammed, O. F., Modulation of broadband emissions in two-dimensional ⟨100⟩-oriented ruddlesden–popper hybrid perovskites. *ACS Energy Letters* **2020,** *5*, 2149-2155.

227. Wei, X.; Zhang, Y.; Zheng, T.; Gao, L.; Jiang, J.; Zhao, W.; Liu, H.; Lu, J.; Ni, Z., Competition between oxygen curing and ion migration in mapbi3 induced by irradiation exposure. *The Journal of Physical Chemistry Letters* **2020**, 8477-8482.

228. Motti, S. G.; Gandini, M.; Barker, A. J.; Ball, J. M.; Srimath Kandada, A. R.; Petrozza, A., Photoinduced emissive trap states in lead halide perovskite semiconductors. *ACS Energy Letters* **2016,** *1*, 726-730.

229. Fu, Y.; Jiang, X.; Li, X.; Traore, B.; Spanopoulos, I.; Katan, C.; Even, J.; Kanatzidis, M. G.; Harel, E., Cation engineering in two-dimensional ruddlesden–popper lead iodide perovskites with mixed large a-site cations in the cages. *Journal of the American Chemical Society* **2020,** *142*, 4008-4021.

230. Kahmann, S.; Tekelenburg, E. K.; Duim, H.; Kamminga, M. E.; Loi, M. A., Extrinsic nature of the broad photoluminescence in lead iodide-based ruddlesden–popper perovskites. *Nature Communications* **2020,** *11*, 2344.

231. Wang, M.; Tang, J.; Wang, H.; Zhang, C.; Zhao, Y. S.; Yao, J., Grain boundary enhanced photoluminescence anisotropy in two-dimensional hybrid perovskite films. *Advanced Optical Materials* **2020,** *8*, 1901780.

232. Qin, Z.; Dai, S.; Gajjela, C. C.; Wang, C.; Hadjiev, V. G.; Yang, G.; Li, J.; Zhong, X.; Tang, Z.; Yao, Y.; Guloy, A. M.; Reddy, R.; Mayerich, D.; Deng, L.; Yu, Q.; Feng, G.; Calderon, H. A.; Robles Hernandez, F. C.; Wang, Z. M.; Bao, J., Spontaneous formation of 2d/3d heterostructures on the edges of 2d ruddlesden–popper hybrid perovskite crystals. *Chemistry of Materials* **2020,** *32*, 5009-5015.

233. Aristidou, N.; Eames, C.; Sanchez-Molina, I.; Bu, X.; Kosco, J.; Islam, M. S.; Haque, S. A., Fast oxygen diffusion and iodide defects mediate oxygen-induced degradation of perovskite solar cells. *Nature Communications* **2017,** *8*, 15218.

234. Zhang, W.; Pathak, S.; Sakai, N.; Stergiopoulos, T.; Nayak, P. K.; Noel, N. K.; Haghighirad, A. A.; Burlakov, V. M.; deQuilettes, D. W.; Sadhanala, A.; Li, W.; Wang, L.; Ginger, D. S.; Friend, R. H.; Snaith, H. J., Enhanced optoelectronic quality of perovskite thin films with hypophosphorous acid for planar heterojunction solar cells. *Nature Communications* **2015,** *6*, 10030.

235. Meggiolaro, D.; Mosconi, E.; De Angelis, F., Mechanism of reversible trap passivation by molecular oxygen in lead-halide perovskites. *ACS Energy Letters* **2017,** *2*, 2794-2798.

236. Feldmann, S.; Macpherson, S.; Senanayak, S. P.; Abdi-Jalebi, M.; Rivett, J. P. H.; Nan, G.; Tainter, G. D.; Doherty, T. A. S.; Frohna, K.; Ringe, E.; Friend, R. H.; Sirringhaus, H.; Saliba, M.; Beljonne, D.; Stranks, S. D.; Deschler, F., Photodoping through local charge carrier accumulation in alloyed hybrid perovskites for highly efficient luminescence. *Nature Photonics* **2020,** *14*, 123-128.

237. Wu, X. X.; Trinh, M. T.; Zhu, X. Y., Excitonic many-body interactions in two-dimensional lead iodide perovskite quantum wells. *The Journal of Physical Chemistry C* **2015,** *119*, 14714-14721.

238. Fu, Y.; Jiang, X.; Li, X.; Traore, B.; Spanopoulos, I.; Katan, C.; Even, J.; Kanatzidis, M. G.; Harel, E., Cation engineering in two-dimensional ruddlesden-popper lead iodide perovskites with mixed large a-site cations in the cages. *Journal of the American Chemical Society* **2020,** *142*, 4008-4021.

239. Gao, Y.; Zhang, M.; Zhang, X.; Lu, G., Decreasing exciton binding energy in two-dimensional halide perovskites by lead vacancies. *The Journal of Physical Chemistry Letters* **2019,** *10*, 3820-3827.

Appendices

APPENDIX A Appendix to CHAPTER 2

A.1 Materials and Methods

A.1.1 Perovskite Film Fabrication and Characterization

A 0.3 M stock solution of $CH_3NH_3PbI_3$ was prepared using $CH_3NH_3PbI_3$ powders, formed by precipitation from an aqueous HI solution. The powder was dissolved in anhydrous DMF (99.8%) at 100 °C for 20 minutes to ensure complete dissolution. The solution was cooled to 70 °C and filtered through a 0.45 μm nylon filter. A small amount of HI (57 wt% in water) was added to the precursor $CH_3NH_3PbI_3$ solution (8% vol/vol) in air just before use to avoid the oxidation of iodide. A perovskite layer was fabricated by spin-coating the as-prepared solution on a No 1.5 glass coverslip at 2,000 r.p.m. for 30 s, followed by annealing at 100 °C for 10 min.[1]

The thickness of the film is uniform and within 100 nm, characterized using cross-sectional SEM.[1] EDS is performed across the film with points selected on the grain boundaries and interiors (six representative data points showed in Figure_Apx A.1). A Pb/I ratio very close to 3/1 is observed on different morphologies which proves our claim that the HI additive is only controlling the morphologies but brings no changes in chemical composition.

The reason why we designed this “island-shaped” films instead of using continuous film is that this is the only way we can study as many morphologies as possible and perform statistical analysis with a large sample size, within a relatively small ROI. The HI additives are the only way we found that could control the grain size without introducing other impurities, as I^- is part

of the $CH_3NH_3PbI_3$ lattice. In the context of a microscopic study on GBs, we want to make sure no other ions are introduced into the system. There are other additives reported to control the grain sizes but there is no strong evidence from microscopic study to prove that these additives did not get into the GBs or concentrated at edges. That is the reason why this grain-size control method was ultimately chosen.

$CH_3NH_3PbI_3$ film fabricated with 0% of HI in the precursor solution were also studied as a control experiment with different morphology (Appendix A.2.2, Figure_Apx A.12).

A.1.2 Correlated SEM

The $CH_3NH_3PbI_3$ perovskite film studied here was deposited on marked glass coverslip (Corning, No 1.5 cover glass). Optical images (Figure_Apx A.2b, e) were first taken along with the TA measurement, and further calibrated using probe transmission map (Figure_Apx A.6c). The SEM images of same regions (Figure_Apx A.2a, c, d, f) were later taken on Hitachi S-4800 SEM (NUANCE, Northwestern University) at 5 kV, with 6 nm Au/Pd coating (Denton Desk IV, NUANCE, Northwestern University). More high-resolution SEM images of perovskite particles on the films of same chemical composition are also included showing the two different morphologies within one particle (Figure_Apx A.2g–i).

A.1.3 Fitting Methods: Band-Filling Model

The model was constructed based on parabolic-band hypothesis and the band-filling effect. The change in absorption is given by

$$\Delta A = A\left(E; E_g - \Delta E_g\right)\left(1 - \frac{1}{1 + e^{\frac{E - E_f}{k_B T}}}\right)^2 - A\left(E; E_g\right) \quad \text{(A.1)}$$

Where $A\left(E; E_g\right)$ and $A\left(E; E_g - \Delta E_g\right)$ represents the absorption before and after the shift of the bandgap. The Fermi distribution function represents the carrier distribution characterized by the quasi-Fermi energy, E_f, and the quasi-temperature, T. This equation only holds true when the effective masses of electrons and holes are similar, as is the case in $CH_3NH_3PbI_3$. [2-5]

The fit is more weighted within 1 eV above the bandgap (1.59–1.73 eV), where the parabolic model should hold well,[6] compared to the high-energy range. R-square values at different times are mapped in Figure_Apx A.8. Only points with an r-square value higher than 0.995 are later used (for the "line scans" done in the air, we used 0.9 due to the small sample size). The fitting algorithm used is the "lsqnonlin" function in MATLAB. The "fit" function was also tried and gave out same results. Unweighted fit was also performed, and the sub-bandgap state was still present.

A.1.4 Fitting Methods: Temperature Cooling Curve

A single-exponential fit of each temperature-time curve gives the cooling rate. Results with a confidence level over 0.9 are later used (for the "line scans" done in the air, we used 0.6 due to the small sample size). This is the way to extract the cooling rate plotted in Figure 2.4 in the main text. A single-exponential fit of sub-bandgap state intensity as a function of time is performed to extract the population lifetime.

A LO phonon emission model was used to fit the temperature cooling curve as well, where the energy loss rate is dominated by the LO phonon-carrier scattering. A well-accepted equation considering both carrier energy dissipated via phonon emission and gained by the thermal excitation is used:[7]

$$\frac{dU_c}{dt} = \frac{3k_B dT_e}{2dt} = -\frac{\hbar\varpi_{LO}}{\tau_{ave}}\left(e^{-\frac{\hbar\varpi_{LO}}{k_B T_e}} - e^{-\frac{\hbar\varpi_{LO}}{k_B T_L}}\right) \quad \text{(A.2)}$$

where T_e is the carrier temperature, T_L is the lattice temperature, ϖ_{LO} is the frequency of LO phonons, and τ_{ave} is the lifetime of LO phonons. Because of the complexity of the system, τ_{ave} is generally used as a time constant for the energy loss via phono-emission and represents the intensity of phonon-bottleneck effect. In other words, the bigger τ_{ave} is, the longer it takes for energy to dissipate through the LO phonon scattering channel, the stronger the phonon-bottleneck effect is.

The fitting result is plotted in Figure_Apx A.7. Clearly, the phonon-bottle effect is more severe in GIs compared to GBs, which further proved our hypothesis in the main text that the strain on phonons are relieved in GBs, indicating the existence of other pathways. The value of τ_{ave} also agrees well with what were reported in the same system at similar carrier density.[2] We tried to add more kinetics as was did in ref [[8]] equation (7), but the fitting quality is already good enough with the simple phonon-scattering model and adding more kinetics only causes over fitting.

To summarize, the two fitting methods give us a similar result, which is the carrier cooling rate is faster in GBs compared to GIs. The phonon-scattering model also suggests that the dominant effect in GIs is still the LO phonon-scattering effect. To avoid confusion, we only used the rate extracted from the single exponential decay in the main text, and we left the scattering model here as supplementary information. If further research with better time resolution is done, it is recommended to use the scattering model where more kinetic equations could be added directly.

Differential equations are solved using the "ode45" solver in MATLAB.

A.1.5 Initial Carrier Density

The overall initial carrier density was estimated to be 8.38×10^{19} cm^{-3} using the following equation:

$$n_{ex} = \frac{j}{h\nu}(1 - R - T)\alpha \tag{A.3}$$

where j is the input pump power density calculated using the input power and beam size, R and T are the reflectivity and transmittance at the pump wavelength, $h\nu$ is the energy of a pump photon, and α is the absorption coefficient. The values of R, T, and α in ref[2] are used for the estimation.

Due to the difficulty of collecting overall reflectance and transmission within the microscope setup, to get the carrier density map, we calculate the initial carrier density at every point given by

$$n = \int_{E_c}^{\infty} Electronic\ density\ of\ states\ \times Fermi\text{-}Dirac\ distribution\ dE \qquad (A.4)$$

$$n = \int_{E_c}^{\infty} \frac{2}{(2\pi)^2}\left(\frac{2m_e^*}{\hbar^2}\right)^{\frac{3}{2}}\sqrt{E - E_c} \times \frac{1}{1 + e^{\frac{E-E_f}{k_B T}}}\, dE \qquad (A.5)$$

A common way to deal with the integration in the equation above is to approximate the Fermi–Dirac distribution for energies $3k_bT$ away from E_f by a Maxwell–Boltzmann distribution. However, this condition does not hold well in perovskite systems, but is still wildly used. Herein, we used the Joyce–Dixon approximation which provided an analytical solution to the Fermi integration.[9] The parameters extracted at 100 fs from the band-filling model were used to calculate the initial carrier density. The results are shown in Figure 2.1. Note that we used the static bandgap value instead of the shifted one to represent E_c in the equation to better simulate the initial condition. It causes a possible loss in the density as the population below the static bandgap is not counted, but the values are still within the same order of magnitude (10^{19} cm^{-3}) as the value calculated using pump power.

Also, the carrier density is insufficient for complete band-filling. More details could be found in the **Fig. S7** of ref[10]. The power used here corresponds to 0.6 μW in that figure, which falls into the regime dominated by bimolecular recombination, with no obvious high-order process present.

A.1.6 Statistical Analysis (Linear Correlation)

A statistical analysis on different properties were performed. The Pearson's linear correlation coefficient was calculated using the "corr" function in MATLAB, which returns the *p*-value for testing the null hypothesis of no correlation. When the returned *p*-value is less than the significance level of 0.05, it indicates rejection of the hypothesis that no correlation exists between the two columns, in other words, it supports that there is a correlation between the two datasets put in. A sample size *N* is reported in the bracket. In total 806 pixels are scanned and only the 452 pixels within the particle is considered. Also, pixels with bad fit are discarded (see details about fitting in section A.1.3 and A.1.4). That is why the *N* value fluctuates below 452.

Apart from the median value reported in the main text, a mean value and accompanied standard deviation are also reported (see section A.3). The mean and median values are generally close to each other. The reason why median value is displayed in the main text is that it better shows the properties of the bi-modal distributions compared to mean and standard deviation which assumes a normal distribution.

It is also worthwhile to mention the changing trend of *p*-values as a function of time. The *p*-value basically went high at 0.9 ps and low at 2.0 ps (according value in section A.3). We think this is because at 2.0 ps, most carriers already cooled down to the room temperature, which means the cooling process is over and its connection to sub-bandgap state or phonons are cut off. What we are taking is a snapshot of mixture of cooled carriers and carriers still under the cooling processes, with the cooled carriers which already lost connection to the cooling process, the overall correlation seems weaker.

A.1.7 Statistical Tests (Statistical Significance)

We chose not to read too much into the means and standard deviations and used median because the distributions of these properties diverge too far away from normal distributions, and in fact, they are more like bimodal distributions and will be inaccurate to describe using parametric statistics, which is statistics based on parameters extracted from the normal distribution, like means, standard deviations, and the tests based on that. The basic assumption to use parametric statistics is that the data studied follow normal distribution, which is not the case here.

However, it is realized that reporting median values only may not be convincing enough in such broad distributions and a further careful analysis is required to prove that the difference between the GB and GI is statistically significant. In fact, the mean and standard deviation will only give an idea of what the distribution is like and is not enough to prove that the difference is statistically significant and not caused by measurement error. T-test (parametric, based on mean and standard deviation) and Kolmogorov–Smirnov test (KS-test, non-parametric) are used to prove the differences between GB and GI are significant.

The t-test is most widely used to determine if the mean values of two datasets are significantly different. It returns a decision for the null hypothesis that the data in two datasets from normal distributions with equal means, with the alternative hypothesis that the data come from populations with unequal means.[11] We used this test to justify that the mean values of certain parameter which forms a distribution close to a normal distribution, like sub-bandgap state intensity and Fermi energy, coming from GB and GI are significantly different.

The KS test is mostly used in nonparametric statistics to determine if the two distributions tested are significantly different. [12, 13] We think it is more valid here, compared to the t-test especially for the properties, like the quasi-temperature and the cooling rate which show a bi-modal distribution. The KS test returns a decision for the null hypothesis that the data in two datasets are from the same continuous contribution, with the alternative hypothesis being that the two datasets are from different continuous distribution.

For both tests, a 5% significance level was used.

A.2 Supplementary Experiments and Discussion

A.2.1 Discussion on Carrier Density and Depth of the Sub-Bandgap States Extracted from the Band-Filling Model

The real-time carrier density is calculated using the integration of time-resolved TA spectra, as the time-dependent absorption spectra could be used to present the product of the joint density of states and the carrier distribution function along the spectral axis. The carrier density maps are shown in Figure_Apx A.3, which are relatively uniform across the whole particle compared to other properties, indicating no increase in bimolecular recombination at the GBs. This aligns well with previous reports on the benign nature of GBs in perovskites. The relatively lower carrier density/weaker TA intensity in the right part of the particle may be explained by the reabsorption from thicker perovskite planks (see PL and absorption maps in Figure_Apx A.6).

Sub-bandgap absorption is also observed in GIs close to the edge of the particle, but similar changes in the Fermi-energy level and carrier cooling dynamics are not observed. To distinguish

the GB states from these edge states, the position of the sub-bandgap peak is studied. As is shown in Figure_Apx A.3b, GB states mainly appear ~75 meV below the shifted bandgap (~1.65 eV, caused by band-filling effect casted by band edge carriers, maps available in Figure_Apx A.9). Such states are precisely identified by integrating at the depth of 75 meV (Figure_Apx A.3c). Note that the number 75 meV used here is referenced to the shifted bandgap extracted from the band-filling model (which causes new states forming below the static bandgap, and is a better reference considering the dynamic picture). A slight positive correlation between the depth of the sub-bandgap state and the population lifetime is also observed (Figure_Apx A.10), indicating a slower population rate at GB states compared to edge states.

A.2.2 Discussion on Small Crystallites Region and Measurement on 0%-HI Film

The small crystallites (sGI) in the center of the particle is more difficult to characterize than either GB or GI because it consists of both grain boundaries and much smaller grain interiors. We showed the TA spectra of the center point of sGI (Figure_Apx A.11). No obvious change in the bandgap or hot carrier dynamics are observed. A minimal amount sub-bandgap bleaching can be observed, likely because the spatial resolution is such that GBs are present to some degree in the measurement (see also the map in Figure 2d in the main text). Nor are these points associated with an increase in the Fermi energy. It suggests that the GBs in the sGI might not behave the same way as the ones in-between big grains. The reason may be that the sGI and the GI regions are formed in two different stages in the synthesis processes. In one paper our collaborator recently published, they pointed out that during the synthesis, a DMF-related intermediate was the cause of quick formation of $CH_3NH_3PbI_3$.[14] Our hypothesis is that in the synthesis of the particle used in this chapter, the sGI is first formed through this DMF-related

pathway, and the formation of this intermediate is quickly suppressed by 8% HI, allowing $CH_3NH_3PbI_3$ growing in a slower and more ordered way. So, in principle the two regions form under different mechanisms. Therefore, it is inappropriate to compare the GBs formed by two different mechanisms, and we focused more on the GBs formed under controlled growth conditions which are the ones between big grains in this study. It explains why in the sGI, where GBs are concentrated, not much sub-bandgap state population was observed.

To further prove the hypothesis that not all GBs are the same, we fabricated films with 0% HI in the precursor solution, which went through the DMF-intermediate pathway mentioned above. This film behaved pretty similar to the sGI region. The bandgap and the hot carrier features remain the same. We applied the same fitting and no strong sub-bandgap bleaching was observed. The intensity of the sub-bandgap state is very weak compared to the 8%-HI film and cannot be correlated to the GBs or edges. The vertical black lines in Figure_Apx A.12e,f marked the location where there should be significant morphology change but still, no obvious signal from sub-bandgap state can be observed. We think the 0% film is a completely different system considering the small grain size, which is likely formed through a fast pathway assisted by DMF-intermediates.[14] Heterogeneity across the film was observed and reflected in the change of the bandgap bleaching signal, but has nothing to do with the sub-bandgap state we reported in this thesis.

A.2.3 Correlated SEM-TAM on Another Particle (Particle 2)

The same data analysis was performed on another particle on a film prepared using the same method. Similar trends are observed (Figure_Apx A.4). The GBs show stronger absorption in the

sub-bandgap state, elevated Fermi-level, and faster temperature relaxation. Sub-bandgap absorption is also observed at particle edges, but is later well separated from the GB sub-bandgap absorption using the depth of sub-bandgap state as well.

A clear link between the carrier temperature and the distribution of the sub-bandgap state was observed from the scatter plots and the histograms (Figure_Apx A.5). The positive correlation between sub-bandgap state intensity and temperature cooling rate also preserves. The bi-peak distribution is not as clear though. This is because this particle is relatively smaller the sub-ensemble effect is playing a more important role.

The results for statistical tests were not as satisfying, which is caused by the small sample size (~200) and the worse sub-ensemble effect. For the particle in the main text, even though some properties showed a clear bimodal distribution, the difference can still be proved to be statistically significant using t-tests due to the relatively large sample size. For this smaller particle, the bi-modal distribution is playing a more important role. For instance, in Figure_Apx A.5c, the difference in distribution is very clear at 0.9 and 2.0 ps, but still did not pass the t-test. We consider this a vivid example of parametric statistics failing at non-normal distribution, and since the KS-test still prove that the difference between distributions is significant, our initial conclusion is still supported.

It is also worthwhile to point out the assignment of GB and GI is based on manually tracing the SEM image, which comes with unavoidable error. With the sub-ensemble blurring the difference within such a small particle, the difference between GB and GI might be as strong. We still recommend paying more attention to the p value from Pearson's linear correlation which

suggest whether the correlation in the two values is strong, since the assignment of GI and GB points might not be accurate, the correlation between properties is certain.

A.2.4 Correlated SEM-TAM on Other Particles in Air

The same measurement was performed on other particles on a film prepared using the same method but in air (without nitrogen protection). Similar trends are observed. The GBs show stronger absorption in the sub-bandgap state, elevated Fermi-level, and faster temperature relaxation, which agrees with our original hypothesis that this is a unique stated formed at the GBs and will not be affected by the environment. The results are shown below in Figure_Apx A.13. We applied the same fitting procedure and extracted the three important parameters, the sub-bandgap state intensity, the quasi-Fermi energy and the temperature cooling rate. The vertical black lines marked positions where GBs were scanned across and we saw clear positive correlations between GBs and the sub-bandgap state. The change in Fermi energy is hard to see here because that is change in only tens of meV, but the correlation between the sub-bandgap state and the accelerated cooling is very clear. The results suggest that the sub-bandgap state behaves similarly in air and nitrogen environments and accelerated the carrier cooling, with probably the same mechanism. It is also evident that this state should be considered something intrinsic about the material.

We tried to do a large area mapping but experienced sample damage after finishing ~80% of the measurement, which we never saw while taking the scan in N_2 protected environment. A clear evidence of sample damage is the newly-formed thread-like structure shown in the correlated SEM (Figure_Apx A.14), which we never saw in pristine or N_2-protected sample

(Figure_Apx A.2). We guess it is the newly formed PbI_2 as it is reported that the reaction of perovskite with water and oxygen in the air is considered to be one of the main reasons why perovskite decays really fast under ambient conditions. [15, 16]

A.3 Statistical Parameters

a

Temp	Median		Mean		Std.	
	GI	GB	GI	GB	GI	GB
0.2	950	919	954	917	116	126
0.9	424	397	421	397	205	85
2.0	339	308	357	330	153	44

r(dT/T)	Median		Mean		Std.	
	GI	GB	GI	GB	GI	GB
0.2	0.71	0.58	0.70	0.59	0.41	0.37
0.9	1.41	1.67	1.46	1.67	0.81	0.75
2.0	1.46	1.76	1.55	1.74	0.79	0.78

b

rate	Median		Mean		Std.	
	GI	GB	GI	GB	GI	GB
avg.	2.58E+00	2.80E+00	2.80E+00	2.87E+00	1.06E+00	8.04E-01

r(dT/T)mean	Median		Mean		Std.	
	GI	GB	GI	GB	GI	GB
avg.	1.50	1.69	1.53	1.70	0.77	0.74

c

Ef	Median		Mean		Std.	
	GI	GB	GI	GB	GI	GB
0.2	1.627	1.635	1.631	1.636	0.017	0.016
0.9	1.649	1.654	1.645	1.651	0.015	0.012
2.0	1.651	1.659	1.647	1.655	0.014	0.012

r(dT/T)	Median		Mean		Std.	
	GI	GB	GI	GB	GI	GB
0.2	0.70	0.58	0.71	0.61	0.41	0.42
0.9	1.41	1.67	1.47	1.67	0.80	0.75
2.0	1.46	1.76	1.55	1.74	0.79	0.78

d

rate	Median		Mean		Std.	
	GI	GB	GI	GB	GI	GB
avg.	2.53E+00	2.73E+00	2.78E+00	2.85E+00	1.06E+00	8.00E-01

Ef mean	Median		Mean		Std.	
	GI	GB	GI	GB	GI	GB
avg.	1.648	1.656	1.646	1.653	0.014	0.011

A.4 Supplementary Figures

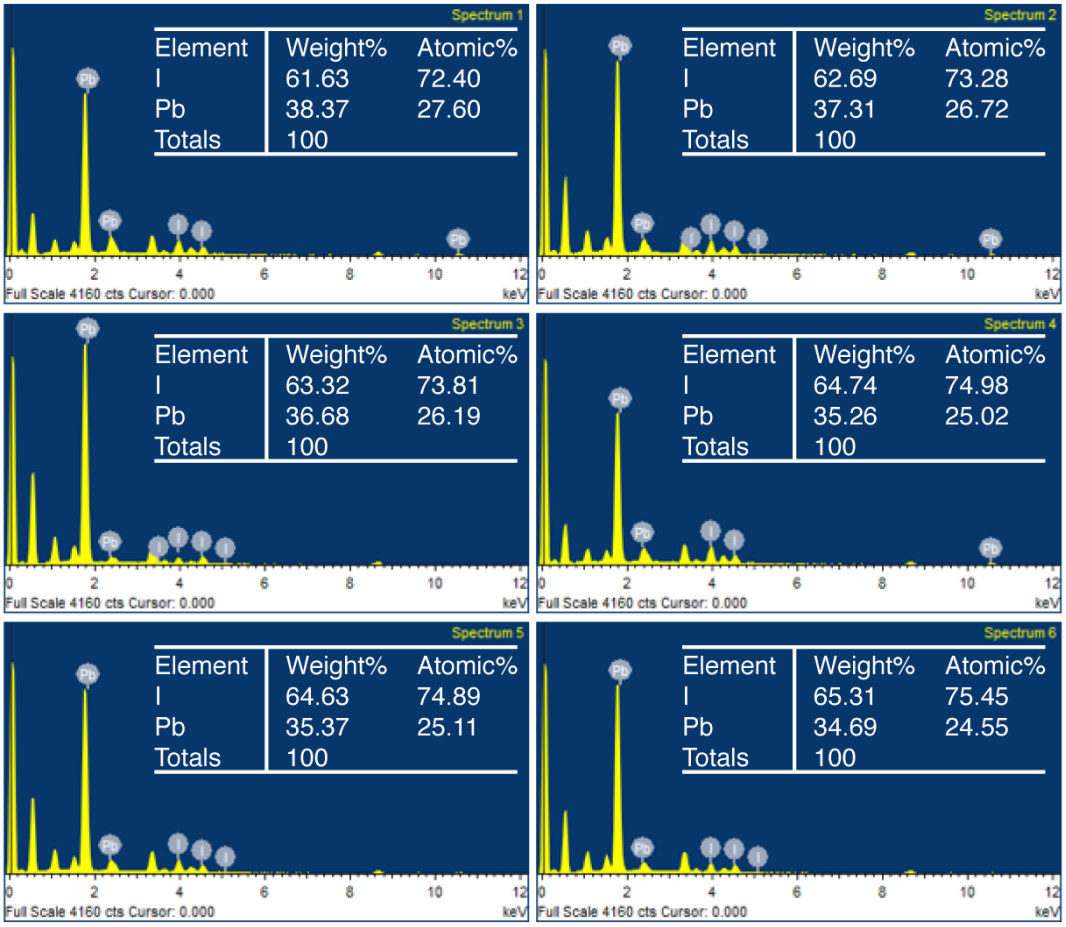

Figure_Apx A.1 EDS analysis performed across the whole $CH_3NH_3PbI_3$ film.

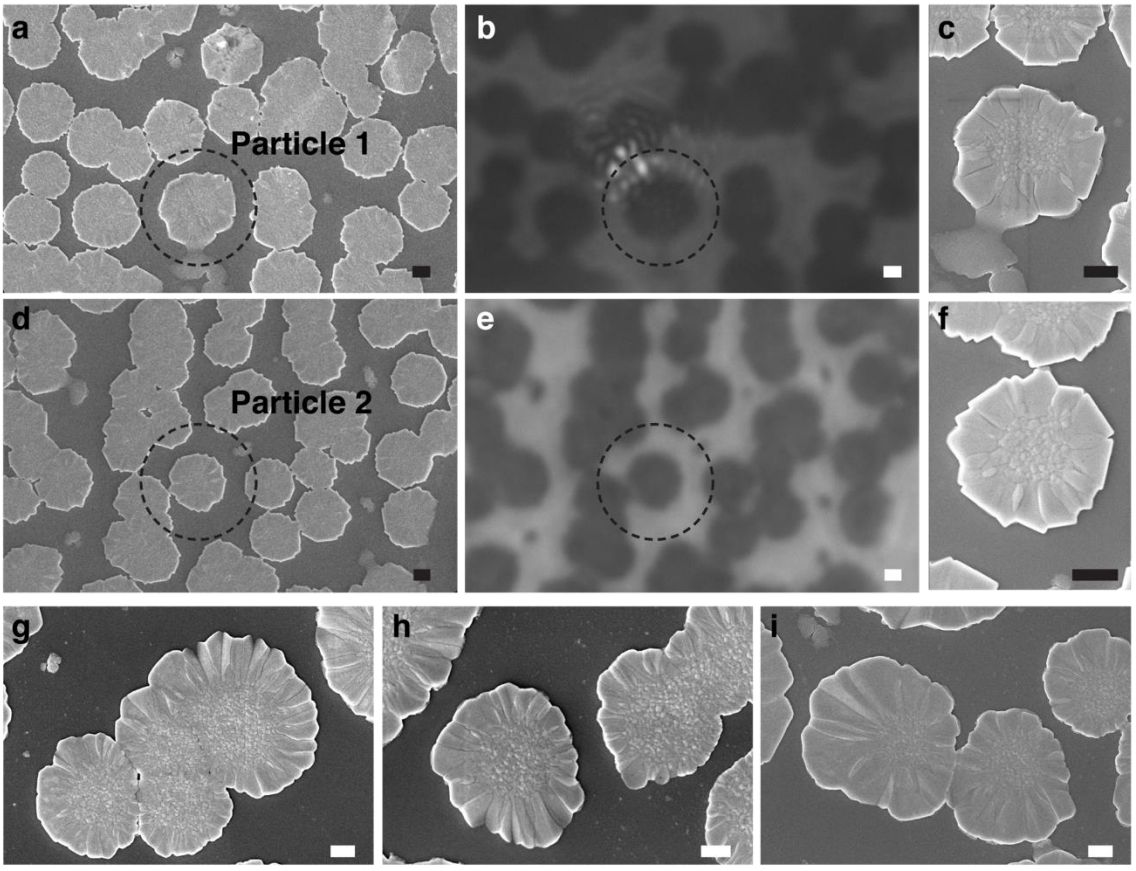

Figure_Apx A.2 Particle 1 (in main text): (a) SEM image of the perovskite film. (b) Correlated optical image of the same region. The bright spot corresponds to the diffraction pattern of the pump beam. (c) Untilted high-resolution SEM image of the particle. Particle 2: (d) SEM image of the perovskite film. (e) Correlated optical image of the same region. (f) Untilted high-resolution SEM image of the particle. (g–i) Untilted high-resolution SEM images of other particles on films of same chemical composition, showing two kinds of dominant morphologies. Scale bar: 1 μm.

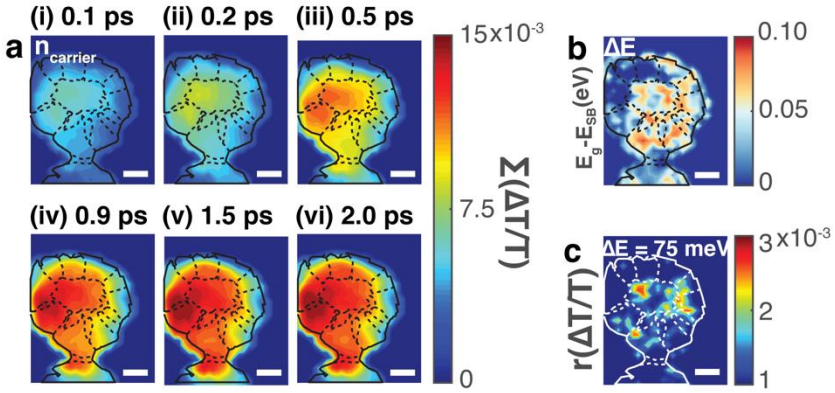

Figure_Apx A.3 (a) Carrier density map within probe range, represented by spectrally integrated TA intensity. (b) Depth of the sub-bandgap state at 2.0 ps, represented by the energy difference between shifted bandgap and the peaking position of the sub-bandgap peak. (c) Integrated sub-bandgap peak intensity at the depth of 75 ± 7.5 meV at 2.0 ps. Scale bar: 1 μm.

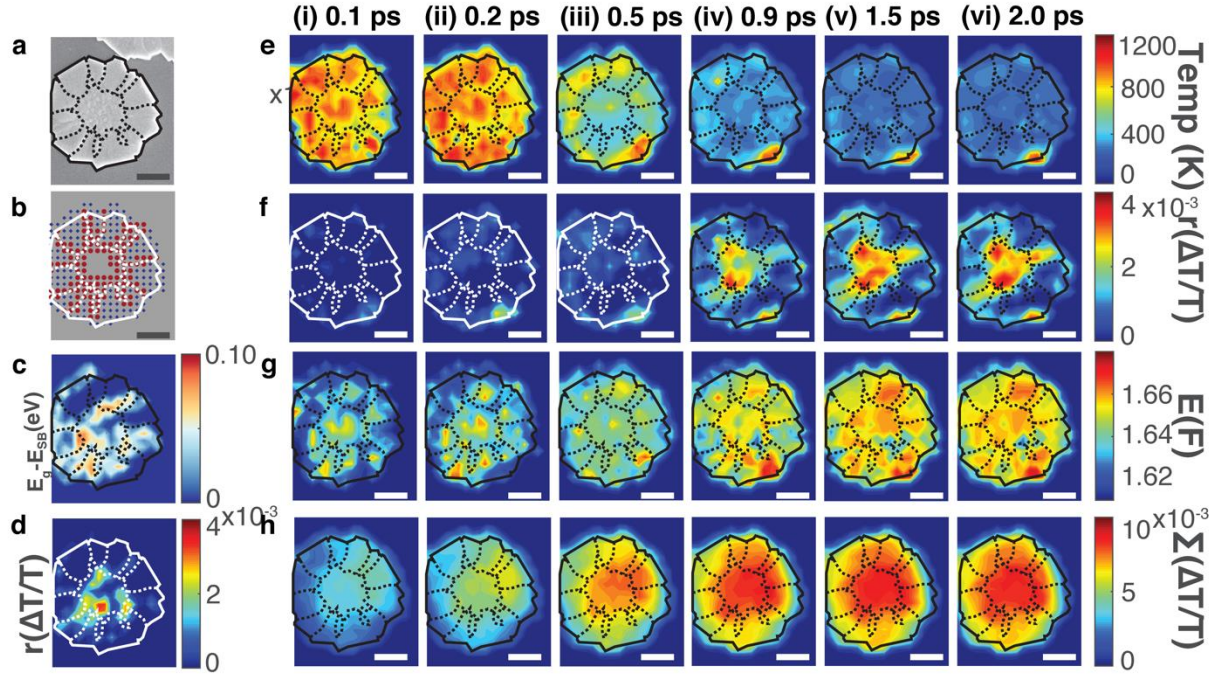

Figure_Apx A.4 (a) SEM image of the perovskite particle. (b) Tracing results from SEM image. Red region: inner circle which mainly contains GBs along with GBs in the outer ring. Blue region: GIs in the outer ring. (c) Depth of the sub-bandgap state represented by the energy difference between shifted bandgap and the peaking position of the sub-bandgap peak. (d) Integrated sub-bandgap peak intensity at the depth of 75 ± 7.5 meV. (e) Temperature map (f) Intensity of the sub-bandgap state map represented by integrated fit residue (1.570 ± 0.015 eV). (g) Quasi-Fermi energy map. (h) Carrier density map within probe range, represented by spectrally integrated TA intensity. Scale bar: 1 μm.

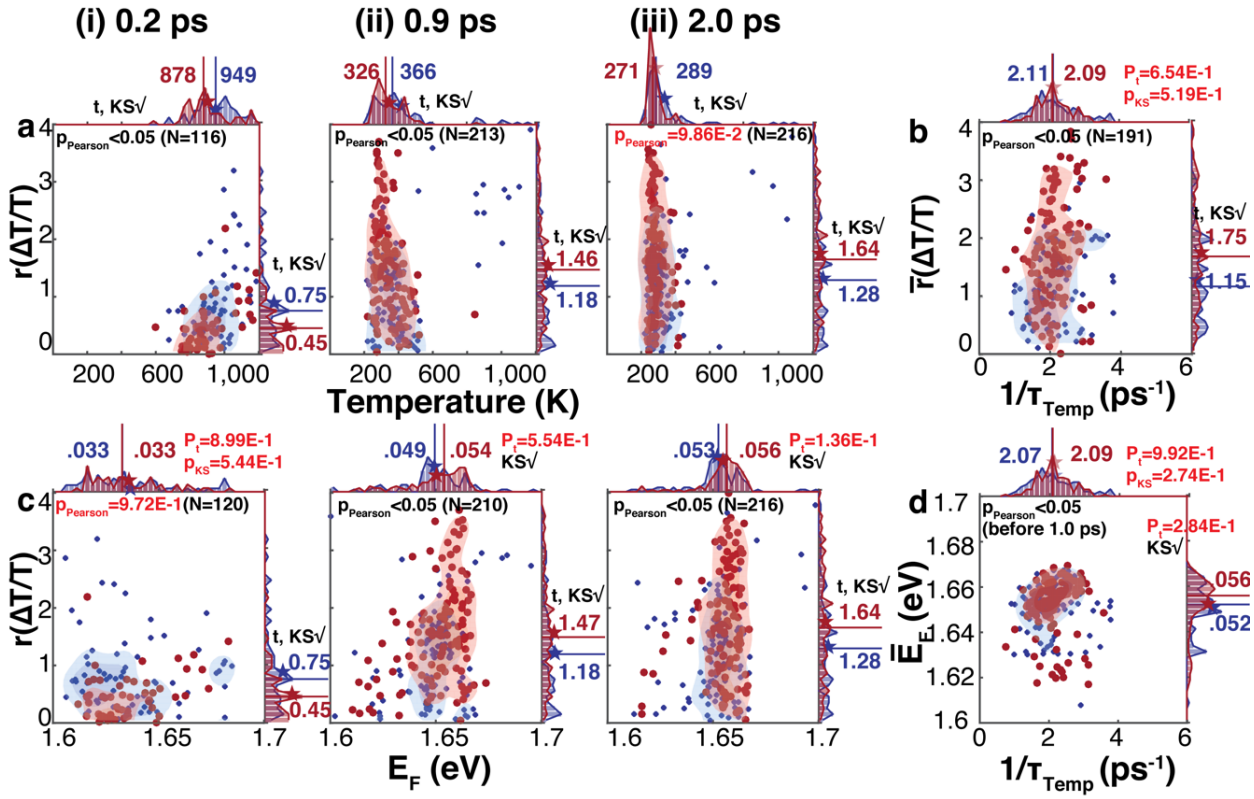

Figure_Apx A.5 Two-dimensional scatter plots of sub-bandgap state intensity and (a) carrier temperature and (c) quasi-Fermi energy at different delay times. Two-dimensional scatter plots of carrier cooling rate and temporally averaged (b) sub-bandgap state intensity and (d) quasi-Fermi energy from 0.9 to 2.0 ps. Contour lines of 25% and 50% probability are marked. The vertical lines show the positions of median values in the histograms, with the value marked nearside. The stars show the mean. The testing results for the t-test and KS-test are marked near each set of histograms. The results for Pearson's linear correlation test are marked on each scatter plot.

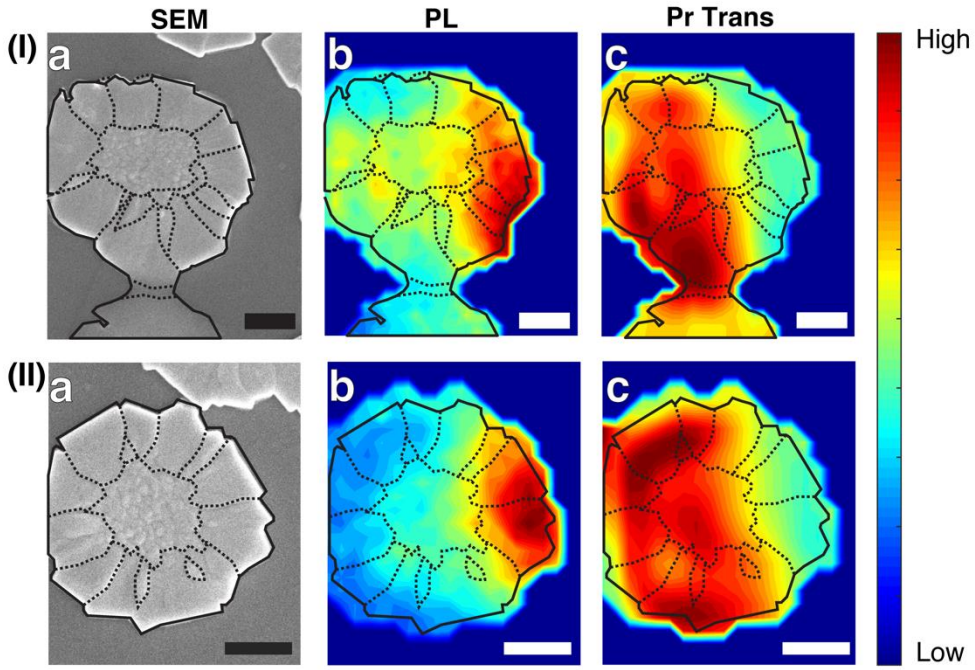

Figure_Apx A.6 Particle 1: (I.a) SEM (I.b) PL map at 1.63 eV (I.c) White-light probe transmission map at 1.63 eV. Particle 2: (II.a) SEM (II.b) PL map at 1.63 eV (II.c) White-light probe transmission map at 1.63 eV.

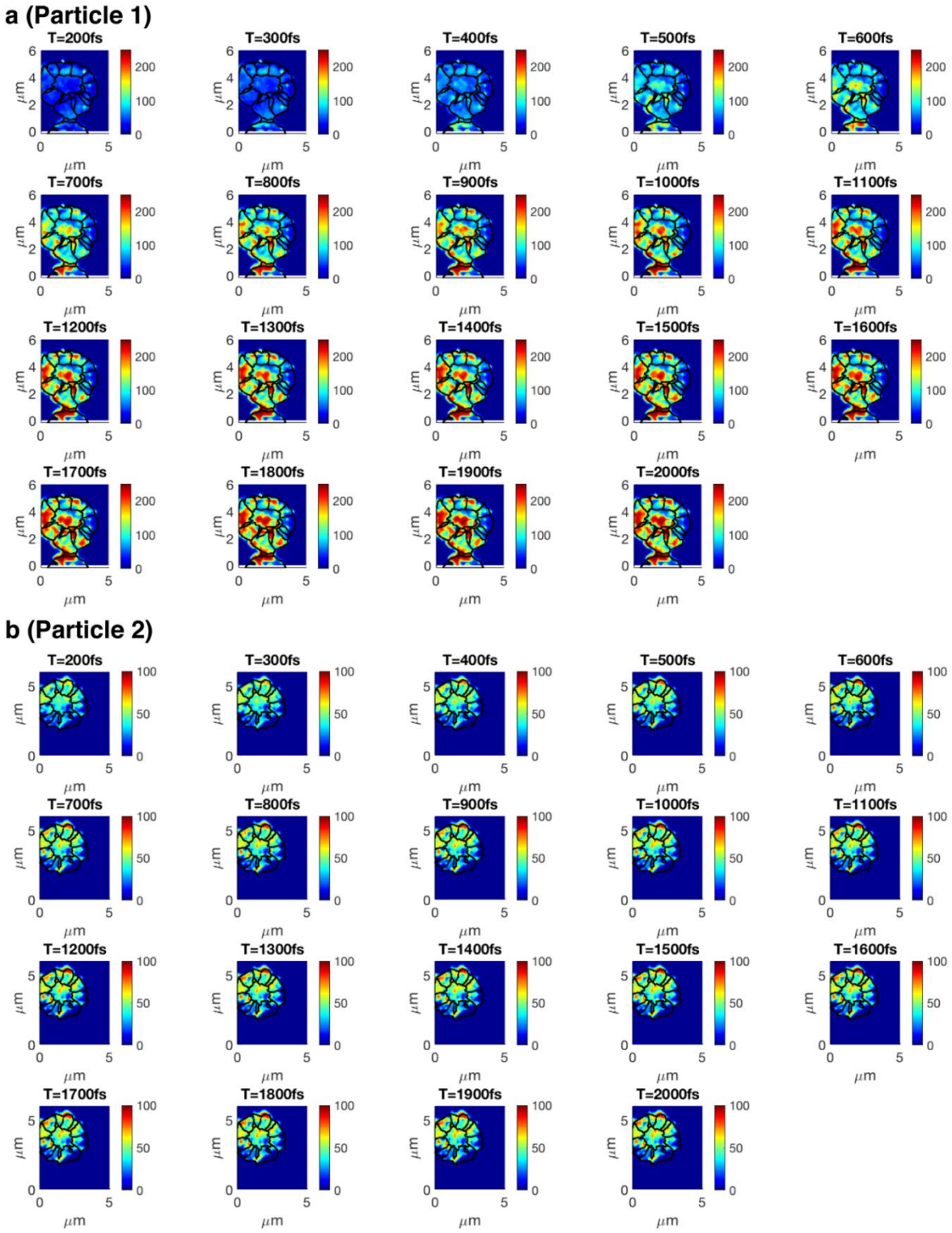

Figure_Apx A.7 τ_{ave} maps of (a) particle 1, (b) particle 2. Unit: fs.

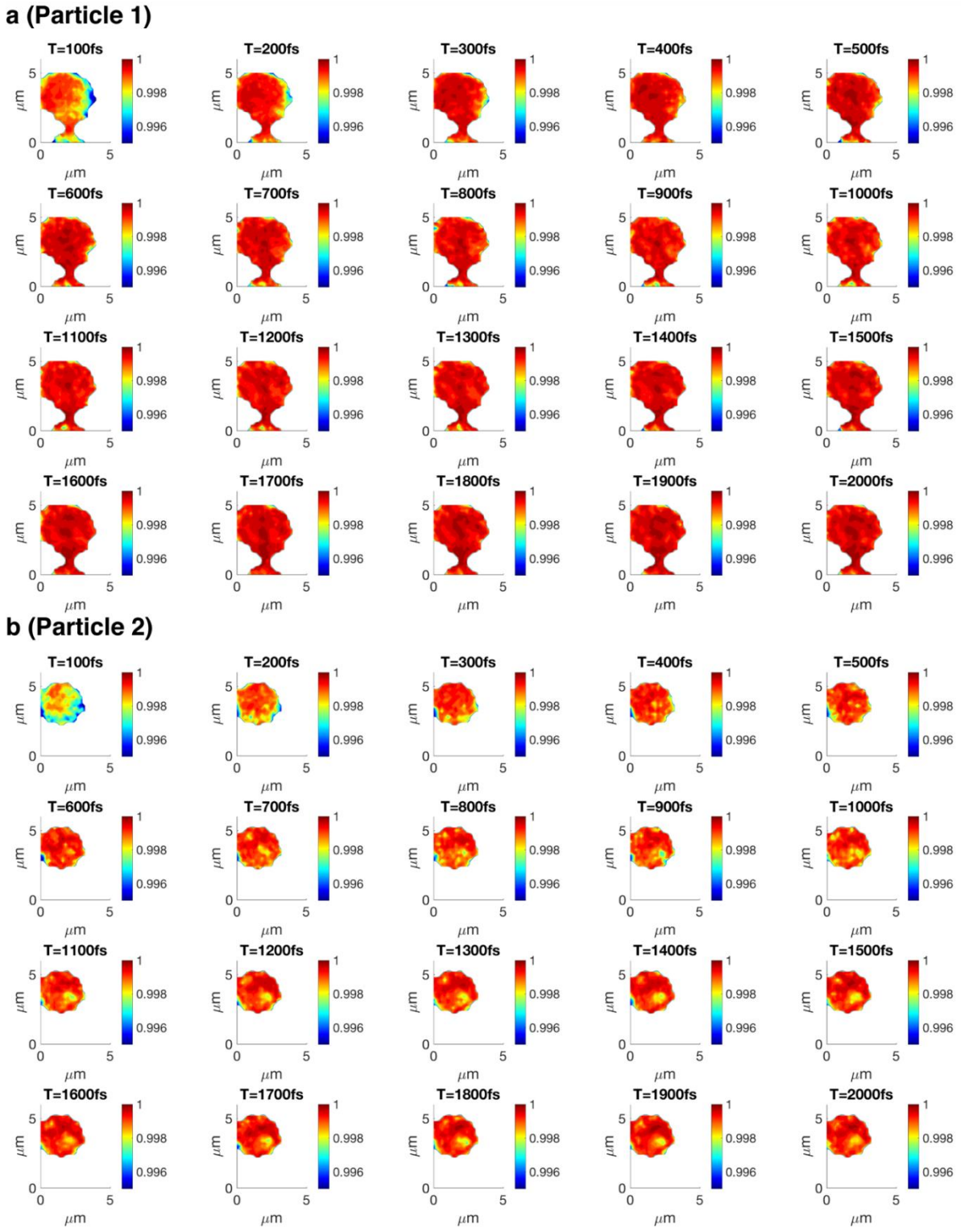

Figure_Apx A.8 R-square value maps of the band-filling model for (a) particle 1, (b) particle 2.

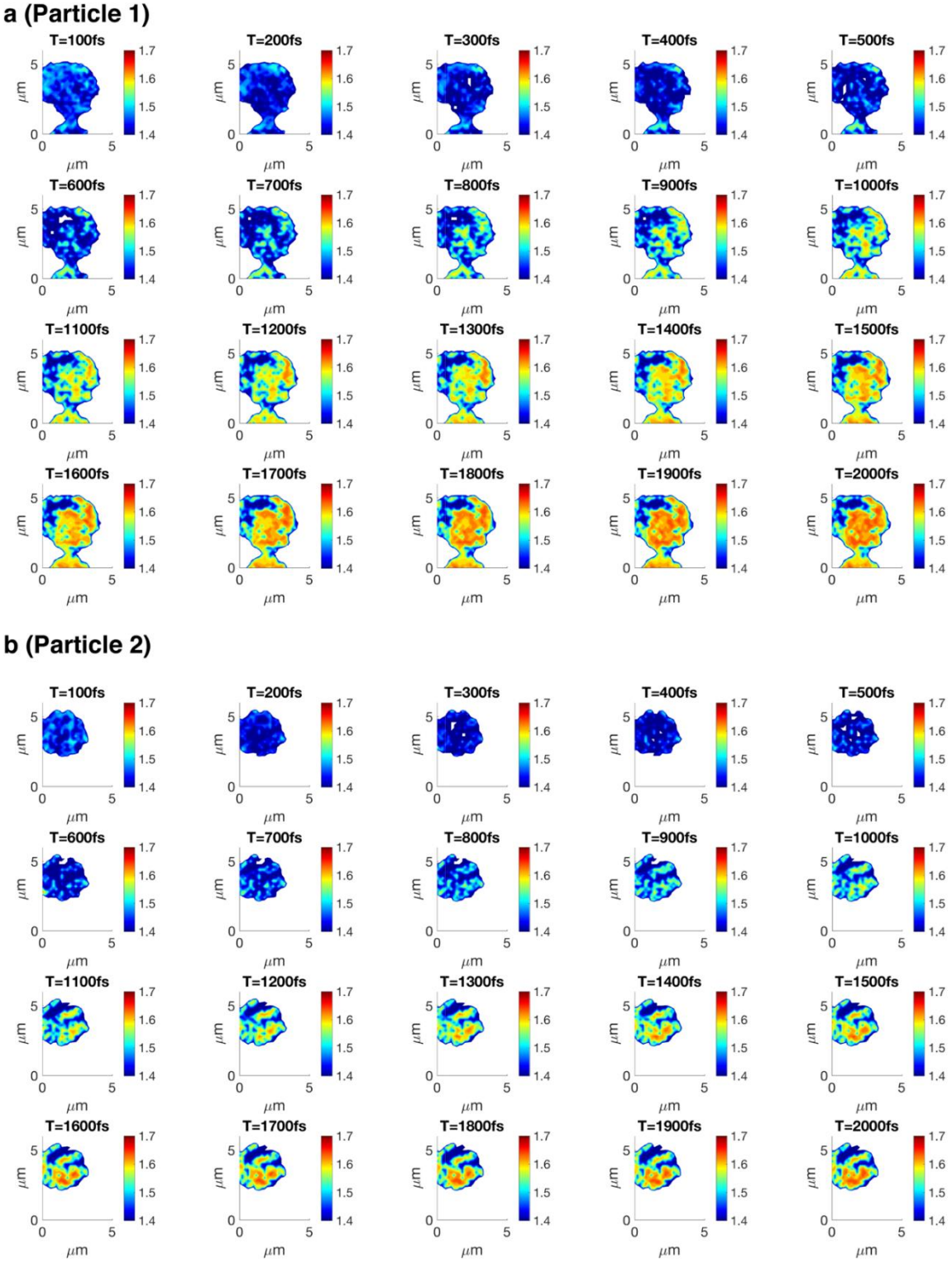

Figure_Apx A.9 Shifted bandgap maps extracted from the band-filling model of (a) particle 1, (b) particle 2. Unit: eV.

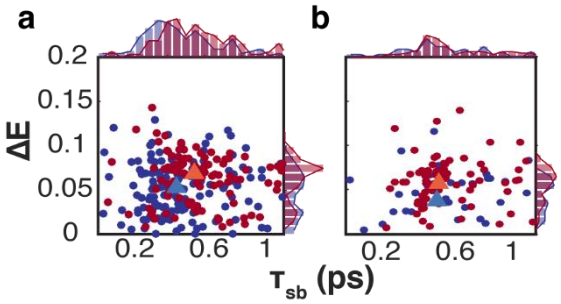

Figure_Apx A.10 Two-dimensional scatter plots of sub-bandgap state depth at 2.0 ps and sub-bandgap state population lifetime of (a) particle 1(integrated within 1.570 ± 0.015 eV), (b) particle 2 (integrated within 1.565 ± 0.015 eV). Triangles show the positions of median values.

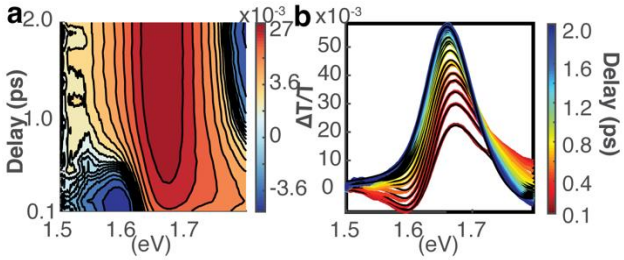

Figure_Apx A.11 (a) TA surface and (b) TA spectra with fits (black solid curves) at different pump-probe delays at the center position in sGI region.

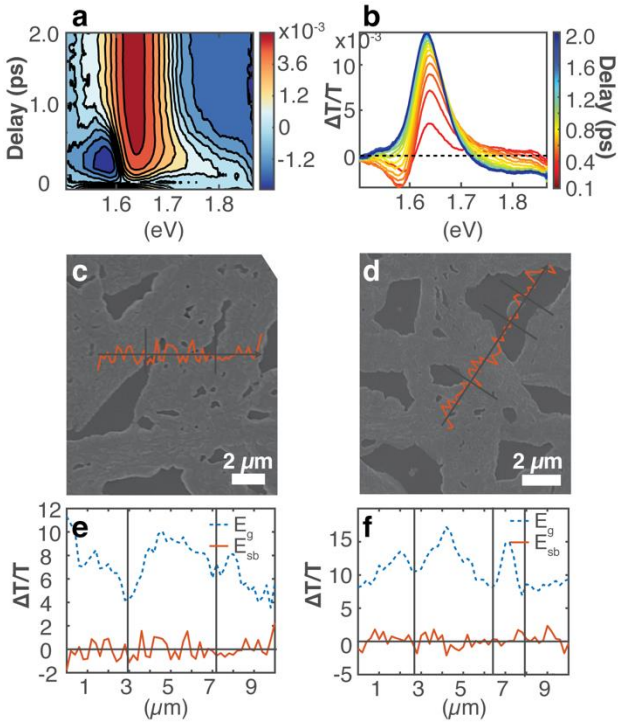

Figure_Apx A.12 Spatially averaged (a) TA surface (with arcsinh-scaled colormap to show small changes below the bandgap) and (b) TA spectra with different pump-probe delays. (c,d) SEM image of the 0%-HI $CH_3NH_3PbI_3$ film, overlaid with the line scanned (black arrows) and the sub-bandgap state intensity (orange curves). (e,f) TA signal intensity: blue dashed line: averaged at bandgap, 1.650 ± 0.015 eV, to show the local morphology of the film, orange line: sub-bandgap state intensity integrated at 1.570 ± 0.015 eV.

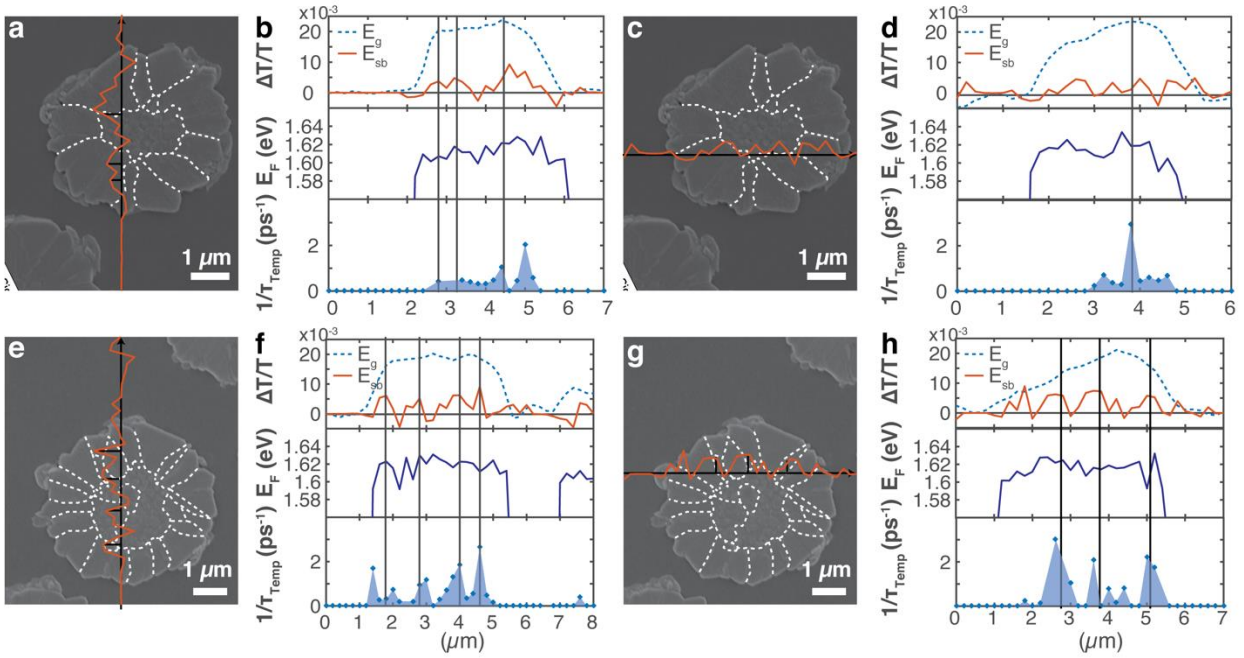

Figure_Apx A.13 (a,c,e,g) SEM images of the $CH_3NH_3PbI_3$ particles studied overlaid with the line scanned (black arrows) and the sub-bandgap state intensity (orange curves). The positions where the scanned line crosses GBs are marked with black short lines. (b,d,f,h) TA signal intensity: blue dashed line: averaged at bandgap, 1.650 ± 0.015 eV, to show the outline of the particle, orange line: sub-bandgap state intensity integrated at 1.570 ± 0.015 eV; Quasi-Fermi energy: dark blue curve; Temperature cooling rate: blue shaded curve.

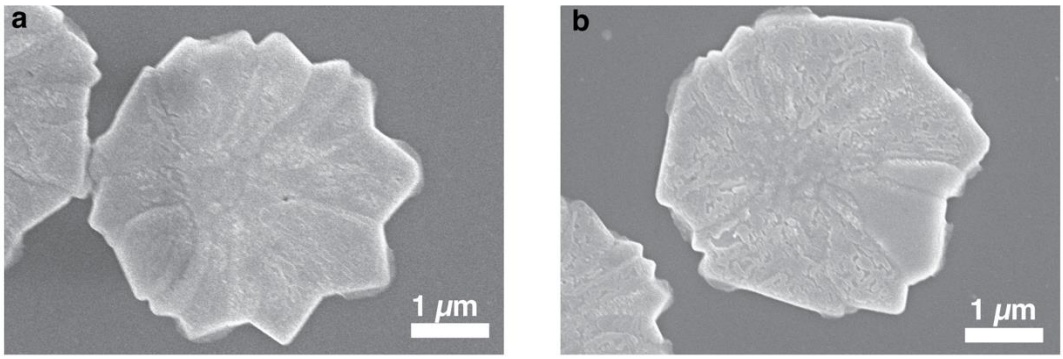

Figure_Apx A.14 SEM images of $CH_3NH_3PbI_3$ particles damaged in the scan in open air.

APPENDIX B Appendix to CHAPTER 3

B.1 Supplementary Figures

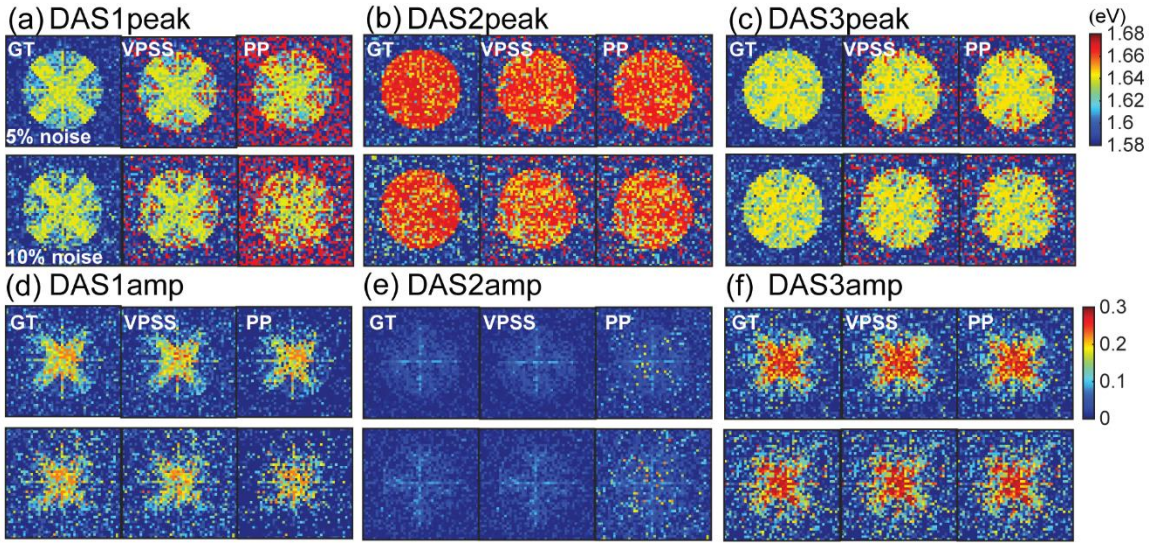

Figure_Apx B.1 Performance test of the VPSS method compared to the GT and PP method at different noise levels. Top: 5% Gaussian noise; bottom: 10% Gaussian noise. (a) Peak position of DAS1. (b) Peak position of DAS2. (c) Peak position of DAS3. (d) Amplitude of DAS1. (e) Amplitude of DAS2. (f) Amplitude of DAS3.

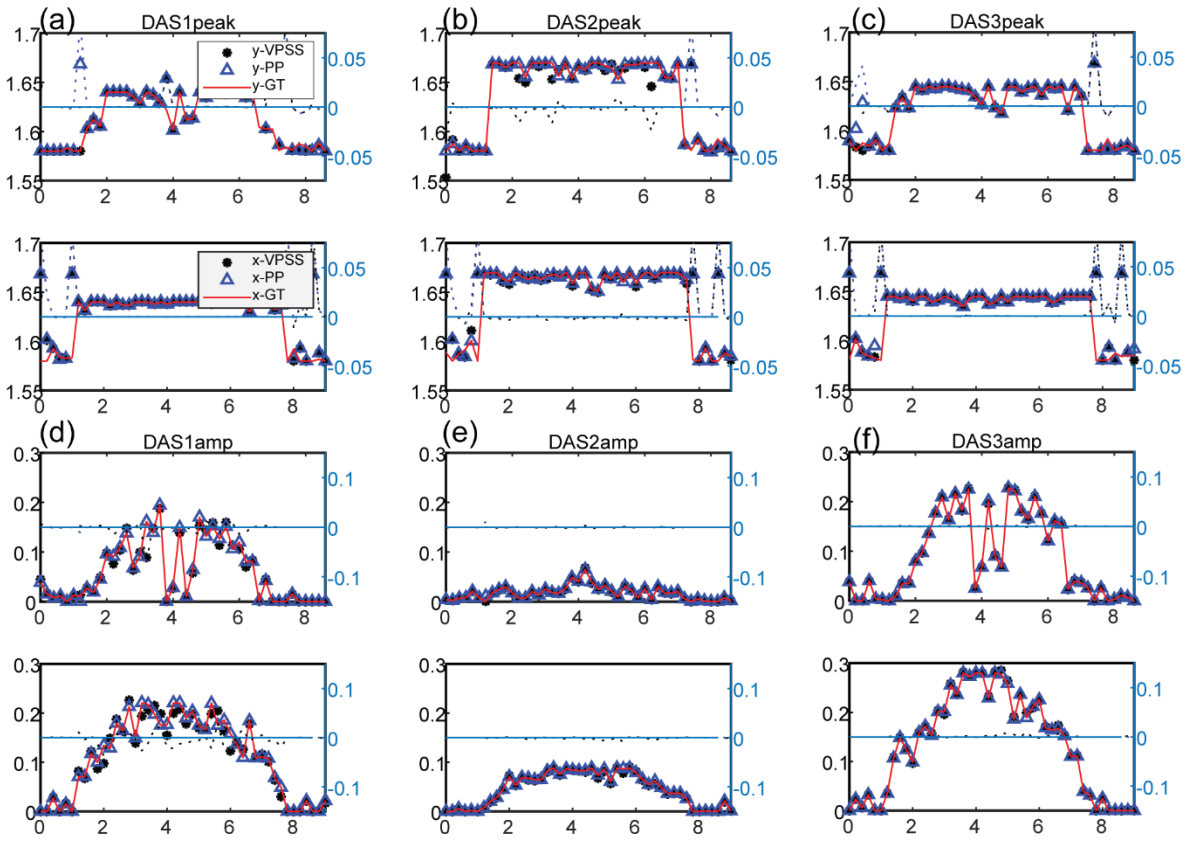

Figure_Apx B.2 Cuts along x and y axes across DAS amplitude and peak position maps calculated using VPSS (black star) and PP (blue triangle) compared to the GT (red line). The dashed curve plotted on the right axes show the difference between the fitting results and the GT. row:4.2 mm, column: 3.0 mm. (a) Peak position of DAS1. (b) Peak position of DAS2. (c) Peak position of DAS3. (d) Amplitude of DAS1. (e) Amplitude of DAS2. (f) Amplitude of DAS3.

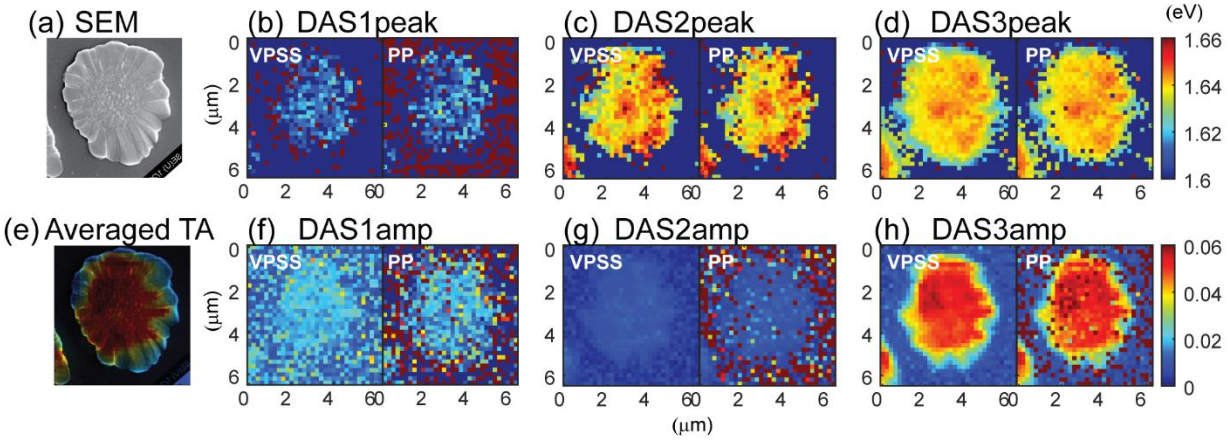

Figure_Apx B.3 Correlated SEM-TAM and DAS. (a) SEM. (b) Peak position of DAS1. (c) Peak position of DAS2. (d) Peak position of DAS3. (e) Spectrally averaged TAM map. (f) Amplitude of DAS1. (g) Amplitude of DAS2. (h) Amplitude of DAS3.

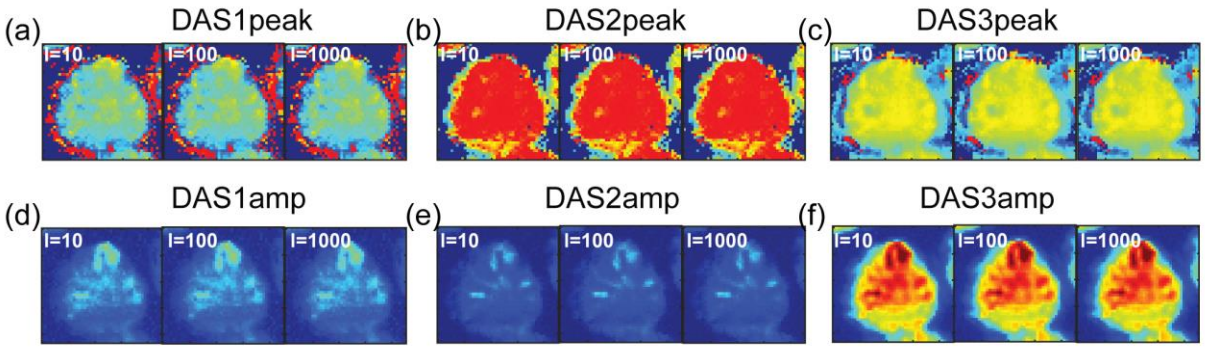

Figure_Apx B.4 DAS amplitude and peak position maps calculated using VPSS with different subsampling interval l = 10, 100 and 1000 (used in the main text). (a) The peak position of DAS1; (b) The peak position of DAS2; (c) The peak position of DAS3; (d) The amplitude of DAS1; (e) The amplitude of DAS2; (f) The amplitude of DAS3.

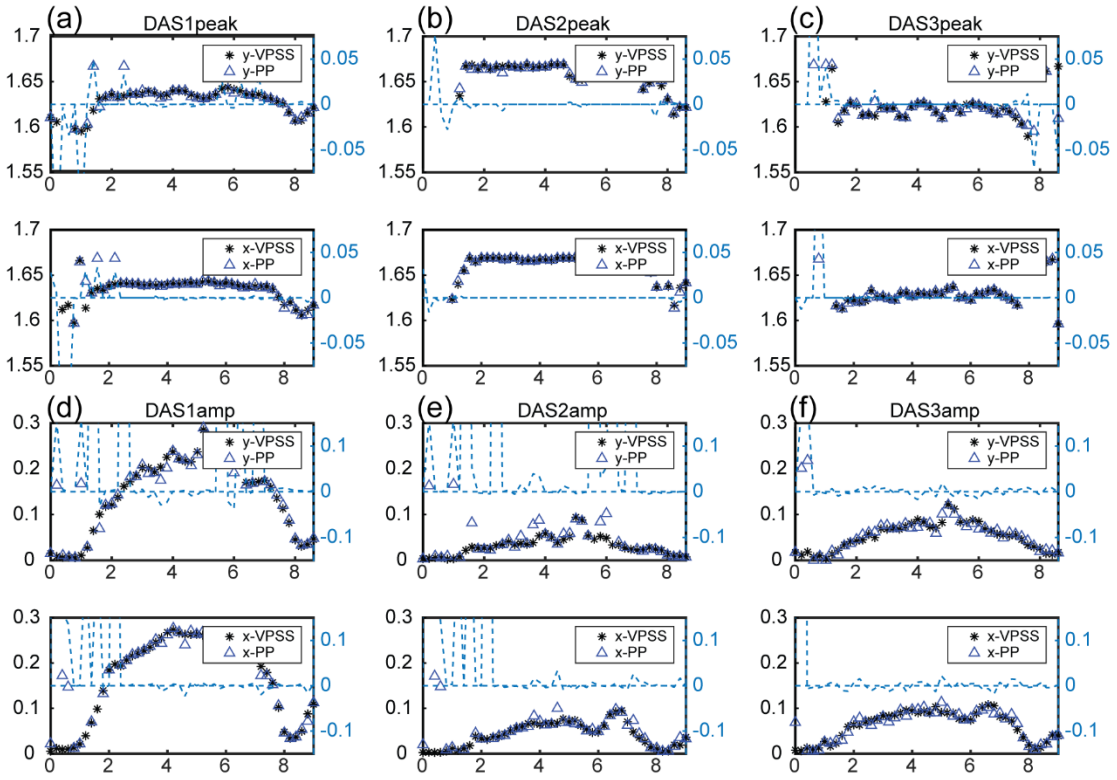

Figure_Apx B.5 Cuts along x and y axes across DAS amplitude and peak position maps calculated using VPSS (black star) and PP (blue triangle). The blue dashed curve plotted on the right axes show the difference between the results calculated using the two methods. row:4.2 mm, column: 3.0 mm. (a) The peak position of DAS1; (b) The peak position of DAS2; (c) The peak position of DAS3; (d) The amplitude of DAS1; (e) The amplitude DAS2; (f) The amplitude of DAS3.

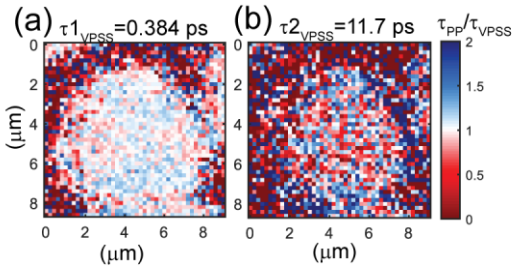

Figure_Apx B.6 Lifetime ratio between PP and VPSS. (a) DAS 1; (b) DAS 2.

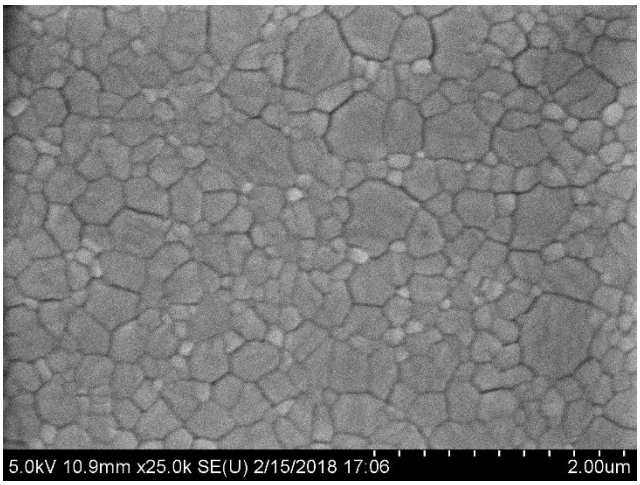

Figure_Apx B.7 SEM of the DMF-cast $CH_3NH_3PbI_3$ film. It shows the morphology in the region the measurement was taken but is not directly correlated like the SEM for perovskite islands.

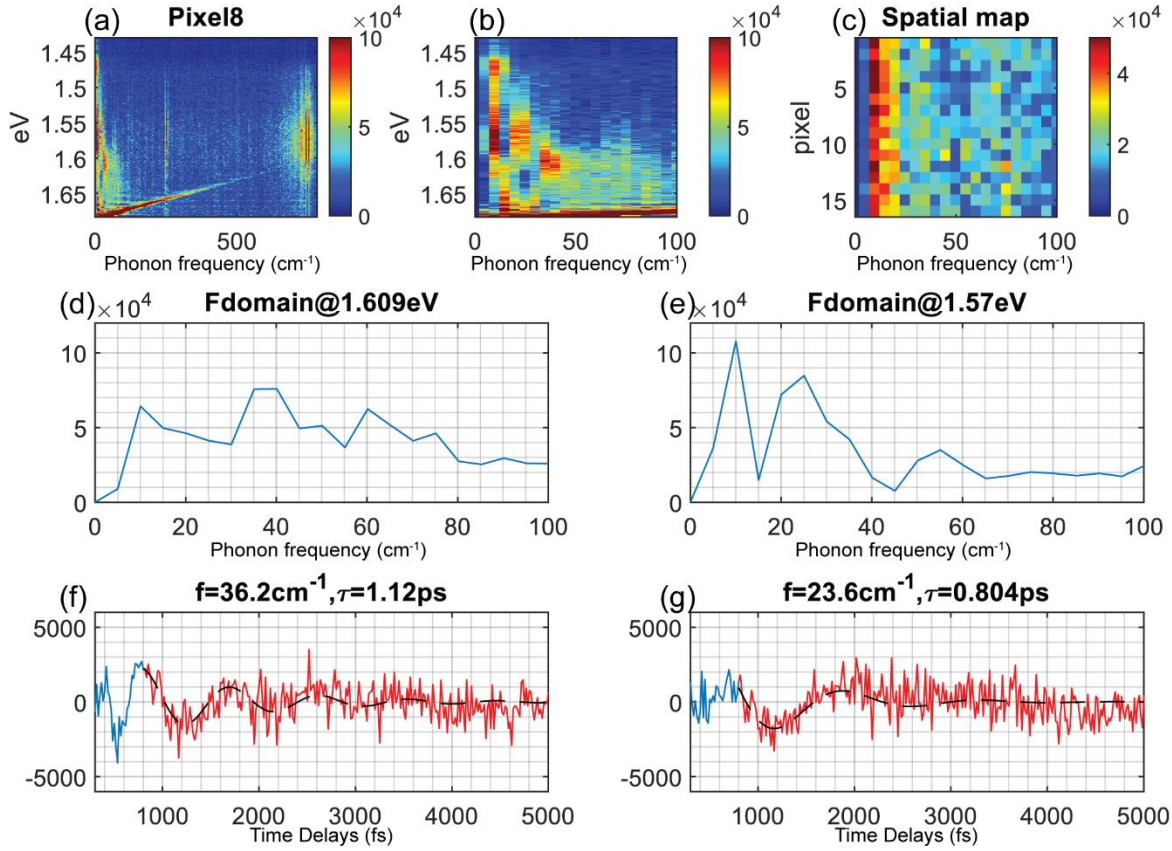

Figure_Apx B.8 PP fit in IVM. (a) Phonon oscillation map of DMF-casted $CH_3NH_3PbI_3$ films at pixel 8. X-axis: phonon mode, y-axis: probe energy. (b) The same phonon map with the low-frequency range enlarged. (c) A spatial map of the spectrally averaged phonon oscillation. X-axis: phonon mode, y-axis: different pixel on the film (16 pixels from a 4-by-4 raster scan, 1.25 mm resolution). (d) Phonon spectra at 1.609 eV. (e) Phonon spectra at 1.570 eV (f) Population Fitting residue at 1.609 eV. (g) Population Fitting residue at 1.570 eV. The red curve shows the region picked to perform the damped sinusoid fitting. The black dashed line shows the damped sinusoid fitting results.

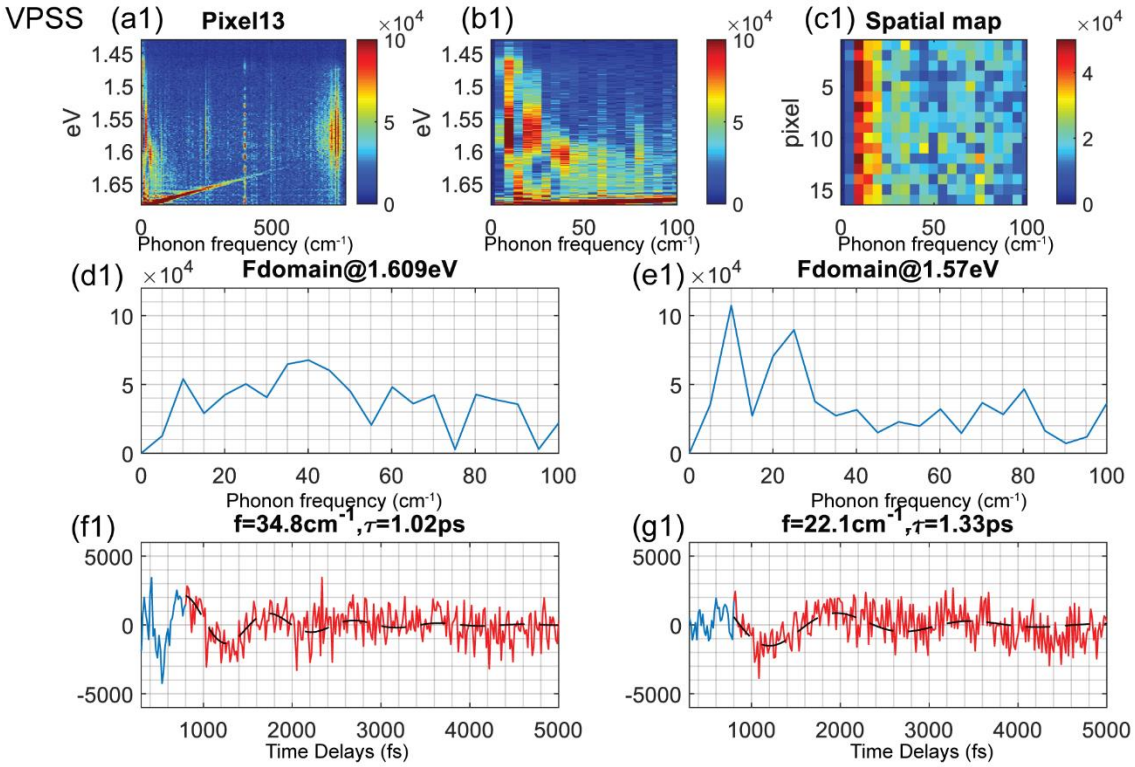
VPSS
(a1) Pixel13
(b1)
(c1) Spatial map
eV
pixel
Phonon frequency (cm-1)
(d1) Fdomain@1.609eV
(e1) Fdomain@1.57eV
(f1) f=34.8cm-1,τ=1.02ps
(g1) f=22.1cm-1,τ=1.33ps
Time Delays (fs)

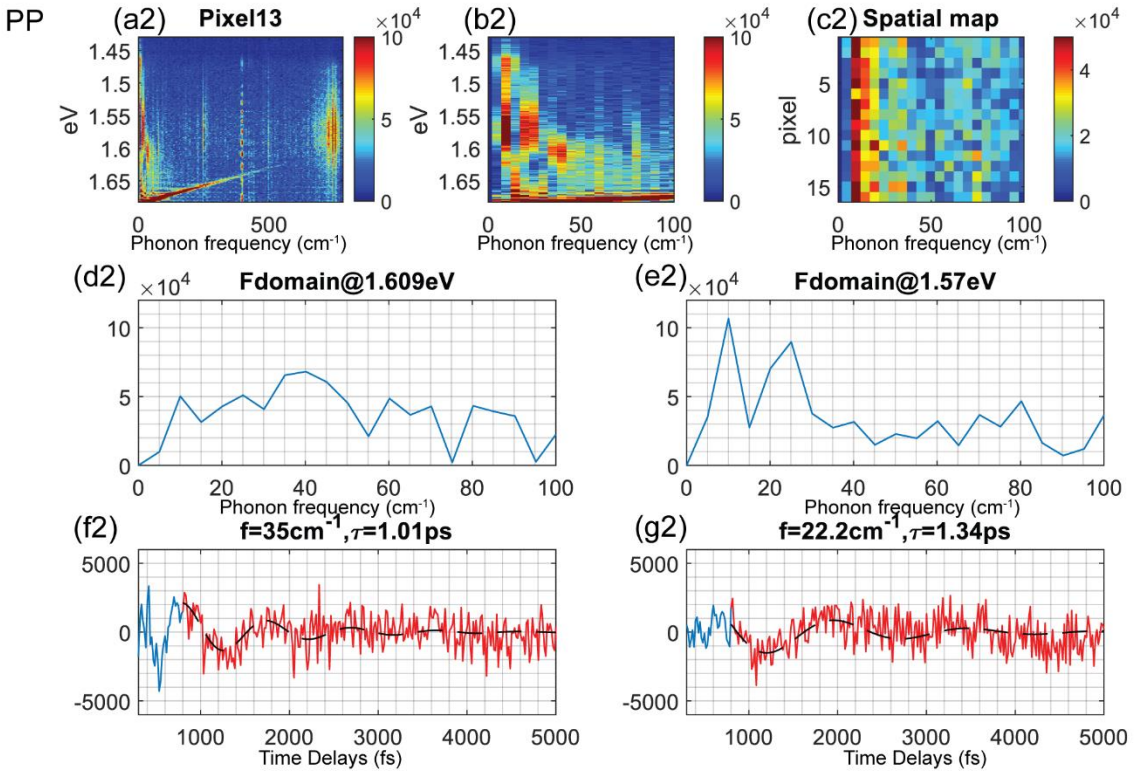
PP
(a2) Pixel13
(b2)
(c2) Spatial map
eV
pixel
Phonon frequency (cm-1)
(d2) Fdomain@1.609eV
(e2) Fdomain@1.57eV
(f2) f=35cm-1,τ=1.01ps
(g2) f=22.2cm-1,τ=1.34ps
Time Delays (fs)

Figure_Apx B.9 VPSS and PP fit in IVM. (a) Phonon oscillation map of DMF-casted $CH_3NH_3PbI_3$ films at pixel 13. X-axis: phonon mode, y-axis: probe energy. (b) The same phonon map with the low-frequency range enlarged. (c) A spatial map of the spectrally averaged phonon oscillation. X-axis: phonon mode, y-axis: different pixel on the film (16 pixels from a 4-by-4 raster scan, 1.25 mm resolution). (d) Phonon spectra at 1.609 eV. (e) Phonon spectra at 1.570 eV (f) Population Fitting residue at 1.609 eV. (g) Population Fitting residue at 1.609 eV. The red curve shows the region picked to do the damped sinusoid fitting. The black dashed line shows the damped sinusoid fitting results.

APPENDIX C Appendix to CHAPTER 4

C.1 Methods

All chemicals and regents were purchased from Sigma-Aldrich and used as received unless noted otherwise.

C.1.1 Growth of $(BA)_2(EA_xMA_{1-x})_2Pb_3I_{10}$ Single Crystals and ^1H NMR Measurements

The crystals were grown from concentrated hydroiodic acid using previously reported off-stoichiometry protocol.[17, 18] Specifically, to grow $(BA)_2(EA)_2Pb_3I_{10}$ single crystals, powders of PbI_2 (1380 mg), EAI (346 mg), and BAI (175 mg) were dissolved in 4.5 mL of HI solution (57 wt % in H_2O) and 0.5 mL of H_3PO_2 in a vial. Note that the solution was heated to 120 °C on a hot plate to completely dissolve all the solids. The solution was kept on a hot plate until ~1/3 of the solution had evaporated. Red rectangular plate-like crystals precipitated during cooling to room temperature. To grow $(BA)_2(MA)_2Pb_3I_{10}$ single crystals, powders of PbI_2 (1380 mg), MAI (318 mg), and BAI (175 mg) were dissolved in 4.5 mL of HI solution (57 wt % in H_2O) and 0.5 mL of H_3PO_2 in a vial. The solution was heated to 120 °C on a hot plate to completely dissolve all the solids. The solution sited undisturbed at room temperature for several hours to yield red-black flake-like single crystals. Similar, the precursor solutions for $(BA)_2(EA)_2Pb_3I_{10}$ and $(BA)_2(MA)_2Pb_3I_{10}$ were mixed at volumetric ratios of 1:2, 1:1, and 2:1 to grow mixed cation alloys. ^1H-NMR spectra were measured on the dissolved crystals with Bruker Avance III 600 MHz system with BBI probe.

C.1.2 Exfoliated Crystal Preparation

Samples for the TAM measurements were prepared by mechanical exfoliation. Plate-like single crystals were picked and were put on a clear scotch one-sided tape, on top of which another clean area of the tape was folded. Parts of the crystals were detached from the crystals for further exfoliation, exposing fresh cleaved layers, and the rest of the crystals remained on the tape. This process was repeated for several times to obtain optically thin 2D perovskite sheets (see Figure S11 for an optical image). The exfoliated crystals were then transferred on to a piece of coverslip by pressing the tape on top of the coverslip. After that, a protective layer of poly (methyl methacrylate) (Mw ~ 120000 by GPC, PMMA) was deposited on the coverslip by spin-coating a solution containing 4 wt% PMMA in chlorobenzene at 3000 rpm for 30 s. The samples were sealed by another coverslip using parafilm as a spacer on a hot plate (100 °C) in the ambient air.

C.1.3 Single Crystal Structure Determination

Single-crystal X-ray diffraction experiments were performed using a STOE IPDS II or IPDS 2T diffractometer with Mo Kα radiation (λ = 0.71073 Å) and operating at 50 kV and 40 mA. Integration and numerical absorption corrections were performed using the X-AREA, X-RED, and X-SHAPE programs. The structures were solved by charge flipping and refined by full-matrix least-squares on F^2 using the Jana 2006 package.

C.1.4 Photoluminescence Spectrum

Steady-state PL spectra of single crystals were collected using HORIBA LabRAM HR Evolution confocal Raman microscope with 532 nm laser excitation. The crystals were

exfoliated by scotch tape once to expose fresh surface, and same excitation power density was used for all the measurements.

C.1.5 DFT Calculations

The calculations were performed within the DFT[19, 20] as implemented in SIESTA package[21] with a basis set of finite-range of numerical atomic orbitals. We used the Generalized Gradient Approximation (GGA) with PBE functional to describe the exchange-correlation term, and norm-conserving Troullier-Martins pseudopotentials were used for each atomic species to account for the core electrons.[22] $1s^1$, $2s^2 2p^2$, $2s^2 2p^3$, $5s^2 5p^5$ and $5d^{10} 6s^2 6p^2$ were used as valence electrons for H, C, N, I, and Pb respectively. Polarized Double-Zeta (DZP) basis set with an energy shift of 50 meV and a Mesh cutoff 200 Rydberg were used for the calculations. The Brillouin zone was sampled with 2×2×6 and 4×4×1 Monckhorst-Pack grids for the primitive cells and slab systems, respectively. The electronic and dielectric properties were calculated with the experimental lattice parameters, and atomic coordinates were transformed to their primitive cells whenever applicable. SOC was taken into account in the calculation of the electronic properties, although it was not considered in the high-frequency dielectric constant computations. For the high-frequency dielectric constant profiles, the (010) surface of $(BA)_2(MA)_2Pb_3I_{10}$ was considered. For technical reasons, the surface was rotated such that the stacking corresponds to the z-axis. Slabs based on the respective systems were constructed and an electric field of 0.01 eV/Å was applied along the [001] direction with the relaxation of the sole electron density as described elsewhere.[23, 24]

Additional TB-mBJ calculations were done with the ABINIT code.[25] The relativistic, norm conserving, separable, dual-space Gaussian-type pseudopotentials of Hartwigsen, Goedecker, and Hutter were used for all atoms.[26] More specifically, we considered $6s^1$, $5s^25p^2$ and $6s^26p^2$ as valence electrons for Cs I, and Pb, respectively. TB-mBJ in ABINIT was invoked from the library of exchange-correlation functionals Libxc.[27] We used optimized pseudopotential TB-mBJ (ppTB-mBJ) parameters $\alpha = 0.65$ and $\beta = 1.023$ for hybrid perovskites within pseudopotential implementation of DFT as detailed elsewhere.[28] All the calculations take SOC into account.

C.1.6 Transient Absorption Microscopy

The block diagram of the home-built TAM is shown in Figure_Apx C.13 and our previous paper.[29] Briefly, the fundamental 1030-nm beam was generated from an Yb:KGW amplifier system (Light Conversion, PHAROS) operating at 200 kHz with a pulse duration of 190 fs. The beam was split into pump and probe arms. The pump was focused into a BBO crystal to produce second harmonic generation light centered at 515 nm. The pump was then delayed relative to the probe with a high resolution motorized linear stage (Aerotech). White-light probe (1.74–2.28 eV) was generated by focusing the fundamental beam into a YAG crystal and then compressed with a pair of chirped mirrors (LayerTec). Both beams were recombined and focused collinearly onto the sample with a 74× reflective objective (NA 0.65, Beck). The beam spot size was ~0.6 μm. The sample was taped on a piezo-driven XYZ stage with a resolution of 0.2 μm (PiezosystemJena, Newport XPS). The signal was collected using a 100× refractive objective (NA 0.70, Leica), spatially filtered through a 300-μm pinhole, and then spectrally dispersed in a spectrometer (Horiba, IHR-320). The TA signal was detected using a high-speed CCD camera (Andor, Ixon Ultra 897). Linear absorption of probe and PL maps were measured within the

same setup. The results shown in the main text are the average of about 10-15 exfoliated flakes on each sample at an excitation power of 450 nW. The decay associated spectra (DAS) was obtained by globally fit the entire TA dataset. Multiple-exponential fit was performed at each wavelength to extract the lifetimes of the DASs. The fitting algorithm used was the "fminuit" package in MATLAB. A "seek" step was added to avoid convergence at the local minimum.

C.2 Supplementary Discussion

Here we discuss our understanding of the origin of the different spatial localization of holes and electrons in $BA_2MA_2Pb_3I_{10}$ and $BA_2EA_2Pb_3I_{10}$.

C.2.1 Localization of $(BA)_2(MA)_2Pb_3I_{10}$

In $(BA)_2(MA)_2Pb_3I_{10}$, the inner layer has the shortest Pb-I bond lengths and the smallest octahedral tilt angles (see Figure_Apx C.1 and Table_Apx C.1).[30] In addition, the octahedra are almost perfect with identical equatorial and axial Pb-I bond lengths (3.15Å). This leads to increased anti-bonding character of Pb(6s)-I(5p) and thus to the most destabilized VBM, which undergoes clear localization on the inner layer. The situation is more involved for CBM due to periodicity, i.e. averaged in-plane Pb-Pb distances are equal. The slight anti-bonding character with halide orbitals leads most likely to localization on the other planes, namely the outer layers where it is expected to be slightly reduced.

C.2.2 Delocalization of $(BA)_2(EA)_2Pb_3I_{10}$

With $(BA)_2(EA)_2Pb_3I_{10}$, in-plane structural features are more homogeneous on the outer-layers than on the inner-layers (small β in-plane octahedral tilt angles and Pb-I bond length

~3.19Å) but the reverse occurs for out-of-plane structural features. For instance, δ (out-of-plane octahedral tilt) is smaller and β larger in the inner layer as compared to the outer ones. This leads to a compensation between the various interactions underlying hybridization and almost full delocalization over all three layers. The slightly more localized nature of CBM might stem from the more uniform distribution of in-plane Pb-Pb distances in the outer-layers (6.33 - 6.35 Å) as compared to the inner layer (6.22 - 6.46 Å) leading to a bonding character between in-plane Pb(p) orbitals slightly increased in the outer-layers (most stabilized CB).

C.3 Supplementary Tables

Table_Apx C.1 Calculated octahedral tilt angles (β, δ) for $(BA)_2(EA)_2Pb_3I_{10}$ and $(BA)_2(MA)_2Pb_3I_{10}$.

		β (deg)	**δ (deg)**
$(BA)_2(EA)_2Pb_3I_{10}$	Outer	0.7	6.1
	Inner	11.7	4.6
$(BA)_2(MA)_2Pb_3I_{10}$	Outer	0	7.4
	Inner	0	5.3

Table_Apx C.2 Crystal and structural refinement data of $(BA)_2(EA)_2Pb_3I_{10}$ in comparison with $(BA)_2(MA)_2Pb_3I_{10}$.[18]

	$(BA)_2(EA)_2Pb_3I_{10}$	$(BA)_2(MA)_2Pb_3I_{10}$
Crystal system	Orthorhombic	Orthorhombic
Space group	*Cmc*2_1	*C*2*cb*
Temperature	298.01 K	298.01 K
Unit cell dimensions	*a* = 52.0158(16) Å	*a* = 8.9275(6) Å
	b = 8.9727(3) Å	*b* = 51.959(4) Å
	c = 8.9745(3) Å	*c* = 8.8777(6) Å
	α=*β*=*γ*=90°	*α*=*β*=*γ*=90°
Volume	4188.6(2) $Å^3$	4118.0(5) $Å^3$

Z	4	4
Density (calc)	3.379 g·cm^{-3}	3.392 g·cm^{-3}
Independent reflections	6246 [R_{int} =0.0564]	3633 [R_{int} = 0.0722]
Completeness to 25°	100%	
Data/restraints/parameters	6246 /15/95	3633/3/84
Goodness-of-fit	1.077	1.103
Final R indices [I>=2σ (I)]	R_{obs} = 0.0444, wR_{obs} = 0.1257	R_{obs} = 0.0781, wR_{obs} = 0.1748
R indices [all data]	R_{all} = 0.0599, wR_{all} = 0.1425	R_{all} = 0.1234, wR_{all} = 0.1997
Largest diff peak and hole	2.088 and -1.696 e· Å^{-3}	3.289 and -1.719 e· Å^{-3}

Table_Apx C.3 Comparison of structural parameters and optical bandgap (i.e. PL emission) for various 2D lead iodide perovskites with n = 3 at 293 K.[18, 31-34] BA is *n*-butylammonium ($C_4H_9NH_3^+$), PA is *n*-pentylammonium ($C_5H_{11}NH_3^+$), HA is *n*-hexylammonium ($C_6H_{13}NH_3^+$), GA is guanidinium ($[C(NH_2)_3]^+$), ODA is Octane-1,8-diammonium [$(NH_3C_8H_{16}NH_3)^{2+}$], NDA is Nonane-1,9-diamino [$(NH_3C_9H_{18}NH_3)^{2+}$], 3AMP is protonated 3-(aminomethyl)piperidinium, 4AMP is protonated 4-(aminomethyl)piperidinium.

	PL emission (eV)	**Ave. Pb-I bond length (Å)**	**Ave. cage volume (Å^3)**	**Ave. Pb-I-Pb bond angle (°)**	**Spacer distances (Å)**
$(BA)_2(EA)_2Pb_3I_{10}$	2.12	3.213	267.21	166.1	13.51
$(BA)_2(MA)_2Pb_3I_{10}$ (ref[18])	2.00	3.165	255.12	169.4	13.83
$(PA)_2(MA)_2Pb_3I_{10}$ (ref[34])	2.00	3.172	253.76	167.9	14.02

$(HA)_2(MA)_2Pb_3I_{10}$ (ref[34])	2.00	3.171	254.51	168.4	15.22
(GA,MA)($MA)_2Pb_3I_{10}$ (ref[35])	1.96	3.163	252.08	169.9	9.22
(ODA)$(MA)_2Pb_3I_{10}$ (ref[33])	2.00	3.168	249.88	167.7	12.52
(NDA)$(MA)_2Pb_3I_{10}$ (ref[33])	2.00	3.171	252.31	162.9	13.22
(3AMP)$(MA)_2Pb_3I_{10}$ (ref[32])	1.90	3.169	251.23	167.7	10.24
(4AMP)$(MA)_2Pb_3I_{10}$ (ref[32])	1.99	3.181	251.42	162.9	10.25

Table_Apx C.4 Crystal and structural refinement data of $(BA)_2(EA_xMA_{1-x})_2Pb_3I_{10}$ alloys

	$(BA)_2(EA)_{0.35}(MA)_{0.65}Pb_3I_{10}$	$(BA)_2(EA)_{0.55}(MA)_{0.45}Pb_3I_{10}$	$(BA)_2(EA)_{0.73}(MA)_{0.27}Pb_3I_{10}$
Crystal system	Monoclinic	Monoclinic	Monoclinic
Space group	*Cc*	*Cc*	*Cc*
Temperature	293 K	293(2) K	293 K
Unit cell dimensions	*a* = 52.297(10) Å *b* = 8.9569(18) Å *c* = 8.9339(18) Å *β* = 90.02(3) °	*a* = 52.424(10) Å *b* = 8.9841(18) Å *c* = 8.9429(18) Å *β* = 90.15(3) °	*a* = 52.169(6) Å *b* = 8.9731(6) Å *c* = 8.9417(11) Å *β* = 90.073(9) °
Volume	4184.8(14) $Å^3$	4211.9(15) $Å^3$	4185.8(7) $Å^3$

Z	4	4	4
Density (calc)	3.338 g·cm^{-3}	3.316g·cm^{-3}	3.3817 g·cm^{-3}
Independent reflections	7134 [R_{int} = 0.0822]	10593 [R_{int} = 0.0609]	7176 [R_{int} = 0.1024]
Completeness to 25°	98%	99.9%	98%
Data/restraints/parameters	7134/16/175	10593/22/174	7176/20/172
Goodness-of-fit	5.09	1.005	4.59
Final R indices [I>=2σ (I)]	R_{obs} = 0.0923, wR_{obs} = 0.1302	R_{obs} = 0.0870, wR_{obs} = 0.2259	R_{obs} 0.0778, wR_{obs} = 0.0870
R indices [all data]	R_{all} = 0.1646, wR_{all} = 0.1316	R_{all} = 0.1577, wR_{all} = 0.3134	R_{all} = 0.0851, wR_{all} = 0.0872
Largest diff peak and hole	4.93 and -3.87 e· Å^{-3}	7.837 and -2.464 e· Å^{-3}	2.20 and -4.49 e· Å^{-3}

Table_Apx C.5 Comparison of optical bandgap (i.e. PL emission) and structural parameters for the perovskite phases of 3D lead iodide perovskites $APbI_3$ (A^+ = Cs^+, MA^+, or FA^+).[36-38]

	T (K)	**Space group**	**PL emission (eV)**	**Average Pb-I bond length (Å)**	**Average cage volume (Å^3)**	**Average Pb-I-Pb bond angle (°)**	**Bond length quadratic elongation**	**Bond angle variance**
$FAPbI_3$ (ref[37])	298	Trigonal *P*3m1	1.52	3.174	256.30	179.8	1.00001	8×10^{-3}

$MAPbI_3$ (ref[38])	298	Tetragonal *I*422	1.60	3.174	250.59	169.1	1.00000	2×10^{-3}
$CsPbI_3$ (ref[36])	300	Orthorhombic *P*bnm	1.75	3.176	238.46	155.5	1.00001	1.1

Table_Apx C.6 Comparison of the effective masses between $(BA)_2(MA)_2Pb_3I_{10}$ and $(BA)_2(EA)_2Pb_3I_{10}$ computed at different levels of theory, namely PBE+SOC and ppTB-mBJ+SOC. m_e, m_h and m_r stand for the electron, hole and reduced effective masses, respectively. The effective masses are in unit of the electron mass at rest (m_0) and $m_r = \frac{m_h.m_e}{m_h+m_e}$

	Direction	**PBE+SOC**			**ppTB-mBJ+SOC**		
		m_h	m_e	m_r	m_h	m_e	m_r
$(BA)_2(MA)_2Pb_3I_{10}$	[100]	-0.11	0.11	0.055	-0.47	0.32	0.19
	[011]	-0.11	0.13	0.06	-0.48	0.34	0.20
$(BA)_2(EA)_2Pb_3I_{10}$	[001]	-0.30	0.22	0.13	-1.66	0.42	0.34
	[011]	-0.34	0.29	0.16	-3.37	0.86	0.69

C.4 Supplementary Figures

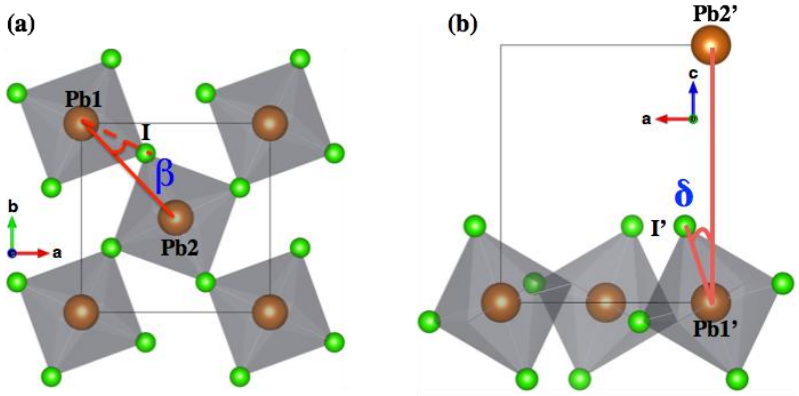

Figure_Apx C.1 Octahedral tilt angles (β, δ) used to rationalize effect of octahedral tilting on the optoelectronic properties of layered halide perovskites.[30] (a) β is the angle between the projection of Pb1−I in the plane perpendicular to the stacking axis and Pb1−Pb2. (b) δ is the angle between Pb1′−I′ and Pb1′−Pb2′. Note that Pb2′ is the periodic image of Pb1′ along the stacking direction.

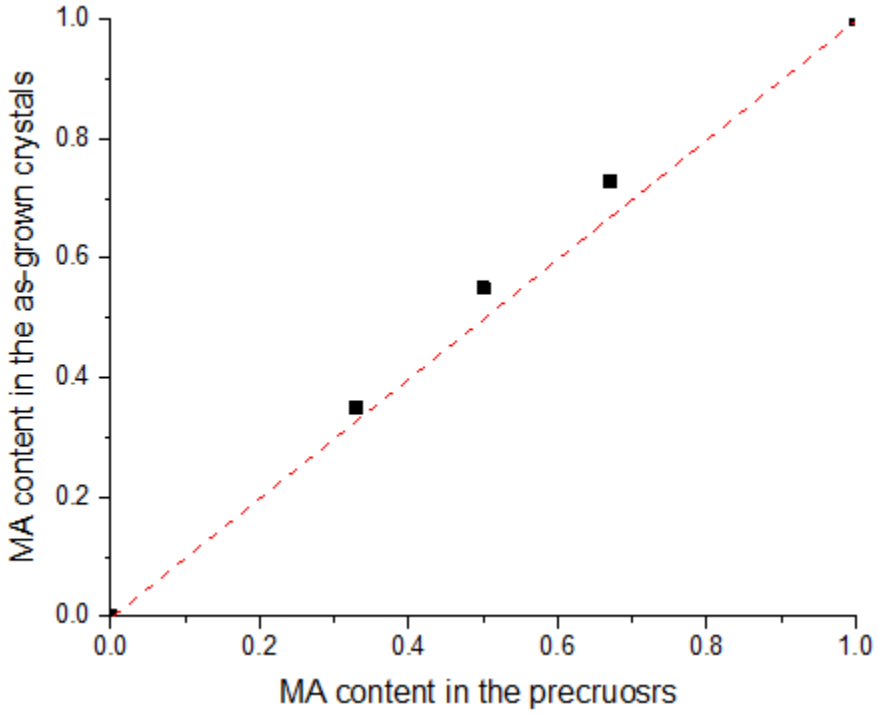

Figure_Apx C.2 The determined MA content in the alloys versus the MA content in the precursor solutions

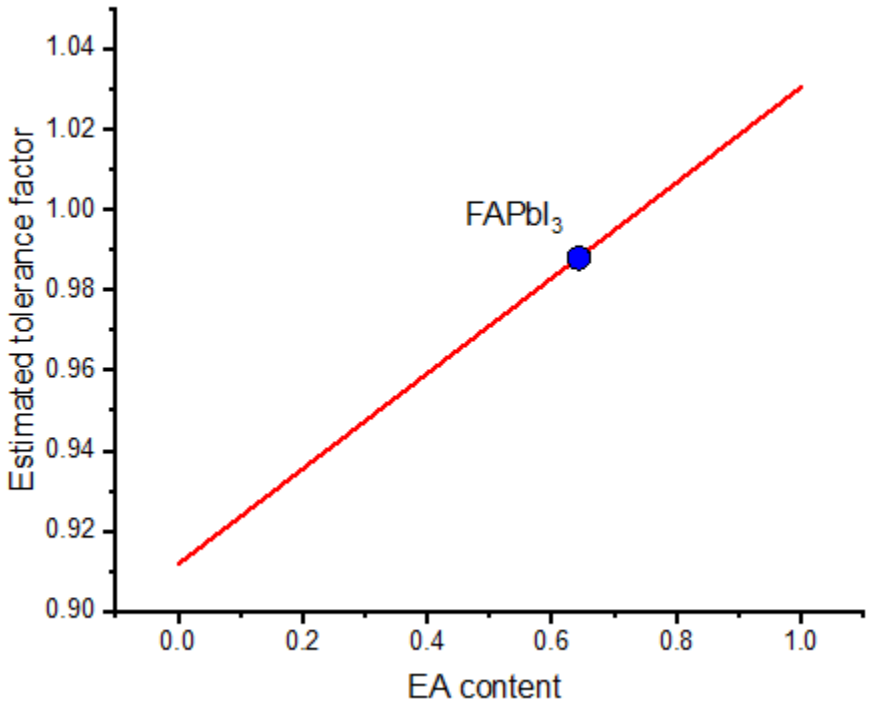

Figure_Apx C.3 Calculated tolerance factor as a function of EA content of the alloys

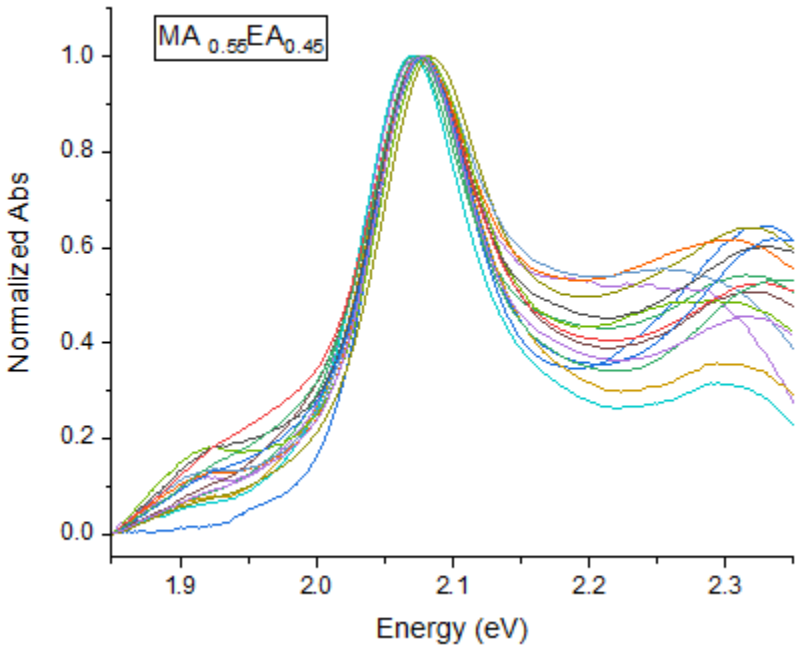

Figure_Apx C.4 Absorption spectra of 15 randomly selected exfoliated crystal of the $MA_{0.55}EA_{0.45}$ structure

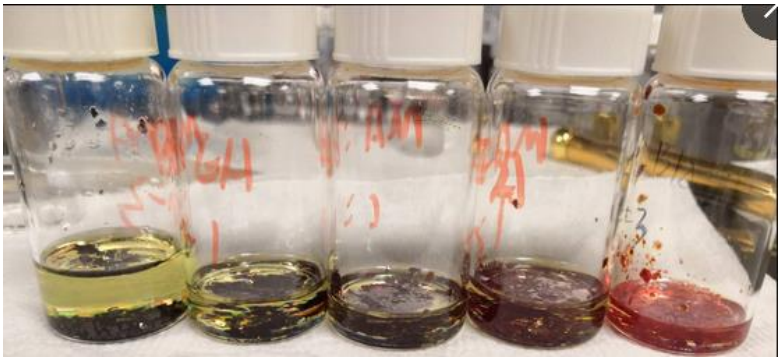

Figure_Apx C.5 Photographs of the set of $(BA)_2(EA_xMA_{1-x})_2Pb_3I_{10}$ (x = 0-1). From left to right, the x value increases from 0 to 1.

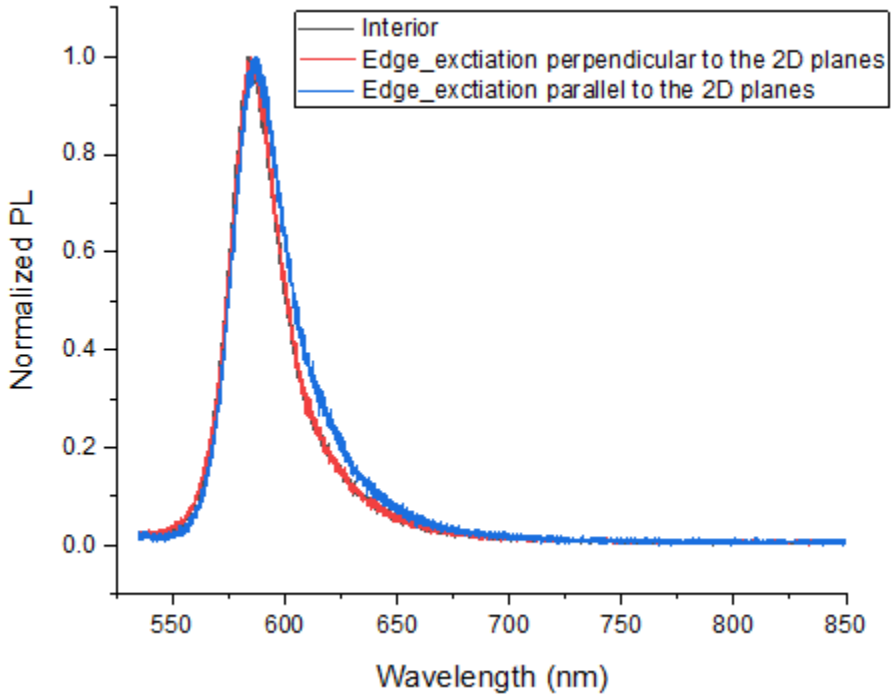

Figure_Apx C.6 PL spectra collected in the interior and edge of $(BA)_2(EA)_2Pb_3I_{10}$ crystal.

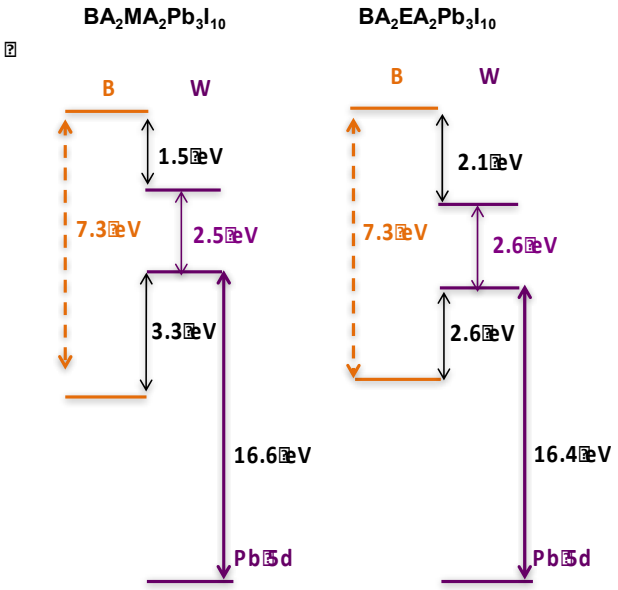

Figure_Apx C.7 Band alignments of $(BA)_2(MA)_2Pb_3I_{10}$ and $(BA)_2(EA)_2Pb_3I_{10}$ using the composite approach described in Ref [39].

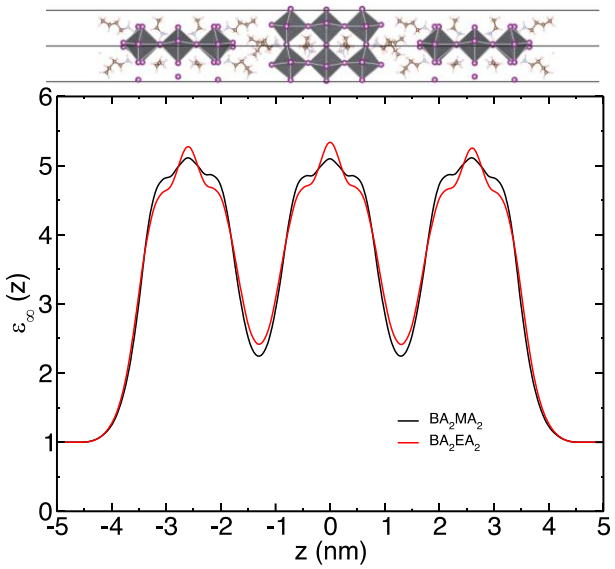

Figure_Apx C.8 High-frequency dielectric profiles $\varepsilon_\infty(z)$ computed without SOC along the stacking axis in $(BA)_2(MA)_2Pb_3I_{10}$ (black) and $(BA)_2(EA)_2Pb_3I_{10}$ (red). This highlights the contrast between the dielectric constants of the molecular spacer and the perovskite sheet. The (010) surface was considered. For technical reasons, the surface was rotated such that the stacking direction corresponds to the z-axis.

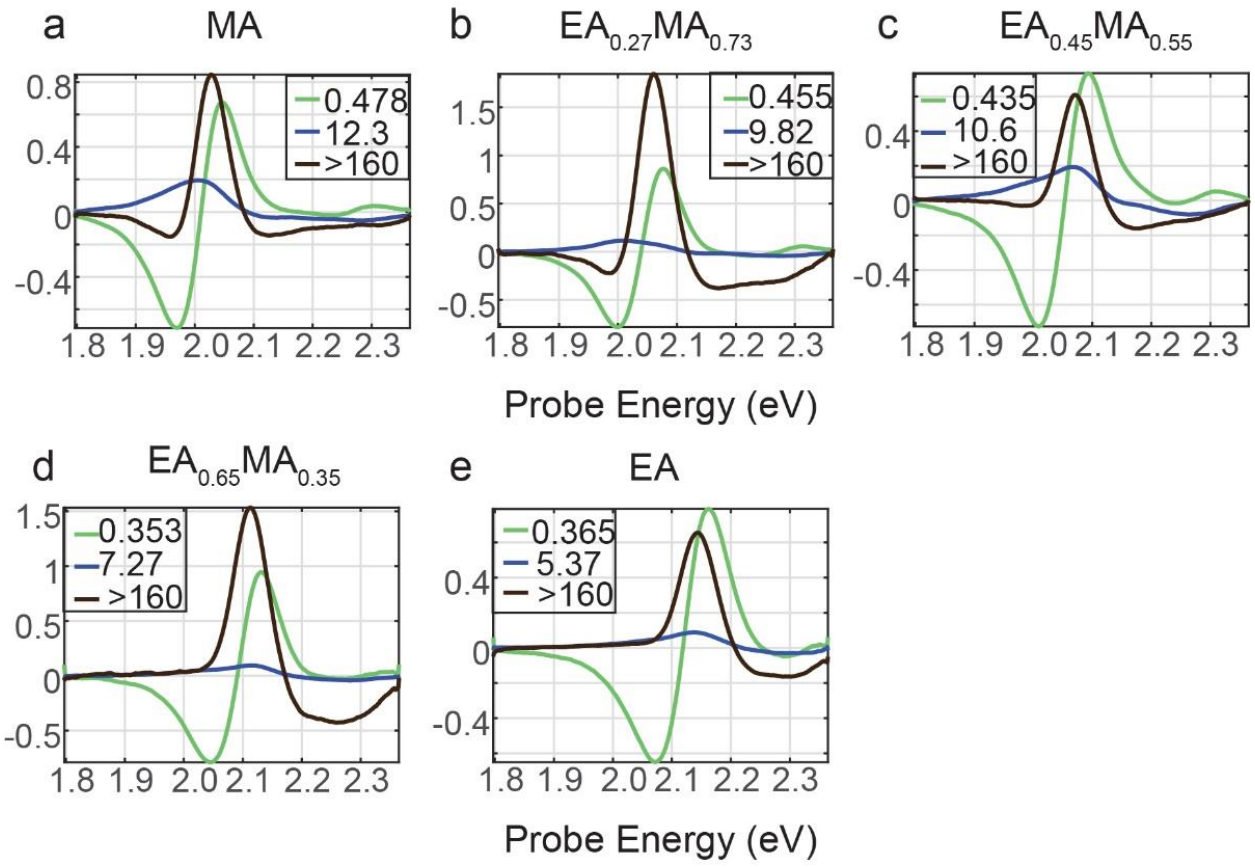

Figure_Apx C.9 Decay associated spectra of the set of $(BA)_2(EA_xMA_{1-x})_2Pb_3I_{10}$ obtained with global analysis.

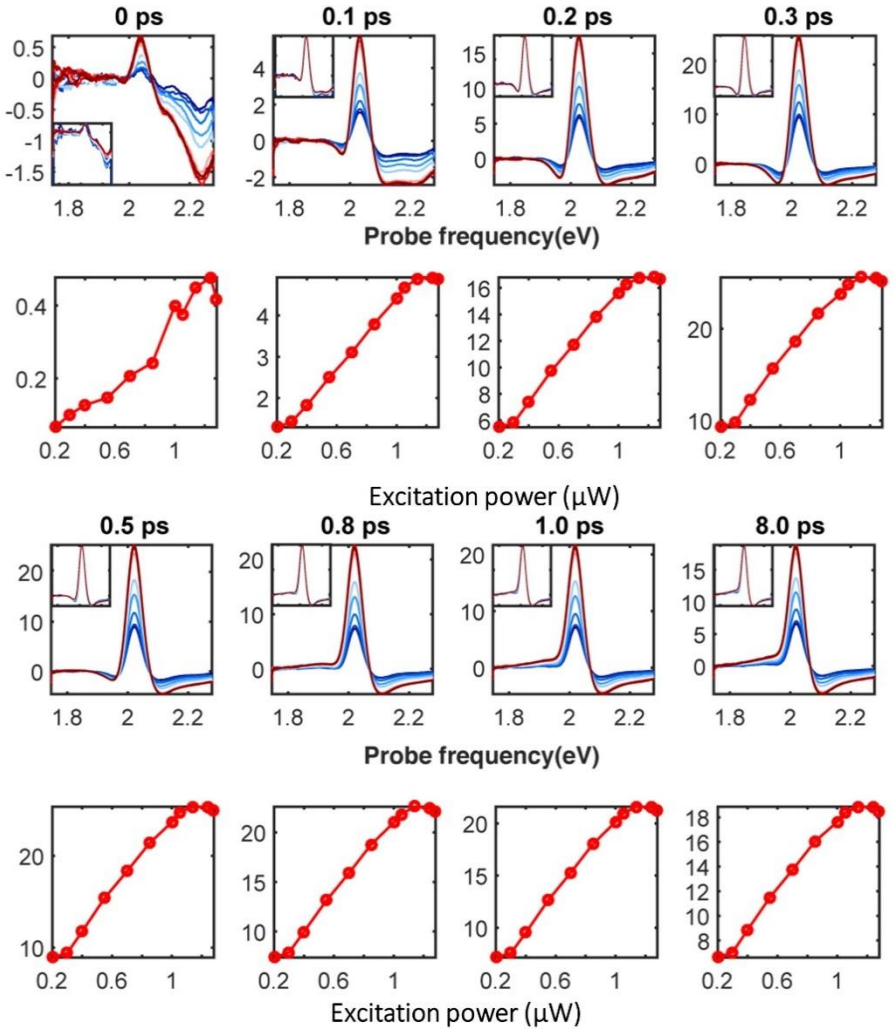

Figure_Apx C.10 Power-dependent study on $(BA)_2(MA)_2Pb_3I_{10}$. (first and third row) TA spectra at representative time points taken with different excitation power (blue: low, red: high) are shown. Inset: normalized TA spectra show minimal change between spectra taken at different excitation power. (second and fourth row) Maximum Intensity of the main bleaching peak as a function of excitation power entering the microscope.

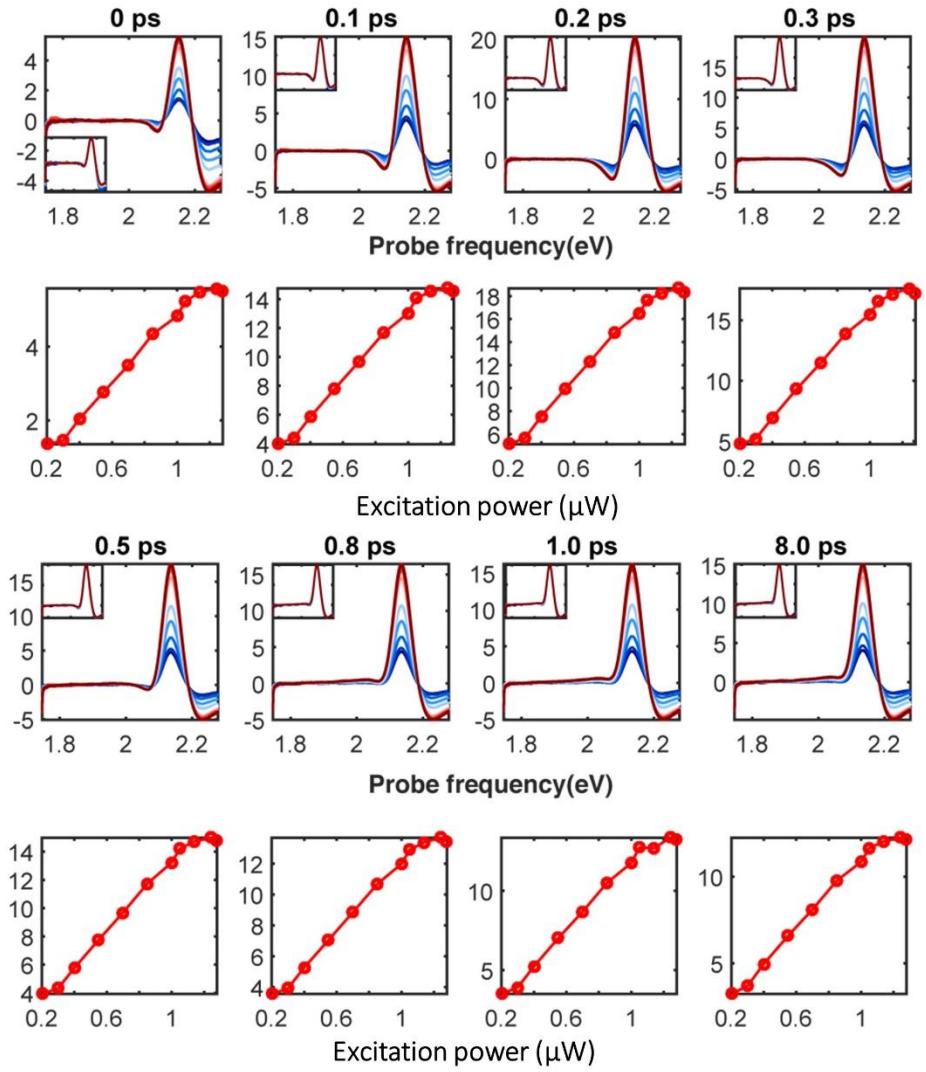

Figure_Apx C.11 Power-dependent study on $(BA)_2(EA)_2Pb_3I_{10}$. (first and third row) TA spectra at representative time points taken with excitation power (blue: low, red: high) are shown. Inset: normalized TA spectra show minimal change between spectra taken at different excitation power. (second and fourth row) Maximum Intensity of the main bleaching peak as a function of excitation power entering the microscope.

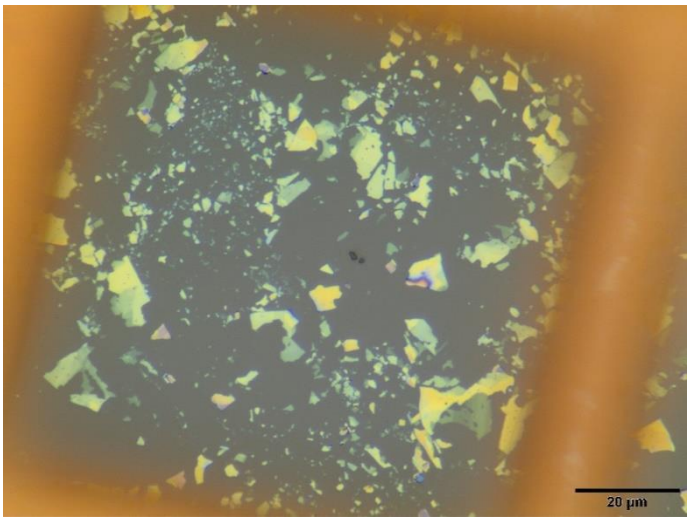

Figure_Apx C.12 Optical image of exfoliated $(BA)_2(MA)_2Pb_3I_{10}$ crystals.

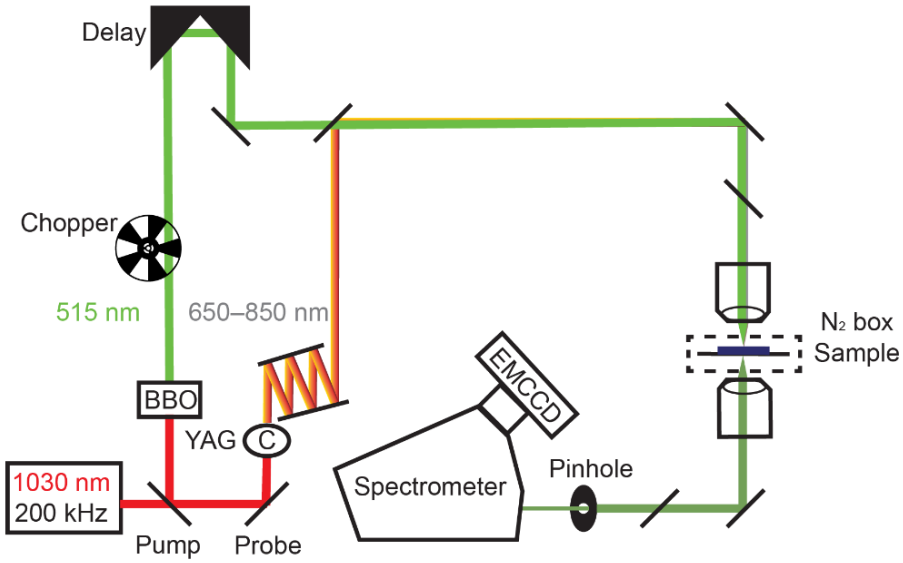

Figure_Apx C.13 Block diagram of the TAM.[29] Beta Barium Borate (BBO), Electron Multiplying CCD (EMCCD).

APPENDIX D Appendix to CHAPTER 5

D.1 Synthesis Methods

All starting materials for synthesis were purchased commercially and were used without further purification, except for Methylamine hydrochloride and Allylamine hydrochloride which were dried in an oven at 70°C. PbO (99.9%), Methylamine hydrochloride ≥ 98% ($CH_3NH_2 \cdot HCl$ = MACl), Hydroiodic acid (HI) (57 wt % in H_2O, distilled, stabilized, 99.95%) and Hypophosphorous acid solution (50 wt % in H_2O) were purchased and used as received from Sigma-Aldrich. Allylamine hydrochloride ($C_3H_5NH_2 \cdot HCl = AA^+Cl^-$) (98%) was purchased from TCI America.

D.1.1 2-Iodopropylammonium iodide (IPA^+I^-)

AA^+Cl^- (10 mmol; 1 g) is dissolved in a mixture of 8 mL HI and 0.5 mL hypophosphorous acid (H_3PO_2) by heating to boiling for four hours, under constant magnetic stirring where a clear solution was obtained. Afterwards, the solution mixture is lowered to 130°C (as stated on hotplate) until the solvent has fully evaporated and a white solid is yielded.

D.1.2 2D Perovskite Series with Allylamine Spacer Cation

$(AA)_2MA_2Pb_3I_{10}$ (*n*=3): PbO (2 mmol; 446 mg) and MACl (1.3 mmol; 88 mg) powders were dissolved in a mixture of 4.5 mL HI and 0.5 mL hypophosphorous acid (H_3PO_2) by heating to boiling under constant magnetic stirring, until a clear yellow solution was obtained. The reaction solution was left on the hotplate to cool to room temperature, under continuing stirring. Next, AA^+Cl^- salt (2 mmol; 187 mg) was added to the reaction solution at room temperature

(R.T.), under continuous stirring. The stirring was discontinued after 10 minutes and the reaction solution was transferred to a petri dish for slow evaporation. Dark red crystals precipitated from the petri dish within 1 day. The crystals were isolated by vacuum filtration and dried under vacuum overnight.

$(AA)_2MA_3Pb_4I_{13}$ (*n*=4): PbO (2 mmol; 446 mg) and MACl (1.5 mmol; 101 mg) powders were dissolved in a mixture of 4.5 mL HI and 0.5 mL hypophosphorous acid (H_3PO_2) by heating to boiling under constant magnetic stirring, until a clear yellow solution was obtained. The reaction solution was left on the hotplate to cool to room temperature, under continuing stirring. Next, AA^+Cl^- salt (1 mmol; 93 mg) was added to the reaction solution at room temperature (R.T.), under continuous stirring. The stirring was discontinued after 10 minutes and the reaction solution was transferred to a petri dish for slow evaporation. Black crystals precipitated from the petri dish within 1 day. The crystals were isolated by vacuum filtration and dried under vacuum overnight.

D.1.3 2D Perovskite Series with Iodopropylamine Spacer Cation

$(IPA)_2MA_2Pb_3I_{10}$ (*n*=3): PbO (2 mmol; 446 mg) and MACl (1.3 mmol; 88 mg) powders were dissolved in a mixture of 4.5 mL HI and 0.5 mL hypophosphorous acid (H_3PO_2) by heating to boiling under constant magnetic stirring, until a clear yellow solution was obtained. Next, IPA^+I^- salt (2 mmol; 372 mg) was added to the reaction solution, under continuous stirring and heating. The stirring was discontinued after 15 minutes and the reaction solution was left on the hotplate to cool to room temperature. Dark red crystals precipitated from the reaction solution. The crystals were isolated by vacuum filtration and dried under vacuum overnight.

$(IPA)_2MA_3Pb_4I_{13}$ (*n*=4): PbO (4 mmol; 892 mg) and MACl (3 mmol; 202 mg) powders were dissolved in a mixture of 8 mL HI and 0.5 mL hypophosphorous acid (H_3PO_2) by heating to boiling under constant magnetic stirring, until a clear yellow solution was obtained. Next, IPA^+I^- salt (2 mmol; 372 mg) was added to the reaction solution, under continuous stirring and heating. The stirring was discontinued after 15 minutes and the reaction solution was left on the hotplate to cool to room temperature. Black crystals precipitated from the reaction solution. The crystals were isolated by vacuum filtration and dried under vacuum overnight.

D.1.4 2D Perovskite Series with Mixed Spacer Cations (Allylamine + Iodopropylamine)

$[(AA)_x(IPA)_{1-x}]_2MA_2Pb_3I_{10}$ (*n*=3): PbO (3 mmol; 669 mg) and MACl (2 mmol; 135 mg) powders were dissolved in a mixture of 5 mL HI and 0.5 mL hypophosphorous acid (H_3PO_2) by heating to boiling under constant magnetic stirring, until a clear yellow solution was obtained. Next, AA^+I^- salt (2 mmol; 187 mg) was added to the reaction solution, under continuous stirring and heating. The stirring was discontinued after 5 minutes and the reaction solution was left on the hotplate to cool to room temperature. Dark red crystals precipitated from the reaction solution. The crystals were isolated by vacuum filtration and dried under vacuum overnight.

$[(AA)_x(IPA)_{1-x}]_2MA_3Pb_4I_{13}$ (*n*=4): PbO (1 mmol; 223 mg) and MACl (0.75 mmol; 55 mg) powders were dissolved in a mixture of 1.5 mL HI and 0.25 mL hypophosphorous acid (H_3PO_2) by heating to boiling under constant magnetic stirring, until a clear yellow solution was obtained. Next, AA^+I^- salt (1 mmol; 93 mg) was added to the reaction solution, under continuous stirring and heating. The stirring was discontinued after 5 minutes and the reaction solution was left on

the hotplate to cool to room temperature. Black crystals precipitated from the reaction solution. The crystals were isolated by vacuum filtration and dried under vacuum overnight.

D.2 Characterization Methods

D.2.1 Single-Crystal X-Ray Diffraction

Single crystal diffraction experiments were performed

(1) Using a four-circle Rigaku XtaLAB Synergy system equipped with a PhotonJet (Mo, λ= 0.71073 Å) micro-focus sealed X-ray tube and Hybrid Pixel Array Detector at 273 K, 293 K and 323 K.

(2) Using either a Bruker Molly or Duo instrument with MoKα IμS microfocus source (λ= 0.71073 Å) with MX Optics at 293 K.

The collected data were integrated and applied with multiscan absorption correction using the APEX3 software. The structure was solved by charge flipping and refined by full-matrix least squares on F^2 with the Jana2006 package. [40]

D.2.2 Powder X-Ray Diffraction

Powder X-ray diffraction patterns were collected on a Rigaku Miniflex system (CuKα radiation) operated at 40 kV and 15 mA. A typical scan rate was 15 sec/step with a step size of 0.02 deg.

D.2.3 Optical Absorption Spectroscopy

Optical diffuse reflectance measurements were performed using a Shimadzu UV-3600 UV−VIS NIR spectrometer operating in the 200−2500 nm region at room temperature. $BaSO_4$ was used as a non-absorbing reflectance reference for all measurements. The bandgap was estimated by diffuse reflectance spectroscopy on powder samples of the studied materials, where the Kubelka-Munk model was used to derive absorption values.

D.2.4 Steady-State Photoluminescence

The samples were excited at 405 nm with an optical parametric amplifier, which was pumped by a Ti:sapphire amplifier (Spectra-Physics) with 800-nm output at 5-MHz repetition rate.

D.2.5 Transient Absorption Microscopy

The fundamental 1030-nm beam was generated from an Yb:KGW amplifier system (Light Conversion, Pharos) operating at 200 kHz with a pulse duration of 190 fs. The fundamental beam was split into pump and probe arms. The tunable pump was generated using a collinear optical parametric amplifier (OPA, 200 – 3000 nm, Light Conversion, Orpheus) and then delayed compared to the probe with a high resolution motorized linear stage (Newport). The pump was modulated at the frequency of 2 kHz by a mechanical chopper (New Focus, Newport). The chopper was synced to the camera using the same clocking source generated by the Pharos laser. The white-light probe (550–750 nm) was generated by focusing the fundamental beam into a YAG crystal. Both beams were recombined and focused collinearly onto the sample with a 74× reflective objective (NA 0.65, Beck). The beam spot size of 0.6 μm was determined by measuring the power passing through a pinhole and then calculated using a Gaussian beam profile. The sample was clamped on a piezo-driven XYZ stage with a resolution of 0.2 μm

(nanoPI, Physik Instrumente). The signal was collected using a 100× refractive objective (NA 0.70, Mitutoyo), spatially filtered through a 150-μm pinhole, and then spectrally dispersed in a spectrometer (Shamrock). The TA signal was detected using a high-speed CMOS camera (Andor, Zyla 4.2). The system was controlled using custom LabVIEW program. Linear absorption and PL maps were measured within the same setup.

D.3 Supplementary Figures

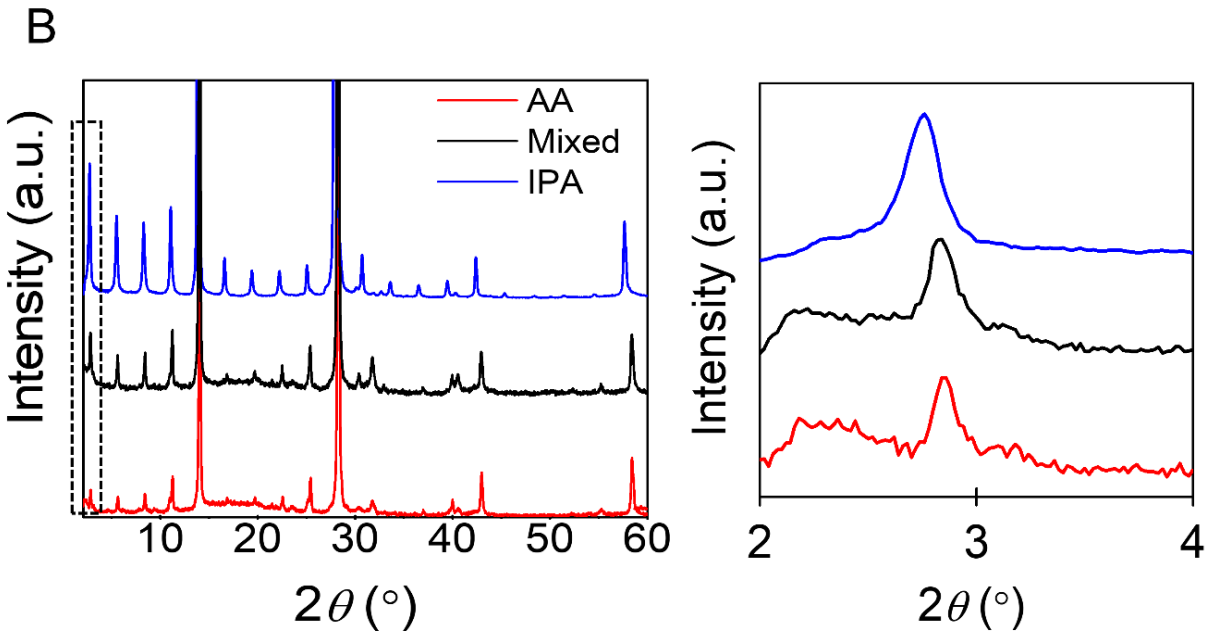

Figure_Apx D.1 (**A**) PXRD pattern for *n*=3 compounds $(AA)_2(MA)_2Pb_3I_{10}$, $[(AA)_x(IPA)_{1-x}]_2(MA)_2Pb_3I_{10}$ and $(IPA)_2(MA)_2Pb_3I_{10}$ along with the expanded view of the (100) reflections. (**B**) PXRD pattern for *n*=4 compounds $(AA)_2(MA)_3Pb_4I_{13}$, $[(AA)_x(IPA)_{1-x}]_2(MA)_3Pb_4I_{13}$ and $(IPA)_2(MA)_3Pb_4I_{13}$ along with the expanded view of the (100) reflections.

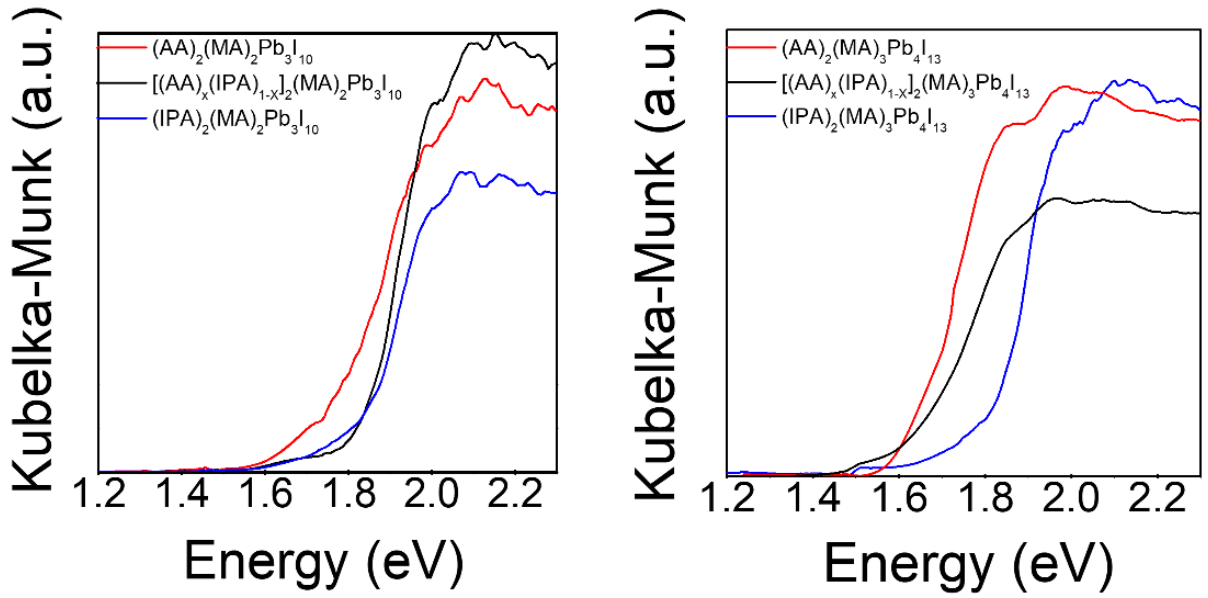

Figure_Apx D.2 Optical absorption spectra of *n*=3 compounds $(AA)_2(MA)_2Pb_3I_{10}$, $[(AA)_x(IPA)_{1-x}]_2(MA)_2Pb_3I_{10}$, and $(IPA)_2(MA)_2Pb_3I_{10}$ and *n*=4 compounds $(AA)_2(MA)_3Pb_4I_{13}$, $[(AA)_x(IPA)_{1-x}]_2(MA)_3Pb_4I_{13}$ and $(IPA)_2(MA)_3Pb_4I_{13}$.

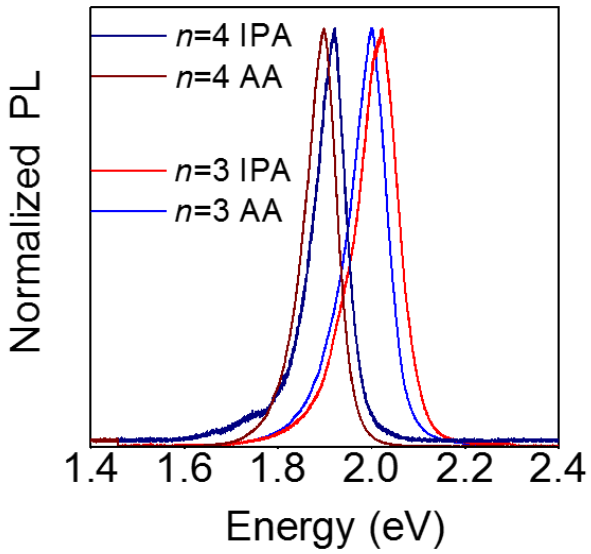

Figure_Apx D.3 Band-edge emission of $(AA)_2(MA)_2Pb_3I_{10}$, $(IPA)_2(MA)_2Pb_3I_{10}$, $(AA)_2(MA)_3Pb_4I_{13}$, and $(IPA)_2(MA)_3Pb_4I_{13}$

Appendix References

1. Nah, S.; Spokoyny, B. M.; Soe, C. M. M.; Stoumpos, C. C.; Kanatzidis, M. G.; Harel, E., Ultrafast imaging of carrier cooling in metal halide perovskite thin films. *Nano Letters* **2018,** *18*, 1044-1048.

2. Yang, Y.; Ostrowski, D. P.; France, R. M.; Zhu, K.; van de Lagemaat, J.; Luther, J. M.; Beard, M. C., Observation of a hot-phonon bottleneck in lead-iodide perovskites. *Nature Photonics* **2015,** *10*, 53-59.

3. Yin, W. J.; Shi, T.; Yan, Y., Unique properties of halide perovskites as possible origins of the superior solar cell performance. *Advanced Materials* **2014,** *26*, 4653-4658.

4. Amat, A.; Mosconi, E.; Ronca, E.; Quarti, C.; Umari, P.; Nazeeruddin, M. K.; Gratzel, M.; De Angelis, F., Cation-induced band-gap tuning in organohalide perovskites: Interplay of spin-orbit coupling and octahedra tilting. *Nano Letters* **2014,** *14*, 3608-3616.

5. Giorgi, G.; Fujisawa, J.; Segawa, H.; Yamashita, K., Small photocarrier effective masses featuring ambipolar transport in methylammonium lead iodide perovskite: A density functional analysis. *The Journal of Physical Chemistry Letters* **2013,** *4*, 4213-4216.

6. Davies, C. L.; Filip, M. R.; Patel, J. B.; Crothers, T. W.; Verdi, C.; Wright, A. D.; Milot, R. L.; Giustino, F.; Johnston, M. B.; Herz, L. M., Bimolecular recombination in methylammonium lead triiodide perovskite is an inverse absorption process. *Nature Communications* **2018,** *9*.

7. Shah, J., Hot-electrons and phonons under high-intensity photoexcitation of semiconductors. *Bulletin of the American Physical Society* **1977,** *22*, 702-702.

8. Fu, J.; Xu, Q.; Han, G.; Wu, B.; Huan, C. H. A.; Leek, M. L.; Sum, T. C., Hot carrier cooling mechanisms in halide perovskites. *Nature Communications* **2017,** *8*, 1300.

9. Joyce, W. B.; Dixon, R. W., Analytic approximations for the fermi energy of an ideal fermi gas. *Applied Physics Letters* **1977,** *31*, 354-356.

10. Nah, S.; Spokoyny, B.; Jiang, X.; Stoumpos, C.; Soe, C. M. M.; Kanatzidis, M. G.; Harel, E., Transient sub-bandgap states in halide perovskite thin films. *Nano Lett* **2018,** *18*, 827-831.

11. Harris, D. C., *Quantitative chemical analysis*. Macmillan: New York, **2010**.

12. Kvam, P. H.; Vidakovic, B., *Nonparametric statistics with applications to science and engineering*. John Wiley & Sons: New Jersey, **2007**.

13. Marsaglia, G.; Tsang, W. W.; Wang, J., Evaluating kolmogorov's distribution. *Journal of Statistical Software* **2003,** *8*.

14. Ke, W.; Spanopoulos, I.; Stoumpos, C. C.; Kanatzidis, M. G., Myths and reality of hpbi3 in halide perovskite solar cells. *Nature Communications* **2018,** *9*, 4785.

15. Grancini, G.; D'Innocenzo, V.; Dohner, E. R.; Martino, N.; Kandada, A. R. S.; Mosconi, E.; De Angelis, F.; Karunadasa, H. I.; Hoke, E. T.; Petrozza, A., Ch3nh3pbi3 perovskite single crystals: Surface photophysics and their interaction with the environment. *Chemical Science* **2015,** *6*, 7305-7310.

16. Sun, Q.; Fassl, P.; Becker-Koch, D.; Bausch, A.; Rivkin, B.; Bai, S.; Hopkinson, P. E.; Snaith, H. J.; Vaynzof, Y., Role of microstructure in oxygen induced photodegradation of methylammonium lead triiodide perovskite films. *Advanced Energy Materials* **2017,** *7*.

17. Leng, K.; Abdelwahab, I.; Verzhbitskiy, I.; Telychko, M.; Chu, L.; Fu, W.; Chi, X.; Guo, N.; Chen, Z.; Chen, Z.; Zhang, C.; Xu, Q.-H.; Lu, J.; Chhowalla, M.; Eda, G.; Loh, K. P., Molecularly thin two-dimensional hybrid perovskites with tunable optoelectronic properties due to reversible surface relaxation. *Nature Materials* **2018,** *17*, 908-914.

18. Stoumpos, C. C.; Cao, D. H.; Clark, D. J.; Young, J.; Rondinelli, J. M.; Jang, J. I.; Hupp, J. T.; Kanatzidis, M. G., Ruddlesden–popper hybrid lead iodide perovskite 2d homologous semiconductors. *Chemistry of Materials* **2016,** *28*, 2852-2867.

19. Hohenberg, P.; Kohn, W., Inhomogeneous electron gas. *Physical Review* **1964,** *136*, B864-B871.

20. Kohn, W.; Sham, L. J., Self-consistent equations including exchange and correlation effects. *Physical Review* **1965,** *140*, A1133-A1138.

21. Soler, J. M.; Artacho, E.; Gale, J. D.; García, A.; Junquera, J.; Ordejón, P.; Sánchez-Portal, D., The siesta method forab initioorder-nmaterials simulation. *Journal of Physics: Condensed Matter* **2002,** *14*, 2745-2779.

22. Troullier, N.; Martins, J. L., Efficient pseudopotentials for plane-wave calculations. *Physical Review B* **1991,** *43*, 1993-2006.

23. Even, J.; Pedesseau, L.; Kepenekian, M., Electronic surface states and dielectric self-energy profiles in colloidal nanoscale platelets of cdse. *Physical Chemistry Chemical Physics* **2014,** *16*, 25182-25190.

24. Sapori, D.; Kepenekian, M.; Pedesseau, L.; Katan, C.; Even, J., Quantum confinement and dielectric profiles of colloidal nanoplatelets of halide inorganic and hybrid organic–inorganic perovskites. *Nanoscale* **2016,** *8*, 6369-6378.

25. Gonze, X.; Amadon, B.; Anglade, P. M.; Beuken, J. M.; Bottin, F.; Boulanger, P.; Bruneval, F.; Caliste, D.; Caracas, R.; Côté, M.; Deutsch, T.; Genovese, L.; Ghosez, P.; Giantomassi, M.; Goedecker, S.; Hamann, D. R.; Hermet, P.; Jollet, F.; Jomard, G.; Leroux, S.; Mancini, M.; Mazevet, S.; Oliveira, M. J. T.; Onida, G.; Pouillon, Y.; Rangel, T.; Rignanese, G. M.; Sangalli, D.; Shaltaf, R.; Torrent, M.; Verstraete, M. J.; Zerah, G.; Zwanziger, J. W., Abinit: First-principles approach to material and nanosystem properties. *Computer Physics Communications* **2009,** *180*, 2582-2615.

26. Hartwigsen, C.; Goedecker, S.; Hutter, J., Relativistic separable dual-space gaussian pseudopotentials from h to rn. *Physical Review B* **1998,** *58*, 3641-3662.

27. Marques, M. A. L.; Oliveira, M. J. T.; Burnus, T., Libxc: A library of exchange and correlation functionals for density functional theory. *Computer Physics Communications* **2012,** *183*, 2272-2281.

28. Traoré, B.; Bouder, G.; Lafargue-Dit-Hauret, W.; Rocquefelte, X.; Katan, C.; Tran, F.; Kepenekian, M., Efficient and accurate calculation of band gaps of halide perovskites with the tran-blaha modified becke-johnson potential. *Physical Review B* **2019,** *99*, 035139.

29. Jiang, X.; Hoffman, J.; Stoumpos, C. C.; Kanatzidis, M. G.; Harel, E., Transient sub-band-gap states at grain boundaries of ch3nh3pbi3 perovskite act as fast temperature relaxation centers. *ACS Energy Letters* **2019,** *4*, 1741-1747.

30. Pedesseau, L.; Sapori, D.; Traore, B.; Robles, R.; Fang, H.-H.; Loi, M. A.; Tsai, H.; Nie, W.; Blancon, J.-C.; Neukirch, A.; Tretiak, S.; Mohite, A. D.; Katan, C.; Even, J.; Kepenekian, M., Advances and promises of layered halide hybrid perovskite semiconductors. *ACS Nano* **2016,** *10*, 9776-9786.

31. Nazarenko, O.; Kotyrba, M. R.; Yakunin, S.; Aebli, M.; Rainò, G.; Benin, B. M.; Wörle, M.; Kovalenko, M. V., Guanidinium-formamidinium lead iodide: A layered perovskite-related compound with red luminescence at room temperature. *Journal of the American Chemical Society* **2018,** *140*, 3850-3853.

32. Mao, L.; Ke, W.; Pedesseau, L.; Wu, Y.; Katan, C.; Even, J.; Wasielewski, M. R.; Stoumpos, C. C.; Kanatzidis, M. G., Hybrid dion–jacobson 2d lead iodide perovskites. *Journal of the American Chemical Society* **2018,** *140*, 3775-3783.

33. Li, X.; Hoffman, J.; Ke, W.; Chen, M.; Tsai, H.; Nie, W.; Mohite, A. D.; Kepenekian, M.; Katan, C.; Even, J.; Wasielewski, M. R.; Stoumpos, C. C.; Kanatzidis, M. G., Two-dimensional halide perovskites incorporating straight chain symmetric diammonium ions, $(nh_3c_mh_{2m}nh_3)(ch_3nh_3)_{n-1}pb_ni_{3n+1}$ (m = 4–9; n = 1–4). *Journal of the American Chemical Society* **2018,** *140*, 12226-12238.

34. Spanopoulos, I.; Hadar, I.; Ke, W.; Tu, Q.; Chen, M.; Tsai, H.; He, Y.; Shekhawat, G.; Dravid, V. P.; Wasielewski, M. R.; Mohite, A. D.; Stoumpos, C. C.; Kanatzidis, M. G.,

Uniaxial expansion of the 2d ruddlesden–popper perovskite family for improved environmental stability. *Journal of the American Chemical Society* **2019,** *141*, 5518-5534.

35. Soe, C. M. M.; Stoumpos, C. C.; Kepenekian, M.; Traoré, B.; Tsai, H.; Nie, W.; Wang, B.; Katan, C.; Seshadri, R.; Mohite, A. D.; Even, J.; Marks, T. J.; Kanatzidis, M. G., New type of 2d perovskites with alternating cations in the interlayer space, $(c(nh_2)_3)(ch_3nh_3)_npb_ni_{3n+1}$: Structure, properties, and photovoltaic performance. *Journal of the American Chemical Society* **2017,** *139*, 16297-16309.

36. Marronnier, A.; Roma, G.; Boyer-Richard, S.; Pedesseau, L.; Jancu, J.-M.; Bonnassieux, Y.; Katan, C.; Stoumpos, C. C.; Kanatzidis, M. G.; Even, J., Anharmonicity and disorder in the black phases of cesium lead iodide used for stable inorganic perovskite solar cells. *ACS Nano* **2018,** *12*, 3477-3486.

37. Weller, M. T.; Weber, O. J.; Frost, J. M.; Walsh, A., Cubic perovskite structure of black formamidinium lead iodide, α-$[hc(nh_2)_2]pbi_3$, at 298 k. *The Journal of Physical Chemistry Letters* **2015,** *6*, 3209-3212.

38. Stoumpos, C. C.; Malliakas, C. D.; Kanatzidis, M. G., Semiconducting tin and lead iodide perovskites with organic cations: Phase transitions, high mobilities, and near-infrared photoluminescent properties. *Inorganic chemistry* **2013,** *52*, 9019-9038.

39. Even, J.; Pedesseau, L.; Katan, C., Understanding quantum confinement of charge carriers in layered 2d hybrid perovskites. *ChemPhysChem* **2014,** *15*, 3733-3741.

40. Petříček, V.; Dušek, M.; Palatinus, L., Crystallographic computing system jana2006: General features. In *Zeitschrift für Kristallographie - Crystalline Materials*, 2014; Vol. 229, p 345.